technische universität
dortmund

mpi
dortmund

Investigation of the properties of Acyl Protein Thioesterases and their role in Ras depalmitoylation

Zur Erlangung des akademischen Grades

Doktor der Naturwissenschaften (Dr. rer. nat.)

der Fakultät für Chemie und Chemische Biologie

der Technischen Universität Dortmund

Dissertation

von

Stefan Baumeister

Dezember 2017

Die vorliegende Arbeit wurde in der Zeit von Mai 2013 bis Dezember 2017 am Max-Planck-Institut für molekulare Physiologie in Dortmund unter Anleitung von Dr. Ingrid Vetter durchgeführt.

1. Gutachter: Prof. Dr. Roland Winter
Technische Universität Dotmund

2. Gutachter: Prof. Dr. Andrea Musacchio
Max-Planck-Institut Dortmund

Tag der mündlichen Prüfung: 30. Januar 2018

Contents

Abbreviations

2-BP	2-Bromopalmitat (actually 2-bromopalmitic acid)
aa	Amino acid(s)
a.u.	Arbitrary unit
au	asymmetric unit
APT	Acyl protein thioesterase
$CaCl_2$	Calciumchloride
CHAPS	3-[(3-Cholamidopropyl)dimethylammonio]-1- propanesulfonate
DiFMUO	6,8-difluoro-4-methylumbelliferyl octanoate
DMSO	Dimethyl sulfoxide
DOPC	1,2-dioleoyl-sn-glycero-3-phosphocholine
DPPC	1,2-dipalmitoyl-sn-glycero-3-phosphocholine
EGF	Epidermal growth factor
eNOS	Endothelial nitric oxide synthase
ERK	Extracellular signal-regulated kinase
ESI-MS	Mass spectrometry by electrospray ionization
FKBP2	FK506 binding protein 2
GAP	GTPase-activating protein
GAP-43	Growth Associated Protein 43
GDP	Guanosine diphosphate
GEF	Guanine nucleotide exchange factor
GTP	Guanosine triphosphate
HPTS	1-hydroxypyrene-3,6,8-trisulfonic acid trisodium salt
IC_{50}	Half maximal inhibitory concentration
k_{cat}	Rate constant
K_d	Dissociation constant
K_i	Inhibition constant
K_m	Michaelis constant
LPTS	1-lauroyloxypyrene-3,6,8-trisulfonic acid trisodium salt
LYPLA	Lysophospholipase (later named APT)
LYPLAL1	Lysophospholipase-like

lyso-PPC	1-palmitoyl-2-hydroxy-sn-glycero-3-phosphocholine
MAPK	Mitogen-activated protein kinase
OPTS	1-octanoyloxypyrene-3,6,8-trisulfonic acid trisodium salt
PDB	Protein data bank
PEG	Polyethylen glycol
pNP	para-Nitrophenol
PPT	Palmitoyl-protein thioesterase
PPTS	1-palmitoyloxypyrene-3,6,8-trisulfonic acid trisodium salt
RMSD	Root-mean-square deviation
SH2	Src homology 2 domain
SNAP-25	Synaptosomal protein 25
SOS	Son of Sevenless
V_i	Initial velocity
V_{max}	Maximum rate in Michaelis-Menten equation
wt	wild type

Amino acids and nucleobases were referred to as their respective one-letter or three-letter code, according to the recommendations of the International Union of Pure and Applied Chemistry (IUPAC) and the International Union of Biochemistry and Molecular Biology (IUB).

List of Figures

List of Tables

Summary

Acyl Protein Thioesterases 1 and 2 (APT1 and APT2) were described to depalmitoylate the small GTPases H- and N-Ras, thus establishing an acylation cycle, in which Ras shuttles between the site of palmitoylation at the Golgi and the site of its biological activity of signal transduction at the plasma membrane. The inhibition of mutated, constitutively active Ras proteins, which occur in 20 - 30 % of all human cancer cells, is an intensively pursued aim. Since direct attempts of Ras inhibition failed so far, alternative strategies were conceived like modulation of Ras signaling by interfering with its proper membrane distribution and hence biological activity. It was shown that the inhibition of APT proteins by palmostatin B changed the localization of palmitoylated Ras and led to a down-regulation of Ras signaling. Besides this particular activity of APT several other protein targets of APT were described, some of them as specific substrates for one of the two isoforms. Furthermore, APT activity was also linked to non-protein substrates like (lyso-)phospholipids and prostaglandin glycerol esters. Still, the real physiological function of the conserved and ubiquitously expressed APT proteins remains elusive.

This thesis provides new insights into possible physiological roles of APT and its isoforms by focusing on the interaction of different substrates, ligands and inhibitors with APT proteins. The results help to answer the question what kind of substrates APT prefers, how substrate specificity is achieved and how APTs might have evolved in the different eukaryotic species.

To achieve this, different *in vitro* assays were successfully established: A robust and reliable fluorogenic activity assay was set up to determine activity and also inhibition of APT proteins, using the octanoyl-ester (OPTS) of the well soluble pyrene-based HPTS fluorophore as substrate. In contrast to standard applications, no detergents are required due to the excellent solubility of OPTS. A second assay allowed detection of ligand binding to two distinct sites of APT via quenching of intrinsic tryptophan fluorescence by using Trp-mutants of *h*APT1. Activity of APT on (lyso-)phospholipids and triglycerides was evaluated with an agar-based turbidity assay, and a fluorescence polarization (FP) approach allowed detection of the binding of palmitoylated peptides to APT and monitoring of depalmitoylation of the membrane-bound peptides.

According to the results of this thesis, both APT isoforms of human (*h*APT1 and

*h*APT2) and xenopus (*xt*APT1 and *xt*APT2), as well as the APT from drosophila (*dm*APT) show comparable activities on the artificial OPTS substrate, as well as on the hydrolysis of (lyso-)phospholipids. Contrary to that, the APT homologue from yeast (*y*APT) appears unique in the conversion of both substrates: While *y*APT is much faster and more efficient at cleavage of the short chained OPTS ester, compared to the other investigated APT proteins, it appears much slower in the conversion of the longer chained (lyso-)phospholipids, indicating a preference for short-chained substrates.

Confirming this, the binding of two different palmitoylated peptides to *y*APT appears to be much weaker compared to *h*APT1, again pointing towards an inability of *y*APT to bind longer-chained substrates with high affinity. In contrast, *h*APT1 shows a preference for long-chained ligands, e.g. palmitoylated peptides or esters with an aliphatic C12 or C16 moiety, as an experiment with synthesized variants of OPTS, containing a lauroyl- or palmitoyl- aliphatic tail, showed.

Experiments using an fluorescence polarization assay revealed that both human APTs are able to cleave a palmitoylated, membrane-bound nonapeptide. This happens much slower than in solution, but probably contains a rate-limiting membrane-extraction step of the peptide that can be performed more efficiently by *h*APT2 than *h*APT1.

The combination of the introduced assay systems with X-ray crystallography allowed a detailed analysis of inhibitor binding to APT: First, the very similar binding mode of 2-bromopalmitate (2-BP) in the binding tunnel of *h*APT1 and *h*APT2 could be revealed. Inhibition of APT proteins by 2-BP occurs for all investigated proteins except for *y*APT, which was not inhibited by this long-chained ligand. Furthermore, 2-BP was shown to influence the structure of *h*APT1 proteins when used at higher concentrations, leading to an increased thermostability. Second, the detailed binding mode of the described isoform-selective inhibitors ML348 and ML349 could be revealed by structural analysis. By using appropriate APT mutants, two amino acids were identified which are not only responsible for the isoform selectivity of both inhibitors, but are - upon mutation - indeed able to switch the selectivity of both isoforms to one or the other inhibitor, which suggest that these residues might also play a role in the selectivity for natural substrates. Finally, a structure-based drug design approach was successful in identifying and improving novel, competitive and isoform selective inhibitors of *h*APT2 activity.

The structural and biochemical comparison of APTs in different organisms, e.g. Yeast, Toxoplasma gondii, Drosophila and Xenopus revealed an evolutionary relationship of the single APT gene in insects to the APT2 isoform of vertebrates, whereas the single “APT” gene of fungi might actually be more active on substrates with shorter acyl chains, contrary to the proposed role of *y*APT in depalmitoylation reactions.

Zusammenfassung

Die Depalmitoylierung der kleinen GTPasen H- und N-Ras durch die Acyl Protein Thioesterasen 1 und 2 (APT1 und 2) etabliert einen Acylierungs-Zyklus, in dem Ras zwischen dem Golgi-Apparat - dem Ort ihrer Palmitoylierung - und der Plasmamembran - dem Ort ihrer biologischen Aktivität - pendeln. Die Inhibition von Ras ist von großer Bedeutung, da mutierte, permanent aktive Ras Proteine in 20 - 30 % aller humanen Tumore gefunden werden. Da die direkte Inhibition von Ras bisher jedoch erfolglos war, wurden alternative, indirekte Strategien entwickelt. Es wurde gezeigt, dass Inhibition von APT Proteinen die Lokalisierung von palmitoylierten Ras Proteinen derart verändern kann, dass eine Reduzierung der Ras Aktivität beobachtet wird. Die genaue physiologische Rolle von APT ist allerdings weiterhin unklar, da sowohl weitere palmitoylierte Proteine, als auch (Lyso-)Phospholipide und Prostaglandine als Substrate von APT beschrieben wurden.

Die hier vorliegende Arbeit liefert, durch Untersuchung der Interaktionen verschiedener Substrate, Liganden und Inhibitoren mit APT, neue Erkenntnisse bezüglich möglicher zellulärer Aufgaben von APT. Die gewonnenen Resultate helfen zu bestimmen, welche Substrate von APT bevorzugt werden, wie eine Substratspezifität erreicht wird und wie sich APT im Laufe der Evolution in verschiedenen eukaryotischen Spezies entwickelt hat.

Verschiedene *in vitro* Assays wurden für die Beantwortung dieser Fragen entwickelt: Ein zuverlässiger Fluoreszenz-basierter Assay wurde etabliert, in dem der Octanoyl-Ester (OPTS) des gut löslichen, Pyren-basierten HPTS-Fluorophors als Substrat für APT dient. Mit Hilfe eines Tryptophan-Assays, der auf der Auslöschung der intrinsischen Tryptophanfluoreszenz beruht, und entsprechender APT Mutanten, kann die Bindung eines Liganden an zwei verschiedene Stellen des APT Proteins detektiert werden. Die Umsetzung von (Lyso-)Phospholipiden und Triglyceriden kann mit Hilfe eines Agar-basierten Trübungsassays verfolgt werden und ein Fluoreszenzpolarisations-Assay (FP-Assay) erlaubt sowohl die Detektion der Bindung von palmitoylierten Peptiden an APT, als auch die Depalmitoylierung dieser Peptide in Gegenwart einer Membran.

Die Resultate dieser Arbeit zeigen, dass sowohl beide humanen APT Isoformen des Menschen (hAPT1 und hAPT2), als auch beide APT Isoformen des Krallenfrosches (xtAPT1 und xtAPT2) und die APT der Fruchtfliege (dmAPT) vergleichbare Aktivi-

täten bei der Umsetzung des artifiziellen OPTS Substrats sowie von (Lyso-)Phospholipiden zeigen. Das APT Protein der Hefe (yAPT) grenzt sich hier eindeutig von den anderen Proteinen ab: Während es das kurzkettige OPTS deutlich schneller und effizienter spaltet, fällt die Aktivität gegenüber den langkettigen (Lyso-)Phospholipiden deutlich geringer aus, was für die Bevorzugung von kurzkettigen Substraten spricht.

Auch die Bindung zweier palmitoylierter Peptide erfolgt gegenüber yAPT mit einer deutlich geringeren Affinität als dies für hAPT1 der Fall ist. Diese Beobachtung weist wieder auf ein gewisses Unvermögen des yAPT Proteins hin, langkettige Liganden mit hoher Affinität zu binden. Im Gegensatz dazu weist hAPT1 eine Präferenz für eben solche langkettigen Substrate auf, wie ein Versuch mit synthetisierten, langkettigen Derivaten von OPTS zeigen konnte.

Mit Hilfe des Fluoreszenzpolarisations-Assays konnte gezeigt werden, dass beide humanen APT Isoformen in der Lage sind ein palmitoyliertes, membran-gebundenes Nonapeptid umzusetzen. Dies geschieht deutlich langsamer als in Lösung, höchstwahrscheinlich weil eine langsame Membranextraktion des Peptids notwendig ist. Dieser Schritt kann deutlich effizienter von hAPT2 umgesetzt werden als von hAPT1.

Die Kombination der eingeführten Assays und der Röntgenstrukturanalyse erlaubte die detaillierte Untersuchung der Inhibitorbindung an APT Proteine: Zunächst konnte der sehr ähnliche Bindungsmodus von 2-Bromopalmitat (2-BP) an hAPT1 und hAPT2 aufgeklärt werden. Die Inhibition der APT Proteine erfolgte mit ähnlicher Affinität, wobei yAPT erneut eine Ausnahme bildete, da es nicht durch das langkettige 2-BP inhibiert wird. Weiterhin konnte der detaillierte Bindungsmodus der bekannten, isoformspezifischen APT Inhibitoren ML348 und ML349 bestimmt werden. Mit Hilfe mehrerer APT Mutanten, konnten zwei Aminosäuren identifiziert werden, die für die Selektivität der beiden APT Isoformen gegenüber dem entsprechenden Inhibitor verantwortlich sind. Ein Austausch dieser beiden Aminosäuren zwischen APT1 und APT2 resultiert in einer kompletten Selektivitätsumkehr, die die Bindung des anderen isoformspezifischen Inhibitors erlaubt. Daher kann von einer Beteiligung dieser Reste auch an der Diskriminierung von natürlichen Substraten ausgegangen werden. Mit Hilfe eines Ansatzes zum strukturbasierten Wirkstoffdesign konnte erfolg verfolgt, welcher neuartige APT2 Inhibitoren hervorbrachte.

Der strukturelle und biochemische Vergleich von APT Proteinen aus verschiedenen Organismen, wie der Hefe, Toxoplasma gondii, der Fruchtfliege und des Krallenfrosches zeigten eine evolutionäre Verwandtschaft des einzelnen APT Gens in Insekten zu der APT2 Isoform der Wirbeltiere, während das einzelne „APT“ Gen in Pilzen vermutlich kürzere Substrate bevorzugt, was im Gegensatz zur postulierten Rolle von yAPT steht.

1 Introduction

1.1 The molecular switch Ras

The small GTPase Ras is a key player in cell signal transduction. By cycling between a GTP-bound active state and a GDP-bound inactive state Ras can act as a molecular switch [1] (see figure 1.1) in the MAPK/ERK pathway [2], [3]. Active Ras is able to interact with effectors that transmit the signal further downstream where it can influence embryogenesis, cell differentiation, cell growth or apoptosis [4]. In a first step of this

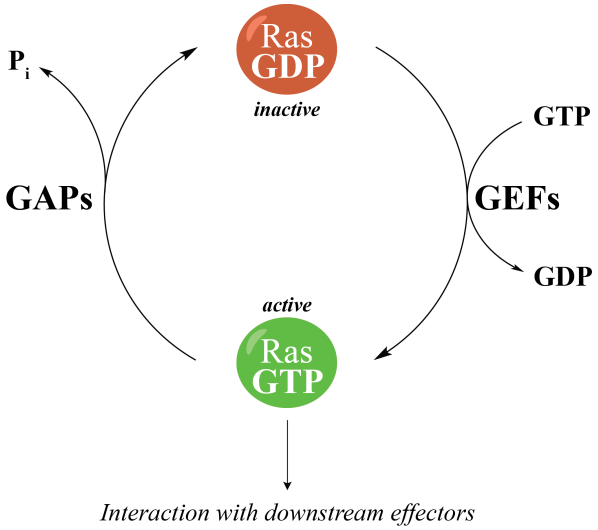

Figure 1.1: The molecular switch Ras. Guanine nucleotide exchange factors (GEFs) catalyze the dissociation of GDP from inactive Ras thereby promoting the exchange to GTP. In the GTP-bound state Ras is active and can interact with downstream effectors to influence various cellular responses. GTPase-activating proteins (GAPs) accelerate the hydrolysis of GTP back to GDP and thus the return of Ras back to its inactive state.

cascade extracellular binding of growth factors, for instance EGF (epidermal growth factor), to the corresponding receptors induces their dimerization and a subsequent transphosphorylation at the cytoplasmatic side. This generates a binding site for SH2 (src homology 2) domain containing proteins, like Grb2 (growth factor receptor binding 2) which is an adaptor for the Ras guanine nucleotide exchange factor (GEF) named SOS (son-of-sevenless) [5]–[7]. This GEF protein catalyzes the dissociation of GDP from Ras and enables the exchange for GTP, which shows a ten times higher cellular con-

centration compared to GDP. The binding of GTP induces a structural rearrangement and thus an activation of the Ras protein [8]. The hydrolysis of GTP back to GDP terminates the signal transduction. This intrinsic slow hydrolysis is accelerated by the interaction of Ras-GTP with GTPase-activating proteins (GAPs) [9], [10].

The most significant reason why the *Ras pathway* is one of the best-studied signal transduction pathways is the frequent appearance of mutated Ras in cancer cells. Up to 30 % of human tumors carry a mutated Ras oncogene. In some cancer types, such as the pancreatic endocrine tumor, Ras is found to be mutated in more than 70 % of the cases [11]. Mutated Ras proteins found in cancer cells are constitutively active due to point mutations predominantly of amino acids G12, G13 or Q61 that all result in the inability of Ras to hydrolyze GTP and thus returning back to the inactive state [12], [13].

There are three human Ras genes encoding for the three versions H-Ras [14], N-Ras [15] and K-Ras [16]. In addition, the latter one can be spliced into two variants K-Ras4A and K-Ras4B [12], [17]. The four Ras isoforms are > 90 % identical but differ in their C-terminal 20 amino acids, also known as the hyper-variable region (HVR) that contains all the information required to target various sub-cellular membrane compartments [18]. All Ras proteins contain a CAAX motif in their HVR, where two aliphatic amino acids (A) and a variable amino acid (X) follow a cysteine residue (C). The identity of X determines how the cysteine is modified [19]. Since in Ras either a serine or methionine residue is present at this position the cysteine gets irreversibly and post-translationally farnesylated [20] by a farnesyltransferase [21], leading to a (weak) affinity to all endomembranes [22]. While in the case of K-Ras4B an additional polybasic region next to the CAAX box is increasing the plasma membrane affinity [23], the other Ras proteins can additionally be lipidated at cysteine residues upstream of the CAAX box. N-Ras and K-Ras4A are reversibly palmitoylated [24] once by palmitoyl acyltransferases (PATs), while H-Ras can get palmitoylated twice at two neighbored cysteines [25], [26]. Palmitoylation is taking place mainly at the Golgi apparatus [27], [28] where the lipidated proteins enter the secretory pathway and are transported to the plasma membrane [19], [29]. Retrograde traffic of N-Ras, H-Ras and K-Ras4A ensures localization back to the Golgi after depalmitoylation. This diffusion is enhanced by the farnesyl-chaperone phosphodiesterase 6 delta-subunit (PDE6δ) [30]. The dynamic acylation [24] leads to a palmitoylation/depalmitoylation cycle that regulates the shuttling of H- and N-Ras between the plasma membrane and the Golgi and prevents Ras from nonspecific distribution to other endomembranes (see figure 1.2) [27]. This control of spatial distribution of Ras via its palmitoylation state also regulates its biological activity that is dependent on proper plasma membrane localization [27]. Acyl Protein Thioesterase 1 (APT1) was identified as a hydrolase responsible for the depalmitoylation of Ras and thus being substantially involved in the described palmitoylation/depalmitoylation cycle [32]. Additionally, the prolyl isomerase FKBP12 was proposed to

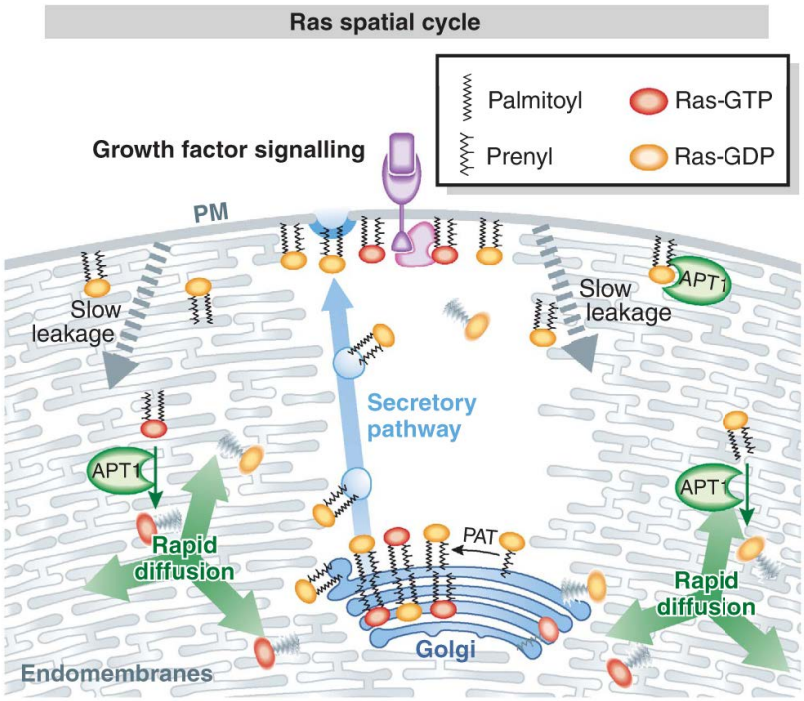

Figure 1.2: The acylation cycle of Ras. Farnesylated H- and N-Ras is additionally palmitoylated at the Golgi by Palmitoyl Transferases (PAT) and transported to the plasma membrane via the secretory pathway. Here it can be activated and transmits an extracellular signal further downstream. Palmitoylated Ras will slowly redistribute to all membranes until depalmitoylation by APT1 corrects this mislocalization, because solely farnesylated Ras will diffuse more rapidly thus increasing the probability to be re-palmitoylated at the Golgi. Figure modified from [31].

participate in the regulation of H-Ras trafficking by promoting its depalmitoylation through cis-trans isomerization of a peptidyl-prolyl bond in proximity to the palmitoylated cysteines [33] .Because of the frequent involvement of Ras in cancer, Ras proteins were identified as potential anticancer targets and strategies for efficient inhibition and downregulation of oncogenic, constitutively active Ras were extensively studied [34] . Although new approaches were recently developed to target Ras, so far no drug or drug candidate was found to disturb protein-protein interaction between Ras and downstream effectors via direct binding to Ras proteins [35], [36] . This might be because Ras proteins do not show any sufficiently deep cavity on their surface that could be targeted by small molecules, beside the nucleotide-binding pocket [36] . Alternative approaches of inhibiting Ras signaling indirectly by interference with downstream effectors failed because of drug resistance development and complex feedback mechanisms [37] . Inhibitors of farnesyl transferase, for instance Tipifarnib or Lonafarnib, were developed to prevent proper membrane localization of Ras [34] . Although they show impressive anti-H-Ras and anti-tumor activity in preclinical cell culture studies [38], [39] and in a mouse model [40] , the clinical efficacy could not be proven, probably because of several reasons, for instance a compensatory lipidation of K-Ras and N-Ras by geranylgeranyl

transferases [41]–[45] . Impairment of Ras localization at the plasma membrane was also exploited in another approach, where APT1, the thioesterase responsible for the depalmitoylation of Ras, was targeted by small molecules. It was shown that β–lactone based inhibitors like palmostatin B [32] and palmostatin M [46] inhibit APT1 as well as the second isoform APT2 [47] (see section 1.2.4), thereby disturbing the accurate H- and N-Ras steady-state localization at the plasma membrane. According to the current hypothesis, this mislocalization led to Ras distribution over all cellular membranes, thus resulted in a decreased local concentration at the plasma membrane and finally to a decreased signaling activity of Ras (see figure 1.3) [32], [48] .

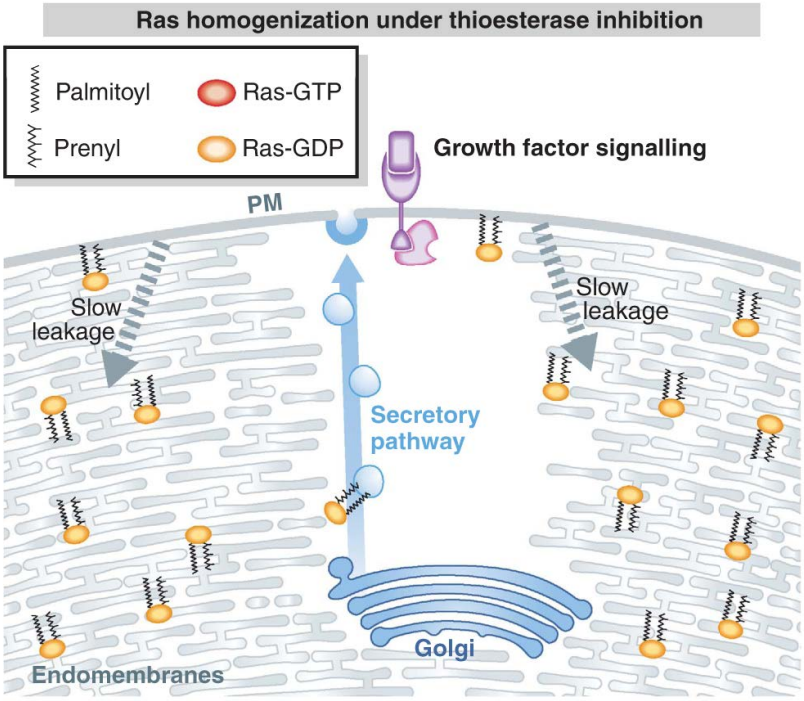

Figure 1.3: Disturbed acylation cycle of Ras upon APT inhibition. Inhibition of APT activity leads to an equilibrium binding of farnesylated and palmitoylated Ras to all cellular membranes. The local concentration at the plasma membrane is lowered and thus also its signaling response. Figure modified from Vartak and Bastiaens [31] .

1.2 Acyl Protein Thioesterase 1 and 2

With the finding that the enzymatic activity of Acyl Protein Thioesterases can be linked to the signaling level of Ras proteins a new, realistic possibility existed to circumvent the unsuccessful direct inhibition of Ras to stop Ras-induced tumor growth. Thus, also the research on APT itself as well as its isoforms and homologues was intensified to decipher the characteristics and biological function of these proteins.

1.2.1 Serine hydrolases

Serine hydrolases (SHs) represent one of the largest and most diverse class of enzymes with more than 200 members in mammalian cells that equals approximately 1 % of their proteome [49],[50]. They can be divided into two subgroups of approximately equal size: the serine proteases and the metabolic serine hydrolases [50],[51]. The latter group includes, beside the Acyl Protein Thioesterases, a range of lipases, peptidases, esterases, thioesterases and amidases that have a diverse substrate repertoire like small molecules, peptides, post-translational ester and thioester protein modifications or triglycerides [51]. Most metabolic serine hydrolases consist structurally of an α/β-hydrolase fold and own a Ser-His-Asp catalytic triad in which the active serine is generally embedded within a GXSXG motif [49],[50]. Although many metabolic serine hydrolases are well known enzymes, a huge number of them are yet only poorly described or still completely uncharacterized with respect to their physiological substrates and functions [51].

1.2.2 Discovery, occurrence and described substrates of Acyl Protein Thioesterases

In 1988 two lysophospholipases, later named Lysophospholipase 1 (LYPLA1) and Lysophospholipase 2 (LYPLA2), were identified in a mouse macrophage-like P388D1 cell line [52]. Isoform 1 was purified and characterized as a specific lysophospholipase with no significant activity on other substrates like phospholipids or triacylglycerols [52]. No substrate specificity within the class of lysophospholipids was found [53]. Further characterization revealed the sequence and described the catalytic mechanism since it was shown that this protein shares common features with serine hydrolases [54]. Simultaneously the LYPLA1 was purified from rabbit kidney [55] but treated as a calcium-independent phospholipase A_2 since a clear phospholipase-activity was observed [56]. Homologues of LYPLA1 from rat [57] and from human [54],[58] were identified, purified and initially characterized. Indications of a second isoform in mammalian cells [52] were proven to be correct, when Toyoda *et al.* described this isoform in detail and showed that this second isoform LYPLA2 shares a very high amino acid sequence identity of around 64 % with isoform 1 [59]. Duncan and Gilman could show that the lysophospholipase homologue in yeast has a significant higher enzymatic activity towards proteins containing acyl thioesters compared to lysophospholipid substrates. They reported the ability of this protein to depalmitoylate the Gα subunit und H-Ras and renamed it Acyl Protein Thioesterase (APT) [60],[61].

Acyl protein thioesterases are well conserved across eukaryotic species, from human to unicellular organisms like *Saccharomyces cerevisiae* and show a widespread tissue

distribution [58], [59], where they were mostly found in the cytosolic fractions of cell lysates [57], [60]–[63]. Interestingly, vertebrates possess two distinct APT enzymes (APT1 and APT2) while in invertebrates only a single APT protein is present [64] as depicted in figure 1.4. In human cells additionally two APT-related proteins can be found.

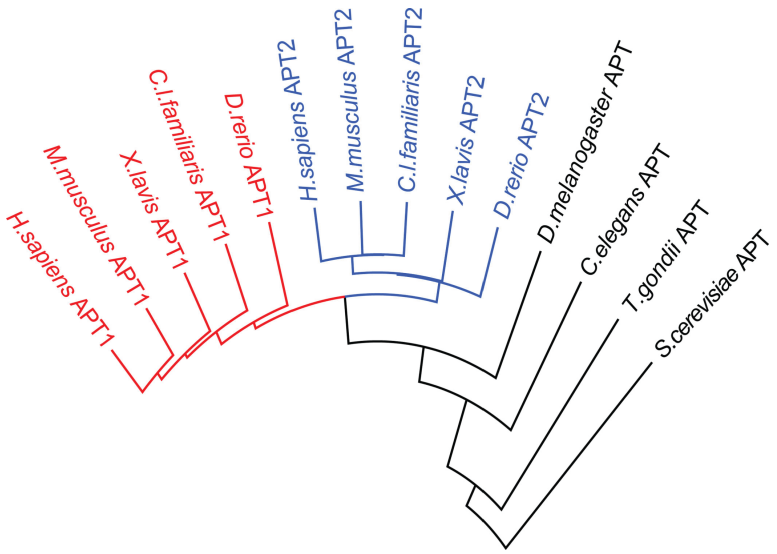

Figure 1.4: Homology of Acyl Protein Thioesterases of vertebrates and invertebrates. While in vertebrates APT1 (red) and APT2 (blue) can be found, in invertebrates only one APT enzyme is present. Figure taken from [64].

Lysophospholipase-like 1 (LYPLAL1) shares 33 % amino acid identity with APT1 but shows a specificity for short esters rather than longer chained substrates caused by point mutations close to the active site [65]. The functionally-related Palmitoyl protein thioesterases 1 and 2 (PPT1/2), also sharing a high sequence identity, were found to be primarily active in lysosomes and thus less relevant for the depalmitoylation of cytosolic or membrane-bound proteins [66], [67].

Even though yeast cells did not show obvious phenotypic alterations in growth characteristics and pheromone response upon APT knockout [61], the conserved orthology suggests a certain essential function of APT within eukaryotic organisms. During the search of this cellular function, beside lysophospholipids and the Gα subunit several other protein substrates of APT were described in the literature, like the mentioned H- and N-Ras [27], [47], [60], endothelial nitric-oxide synthase (eNOS) [68] or SNAP-23 [69]. APT1 and 2 seem to share most of their substrates, only a few are described as being specifically depalmitoylated by one isoform, like BK potassium channels [70] and the melanoma adhesion molecule MCAM [71] by APT1 or GAP-43 by APT2 [72]. Recent studies consider *h*APT2 not to be an acyl protein thioesterase in first line, but to act as the major prostaglandin glycerol esterase in human cancer cells [73].

Human APT isoforms can get palmitoylated on a single cysteine (Cys2) at their N-termini [74], which leads to a generally increased affinity to and a longer residence time at membranes [28]. Interestingly, APT1 seems to be able to depalmitoylate itself and

also APT isoform 2, but not *vice versa.*[74],[75] Whether this modification only increases the membrane affinity and thereby proximity to membrane bound substrates or if it also promotes direct interaction with cofactors or substrates still remains unclear. These studies imply a certain substrate-specific activity of APT in general and also for each isoform, but a possible contribution of other thioesterases in depalmitoylation *in vivo,* like shown for ABHD17 [76] , must not be neglected.

1.2.3 Structural characteristics of APT

APT1 and APT2 show the structural characteristics of the α/β-hydrolase family, thus also containing the typical Ser-His-Asp catalytic triad and sharing a close structural relationship to lipases and carboxylesterases [54],[58] . They are classified as family *abH22.03* in the lipase engineering database (LED) [77],[78] and belong to the family of *LYsophospholipase-carboxylesterase* in the ESTHER database [79],[80] .

In contrast to the canonical α/β-hydrolase fold *h*APT1 shows some significant deviations in its topology. As shown for the only published apo structure (PDB code 1FJ2)[62] and depicted in figure 1.5 , *h*APT1 lacks the first α/β-strand of the canonical fold and the fourth helix (αD) is replaced by the short segment G3. On the other

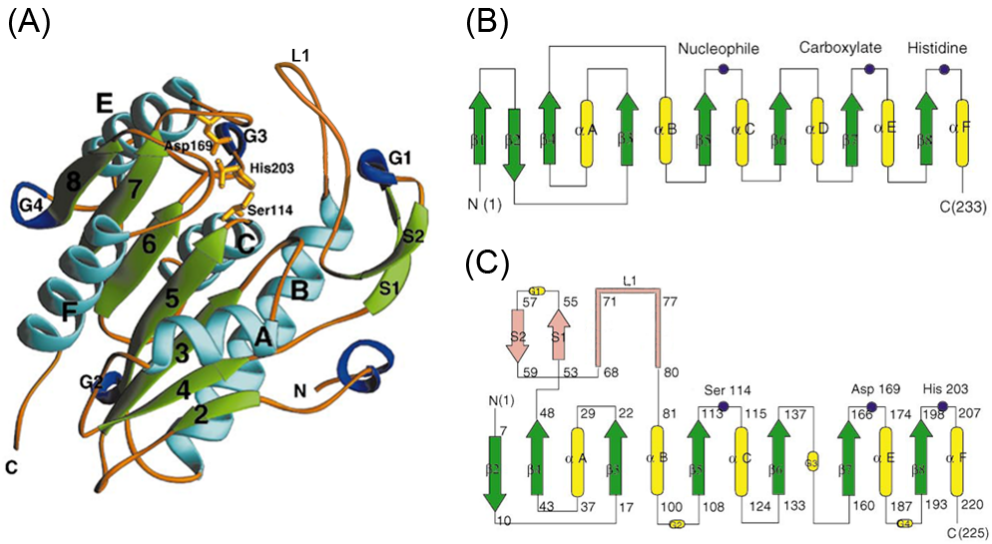

Figure 1.5: Structure of human APT1 and comparison to the canonical α/β-hydrolase fold. (A) Representation of secondary structure elements of *h*APT1 (C, PDB code 1FJ2). β-Strands (green) are numbered from 2 to 8, two irregular strands are labeled as S1-S2 and an additional loop as L1. The α helices (blue) are denoted A-F. Labels G1 to G4 belong to four short helical segments. Catalytic residues are shown as golden sticks. Topology diagrams of a canonical α/β-hydrolase (B) and of *h*APT1 (C) are shown as well. Eight β strands (green arrows) are labeled as β1– β8 and six helices (yellow rods) as αA– αF. Compared to the canonical α/β-hydrolase, *h*APT1 lacks the first strand (β1), the fourth helix (αD) is replaced by the short segment G3 and there are additionally two strands (S1–S2) and a loop region L1. Blue dots show the catalytic residues in *h*APT1 and in the canonical α/β-hydrolase. The figure was modified from [62] .

hand, *h*APT1 contains a long loop that connects sheet β4 with helix αB and is made of two short β strands (S1-S2) and a loop region L1 [62]. Although belonging to the same structural family of α/β-hydrolases, lipases, carboxylesterases and Acyl Protein Thioesterases differ in some main structural features as well as in substrate specificity. Most lipases show an interfacial activation behavior in the presence of a water/lipid surface [81]. During this activation a long insertion of the core fold called *lid* is opening up. In the closed-lid state the active site of the lipases is covered to prevent substrate access, while the transition to the open-lid state uncovers a substrate binding tunnel and allows cleavage of typically water-insoluble long-chained mono-/di-/triglycerol esters [82]. Lid opening also exposes a hydrophobic patch that contributes to the substrate-binding region [83]. In contrast, a lid-like structure is completely absent in carboxylesterases. The catalytic center is instead surface-exposed and allows direct access for usually water-soluble short chain esters [84] and also drugs, since carboxylesterases are also important mediators in drug metabolism [85]. In a structure of a carboxylesterase from *Pseudomonas aeruginosa* (PDB code 3CN9) a PEG molecule was found bound to an elongated shallow groove next to the catalytic triad [86]. A very similar groove can be found in structures of Acyl Protein Thioesterases (see figure 1.6). Although APT

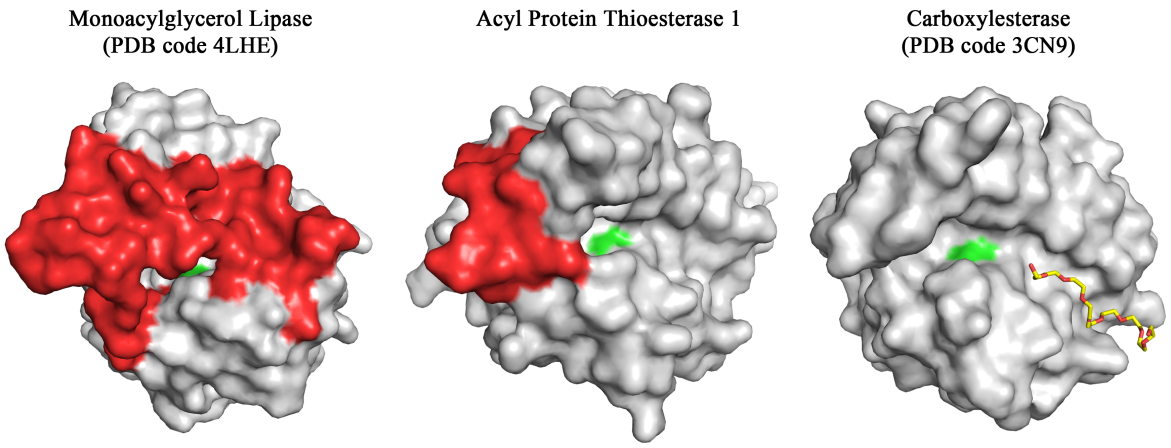

Figure 1.6: Structural comparison of three different members of α/β-hydrolases. Shown are the surfaces of a monoacylglycerol lipase, APT1 and a carboxylesterase. The lid structures are highlighted in red and the active centers in green. While the lid is shielding the entire active center of the lipase, no lid structure is present in carboxylesterases. A PEG molecule, shown as yellow sticks, binds to a shallow groove next to the catalytic center of the carboxylesterase.

shares a very high structural similarity to the *P. aeruginosa* carboxylesterase (overall RMSD of 1.1 Å) the APT groove is partially covered by a loop, similar to the lid structure in lipases, but reduced in size, thus not covering the active center completely (see figure 1.7). Previous structural studies in our group of both *h*APT1 and *h*APT2 showed that this lid of Acyl Protein Thioesterases, formed by the additional loop L1 (see figure 1.5C), preform a substrate binding tunnel, a unique feature which has so far

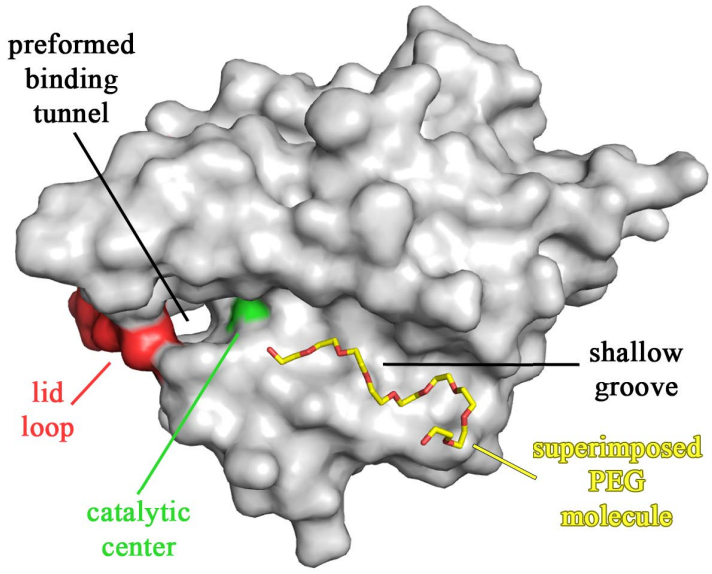

Figure 1.7: Structural features of APT. The depicted view onto the structure allows the perspective through the binding tunnel, preformed by the lid loop (highlighted in red). The catalytic center (green spot) is located at the entrance of the binding tunnel and next to it a shallow groove is present on the surface. In a crystal structure of a structurally very closely related carboxylesterase (PDB code 3CN9) a PEG molecule can be found at this position. Here the molecule (shown in yellow sticks) is superimposed to the APT structure to emphasize that this groove could be also involved in substrate binding, especially of lipidic moieties.

not been described for any other member of α/β-hydrolases and is most likely involved in ligand binding into the tunnel [87],[88]. The loop L1 of APT (in the following referred to as lid loop), is inserted between strand β4 and helix αB, is located at a different position than the lid structure of lipases that connects strands β6, β7 and β8.

The residues lining the binding tunnel are very similar in APT1 and APT2, only at 3 positions amino acids seem to be conserved in only one of the isoforms. Whether these differences are influencing the substrate specificity or catalytic efficiency of APTs is unclear to date [87]. In contrast to lipases, the phenomenon of interfacial activation could not be observed for Acyl Protein Thioesterases [53],[58].

1.2.4 Inhibitors of APT activity

To study the role of APTs *in vivo,* several small molecules have been described to bind to APT and inhibit its catalytic activity. Boron-based inhibitors were shown to bind APT enzymes *in vitro* reversibly, covalently, but also unspecifically [89]. Peptide-mimicking benzodiazepinediones based on the C-terminus of H-Ras showed high affinities towards APT *in vitro* but were not active in cellular assays [90],[91]. Members of the class of palmostatin inhibitors based on the anti-obesity drug Orlistat [92],[93] bind competitively and covalently to the active serine of APT proteins but hydrolyze again from this catalytic site with a halftime of 25 min [32]. *In vivo* studies showed that palmostatin

B perturbs the acylation cycle of oncogenic Ras leading to a decreased downstream signaling [32],[46],[48]. *h*APT1 and 2 were identified as cellular targets of palmostatin B and thus became potential anti-cancer targets to bypass direct Ras treatment [47]. Especially at higher concentrations of palmostatin off-target effects to other serine hydrolases have to be considered [32],[47],[94]. In a study on N-Ras mutant melanoma cells, treatment with Palmostatin B resulted in a dose-dependent cell viability decrease in most tested cell lines [95]. The palmitate analogue 2-bromopalmitate which is usually

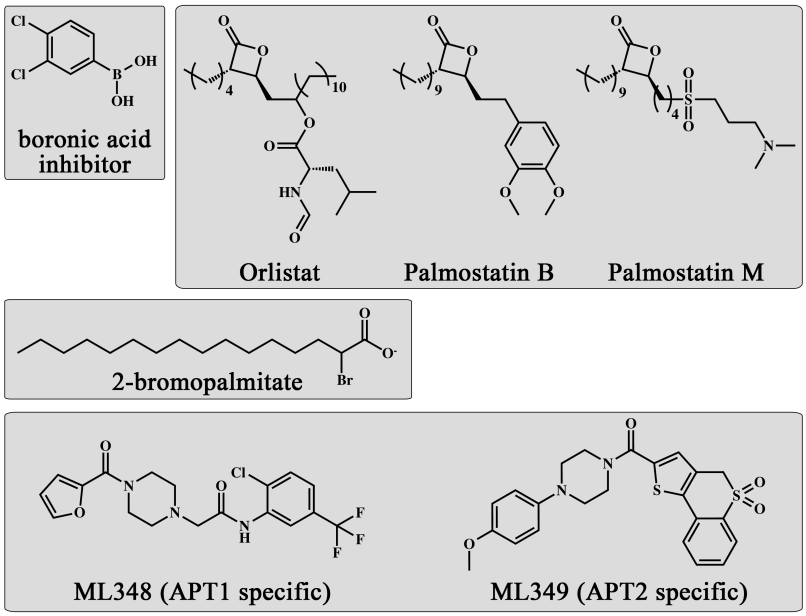

Figure 1.8: Chemical structure of known APT inhibitors.

used to prevent S-palmitoylation by Protein Acyl Transferases (PATs) [96] was also reported to inhibit the enzymatic activities of *h*APT1 and *h*APT2 non-covalently and in an uncompetitive mode of action [97]. Furthermore, the inhibition of APT by 2-BP was reported to perturb the acylation cycle of GAP-43 at the level of depalmitoylation and affect its kinetics of membrane association [97].

Competitive, reversible, non-covalent, isoform specific inhibitors ML348 (APT1 specific) and ML349 (APT2 specific) with reasonable K_is of 300 nM and 230 nM, respectively, were reported by Adibekian *et al.*[98] Both isoform-specific inhibitors did not show biologically significant effects in N-Ras mutant melanoma cells [95].

2 Objectives

Over the last decades Acyl Protein Thioesterases (APTs) were attributed to completely different cellular tasks. First found and described as lysophospholipases they later were implicated in the hydrolysis of thioester-linked palmitoyl moieties from protein substrates. Several protein targets of both human APT isoforms were described as well as a prostaglandin-esterase function of *h*APT2, indicating that either APT proteins have a widespread universal esterase-function or the cellular process in which they are absolutely mandatory remains to be identified. The latter hypothesis is supported by the conservation of APT throughout eukaryotic species, which suggests an essential function of this protein. When the palmitoylated Ras proteins, one of the most prominent oncogenes and responsible for 30 % of human tumor growth, were also described as substrates, APT proteins moved into the focus of cancer research. Since direct inhibition of Ras failed so far, APT became a potential anti-cancer target. Driven by these prospects, structural and functional research on APT was intensified. With the use of the APT inhibitor palmostatin B, indeed, a decrease in signaling of oncogenic Ras upon APT inhibition could be observed. However, in order to use their inhibition as a viable tool in cancer therapies APT proteins have to be fully characterized, but structural and functional information explaining substrate-specificity between the two APT isoforms in higher eukaryotes and evolutionary APT development from yeast to human, is lacking, as well as detailed knowledge about binding mode and isoform-selectivity of recently described inhibitors of APT activity.

The objective of this work was to provide new insights into possible physiological roles of APT and its isoforms, thereby focusing on the interaction of different substrates, ligands and inhibitors with APT proteins. For this purpose, different assay systems had to established: A reliable and robust activity assay was needed that is independent of additives, e.g. detergents, to detect catalytic activities and also the inhibition of APT. Using this assay, described APT inhibitors like 2-bromopalmitate and the isoform specific inhibitors ML348 and ML349, as well as compounds from a high-throughput screen and their optimized versions can be validated. Structural analysis using X-Ray crystallography could reveal their binding site, exact binding mode and in case of the isoform selective inhibitors also the isoform-specific amino acids that are responsible for the inhibitor selectivity. Beside the artificial inhibitors also the binding and/or catalysis

of natural substrates should be explored, from palmitic acid and (lyso-)phospholipids to palmitoylated peptides. Depalmitoylation of these peptides by APT in the presence of model membranes would constitute a step towards natural conditions to reveal if APT is able to access and convert membrane bound substrates. Therefore, also suitable assay systems had to be setup that allow the detection of relevant parameters. The combination of the results of the different approaches should create more evidence about the preferred substrates of APT proteins in general and comparison of different APT isoforms and homologues from different species might reveal significant, characteristic differences between them. Considering also homologues from lower eukaryotic species might also provide insights onto APT from an evolutionary point of view.

3 Results

3.1 Assay development and optimization

Unless otherwise stated, the human APT constructs *h*APT1 M6 and *h*APT2 M6 that lack the first five amino acids (see section 5.2.1) were used by default for all types of assay. In the following they are referred to as *wild type* (wt) proteins, according to their non-mutated amino acid sequence. All other proteins contain either the full length wild type sequence or are labeled accordingly to their mutation.

3.1.1 Fluorescence based activity assay

A robust and reliable assay system is mandatory to obtain reproducible results. The setup should be as simple as possible, thus ideally containing only the essential ingredients and as little compounds like e.g. detergents. Furthermore an environment has to be created which satisfies the needs of all components, e.g. with respect to their solubility. The readout requires a sensitive method which should be ideally not be influenced too much by minor changes of the environment, like the pH value or temperature.

Previous assays in our group determining the substrate conversion by APT were most commonly based on a colorimetric approach using fatty acid modified *para*- nitrophenole (pNP) esters (see figure 3.1). Although pNP esters are commercially available in great variety and the chromophore is rather small in size and thus less interfering with binding to the protein, the insolubility of the substrates becomes a relevant issue with increasing concentration and/or fatty acid chain length. To allow measurements, detergents like CHAPS or Triton X-100 had to be used to dissolve the pNP substrates properly. Even though a comparable initial velocity V_i can be measured in the presence of detergent compared to conditions without, clearly less substrate is available for cleavage by APT, as shown in figure 3.2A. Since detergents have to be used above their critical micelle concentration (CMC, see figure 3.2B), the substrate will be sequestrated in mixed micelles and its availability and hydrolysis rate is also dependent on the dissociation rate of pNP substrates from these micelles. Thus, the calculated Michaelis constant K_m (1906 $\pm$ 190 µM) and the turnover k_{cat} (4.6 s^{-1}) for conversion

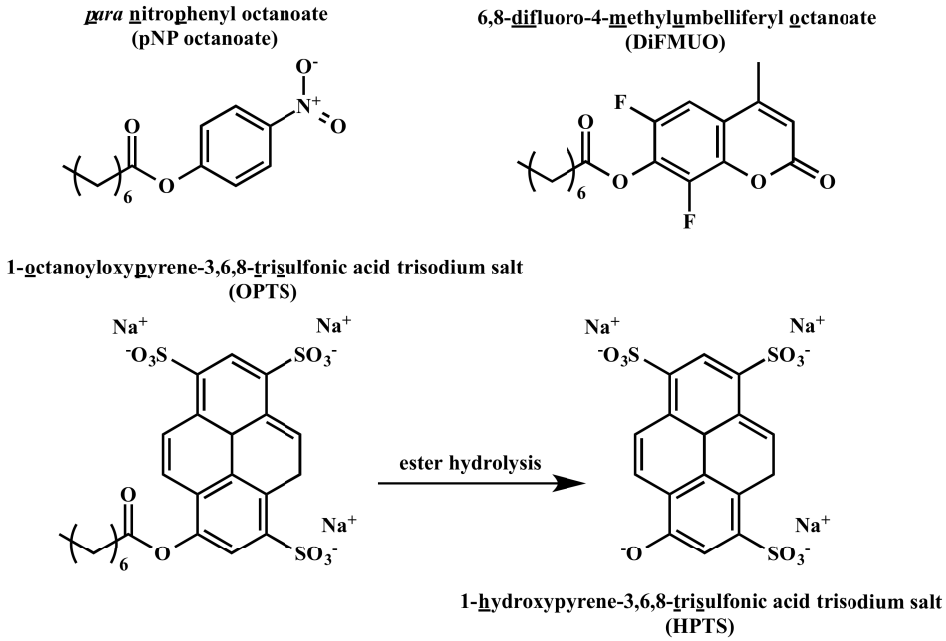

Figure 3.1: Overview of different artificial substrates to measure APT activity *in vitro*. Assays using pNP (*para* nitrophenyl) substrates are absorbance-based, while usage of DiFMUO (6,8-difluoro-4-methylumbelliferyl octanoate) and OPTS (1-octanoyloxypyrene-3,6,8-trisulfonic acid trisodium salt) allows the more sensitive measurement of fluorescence. The sodium-sulfonate modified pyrene system of OPTS provides good solubility. After hydrolysis of the fatty acid ester the fluorescent species HPTS (1-hydroxypyrene-3,6,8-trisulfonic acid trisodium salt) is released.

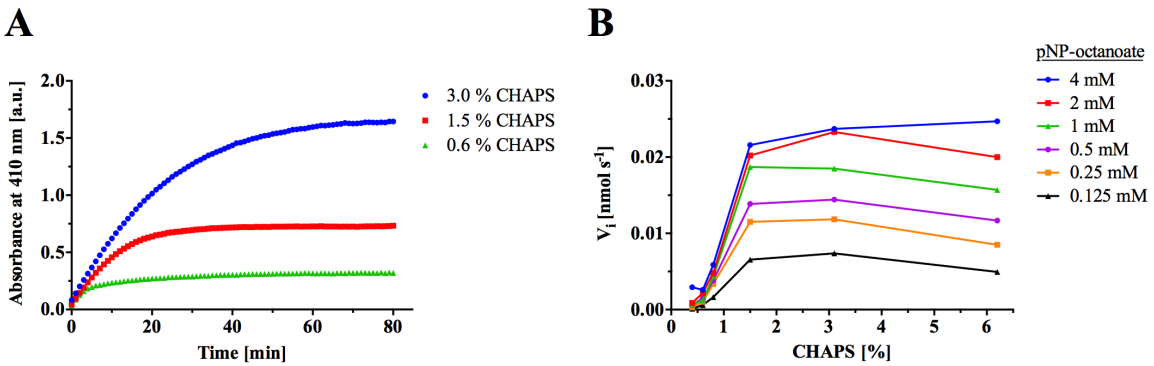

Figure 3.2: Influence of the detergent CHAPS on pNP substrate conversion by *h*APT1. (A) The amount of converted pNP-octanoate (4 mM, see figure 3.1) by 100 nM wild type *h*APT1 is clearly dependent on the concentration of CHAPS detergent. (B) The same is true for the initial slope of substrate conversion at different amounts of CHAPS. Below the critical micelle concentration (6-10 mM, 0.3-0.6 % (w/v) [99]) the substrate is almost not accessible.

by *h*APT1 are apparent values that might differ from the real kinetic numbers (see section 3.1.1.1 for explanation of parameters). In addition, absorbance based assay systems could also be influenced by the cloudiness of the tested solutions, which definitely occurs when working with higher concentrations of these substrates and will

lead to an unsatisfying reproducibility.

Considering this problem the assay system had been improved by switching to the fluorescent coumarin-based substrate DiFMUO [87] (6,8-difluoro-4-methylumbelliferyl octanoate, see figure 3.1), which is also increasing the sensitivity at low substrate concentrations compared to the colorimetric approach. But even in this assay 0.01 % (v/v) Triton X-100 had to be used to solubilize the substrates [87], thus the problem of apparent kinetic values that are biased by the competition between protein and micelles for the binding of the substrate still remains. To further optimize the APT activity assay regarding this issue, a new approach was tested using a pyrene based fluorophore, described by Wolfbeis and Koller [100]–[102].

Even though this fluorophore has a larger molecular weight compared to pNP and DiFMUO it offers a number of advantages. The fluorescent species 1-hydroxypyrene-3,6,8-trisulfonic acid trisodium salt (HPTS; shown in figure 3.1) shows a large Stokes' shift of 60 nm, and when excited (λ_{ex}) at the isosbestic point of 415 nm no pH dependency of fluorescence intensity at 520 nm (λ_{em}) occurs [100] (figure 3.3). Most im-

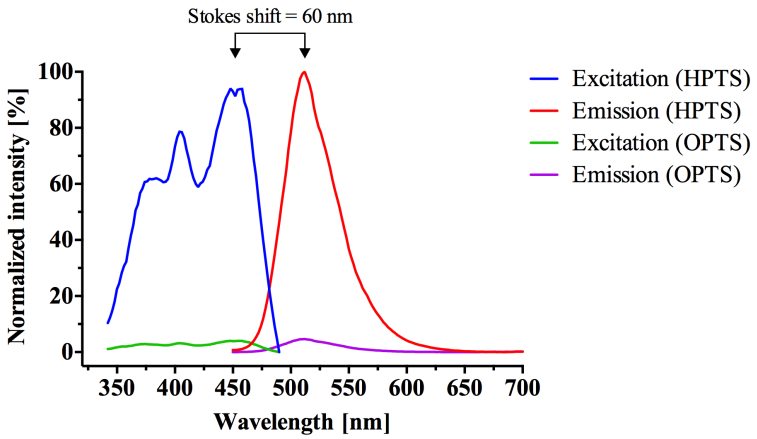

Figure 3.3: Excitation and emission scans of HPTS and OPTS. In contrast to HPTS, the actual fluorescent species, the fluorescence of the OPTS substrate is negligible and thus not disturbing in readout of the HPTS fluorescence. For emission scans the excitation wavelength was set to 415 nm, for excitation scans the emission wavelength was set to 520 nm.

portantly, due to the modification of the pyrene with three sodium-sulfonate moieties, the solubility of fatty acid esters of HPTS, like the commercially available octanoyl-modified substrate 1-octanoyloxypyrene-3,6,8-trisulfonic acid trisodium salt (OPTS, figure 3.1) is dramatically increased. Aqueous solutions of OPTS $>$ 1 mM are easily feasible, for oleic acid esters of HPTS solutions up to 0.5 mM are reported without the need of an additional detergent [100]. Thus, OPTS was tested as assay substrate in a buffer containing 150 mM KH_2PO_4/K_2HPO_4 and 100 mM NaCl to maintain the adjusted pH (see figure 3.5) also after release of carboxylic acids from the enzymatic reaction. The fluorescence of the OPTS substrate is, at the described settings of the

wavelengths ($\lambda_{ex} = 415\,nm$ and $\lambda_{em} = 520\,nm$), negligible compared to the product HPTS and not disturbing the detection of the HPTS release (figure 3.3).

Interestingly, the use of detergents in an OPTS assay shows the opposite effect than in approaches using pNP (figure 3.4). Instead of being essential for substrate

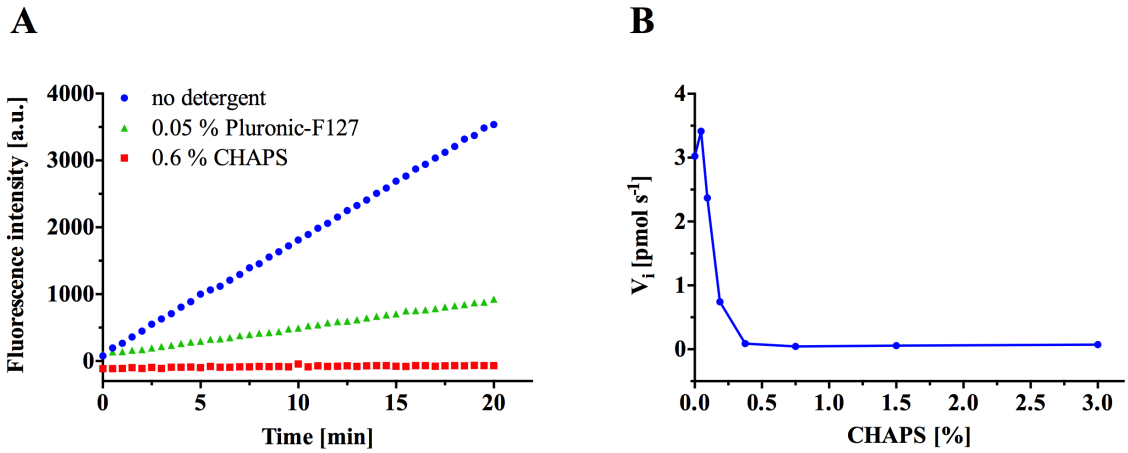

Figure 3.4: Influence of detergents on substrate availability in OPTS assay. (A) The use of two different detergents is decreasing the hydrolysis rate of 250 µM OPTS by 5 nM *h*APT1 by 80 % in the case of 0.05 % Pluronic-F127 and 98 % when using 0.6 % CHAPS. (B) Even small amounts of CHAPS lead to a decrease of the initial slope of hydrolysis of 250 µM OPTS by 10 nM *h*APT1. When more than 0.4 % of CHAPS are added almost no *h*APT1 activity can be measured.

availability as in the case of the pNP-substrates, the addition of 0.6 % CHAPS or 0.05 % Pluronic-F127 apparently leads to a decreased accessibility of OPTS to *h*APT1. OPTS might have a high affinity towards detergent aggregates, thus forming mixed micelles to which APT has no access. Thus, in the standard setup of assays using fatty acid esters of HPTS no detergent was added, but also not crucial due to the intrinsically good solubility of HPTS esters [100].

Since the fluorescence of HPTS is pH independent, when using a setup of $\lambda_{ex} = 415\,nm$ and $\lambda_{em} = 520\,nm$ [100],[101], the pH optimum for APT activity could be determined. As seen in figure 3.5 *h*APT1 shows a maximum turnover k_{cat} and a minimal K_m (corresponding to maximal substrate affinity) at a pH of 7.4 of the potassium phosphate assay buffer (see 5.2.2.1), thus the pH of the assay buffer for following measurements was set to this catalytically optimal value (see section 3.1.1.1 for explanation of kinetic parameters).

To investigate the substrate specificity of APTs concerning the fatty acid chain length of the substrates, more derivatives of HPTS were needed. Since only the octanoyl ester of HPTS (OPTS) is commercially available, longer chained variants had to be synthesized. Largely following the instructions for synthesis given by Koller and Wolfbeis [102],[103] (see methods 5.2.9), two additional substrates were obtained: The lauroyl ester (LPTS) and the palmitoyl ester (PPTS) with an aliphatic chain of 12

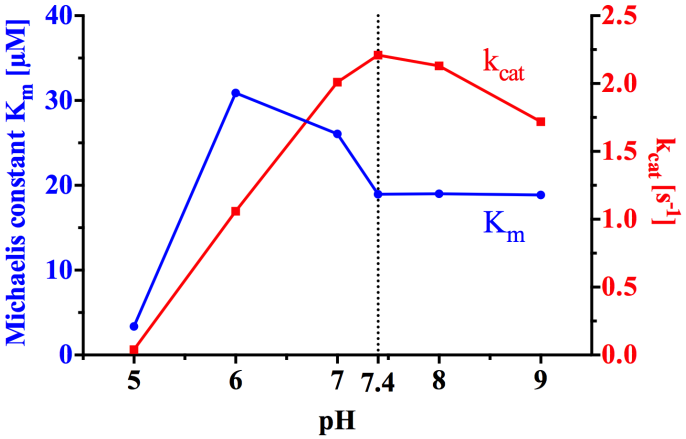

Figure 3.5: pH dependency of *h*APT1 activity in the OPTS assay. Plot of the Michaelis constant K_m and the catalytic constant k_{cat} for the conversion of OPTS by 5 nM *h*APT1 against the pH of the assay buffer.

and 16 carbon atoms, respectively. When testing the behavior of the new substrates in the activity assay using *h*APT1 a strange behavior was observed: While all APTs show reasonable Michaelis-Menten kinetics for OPTS (see section 3.1.1.1) with a stable plateau of activity up to 500 µM, the activity of the proteins decreases at higher concentrations of LPTS and PPTS. No activity of *h*APT1 could be detected above concentrations of 250 µM for LPTS, and 30 µM for PPTS, respectively (see figure 3.6). Contaminants from synthesis that could be potentially responsible for this phenomenon

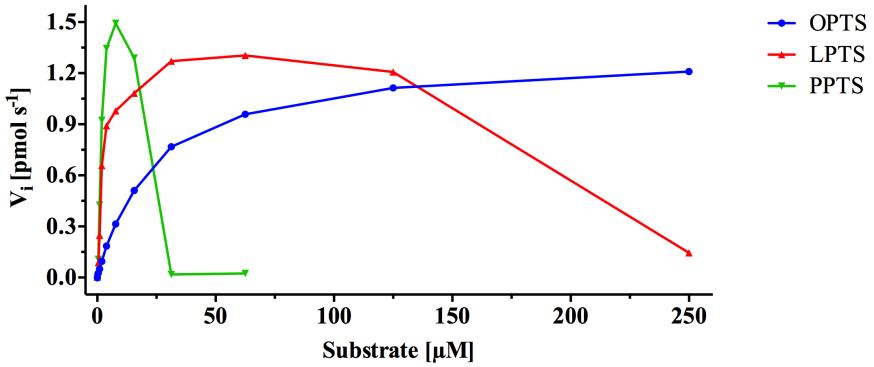

Figure 3.6: Michaelis-Menten kinetics of HPTS-based substrates with different chain length converted by *h*APT1. While OPTS shows a constant plateau of activity up to 500 µM (not completely shown here), *h*APT1 does not show an activity at LPTS concentrations higher than 250 µM and PPTS concentrations above 30 µM. The DMSO concentration was kept at 1 %.

could be excluded by mass spectrometry. Therefore the effect was investigated in more detail using PPTS as substrate.

The dramatic loss of protein activity at PPTS concentrations higher than 20 µM could be explained by product inhibition, if the formed palmitic acid is binding to APT with a reasonable affinity, thereby competing with the actual substrate PPTS. To test

this hypothesis, an inhibition assay was setup, using 125 µM OPTS as substrate and titrating palmitic acid as a potential competitor. Since the fatty acid is practically insoluble in aqueous solutions, first a suitable method had to be found to provide palmitic acid to the protein in defined amounts. After testing different approaches, it turned out that dissolving sodium palmitate 100 mM in 50 % ethanol/water, followed by intense mixing, sonication and final heating works best (see section 5.2.2.2 for details). The resulting one-phase "solution" appeared clear and stable, most likely because micelles of sodium palmitate were formed. The presence of micelles can be assumed for the stock of 100 mM sodium palmitate and most likely also for the diluted solutions under assay conditions (2 mM and lower). In the literature a critical micelle concentration (CMC) of 2.1 mM can be found for sodium palmitate, determined in water at 50 °C [104]. Further publications claim that the CMC of ionic detergents is reduced by increase of the ionic strength of the buffer but stays relatively unaffected by changes of the temperature [91]. For instance, the CMC for sodium dodecyl sulfate (SDS) drops from 6.5 mM at 0 mM NaCl to 1.4 mM in the presence of 150 mM NaCl [105]. Thus, it seems likely that the CMC of 2.1 mM determined in pure water may be significantly decreased in the assay buffer used here containing 150 mM NaCl and 100 mM K_2HPO_4/KH_2PO_4.

Performing the inhibition assay with OPTS using the prepared sodium palmitate solution, indeed an inhibition of APT activity could be observed for both *h*APT isoforms, with IC_{50} values of 791 µM and 350 µM for *h*APT1 and *h*APT2 respectively (figure 3.8). Because both proteins show different affinities towards the OPTS substrate (see figure 3.14 and table 3.2) also the K_i, a measure of affinity (for explanation see section 3.3.1), was determined to allow comparison of binding strength of sodium palmitate to the two proteins. The calculated K_i values of 130 µM for *h*APT1 and 106 µM for *h*APT2 would imply a product inhibition of APT by palmitic acid, but only at high micromolar concentrations that cannot explain the total loss of APT activity at a PPTS concentration of 30 µM. However, it is important to bear in mind that the presence of sodium palmitate micelles in the assay buffer might lower the concentration of "free" sodium palmitate that is actually available for APT inhibition. This effect would lead to artificially high observed (apparent) IC_{50} values, while the real values might actually be lower. Thus, it seems unlikely, but it cannot be totally excluded that in case of a very high affinity binding of palmitic acid a product inhibition might be the reason for the significant loss of APT activity at PPTS concentrations above 20 µM. Since other explanations are possible, like sequestration of OPTS by the palmitate vesicles, or effects on the stability of APTs, this effect was investigated in more detail as discussed in the following. These additional studies were important to perform, because it is not uncommon that unanticipated phenomenons occur when working with fatty acids or related compounds. For instance, the serendipitous co-crystallization of *xt*APT1 with palmitic and stearic acid [87] implies a strong interaction, since the fatty

acids survived the complete process of protein purification bound to the protein, while the intended co-crystallization of APT proteins with fatty acids resulted at best in a weak occupancy of the APT binding tunnel by these ligands, suggesting a much weaker affinity or at least the wrong way of supplying the fatty acid to APT. Having this contradictory results in mind, the determined inhibition of APT by sodium palmitate was re-evaluated.

Assuming the presence of micelles, a sodium palmitate concentration-dependent sequestration of the OPTS substrate by these micelles could be considered to cause the observed effect. The excellent solubility of OPTS (see beginning of this section) and the fact that *h*APT1 and *h*APT2 show different IC_{50} values does not completely exclude a partial sequestration of OPTS to micelles, but argues against a complete substrate-removing effect that explains the detected APT inactivity at high sodium palmitate concentrations.

Another possible reason for the decrease of APT activity at higher sodium palmitate concentrations might be that sodium palmitate, a soap of palmitic acid, acts as a surfactant. Similar to 2-bromopalmitate (2-BP, see section 3.3.1) sodium palmitate might be able to interact in a detergent-like manner with APT thereby changing the three dimensional structure of APT and thus eliminating its enzymatic function. In this case the determined IC_{50} value would reflect the inactivation by unfolding half of the protein. To test this hypothesis, an activity assay using 5 nM *h*APT1 and 40 µM PPTS at different amounts of sodium palmitate was performed, that showed an interesting trend (figure 3.7A): While APT is inactive at low concentrations of the fatty acid it started to be active at sodium palmitate concentrations above 60 µM and reaches a plateau in activity in the presence of 500 µM. This clearly contradicts the hypothesis that sodium palmitate might influence the APT structure or even inactivate the enzyme because at concentrations of 500 µM already some inhibition was observed in the OPTS experiment (figure 3.8B). The reason why APT shows no sign of inhibition by 500 µM sodium palmitate when PPTS is used as substrate could be explained by the 25-fold stronger affinity of the PPTS substrate to *h*APT1 compared to OPTS (see section 3.1.1.2 and table 3.4), meaning that much more fatty acid would be necessary to gain a comparable competition effect. Given the determined K_i of 130 µM for *h*APT1, the K_m of 0.7 µM of PPTS to *h*APT1 (see table 3.4) and the concentration of 40 µM PPTS as used in the sodium palmitate-titration experiment (figure 3.7A), one could estimate an IC_{50} value of 7.6 mM for sodium palmitate competing PPTS, according to the Cheng-Prusoff equation (see equation 3.3 in section 3.3.1). Additionally, experiments using APT1 from *Xenopus tropicalis* in the tryptophan assay, that detects changes of the intrinsic tryptophan fluorescence und thus not only binding of ligands to APT, but also changes of the entire protein structure (explained in detail in section 3.1.2), did not show indications of palmitate binding, in contrast to 2-BP (section 3.3.1), or changes

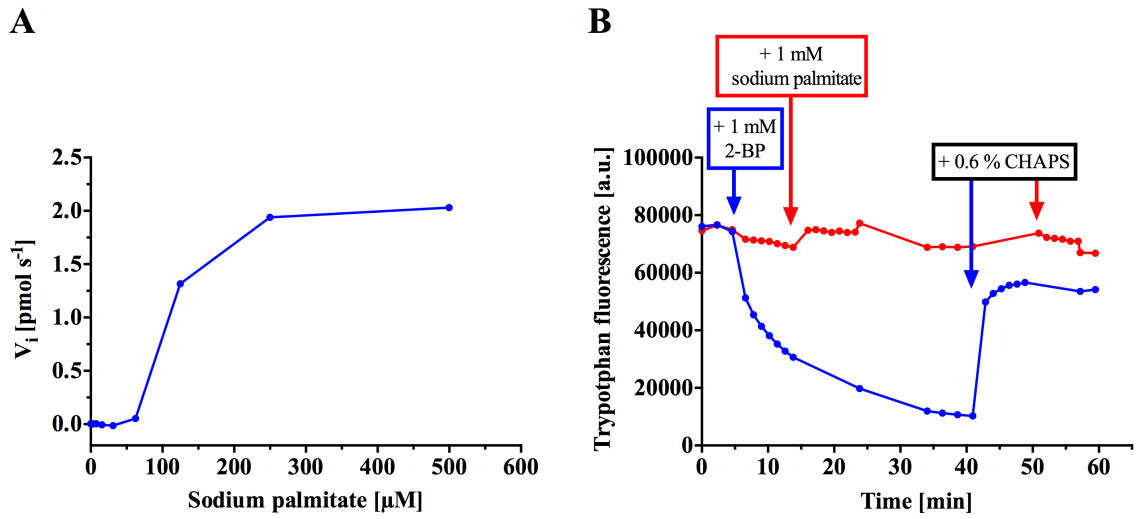

Figure 3.7: Sodium palmitate does allow PPTS conversion and does not influence tryptophan fluorescence of *xt*APT1 in contrast to 2-BP. (A) The initial velocity of 5 nM *h*APT1 on 40 µM PPTS was determined at different concentrations of sodium palmitate. The trend shows that the more sodium palmitate is used the more active *h*APT1 appears, coming to a saturation at 500 µM sodium palmitate. (B) Using the tryptophan assay (see section 3.1.2), 1 mM of 2-bromopalmitate (2-BP, blue curve) or sodium palmitate (red curve) were added to 10 µM of *xt*APT1. While the tryptophan fluorescence is significantly decreased upon 2-BP addition and almost rescued by adding CHAPS detergent that strongly binds to 2-BP (see section 3.3.1 and figure 3.33 for details), sodium palmitate has almost no effect on the fluorescence, indicating that no destabilization/unfolding of the protein occurs.

of the APT structure up to sodium palmitate concentrations of 1 mM (see figure 3.7B).

Since both explanations that were considered to cause the APT inactivity at high sodium palmitate concentrations and thus mimic the observed effect of product inhibition can be most likely excluded, i.e. the sequestration of OPTS by sodium palmitate-micelles and the inactivation of APT by the fatty acid in a detergent-like manner, it seems that the competitive effect at the substrate binding site of APT between sodium palmitate and OPTS is real, but most likely not strong enough to explain the loss of APT activity at higher PPTS concentrations.

Besides product inhibition, also the possibility of "unavailability" of PPTS for APT at higher concentrations was considered, e.g. due to formation of aggregates. For instance, the tendency of pyrene moieties to form excimers (excited-state dimer), i.e. dimers that are only formed by $\pi - \pi$ interactions of the aromatic ring system if at least one monomer is present in its excited state, is a well known phenomenon for pyrene moieties [106]–[108]. It seems likely that the linkage of hydrophobic fatty acids to the fluorophore could amplify this effect in a fatty acid chain length dependent manner, leading to the formation of multimers of PPTS [109] that are not accessible for APT. But, the complete loss of activity can not be explained solely by substrate aggregation because in an equilibrated system accessible substrate should always be

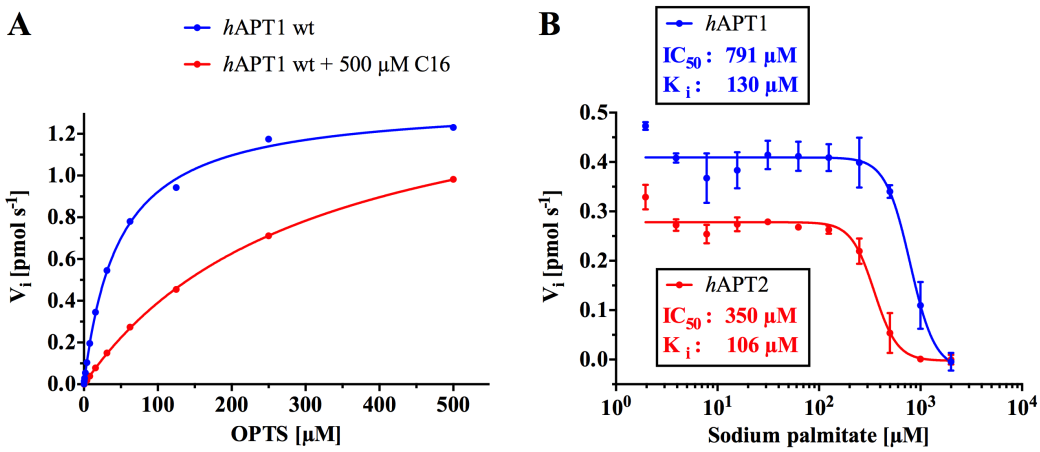

Figure 3.8: Sodium palmitate shows weak affinity to *h*APT1. In inhibition experiments a competitive interaction of sodium palmitate and OPTS was observed (A) and a K_i of 130 µM was determined using 125 µM OPTS substrate (B).

present, even if the concentrations of "free" PPTS would be very low. This is especially true for the well soluble PPTS (solubility $>$ 500 µM [100]). Supporting this, dilution of the substrate from 40 µM to 20 µM in the presence of protein does not lead to any detectable activity (figure 3.9), although *h*APT can be very significantly active

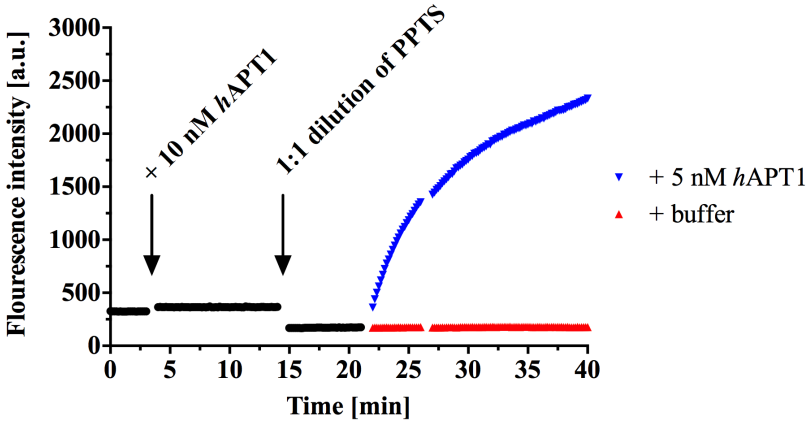

Figure 3.9: *h*APT1 is inactivated by 40 µM PPTS. No activity of 10 nM *h*APT1 can be detected converting 40 µM PPTS. Dilution of the reaction mixture with buffer to 20 µM PPTS and 5 nM *h*APT1 did not result in a visible APT activity. Further addition of 5 nM *h*APT1 leads to a very significant enzymatic conversion of PPTS.

at this PPTS concentration as seen in figure 3.6. This implies that the loss of APT activity does not occur due to the lack of PPTS at high concentrations and leads to the assumption that APT activity itself is destroyed by high PPTS concentrations and cannot be recovered. Furthermore, this observation also excludes the previously discussed hypothesis that product inhibition might be causing the loss of APT activity at these PPTS concentrations.

To prove the hypothesis of APT destruction by PPTS aggregates, fresh and ac-

tive APT protein was added to the reaction after the PPTS solution was diluted to 20 µM (figure 3.9, at 20 min timepoint). As seen in the blue curve in figure 3.9, a very significant conversion of PPTS can be observed upon APT addition. Thus, it seems plausible that at higher concentrations of PPTS excimers are formed by $\pi - \pi$ interactions (most likely supported by the long fatty acids moieties, since OPTS and LPTS apparently need higher concentrations to form this aggregates) which are able to interfere with APT, thereby leading to its irreversible inactivation. To see if high concentrations of PPTS change the structure of the protein, CD spectra of the catalytically inactive *h*APT1 mutant S119A were taken, with and without PPTS present. Indeed, after addition of PPTS the CD-signal of the secondary structure elements of APT is decreased by 50 %, indicating a substantial change in protein structure that obviously leads to the loss of enzymatic function in the wild type protein (figure 3.10A). To see

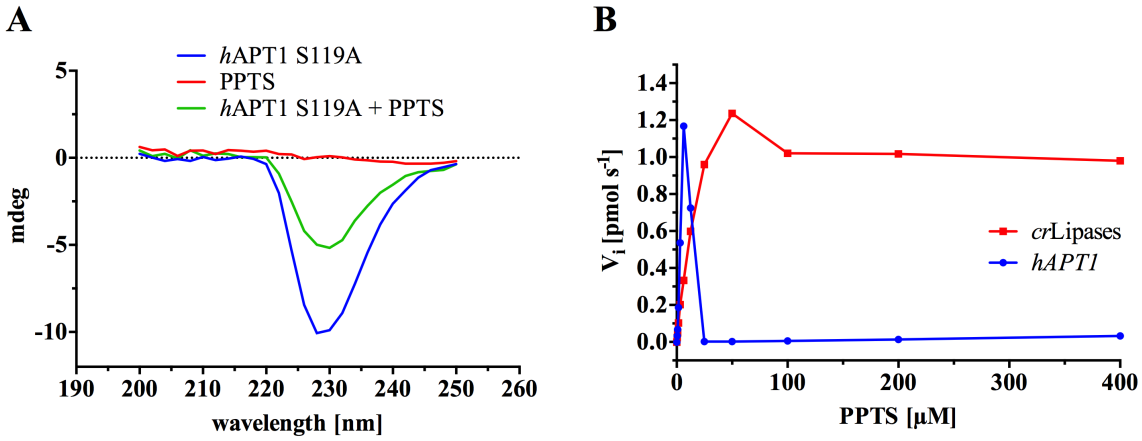

Figure 3.10: CD spectra of *h*APT1 with and without PPTS substrate and lipase activity on PPTS. (A) For the shown CD experiment 20 µM of the catalytically inactive APT mutant *h*APT1 S119A and 500 µM PPTS were used. Addition of PPTS halves the measured ellipticity of APT. The red line shows PPTS alone as control. (B) In contrast to 5 nM *h*APT1 a lipase mixture from *Candida rugosa* (*cr*Lipases, 100 nM) is still active at PPTS concentrations up to 400 µM.

if the observed effect is also true for other fatty acid-hydrolyzing enzymes the activity of a lipase mixture (100 nM) from *Candida rugosa* (Sigma-Aldrich, St. Louis, USA) was tested in presence of up to 400 µM PPTS. The experiment shows that the lipases were showing almost unchanged activity at 400 µM PPTS (figure 3.10B), which implies that the observed destructive interaction between APT and PPTS might be specific for APTs, maybe because they offer a vulnerable binding site for PPTS aggregates at their surface or for single PPTS monomers that could act as origins for PPTS aggregation, or maybe because APTs are intrinsically less stable proteins.

To prevent PPTS from forming these aggregates two different approaches were pursued. In a first approach, fatty acid binding protein 2 (FABP2) was added to the dissolved PPTS substrate. As the name suggests, FABP proteins are fatty acid

binders [110] that might "chaperone" a significant fraction of PPTS to avoid its aggregation. A too tight interaction between PPTS and FABP2 would be counterproductive, since this would lead to ligand-depletion. Since fatty acids usually bind head-first into the binding tunnel of FABP [111], which is not possible for PPTS because of the huge pyrene head-group, the interaction between PPTS and FABP2 is expected to be much weaker than the fatty acids alone (K_d for palmitic acid = 120 nM [111]). Indeed, addition of 10 µM FABP2 rescues *h*APT1 activity also at higher PPTS concentrations (60 µM) as shown in figure 3.11, but the order of addition seems to be crucial, confirming the

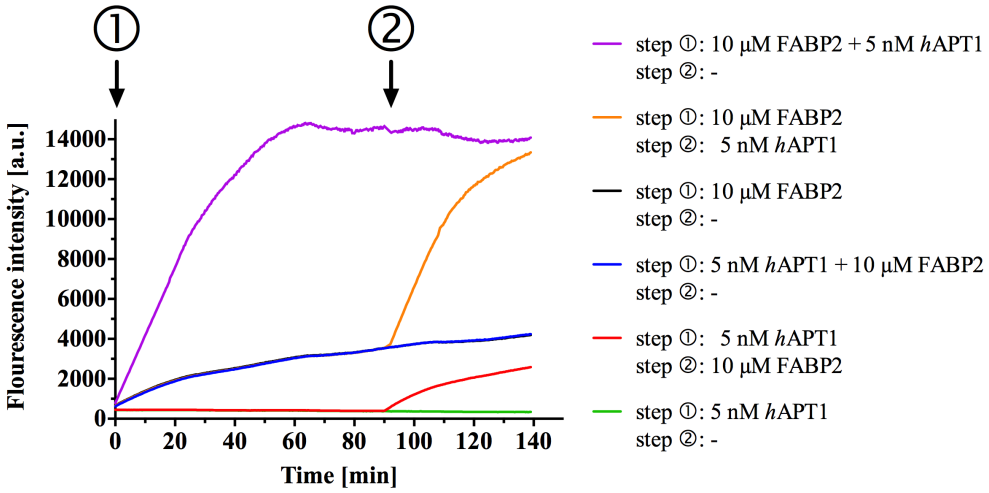

Figure 3.11: FABP2 can ensure hydrolysis of PPTS by *h*APT1. When only *h*APT1 is added (green line) to a solution of 60 µM PPTS in assay buffer no conversion is detectable. If 10 µM FABP2 is added after APT (red & blue trace) only the increased background hydrolysis (equivalent to the slope of the black curve) can be seen, no matter if added immediately after APT or after 90 min. Only if FABP2 is added first (violet & orange line) to 60 µM PPTS hydrolysis by *h*APT1 can be seen. Here, it does not matter if APT is added subsequently after FABP2 or 90 min later.

above conclusions about the irreversible inactivation of APT. When APT is added first to a solution of 60 µM PPTS, additional FABP2 cannot rescue its enzymatic activity (red and blue lines in figure 3.11). In contrast, when FABP2 is added prior to APT, a significant PPTS conversion by the thioesterase can be observed (violet and orange lines in figure 3.11). This effect cannot be explained by an equimolar sequestration of PPTS (initially 60 µM) by FABP (10 µM), since the resulting concentration of 50 µM PPTS would still be above the "PPTS aggregation threshold" that leads to an APT inactivation. Even a second fatty acid binding site, as reported for FABP1 [112] would not be sufficient. Thus it seems possible that FABP2 prevents formation of the protein-destroying species of PPTS aggregates by inserting into the PPTS "micelles" and affecting much more than one PPTS molecule per protein molecule. An experiment using different ratios of FABP2 and PPTS revealed that a concentration of 10 µM FABP2 is enough to ensure APT activity up to 120 µM PPTS (figure 3.12A).

From the respective FABP2 concentrations at which the plateau was reached for each

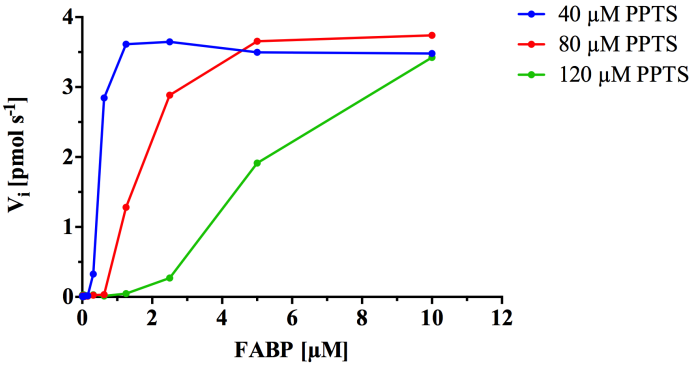

Figure 3.12: *h*APT1 activity on PPTS in the presence of different amounts of FABP2. The more PPTS is used, the more FABP2 is necessary to ensure activity of 5 nM *h*APT1. 10 µM FABP2 seem to be sufficient to reach the maximum APT activity up to 120 µM PPTS.

PPTS concentration (figure 3.12A), 11-19 PPTS molecules were calculated to be able bind to a single FABP2 protein. Thus it appears plausible that at high PPTS concentrations the entire cavity and the surface of FABP2 gets covered by the substrate. Thus, aggregation of PPTS will be prevented whilst the substrate is still accessible for *h*APT1.

A drawback of using FABP2 concentrations of 10 µM or 5 µM is the increased high background hydrolysis in absence of APT, which is surprising since FABP2 does not have an active site (see black and blue curve in figure 3.11). A possible explanation would be that FABP2 shows a high affinity to palmitic acid (K_d = 120 nM [111]) which is the reaction product of hydrolysis of PPTS. By binding of palmitic acid to FABP2 it is removed from equilibrium state of autohydrolysis, which would, according to Le Chatelier's principle, cause a shift of the reaction more to the side of the products and thus accelerate the non-enzyme-mediated hydrolysis of PPTS. In addition, binding of the substrate itself to FABP2, with the fatty acid moiety binding inside the binding tunnel and the head group outside, might put a certain strain to the ester bond connecting fluorophore and fatty acid, which could also result in an increased PPTS "hydrolysis".

A second approach for rescuing APT activity at high PPTS concentrations was aspired by reports about the ability of DMSO to increase the critical micelle concentration of hexadecanylated (cetylated) compounds and thus to disturb the formation of micelles [113],[114] , so perhaps also the aggregation of PPTS. Indeed, when increasing the DMSO concentration from the usually used 1 % up to 3 %, 5 % or 10 %, the plateau phase of *h*APT1 activity stays stable at PPTS concentrations higher than 10 µM (figure 3.13B). On the other hand, the increasing amount of DMSO is significantly influencing the maximal velocity of APT converting PPTS (V_{max}) and the Michaelis

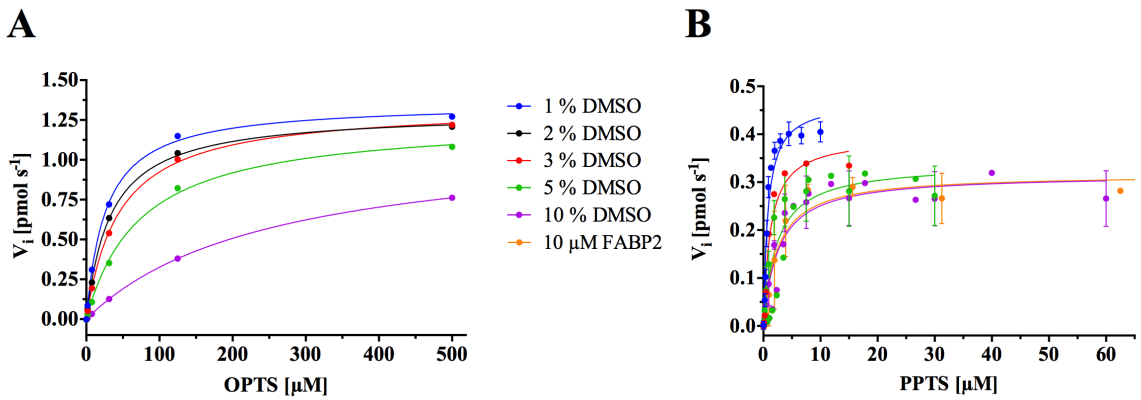

Figure 3.13: *h*APT1 activity on OPTS and PPTS in the presence of different amounts of DMSO. (A) The activity of 5 nM *h*APT1 converting OPTS at different amounts of DMSO was determined. While V_{max} is not influenced much, the K_m is increasing with increasing DMSO concentration (see table 3.1). (B) The activity of *h*APT1 converting PPTS at different amounts of DMSO was determined. Because of deviations between different measurements all available data was collected. To allow best comparison, all values of velocity were "normalized" to 1 nM APT if necessary, because varying concentrations of APT were used in the different experiments. The last data point shown for each DMSO concentration marks the highest possible concentration of PPTS were APT was still completely active, except 10 % DMSO where APT was still active at PPTS concentrations $>$ 100 µM. Compared to OPTS, the increasing amount of DMSO influences K_m less but V_{max} much more (table 3.1). As comparison also the activity of *h*APT1 on PPTS in presence of 10 µM FABP2 is plotted (orange curve). The legend is true for both charts.

constant K_m (for detailed information about the determination of K_m values see section 3.1.1.1). Compared to the condition with 1% DMSO present, the K_m is increased more than 200 % when 10 % DMSO are used, while V_{max} is decreased by 32 % (table 3.1). To see if the changes of K_m and V_{max} are due to a direct effect of DMSO on the enzyme, the experiment was also performed with OPTS as substrate (figure 3.13A). Surprisingly, the K_m of OPTS is much more negatively influenced by DMSO compared to PPTS, while the V_{max} stays almost unaffected up to 10 % DMSO. The influence of organic solvent like DMSO on the kinetics of enzyme is a known phenomenon [115], also for esterases [116]. The significant increase of the K_m value could be an effect triggered by the competitive interaction of the solvents with the substrate [115],[117]. In the case of PPTS this effect might be less pronounced because of the simultaneous improved availability of PPTS at higher DMSO concentrations which might partially compensate for competition with the solvents. The observed effect on V_{max} can generally be explained by disruption of the integrity of the enzyme at higher DMSO concentrations [115] and the decreased water concentration, which has to be considered too, since a water molecule is necessary in the hydrolization step of the ester bond [117]. But, since both substrates show different intensities of this effect, also the substrate itself, especially PPTS, must have an influence. It might be conceivable that DMSO indeed

Table 3.1: Kinetic parameters of *h*APT1 converting PPTS at different conditions. Listed are the calculated kinetic parameters from the curves shown in figure 3.13. 5 nM *h*APT1 was used in the case of the OPTS substrate, values for the PPTS substrate refer to 1 nM *h*APT1.

	OPTS substrate		**PPTS substrate**	
	K_m [µM]	**V_{max} [pmol s^{-1}]**	**K_m [µM]**	**V_{max} [pmol s^{-1}]**
1 % DMSO	26.58 ± 1.55	1.36 ± 0.02	0.79 ± 0.07	0.47 ± 0.01
2 % DMSO	33.23 ± 1.49	1.30 ± 0.02	-	-
3 % DMSO	45.02 ± 1.73	1.34 ± 0.01	1.23 ± 0.31	0.39 ± 0.03
5 % DMSO	73.67 ± 6.37	1.26 ± 0.03	2.33 ± 0.66	0.34 ± 0.03
10 % DMSO	251.5 ± 4.30	1.15 ± 0.01	2.60 ± 0.57	0.32 ± 0.02
10 µM FABP2	-	-	2.43 ± 0.54	0.32 ± 0.02

prevents APT inactivation by PPTS aggregates and ensures a APT activity also at higher concentrations, but traps PPTS in a way that the V_{max} value observed at only 1 % DMSO cannot be reached. Interestingly, the use of 10 % DMSO to prevent destructive PPTS aggregation has the same effect on APT kinetics as the use of 10 µM FABP2 (3.12B). Compared to the FABP2-approach usage of DMSO does not lead to an accelerated background hydrolysis.

In conclusion, the use of OPTS in standard activity assays or inhibition studies combines different advantages. OPTS is highly soluble and does not require any additional detergents, which are not only influencing the substrate or its interaction with the protein (figures 3.2 and 3.4), but also the behavior of other, especially fatty acid-based compounds in the assay (section 3.3.1, figure 3.33). This leads to a simpler and more controllable assay system that can be used to determine the kinetic parameters of different APT proteins. The fluorescence of the pyrene head group with its large Stokes' shift also encourages the use of HPTS-based substrates. However, unexpected side effects occurred with the use of HPTS derivatives containing longer chained fatty acid moieties. Although their solubility is still excellent without detergent, they tend to form aggregates at high concentrations that seem to inactivate APT irreversibly by damaging its structure. To overcome this problem further investigations on *h*APT1 were carried out, showing that addition of FABP2 in micromolar concentrations or 5-10 % DMSO to the assay buffer maintains *h*APT1 activity also at higher PPTS concentrations. Unfortunately both additives at higher concentrations do also influence the kinetics of APT, leading to a decreased affinity of the substrate to APT and also to a reduced maximal velocity of catalysis. Thus, the use of 1 % DMSO is the best compromise for the determination of kinetic parameters of APT converting HPTS-based substrates. At least for *h*APT1 this is feasible since a V_{max} is reached before PPTS aggregates abolish the APT activity. However, to determine more reliable parameters

using PPTS as substrate the assay has to be improved. Determination of Michaelis-Menten kinetics at varying amounts of FABP2, as done for DMSO, could show if the use of lower FABP2 concentrations lead to a reduction of background hydrolysis and less influence on APT kinetics, while still preventing PPTS aggregates. Also the use of bovine serum albumin (BSA) instead of FABP2 could be tested. In cell biology, conjugates of fatty acids and BSA, a known fatty acid transporter [118], are used to provide the fatty acids for the cells in aqueous solution. This principle could also succeed using PPTS-BSA conjugates, but - similar to the FABP2 case - the affinity of PPTS to BSA has to be considered as a potential competitive effect.

3.1.1.1 Determination of basic Michaelis-Menten kinetic parameters of APT proteins

Using the fluorescence-based activity assay with OPTS as substrate that was established in this thesis, kinetic parameters were determined for different APT homologues from *Human* (*h*APT1 and *h*APT2), *Xenopus tropicalis* (*xt*APT1 and *xt*APT2), *Drosophila melanogaster* (*dm*APT) and *Saccharomyces cerevisiae* (*y*APT). Information on the investigated APT proteins including their NCBI reference can be found in table 6.1 in the appendix, as well as the calibration curve used to convert initial slopes of substrate conversion to substrate turnover (figure 6.1). Because the stocks of OPTS and the later used inhibitors were dissolved in DMSO, the DMSO concentration was kept at 1 % for all standard OPTS assays, including inhibition studies, to maintain comparability of parameters. The Michaelis constant K_m represents the concentration of OPTS necessary to reach the half-maximum reaction velocity, while the catalytic rate constant k_{cat} describes the maximum number of substrate molecules (turnover) converted by a single active site per time unit. k_{cat}/K_m can be used to describe the catalytic efficiency of a protein. It has to be noted that these parameters should be determined under "Michaelis-Menten conditions" which assume certain circumstances: First, the system has to be in a steady-state, meaning the concentration of the formed enzyme-substrate complex [ES] does not change over time. Therefore the concentration of the substrate [S] should be much higher than the enzyme [E] to saturate the formation of the enzyme-substrate complex ES. Second, the formation of ES is assumed to be much faster than the product formation, which is then the rate limiting step that can be measured by determination of the initial velocity V_i of the reaction. This is the slope of the linear phase at the beginning of substrate conversion by the enzyme. This slope is depending on the concentration of the substrate but will reach a saturation at high concentrations, called the maximal reaction velocity V_{max}. Division of V_{max} by the number of active sites (in the case of APT equal to the number of proteins) gives the k_{cat} value. A third requirement for the "Michaelis-Menten conditions" is that the substrate concentration should be constant during the measurement, which can

be approximately achieved if the concentration of the enzyme is much lower than the determined K_m value. While the first and third requirements are fulfilled according to the used conditions in this assay (see also section 5.2.2.1), the second assumption of a fast ES formation and dissociation may be not entirely fulfilled in activity assays presented here. Because of the participation of the lid-loop of APT that forms a binding tunnel in substrate-binding (see section 5.2.2.1 and [88]) and the hydrophobic nature of the substrates, a slower binding and release of substrate molecules might occur compared to a directly accessible, hydrophilic active site. This effect might be become more prominent in the cases of longer chained substrates like LPTS and PPTS compared to OPTS, because a stronger interaction with the lid loop and binding tunnel can be assumed. Thus, it cannot be excluded that the (potentially slow) assembly and disassembly of the enzyme-substrate complex is limiting the rate of product formation as explained below. Under Michaelis-Menten conditions the close relationship between K_m and the dissociation constant K_d , the Michaelis constant is often used as measure of substrate affinity to the enzyme. As apparent by the equations 3.1 and 3.2

$$K_m = \frac{k_{off} + k_{cat}}{k_{on}} \tag{3.1}$$

$$K_d = \frac{k_{off}}{k_{on}} \tag{3.2}$$

where k_{off} is the dissociation rate constant and k_{on} the association rate constant, this assumption is only entirely true if k_{cat} equals zero or is negligible small compared to k_{off}. As mentioned above, this might not be the case for substrate conversion by APT , thus K_m corresponds to an upper limit of the K_d value as an expression of the binding affinity. However, it is still possible to compare K_m values of different APT enzymes or different substrates measured under similar conditions. Figure 3.14 shows the performance of the APT proteins and the corresponding kinetic results obtained by fitting the classic Michaelis-Menten equation (see methods section 5.2.2.1) are listed in table 3.2.The determined K_m values range between 20 - 60 µM, which seem to be plausible values for the OPTS substrate, since the short 8 carbons long tail is not expected to lead to a high affinity binding, especially with the big pyrene head group that also has to fit next to the active site. The K_m values are higher than for DiFMUO which has a slightly smaller fluorescent head group, but k_{cat} is significantly increased, probably because detergens was used in the case of DiFMUO. Interestingly, the two APT2 isoforms of human and xenopus show a 55 - 70 % higher K_m compared to their isoform 1 equivalents. The determined catalytic rate constants k_{cat} are between 1.2 s^{-1} and 13 s^{-1}, whereby most tested APT proteins can convert 2.2 to 3.1 substrate molecules per second, which is far slower than the theoretical limit of 10^6 - 10^7 s^{-1} but the the typical range for metabolic enzymes [119] (see also end of section 3.1.1.2).

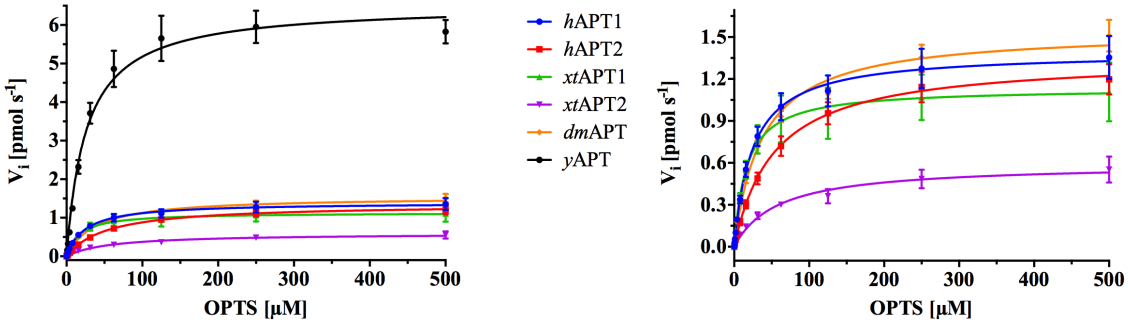

Figure 3.14: Michaelis–Menten kinetics of APT proteins from different species, using OPTS as substrate. The activity of 5 nM APT enzymes was determined using OPTS as substrate. Since the APT protein from yeast shows a very high activity, the chart on the right is lacking *y*APT to illustrate the kinetics of the other APTs in greater detail. Plotted are the mean values of a measured triplicate with the corresponding standard error bars and the fitted Michaelis-Menten equation.

*xt*APT2 catalyzes the reaction below-average with a k_{cat} of 1.2 s^{-1} while the fastest APT, *y*APT, is able to hydrolyze 13 OPTS molecules per second, a 5 fold higher rate than for most of the other APTs. Since the affinity of OPTS to *y*APT is comparable to the other proteins, the catalytic efficiency of the yeast homologue, represented by k_{cat}/K_m , appears also 5-times higher than isoform 1 APTs and 10-times better than APTs of isoform 2.

3.1.1.2 APT kinetics using synthesized substrates LPTS and PPTS

Two additional substrates containing longer chained fatty acid moieties, LPTS and PPTS, were synthesized (see section 5.2.9) , to investigate the substrate specificity of APTs depending on the fatty acid chain length of the substrates (see section 3.1). As previously shown, HPTS-based substrates tend to form aggregates that destroy the APT structure irreversibly (end of section 3.1.1). This tendency seems to be fatty acid chain length-dependent and thus most pronounced for PPTS, but was also observed for LPTS. As shown in figure 3.15A, even with 5 % DMSO *h*APT2 and *xt*APT2 are inactivated at LPTS concentrations above ∼100 µM, while APTs of isoform 1 appear to be more robust. Although the influence of 5 % DMSO on APT kinetics have to be considered (see previous section), Michaelis-Menten kinetics could be obtained for both APT isoforms of Human and Xenopus. Under these conditions, all proteins show a significant decrease of K_m values compared to the OPTS substrate, indicating a stronger interaction of LPTS with the proteins, explainable by the increased interaction surface between substrate and the APT binding tunnel. Compared to OPTS, *h*APT1 and *xt*APT1 show a 75 % reduced K_m, *h*APT2 and *xt*APT2 a 85 % lower value. *h*APT1 and *xt*APT2 are able to convert a similar amount of OPTS and LPTS molecules per time unit. Although the turnover of *h*APT2 and *xt*APT1 is halved compared to OPTS,

Table 3.2: Kinetic parameters of APT proteins from different species, using OPTS as substrate. The table reports the determined kinetic parameters from the Michaelis-Menten kinetics shown in figure 3.14. As reference the kinetic parameters of *h*APT1 and *h*APT2 obtained with the DiFMUO substrate [87] (0.01 % Triton X-100) are also listed (marked with an asterisk *).

	K_m [µM]	k_{cat} [s^{-1}]	k_{cat}/K_m [s^{-1} μM^{-1}]
*h*APT1	24.46 ± 1.62	2.78 ± 0.05	0.11
*h*APT2	53.63 ± 3.07	2.71 ± 0.05	0.05
*xt*APT1	16.57 ± 2.30	2.27 ± 0.08	0.14
*xt*APT2	57.96 ± 7.33	1.19 ± 0.05	0.02
*dm*APT	37.28 ± 2.71	3.10 ± 0.06	0.08
*y*APT	26.09 ± 2.18	13.06 ± 0.29	0.50
*h*APT1*	2.1 ± 0.6	0.014	0.007
*h*APT2*	6.1 ± 0.8	0.26	0.04

probably because of the higher amount of DMSO, the efficiency of catalysis is increased 2 - 6 fold for all proteins compared to OPTS, mainly caused by the significant drop in the K_m values. For the *h*APT1 enzyme, which appears to be the most aggregate-resistant protein and also the most thermostable protein according to melting point analysis (see figures 3.18 and 6.7), Michaelis-Menten kinetics could also be determined in presence of only 1 % DMSO, as used for OPTS. A comparison of *h*APT1 kinetics on LPTS at 1 % and 5 % DMSO is shown in figure 3.15 and table 3.3. As seen for

Table 3.3: Kinetic parameters of APT proteins from different species, using LPTS as substrate at a DMSO concentration of 5 %. The table reports the determined kinetic parameters from the Michaelis-Menten kinetics shown in figure 3.15.

	K_m [µM]	k_{cat} [s^{-1}]	k_{cat}/K_m [s^{-1} μM^{-1}]
*h*APT1 (1% DMSO)	2.46 ± 0.18	2.65 ± 0.04	1.08
*h*APT1 (5% DMSO)	6.18 ± 0.56	2.50 ± 0.05	0.40
*h*APT2 (5% DMSO)	7.02 ± 0.99	1.17 ± 0.01	0.17
*xt*APT1 (5% DMSO)	3.99 ± 0.58	1.08 ± 0.03	0.27
*xt*APT2 (5% DMSO)	8.80 ± 1.32	1.13 ± 0.05	0.13

OPTS with different amounts of DMSO (figure 3.13A), the V_{max} value, thus also k_{cat}, is only slightly influenced, while K_m appears 2.5-times better at 1 % DMSO than at 5 % DMSO.

Because of the destruction of APT proteins by PPTS-aggregates (see end of section 3.1) on one hand, and the drastic influence of DMSO on APT kinetics with PPTS (see figure 3.13) on the other, a reasonable determination of kinetic parameters using

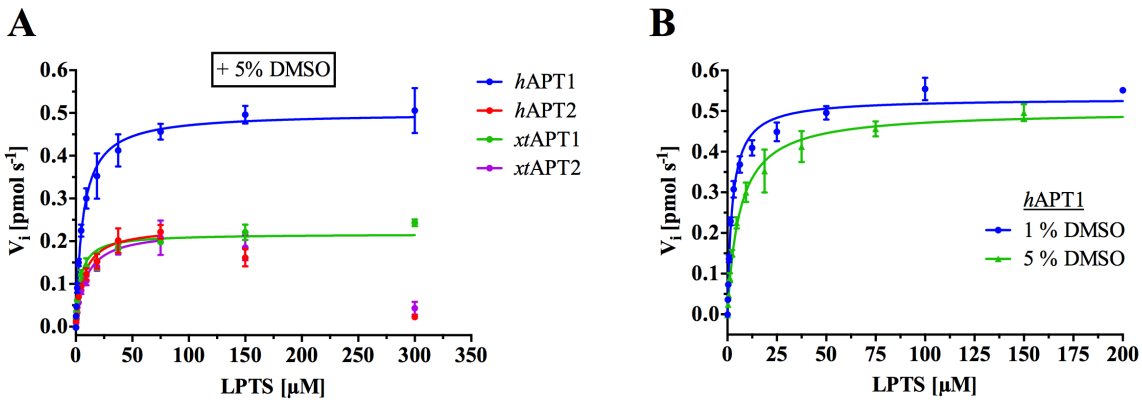

Figure 3.15: Michaelis–Menten kinetics of APT proteins from different species, using LPTS as substrate. (A) Although the perturbing effect of 5 % DMSO on the kinetic parameters is known (see previous section) Michaelis-Menten kinetics were determined for 2 nM of both APT isoforms of Human and Xenopus. While isoform 1 APTs show a stable plateau up to 300 µM LPTS, *h*APT2 and *xt*APT2 seem to react more sensitive to the given conditions and a decrease in enzymatic activity can be seen at LPTS concentrations of 150 µM and 300 µM. V_i values of these concentrations were thus excluded from the Michaelis-Menten fit for both proteins. (B) Using 2 nM *h*APT1 it was possible to obtain acceptable kinetics with just 1 % DMSO (blue curve) to get less DMSO-influenced kinetic parameters. For comparison, the data of *h*APT1 activity on LPTS at 5% DMSO are also shown (green curve). Plotted are the mean values of a triplicate with the corresponding standard error bars and the fitted Michaelis-Menten equation.

PPTS as substrate was so far only done for *h*APT1 at 1 % DMSO (lowest possible amount). As shown in figure 3.16, a stable plateau phase up to 10 µM PPTS is observed for *h*APT1, that allows a fit with the classical Michaelis-Menten equation, but the measured velocities show systematic deviations from the fitted curve. Since this was already observed to a lesser extent in case of LPTS (figure 3.15B) but not for OPTS, these deviations seem to be dependent on the chain-length of the substrate and thus possibly also on an early formation of aggregates, since the experiments were performed at only 1 % DMSO, a concentration that cannot completely prevent PPTS aggregation (section 3.1.1) It is conceivable that already at low concentrations aggregates or aggregate-precursors are formed by the substrate which might either change its availability and/or influence the activity of APT, without leading to a complete destruction of APT structure, thus lowering the values at high PPTS concentrations, which would explain the systematic deviations from the Michaelis-Menten kinetic. For all measurements background hydrolysis has been taken into account by subtracting a control with no enzyme present from the APT-containing reaction. Background hydrolysis seems to increase with substrate concentration and chain length of the substrate but was always less than 5 % of the corresponding reaction with APT present.

Since the experiment with *h*APT1 and PPTS could be measured in the presence of

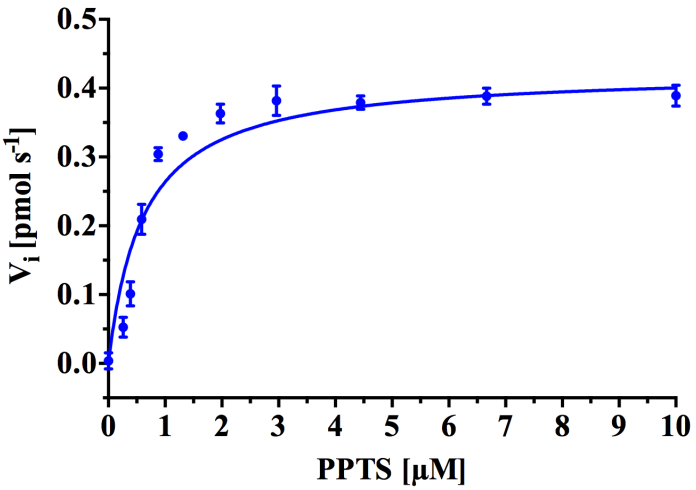

Figure 3.16: Michaelis–Menten kinetics of *h*APT1, using PPTS as substrate. The kinetics of 1 nM *h*APT1 converting PPTS in the presence of 1 % DMSO are shown. Plotted are the mean values of a triplicate with the corresponding standard error bars and the fitted Michaelis-Menten equation. The systematic deviations of the data from the fit are explained in the text. Determined parameters are listed in table 3.4.

1 % DMSO, the determined kinetic parameters could be directly compared to the other substrates OPTS and LPTS, that were also measured with 1 % DMSO (table 3.4). As

Table 3.4: Comparison of kinetic parameters of the conversion of the three different substrates OPTS, LPTS and PPTS by *h*APT1 at 1 % DMSO.

	K_m [µM]	k_{cat} [s^{-1}]	k_{cat}/K_m [s^{-1} μM^{-1}]
OPTS	24.46 ± 1.62	2.78 ± 0.05	0.11
LPTS	2.46 ± 0.18	2.65 ± 0.04	1.08
PPTS	0.70 ± 0.10	4.5 ± 0.18	6.43

mentioned for the LPTS substrate, it is obvious that the affinity of the substrates to *h*APT1 (as judged by the K_m values) increases with growing chain length, which can be explained by an enlarged interaction surface between ligand and protein, most likely in the binding tunnel, that increases the entropy driven hydrophobic effect and promotes a binding with higher affinity. The catalytic rate constant k_{cat} seems to increase especially for the long-chained PPTS substrate, which results in a 60-times higher catalytic efficiency for PPTS conversion compared to hydrolysis of OPTS. Therefore, at least for *h*APT1, increasing chain length of the substrate leads to an increased affinity to the protein and also to a much higher efficiency, since also the catalytic turnover appears higher, indicating that the protein prefers long-chained substrates. This would suggest a preference of at least *h*APT1 for the assumed physiological substrates, i.e. palmitoylated proteins. Unfortunately, co-crystallization attempts of PPTS with the catalytically inactive mutant *h*APT1 S119A were not successful. A reason for this could

be the change of the global APT structure by PPTS aggregates that will definitely be present because PPTS has to be provided in high concentrations (> 1 mM) to ensure a proper occupancy at the APT binding site. Since APT is typically forming dimers within the crystal, mostly with the active site buried in the dimer interface, also the huge pyrene head group of PPTS could perturb and prevent crystallization.

To evaluate the determined APT kinetics and to be able to rank the activity of APT, the literature was browsed for comparable values of K_m and k_{cat}. Bar-Even and coworkers analyzed the entire BRENDA enzyme database [120],[121] according to published K_m and k_{cat} values of enzymes to their natural substrates [119]. They found that the median k_{cat} value of 1942 unique reactions is ∼10 s^{-1} and the median K_m of 5194 unique reactions equals 130 µM. They also found that the k_{cat} is depending on the metabolic pathway the enzyme is involved in. While enzymes of the primary metabolism, dealing with carbohydrate energy (e.g. glycolysis) show an average k_{cat} of 79 s^{-1}, proteins of the primary metabolism managing amino acid, fatty acid and nucleotide supply (e.g. fatty acid biosynthesis) have a reduced average k_{cat} of 18 s^{-1}. Enzymes of intermediate or secondary metabolism only reach an average k_{cat} of 5.2 s^{-1} or 2.5 s^{-1}, respectively. Thus, APT proteins seem to be relatively slow enzymes at least when converting the artificial, non-physiological HPTS-based substrates. This might be different for physiologically relevant substrates as suggested by the (apparent) k_{cat} of both human APTs for hydrolysis of palmitoylated peptide in solution ($k_{cat} \sim 27$ s^{-1}, see section 3.2.2).

3.1.2 Intrinsic tryptophan fluorescence assay (Trp-assay)

When a ligand binds to a protein, the microenvironment around the binding site is changed and thus also the characteristics in fluorescence of neighboring amino acids. At an excitation wavelength of 280 nm tryptophan residues dominate the fluorescence spectra since they show a much stronger fluorescence and a higher quantum yield than the other two aromatic amino acids, phenylalanine and tyrosine [122]. By taking advantage of these two properties, binding events can be detected based on the change of tryptophan fluorescence. The human APT1 protein contains three tryptophan residues at amino acid positions 37, 72 and 145. While Trp72 is part of the protein's hydrophobic core, the two other tryptophans are placed at two strategic positions, which allow monitoring of ligand binding in an ideal way. As depicted in figure 3.17, Trp37 is exposed at the surface of the shallow groove that might serve as a second binding site (see section 1.2.2 and figures 1.7and 3.17), whereas Trp145 is located at the inner wall of the substrate binding tunnel and oriented in parallel to the tunnel direction.

To distinguish binding to the different positions on the protein's surface, mutants of *h*APT1 were used, where either Trp37 or Trp145 or both were mutated to a pheny-

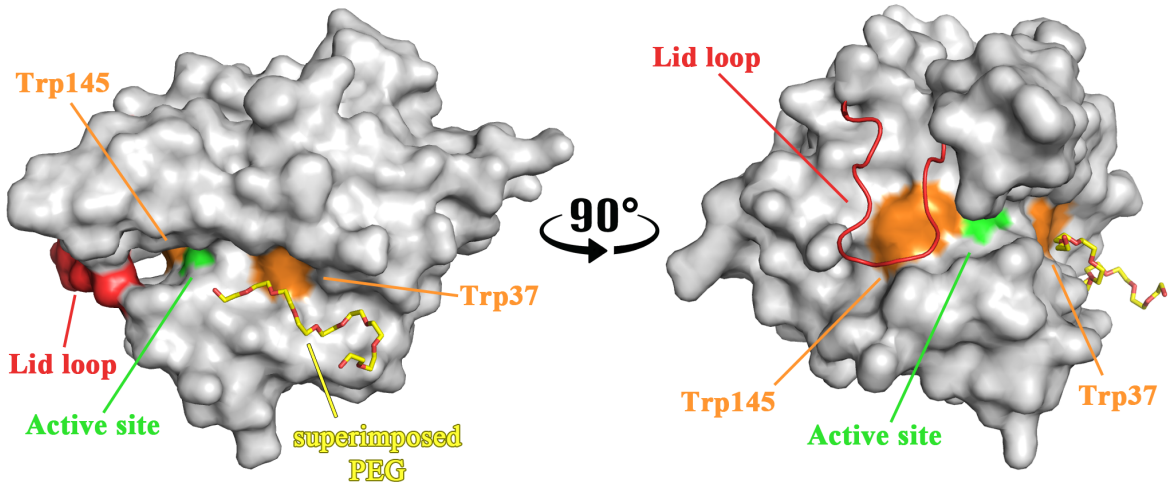

Figure 3.17: Positions of tryptophans Trp37 and Trp145 at *h*APT1 surface. Trp 37 is located within the shallow groove that might serve as a substrate interaction site, as the superimposition with the PEG molecule from a structurally closely related carboxylesterase from *Pseudomonas aeruginosa* (PDB code 3CN9) implies. Trp145 is located in the middle of the substrate binding tunnel. The *h*APT1 protein is shown as a grey surface in both views. The lid loop structure is colored in red, the active site in green and the two tryptophan residues in orange. The superimposed PEG is shown as yellow sticks. For the sake of clarity the surface of the lid loop is omitted in the right view, because otherwise the position of Trp145 would not be visible.

lalanine. The exchange to phenylalanine still maintains the hydrophobic character but almost abolishes the fluorescence signal from this position when excited at 280 nm. So, changes in fluorescence of the mutant *h*APT1 W37F displays binding close to Trp145 in the binding tunnel, while an interaction next to Trp37 in the shallow groove will be detected by the mutant *h*APT1 W145F. The double mutant *h*APT1 W37F W145F will show indirect effects of the substrate binding, e.g. due to global changes of the protein, since the remaining Trp72 is buried in the protein core. Mutation of all three tryptophan residues to phenylalanine failed because the protein was not stable and was degraded during the purification process. All tryptophans show an enormous effect on the protein stability that can be seen in the melting curves determined using circular dichroism spectroscopy (figure 3.18). While the wild type *h*APT1 protein shows a melting temperature T_m of 61.6 °C, the introduction of a single Trp mutation leads to a decrease in T_m of 6 - 8 °C. Further mutation of the second tryptophan resulted in a stable protein at room temperature but with a melting temperature of only 45 °C and, as mentioned, after mutation of all three tryptophans no stable protein could be obtained. So, all tryptophan-mutants used in this thesis were stable at room temperature but were not allowed to warm up to 37 °C and were kept on ice during assay preparation. In time-dependent binding experiments the fluorescence was tracked at the individual emission maxima of each protein when excited at 280 nm. Emission spectra of each mutant are shown in the appendix (figure 6.2).

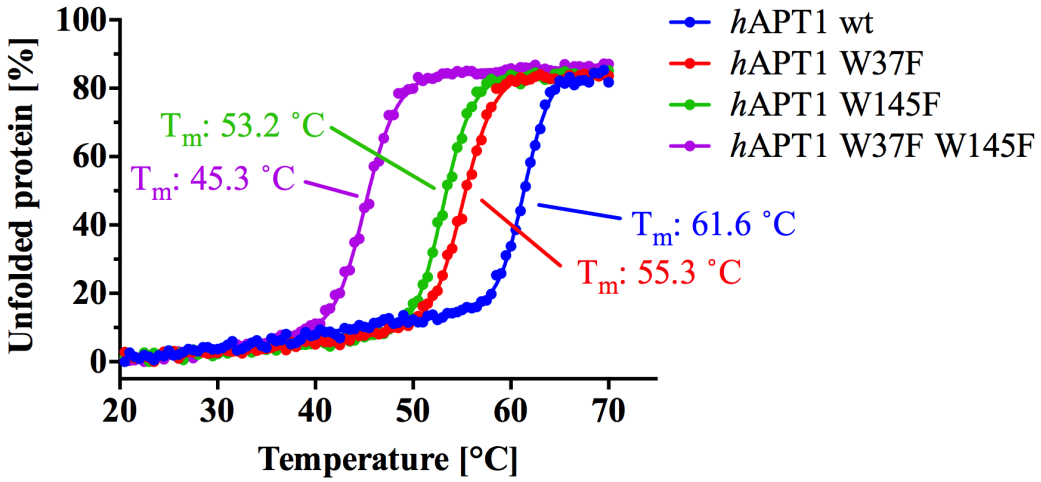

Figure 3.18: Thermal stability of APT mutants used in the intrinsic tryptophan fluorescence assay. The melting curves were obtained using CD spectroscopy and the protocol stated in the methods section 5.2.7.

3.1.2.1 Proof of principle of the Trp-assay

The first studies aiming at the development and characterization of highly potent APT inhibitors generated a group of palmostatins [32],[46]–[48]. These inhibitors are based on tetrahydrolipstatin (Orlistat), a drug used in the treatment of obesity by targeting the gastric lipase [123]. Because of the structural similarity of the ligand sensing cores of APT and gastric lipase, the active β-lactone core structure of Orlistat was used as reactive group in the palmostatins [48]. Palmostatins are rather unspecific and bind covalently via their β-lactone core to the active serine of APT, but the resulting bond is hydrolyzed after a certain time, thereby restoring the serine side chain [32]. Because of this inhibitor-hydrolysis co-crystal structures are hard to obtain. Our group was able to solve structures of complexes of palmostatin B and M with *y*APT, the only available structural information so far [88]. According to these crystal structures both inhibitor variants bind covalently to the active site serine via the β-lactone moiety, while the aliphatic tail is coordinated in a curved binding groove, since the actual hydrophobic binding tunnel of *y*APT is blocked by Phe81 and not accessible in its entire length, in contrast to *h*APT1 (figure 3.19).

This well characterized interaction between palmostatin M and *h*APT1 was chosen to validate the concept of the Trp-assay described above (section 3.1.2). As shown in figure 3.20A, the covalent binding mode to the active S119 of *h*APT1 can be confirmed, because tryptophan fluorescence was only quenched when the catalytically active serine was present, while no quenching was detectable using the catalytically inactive mutant *h*APT1 S119A (figure 3.20A). In contrast to *y*APT it seems that the aliphatic tail reaches deep into the hydrophobic binding tunnel of *h*APT1 since Trp145 is placed in the middle of this cavity that spans the whole protein, and a significant influence on its

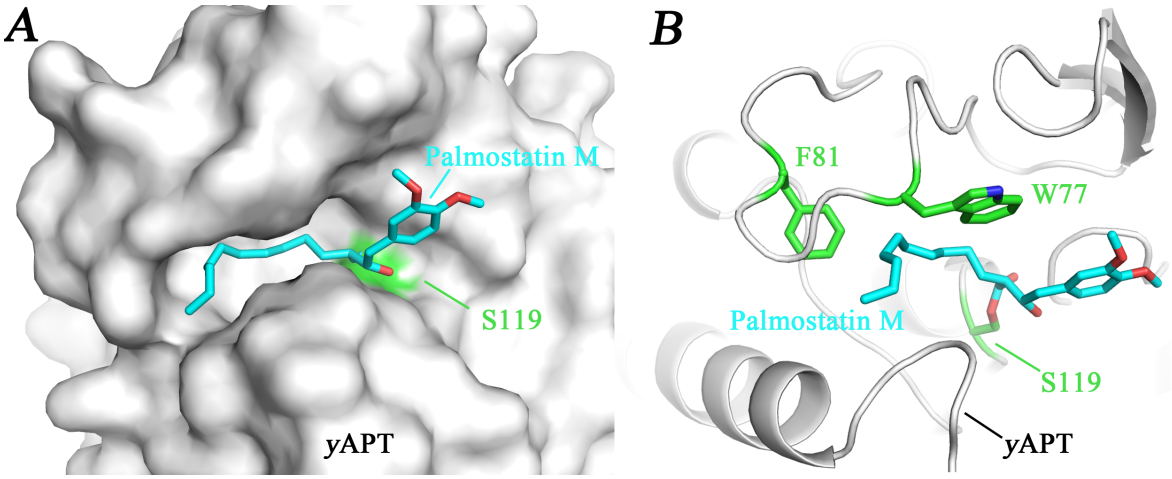

Figure 3.19: Palmostatin M bound to *y*APT. (A) The surface of the *y*APT protein is shown in grey, palmostatin M as cyan sticks. The inhibitor is covalently linked to Ser119 in the active center (green patch). Because the binding tunnel that is open in *h*APT1 and *h*APT2 is blocked and shortened by Phe81 of *y*APT, the aliphatic tail of palmostatin M has to rearrange and is thus bent towards the outside, but still in contact to the protein's surface. (B) *y*APT is shown as grey cartoon. Additionally to (A), the side chains of Ser119, Trp77 and Phe81 are shown as sticks and highlighted in green. The crystal structure was solved by Arthur Porfetye [88] .

fluorescence could be observed upon palmostatin M binding. In contrast, no binding was detected close to the second sensor-tryptophan Trp37 at the shallow groove (figure 3.17). When tracking the fluorescence of Trp145 over time (figure 3.20B) the instability of the covalent bond of palmostatin M can be seen, because hydrolysis of the bound inhibitor results in the recovery of the initial tryptophan fluorescence. The halftime of this cleavage could be determined for the three highest concentrations of palmostatin M (see figure 6.3 in appendix) and was 8.3 ± 0.4 min which is in the range of the reported 3.5 ± 0.1 min for palmostatin M and also palmostatin B [46] .

The validation of the postulated, covalent but reversible binding mode of palmostatin M and the good agreement of the determined halftime of the inhibitor at the active site with published results indicate that the established Trp-assay can indeed be used to determine ligand binding to APT. Using the three described mutants *h*APT1 W37F, *h*APT1 W145F and *h*APT1 W37F W145F also a discrimination of ligand binding sites (substrate binding tunnel vs. shallow groove) is possible.

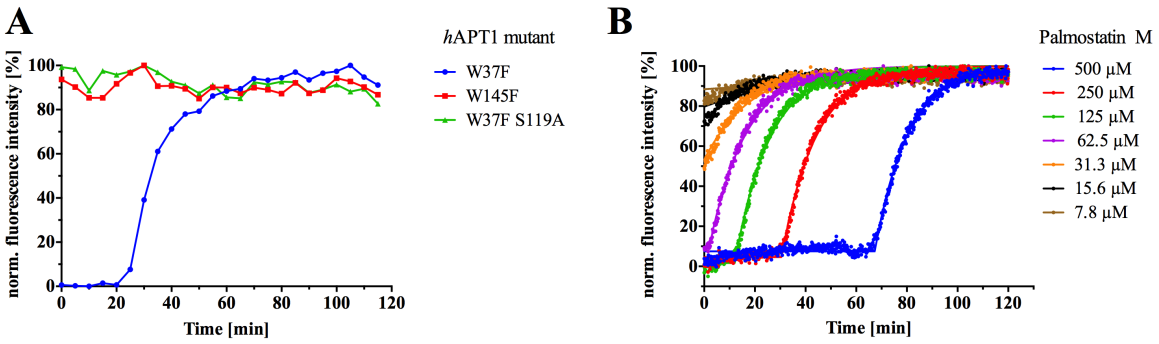

Figure 3.20: Quenching and restoring of tryptophan fluorescence by covalent binding of palmostatin M to *h*APT1 and subsequent hydrolysis. (A) Addition of palmostatin M leads to fluorescence quenching of Trp145 (blue curve) but not of Trp37 (red curve), indicating a binding into the substrate binding tunnel. Furthermore, a quenching is only detected when the active serine Ser119 is present (green curve), confirming the proposed covalent binding mode to Ser119. (B) Fluorescence quenching of Trp145 is time-limited and thus dependent on the available amount of palmostatin. When no more non-hydrolyzed inhibitor is present, the initial fluorescence is restored with a halftime of 8.3 ± 0.4 min (figure 6.3). The assay was performed with 10 µM APT protein to achieve a sufficiently high fluorescence signal.

3.2 Physiological APT substrates

3.2.1 Lipids as substrates of APT - The turbidity assay

As discussed earlier (see section 1.2.2) a variety of potential substrates of APT proteins are described in literature. Before research focused on protein substrates like Ras, also phospholipids and lysophospholipids were shown to be hydrolyzed by rat and rabbit APT1 and human APT1 respectively [55], [57]. It was not reported whether one of the two isoforms shows higher activity on these substrates or if homologues from lower organisms have a different substrate specificity. To answer this question a method is required that is independent of the poor solubility of these substrates in aqueous media, does not require detergents and allows an easy readout and thus a convenient comparison of the activity of the different APTs on (lyso-)phospholipids. For this purpose a turbidity assay was established in this thesis according to the instructions of Liu *et al.* [124] Petri dishes with solid agar were prepared, containing either egg yolk - to test for (lyso-)phospholipid hydrolysis - or olive oil - to test for triglyceride hydrolysis. Lipids represent 62.5 % of the total egg yolk solids, of which triglycerides account for 62 % and (lyso-)phospholipids for 33 % [125] (20-30 % of the total egg yolk solids [126]). Beside minerals and carbohydrates, proteins make up the rest (33 %) of the egg yolk solids. In contrast, olive oil consists of 99 % triglycerides [127]. Before pouring the fluid agar to the dishes, 1 % (v/v) 0.01 M $CaCl_2$ was added, because some groups of mammalian phospholipases require at least low calcium levels for their activity [55].

After hardening of the agar, cavities for different APT proteins were cut out in each petri dish. Hydrolysis of the turbidity-inducing substrates leads to a clear zone around the cavity after incubation at 37 °C for 16 hours . As seen in figure 3.21A, almost all tested APT proteins could hydrolyze (at least part of) the egg yolk substrate, resulting in clear zones. As negative control the catalytically inactive mutant *h*APT1 S119A was tested (well 9), showing that formation of a clear zone is indeed dependent on the catalytic activity of the protein. To test the importance of calcium for the APT proteins, the assay with egg-yolk present was also performed without the addition of $CaCl_2$. The resulting clear zones showed the same size after the same time as seen in the first experiment with $CaCl_2$ present, which is in agreement with observed calcium-independent activity of APT [55], [56] .

While APTs from Xenopus seem to be slightly less active than the APTs from Human and Drosophila, their yeast counterpart (well 5) shows a significant lower activity resulting in a 50 % reduced diameter of the clear zone compared to *h*APT1. As a reference, lipases from *Candida rugosa* were also tested (well 7). They produce a very clear circle, probably because of the additional hydrolysis of present triglycerides, and an almost opaque inner zone, which could be caused by the precipitation of hydrolysis products like fatty acids. Using olive oil instead of egg yolk as substrate (see figure 3.21B) revealed that *h*APTs are not able to clear the agar around the cavity, not even when used at a very high concentration of 1.4 mM (well 8). In contrast, the lipase mix from *C. rugosa* produced a nice clear zone as expected (wells 5-7). These results confirm that APTs show no lipase-like activity on triglycerides but a significant activity on egg-yolk components which are most likely (lyso-)phospholipids since they are the only substrate present in large amounts besides the triglycerides in egg yolk.

Interestingly, the APT homologue from yeast, which shows a very high activity in hydrolyzing the short OTPS substrate (see figure 3.14), is not able to hydrolyze (lyso-)phospholipids as fast as the other APTs do. This might either indicate that *y*APT is not able to efficiently hydrolyze substrates decorated with two or more fatty acids, like phospholipids, or that *y*APT is slow in hydrolysing of any substrate containing long chain fatty acids, thus having a substrate specificity for short-chained esters similar to carboxylesterases. To test these hypotheses, mutants of *y*APT, which shows 35 % sequence identidty to *h*APT1 and 31 % to *h*APT2, were produced based on the available structures in our lab. Trp77 of *y*APT is placed in the lid loop and not present in all the other APT proteins investigated (see sequence alignment in appendix, figure 6.8). As seen from the crystal structure (see figure 3.19), Trp77 is placed right opposite of the catalytically active Ser119, thus probably influencing the binding of a substrate at the active site, either by stabilizing the (thio-)ester properly or by sterically preventing a substrate from binding at this site. To extend the space next to the active site, the the mutants *y*APT W77Y and *y*APT W77A were prepared to provide slightly

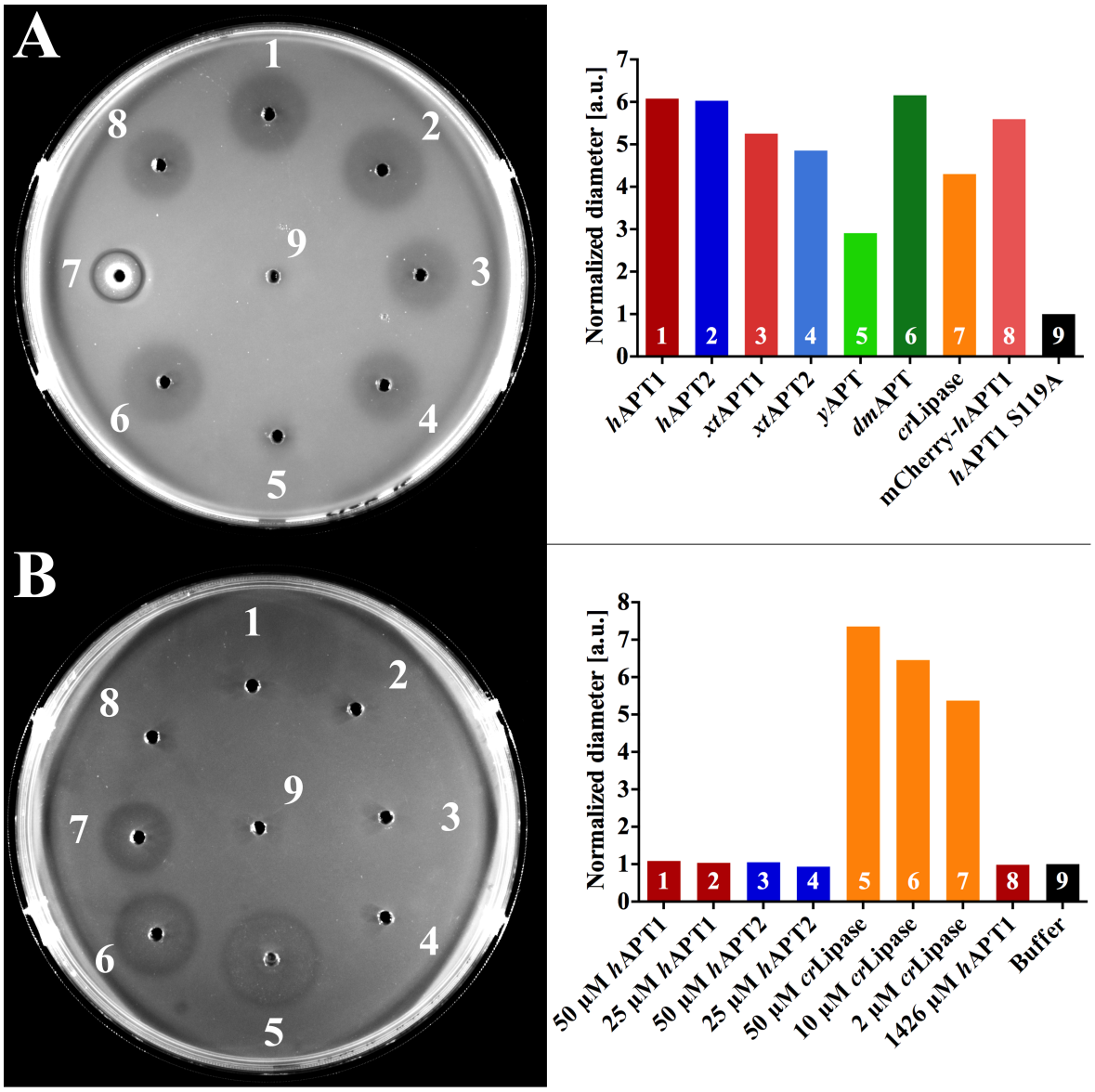

Figure 3.21: An agar-based turbidity assay to test for APT activity on (lyso-)phospholipids and triglycerides. (A) Egg yolk containing agar to test for activity on (lyso-)phospholipids. **1:** 5 µM *h*APT1. **2:** 5 µM *h*APT2. **3:** 5 µM *xt*APT1. **4:** 5 µM *xt*APT2. **5:** 5 µM *y*APT. **6:** 5 µM *dm*APT. **7:** 5 µM lipases (*Candida rugosa*). **8:** 5 µM *h*APT1 mCherry. **9:** 5 µM *h*APT1 S119A. The use of mCherry tagged *h*APT1 (well 8) allowed a control of the diffusion of the protein into the agar when excited with the corresponding wavelength (fluorescent zone corresponds to 95 % of the clear zone). (B) Olive oil containing agar to test for activity on triglycerides. **1:** 50 µM *h*APT1. **2:** 25 µM *h*APT1. **3:** 50 µM *h*APT2. **4:** 25 µM *h*APT2. **5:** 50 µM lipase from *C. rugosa*. **6:** 10 µM Lipase. **7:** 2 µM Lipase. **8:** 1426 µM *h*APT1. **9:** buffer. The bar charts on the right side show the relative diameters of the clear zones. The number of each bar refer to the number shown in the corresponding agar plate. All diameters were normalized to the negative control, *h*APT1 S119A (A) or buffer (B) that was set to a value of 1.

(W77Y) or significantly more space (W77A). The inactive mutant *y*APT S119A was used as negative control. As depicted in figure 3.22 the *y*APT variant containing W77A

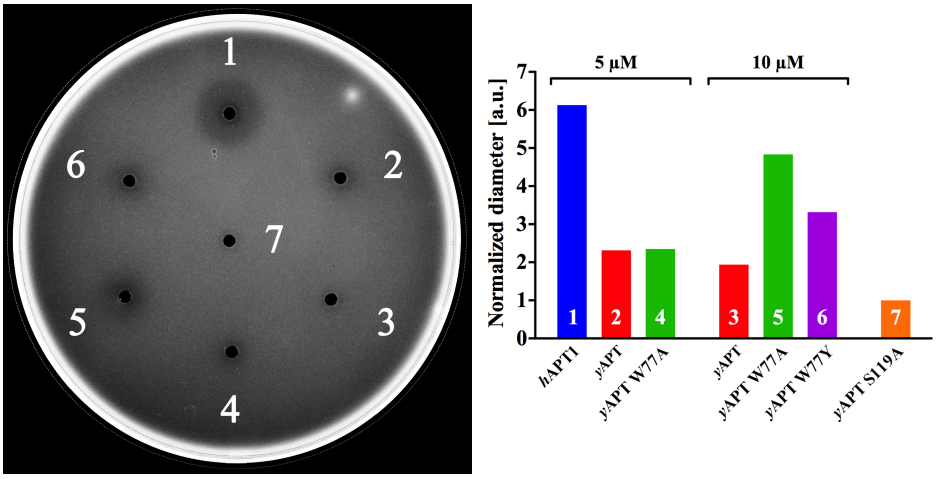

Figure 3.22: Agar-based turbidity assay to test hydrolysis activity of *y*APT mutants on (lyso-)phospholipids. *h*APT1 was included as a reference protein. **1:** 5 µM *h*APT1. **2:** 5 µM *y*APT. **3:** 10 µM *y*APT. **4:** 5 µM *y*APT W77A. **5:** 10 µM *y*APT W77A. **6:** 10 µM *y*APT W77Y. **7:** 5 µM *y*APT S119A (negative control). The bar chart on the right side shows the relative diameters of the clear zones. The number of each bar refer to the number shown in the agar plate. All diameters were normalized to the negative control *h*APT1 S119A that was set to a value of 1.

(well 5) seems to be able to hydrolyze the substrate much better than the wild type (well 2) or the W77Y mutant (well 6), but still less efficiently than the *h*APT1 protein (well 1), whereas W77Y has a less drastic effect. Obviously, sterically demanding amino acid side chains at position 77 of *y*APT do have an influence on (lyso-)phospholipid hydrolysis. Another potentially important amino acid is Phe81 which seems to block the binding tunnel of *y*APT (figure 3.19). In following studies also the effect of a mutation of Phe81 will be tested as a single mutation as well as in combination with the W77A mutation.

These experiments already indicated certain substrate specificity for APT but used the not very well defined egg-yolk substrate and did not provide any information about the catalytic turnover. Therefore electrospray ionization-mass spectrometry (ESI-MS) approaches were established (see methods section 5.2.6) together with Kathrin Estel to determine the velocity of catalysis of *h*APT1 and *h*APT2 on lyso-palmitoylphosphocholine (lyso-PPC) and di-palmitoylphosphocholine (DPPC). Since introduction of a fatty acid standard, e.g. palmitic acid, was not successful because of a very weak ionization efficiency, the resulting intensities of the ESI-MS spectra could not be properly quantified. However, the decrease of the substrate peak could be monitored quite reproducibly, and the relative intensities of the peaks corresponding to the correct mass of the substrate could be measured at different time points of the reaction. To increase the accuracy, at least six samples were taken and measured for each time

point. As depicted in figure 3.23, the error bars are acceptable and a decrease of the corresponding peaks was observed over time for lyso-PPC as well as DPPC, indicating a hydrolysis activity of *h*APT1 and *h*APT2. For estimation of the turnover of the APT

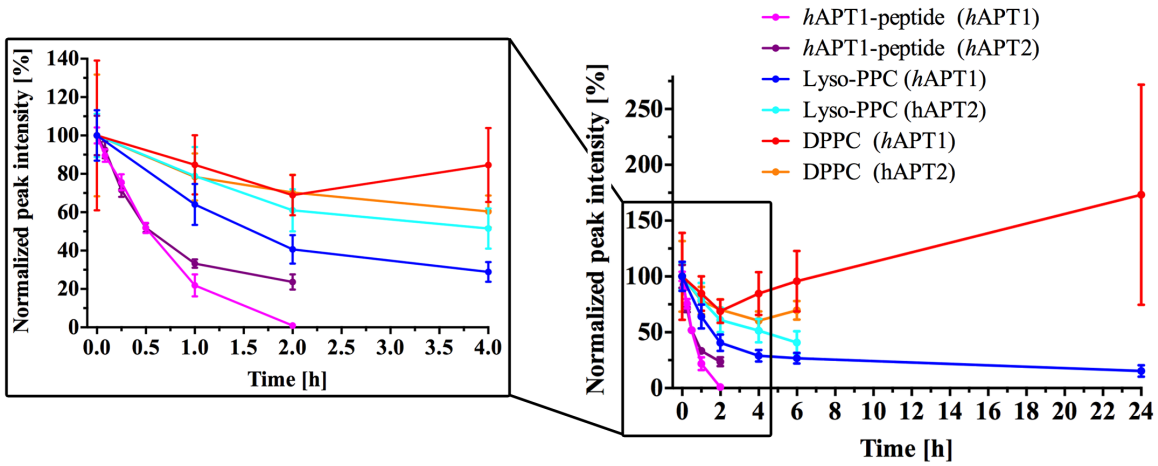

Figure 3.23: ESI-MS measurements to determine activity of *h*APT1 on different substrates. The reaction of APT with each substrate was started in ESI-buffer (5 mM $(NH_4)_2CO_3$) and samples were taken at different time points (see methods section 5.2.6). The relative peak intensities of each substrate at different time points are plotted, after they were normalized so that the initial (highest) value was set to 100 %, and the lowest (i.e. no intensity) to 0 %. For each substrate at least 6 measurements were taken for each time point. The error bars indicate the standard error.

proteins the slope of the initial linear phase was determined and apparent k_{cat} values were calculated, taking the used amount of substrate (0.2 µM for lyso-PPC and 0.1 µM for DPPC) and of the protein (100 nM) into account. According to these calculations a single *h*APT1 protein is able to convert $1.7 \cdot 10^{-4}$ molecules of lyso-PPC and $4.3 \cdot 10^{-5}$ DPPC phospholipids per second in solution, which are very slow rates compared to the artificial HPTS-based substrates (e.g. 4.5 s^{-1} for PPTS by *h*APT1, see table 3.4). *h*APT2 shows very similar rates of $1.2 \cdot 10^{-4}$ s^{-1} for lyso-PPC and $4.0 \cdot 10^{-5}$ s^{-1} for DPPC (table 3.5).

Table 3.5: Determined (apparent) k_{cat} of *h*APT1 and *h*APT2 hydrolyzing the palmitoylated *h*APT1-peptide, Lyso-PPC and DPPC. *h*APT1 and *h*APT2 show almost identical activity on the palmitoylated N-terminal *h*APT1-peptide (see next section), Lyso-PPC and DPPC. For comparison also the determined k_{cat} of *h*APT1 on PPTS is listed. *h*APT2 activity on PPTS was not determined due to an increased instability of *h*APT2 in in contrast to *h*APT1 (see section 3.1.1.2).

	palm. APT-peptide	PPTS	Lyso-PPC	DPPC
k_{cat} (*h*APT1) [s^{-1}]	26.2	4.5	$1.7 \cdot 10^{-4}$	$4.3 \cdot 10^{-5}$
k_{cat} (*h*APT2) [s^{-1}]	27.2	-	$1.2 \cdot 10^{-4}$	$4.0 \cdot 10^{-5}$

Besides the mentioned limits of the ESI-MS approach, the poor solubility of lyso-PPC and DPPC in aqueous buffer (here 5 mM $(NH_4)_2CO_3$) will also influence the

determined parameters, thus they have to be regarded as rough estimates. Since the accessible amount of substrate for APT might actually be much lower than the theoretical input (because of formation of (inaccessible) aggregates or hydrophobic interactions with any surface like pipette tips or the reaction tube) the k_{cat} values determined here are reflecting an upper limit of the actual turnover of *h*APT1 and *h*APT2. Also, the observed increase of the DPPC peak intensity after 24 hours might result from an unequal distribution of the substrate. Also the addition of detergent was tested, but since it has to be used in high concentrations (above the critical micelle concentration (CMC)) it appears very prominent in the ESI-MS spectrum. Furthermore, detergents in this amounts are lowering the ionization efficiency of the substrates and thus complicating their detection, besides the already described influence of detergents on the catalytic turnover of the enzymes (see section 3.1.1).

A comparison of the ESI-MS derived values to the (visible) activity in the egg yolk plates is of course not straight forward, but assuming phospholipids to represent 10 % of the wet weight of the egg yolk [126] and taking the dilution steps of the protocol (see section 5.2.5) into account, the concentration of (lyso-)phospholipids in the final agar will be approximately 1.6 mM. Further assuming a clear zone of 1 cm in diameter, the addition of 40 µL APT (5 µM) and an incubation time of 12 hours, a k_{cat} of $7.5 \cdot 10^{-5}$ s^{-1} can be determined, which appears in good agreement with the values determined with ESI-MS approach.

In summary, APTs seem to be able to (slowly) hydrolyze (lyso-)phospholipids, and differences in activity on these substrates between APTs from different species, for instance for *y*APT, could be shown. The determined kinetic parameters have to be regarded as very rough estimation due to the poor solubility in aqueous media. This also underlines the difficulties of working with fatty acid based substrates in *in vitro* assay systems.

3.2.2 Protein substrates of APT - The FP-assay

The proposed natural protein substrates of APT (see section 1.2) received more attention than the non-protein molecules, perhaps because most of the proteins could be directly linked to malfunctions in biological systems, although lipid signaling also plays an important role in diseases [128]. Since production of lipidated proteins requires advanced techniques, initially palmitoylated peptides were used for assay establishment as representatives of the lipidated termini of substrate-proteins.

*h*APT1 and *h*APT2 were reported to be N-terminally palmitoylated on their Cys2 and to show both cis-autodepalmitoylation [74]. Additionally, it was claimed that *h*APT1 is able to depalmitoylate isoform 2 (trans-autodepalmitoylation) *in vivo*, but not *vice versa* [74], [75]. To test the activity of APTs on palmitoylated peptides and in

particular the activity on their own palmitoylated N-terminus, a palmitoylated and fluorescein-labeled nonapeptide was ordered (Storkbio, Tallinn, Estonia) according to the sequence of the *h*APT1 N-terminus (see figure 3.24). As previously described for

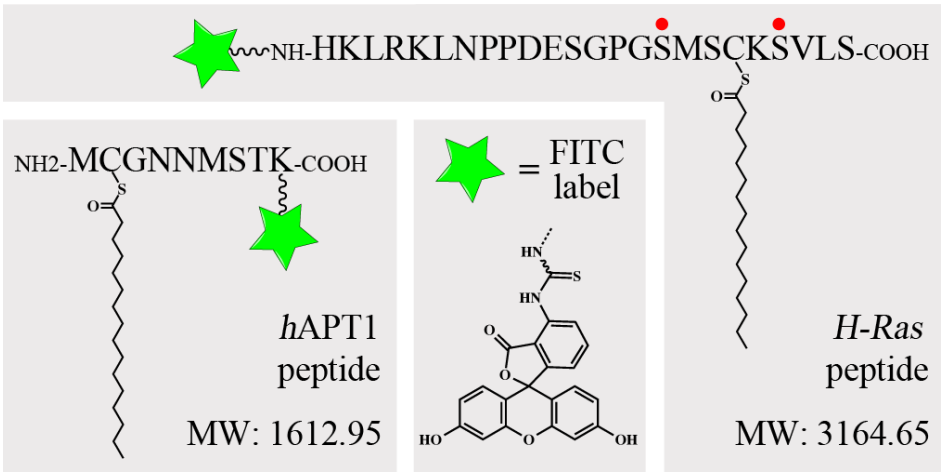

Figure 3.24: Palmitoylated peptides used in fluorescence polarization approaches. The peptides are representing the palmitoylated N-terminus of APT (lower left) and C-terminus of H-Ras (upper right) and are labeled with a fluorescein isothiocyanate moiety (FITC, green star); in the case of the APT peptide via the amino group of a lysine side chain, in the case of the H-Ras peptide via the free N-terminus. The curved line connecting the fluorophore to the peptides corresponds to the curved line shown in the structure of the FITC label. For both peptides also the molecular weight (MW) is stated. Compared to the wild type sequence of H-Ras the two cysteines that are naturally also lipidated were mutated to serine to prevent dimerization due to formation of disulfide bridges (indicated by red dots).

lyso-PPC and DPPC, the hydrolysis of this peptide (100 µM) by *h*APT1 and *h*APT2 (1 nM) was tracked via ESI-MS (figure 3.23). In contrast to lyso-PPC and DPPC the solubility of the peptide is enhanced and thus also the reliability of the measured values, indicated by small error bars. The analysis of the initial, linear phase revealed apparent k_{cat} values of 26.2 s^{-1} for *h*APT1 and 27.2 s^{-1} for *h*APT2 for the depalmitoylation in solution (table 3.5). Contrary to what was claimed from *in vivo* experiments [74], the second human isoform was able to cleave the thioester even (slightly) faster than *h*APT1, showing that *h*APT2 is also able to cleave the palmitoylated N-terminus of *h*APT1. Thus, the fact that no *h*APT2 trans-autodepalmitoylation of *h*APT1 was observed *in vivo* must have another reason than the simple inability of *h*APT2 to cleave this thioester.

In several publications it remained unclear if APT alone is able to depalmitoylate membrane-bound substrates or if cofactors, for instance FKBP12 that was proposed as cofactor of Ras depalmitoylation [33], are necessary to obtain a physiologically relevant speed of depalmitoylation. To check the activity of APT on membrane-bound peptides, a fluorescence polarization approach using fluorescein-labeled peptides inserted into DOPC vesicles was established. Two different substrates were used, the aforementioned

*h*APT1-peptide and a peptide representing the mono-palmitoylated C-terminus of H-Ras (figure 3.24). Large, unilamellar DOPC (1,2-dioleoyl-sn-glycero-3-phosphocholine) vesicles with a diameter of 0.1 µm prepared by repetitive freeze-thaw cycles, sonication and extrusion (see methods section 5.2.8) were used as model membranes.

Figure 3.25 shows that the fluorescence polarization of the *h*APT1-peptide dissolved in FP-buffer (see methods section 5.2.8) increases upon addition of the vesicles, indicating a strong interaction between both. This is expected since the tumbling of

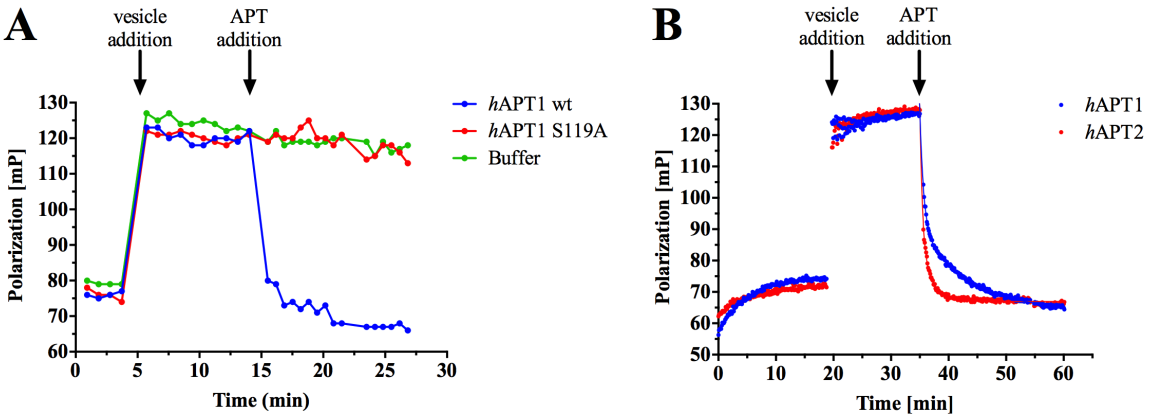

Figure 3.25: APT activity on vesicle-bound peptides. (A) Upon DOPC-vesicle addition (500 µM) to the fluorophore-labeled and palmitoylated *h*APT1-peptide (200 nM) the polarization increases because of the binding of the fluorescent peptide to the membranes. Addition of 5 nM active *h*APT1, but not catalytically inactive APT or buffer, leads to a subsequent decrease in polarization due to cleavage of the palmitoyl moiety and the associated loss of affinity of the peptide to the vesicles. (B) Measurements of 5 nM *h*APT1 and 5 nM *h*APT2 with better time resolution allowed for determination of an apparent cleavage rate.

the fluorophore is slowed down upon binding to the vesicles (see section 5.2.8 for details). This binding is not disrupted if only buffer or the catalytically inactive *h*APT1 S119A mutant are added (figure 3.25A). When active APT protein is admixed, the polarization decreases because the depalmitoylated peptide is obviously no longer able to interact with the vesicles. Comparison of the activity of both human APT isoforms in depalmitoylation of the membrane-bound *h*APT1-peptide confirmed the result from the ESI-MS experiment: both isoforms are able to depalmitoylate the *h*APT1-peptide (see figure 3.25B), in this experiment also in presence of membranes. Interestingly, while both isoforms hydrolyze the "dissolved" *h*APT1-peptide with similar rates (table 3.5), the polarization experiments show that *h*APT2 is able to cleave the palmitoyl moiety of this peptide significantly faster than *h*APT1 if membranes are present. Such a significant difference in activity between *h*APT1 and *h*APT2 was not observed for the catalysis of OPTS, (lyso-)phospholipids or *h*APT1-peptide in solution, so it is unlikely that a mistake in determining the protein concentration is responsible.

The velocity of catalysis was determined by converting the slope of the initial linear

phase to a k_{cat} value assuming that all peptides (200 nM) are bound to vesicles before the addition of 5 nM APT and that all peptides are depalmitoylated when reaching the final plateau. The resulting k_{cat} values will be called "apparent" in the following and correspond more to a k_{obs} value, since the assay conditions (200 nM peptide, 5 nM enzyme) do not guarantee a depalmitoylation at maximum velocity. Thus, the apparent k_{cat} values (or k_{obs} values) represent a lower limit of the real catalytic turnover. The analysis of the polarization-decrease upon APT addition reveals k_{obs} values of 0.38 s^{-1} for *h*APT1 and 0.62 s^{-1} for *h*APT2, which appear to be 40 to 70 times slower than the determined k_{cat} values for this peptide in solution ($\sim$27 s^{-1}) as described before. In experiments performed by Kathrin Estel using a FRET based stopped-flow approach, a dissociation rate (k_{off}) of 0.5 s^{-1} was determined for the bound *h*APT1-peptide dissociating from DOPC vesicles. Since this value is in range of the determined k_{obs} values for *h*APT1 and *h*APT2 it cannot be excluded that the k_{off} of the peptide from the membrane is a rate-limiting step or at least significantly influencing the catalysis of the palmitoylated *h*APT1-peptide by APT, which would indicate that APT does not have direct access to membrane-bound peptides. But, assuming a high affinity of the palmitoylated *h*APT1-peptide to the DOPC vesicles the concentration of "free", dissociated peptide would only represent a minor fraction of the total peptide concentration of 200 nM, thus further reducing the observed catalytic turnover tremendously. Thus, the observed catalysis of the palmitoylated *h*APT1-peptide in presence of DOPC membranes by *h*APT1 and *h*APT2 strongly hint to an active extraction process by APT, whereby *h*APT2 seems to be more efficient than *h*APT1. To verify this hypothesis, experiments using more substrate could reveal the maximum velocity of catalysis in the presence of membranes, but it has to be ensured not to overload the DOPC vesicles. Under the conditions described above approximately 40 peptides are bound to each vesicle that should definitely allow the use of higher concentrations of peptide. Approaches with different amounts of enzyme could show if the k_{off} of the peptide from the DOPC vesicles is really the rate limiting step. If the velocity can be increased further when measured using the FP- or a stopped flow approach, a direct effect of APT on the membrane bound peptide can be assumed.

To see if peptides from other natural protein substrates, especially with more residues that might interact with APT in regions outside the binding tunnel, are also depalmitoylated by APT in the presence of vesicles, a 24 amino acids long peptide covering the C-terminal sequence of mono-palmitoylated H-Ras was tested (see figure 3.24). Unexpectedly, as depicted in figure 3.26, even multiple additions of DOPC vesicles up to a concentration of 1 mM (with regard to single DOPC molecules) to the H-Ras peptide did not result in an increase of fluorescence polarization as seen for the *h*APT1 peptide. Because the H-Ras peptide does not contain particularly many charged residues that could cause electrostatic repulsion and since the fluorophore is

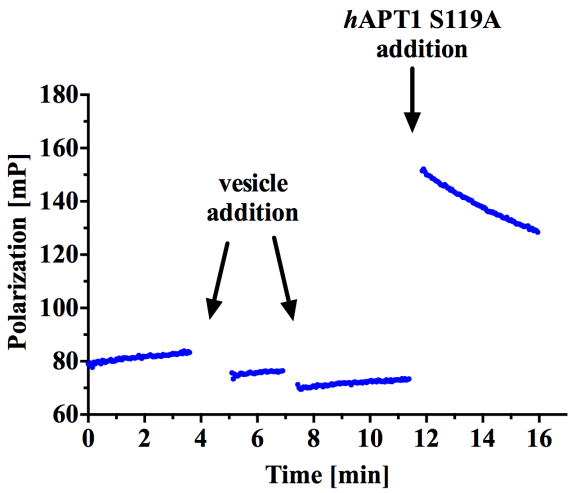

Figure 3.26: The fluorescence polarization of the H-Ras peptide is not increased upon vesicle addition, but when APT is present. In contrast to the APT-peptide, the fluorescence polarization of the H-Ras peptide (200 nM) is not increased when DOPC vesicles are added (made of 500 µM DOPC monomers), but upon addition of 10 µM *h*APT1 S119A. The slow decrease after addition of the catalytically inactive mutant indicates residual hydrolysis activity.

not placed in close proximity to the palmitoylated cysteine thus ruling out steric hindrance of binding, the general ability of the H-Ras peptide to insert into vesicles can be assumed. In experiments performed by Kathrin Estel using a microscope, attachment of the fluorescent H-Ras peptide to DOPC vesicles was observed (private communication). Probably, the expected increase in fluorescence polarization is not happening because of the so-called "propeller effect". This phenomenon appears if the fluorescent label is attached at a highly mobile position that maintains its local mobility even when bound to the vesicle. In those cases the fluorescence polarization of the bound state is almost the same as in the "free" form [129].

Interestingly, the fluorescence polarization approach can still be used to determine the affinity of the H-Ras peptide to APT proteins directly. For this purpose the catalytically inactive mutant has to be used where the palmitoyl-moiety is bound inside the binding tunnel but not cleaved. As shown in figure 3.26, addition of 10 µM of catalytically inactive mutant *h*APT1 S119A to the peptide immediately led to an increase in fluorescence polarization, in contrast to the previous additions of vesicles, indicating binding of the peptide to the protein. Since this effect is visible in presence of DOPC vesicles (made from 1 mM (2x 500 µM) DOPC monomers) the *h*APT1 S119A seems to be able to extract a very significant fraction of the peptide from the vesicles, indicating a high affinity. Furthermore, the absence of the "propeller effect" might imply that this increased affinity is due the fact that a significantly larger part of the peptide is involved in the interaction compared to the binding to vesicles, thereby reducing the mobility of the peptide and thus leading to an increase in fluorescence polarization.

The slow but continuous decrease visible in fluorescence polarization after addition of 10 µM *h*APT1 S119A (figure 3.26) can be observed for all catalytically inactive APTs used in this thesis. Calculations of the rates showed that their "activity" is about 10,000-fold slower than the APTs containing the active serine residue. Interestingly, this rate is approximately equal to the observed increase of background hydrolysis rates when 10 µM FABP2 are used to protect APT during PPTS hydrolysis (see section 3.1.1 and figure 3.11). This residual activity is not visible in assays where proteins are used in nanomolar concentrations, but it becomes detectable when proteins are used in micromolar concentrations, for instance during the determination of dissociation constants of palmitoylated peptides as described in the following. As in the case of FABP2, the reason for this could either be the shift of the auto-hydrolysis equilibrium towards the products by binding and thus sequestration of the free palmitic acid, or it could be an example for catalysis oby "straining" the substrate. Since the substrate is obviously still able to bind the catalytically inactive APT protein (see figure 3.26), hydrolysis could also be observed when the bound ligand is strained towards the transition state configuration, without the serine side chain present. This phenomenon is exploited in antibody catalysis, where artificial active sites are constructed that resemble the transition state of a given reaction and also lead to accelerated hydrolysis [130]–[132] . In the particular case of APTs a coordinated water molecule would be able to perform the nucleophilic attack to the substrate in transition state configuration. Especially in the case of the relatively labile thioesters this possibility has to be considered.

The affinity for both, the palmitoylated *h*APT1 and the H-Ras peptide was measured using different concentrations of the catalytically inactive mutants of *h*APT1 and *y*APT (figure 3.27). The fluorescence polarization was measured immediately after addition of the protein, although hydrolysis had already begun. The dissociation constant K_d of 36 nM of the Ras peptide to *h*APT1 S119A appears 25 times stronger than the K_d of 960 nM of the N-terminal *h*APT1 peptide. Obviously, the H-Ras peptide is able to form stronger interactions with the *h*APT1 protein, since both peptides appear to be equally soluble. This may be because the H-Ras peptide is the significantly longer peptide and a larger number of contacts in addition to the palmitoyl chain in the binding tunnel can be established. But, as a molecular docking by Dr. Ingrid Vetter depicted in figure 3.28 impressively shows, already the only nine amino acids long APT peptide is theoretically able to address the complete shallow groove while bound to the substrate binding tunnel with its palmitoyl moiety. This would argue that either the H-Ras peptide has somehow wrapped around the protein or that the sequence of the peptide that potentially interacts with the shallow groove matters as well. This groove is a likely interaction site since a PEG molecule was found bound to this site in a crystal structure of a closely related carboxylesterase (PDB code 3CN9, see figures 1.6 and 1.7). Of course, interactions at other regions cannot be excluded. A co-crystal

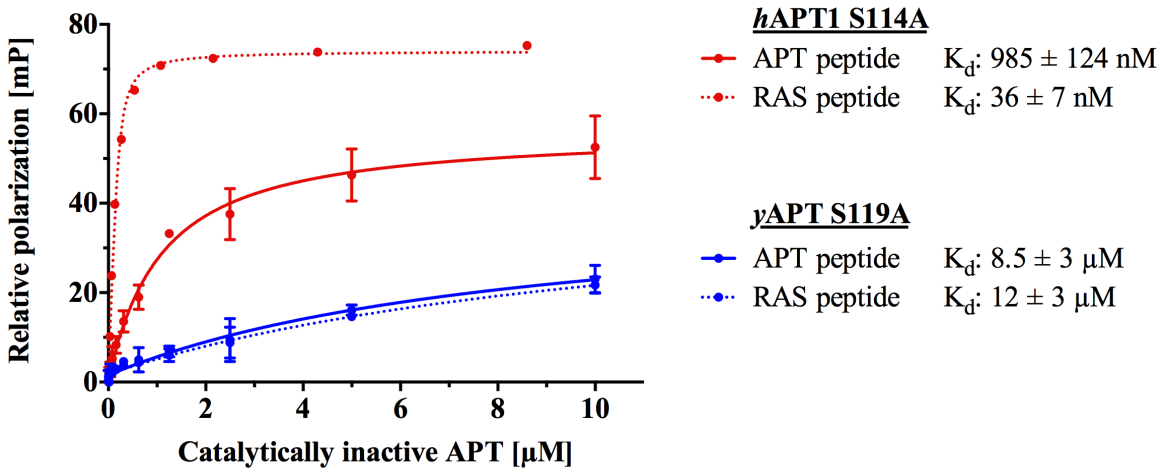

Figure 3.27: Binding of palmitoylated peptides to catalytically inactive *h*APT1 and *y*APT mutants. The concentration-dependent change in fluorescence polarization was recorded upon addition of catalytically inactive versions of the indicated amounts of *h*APT1 and *y*APT to 200 nM of the fluorescent *h*APT1- and H-Ras peptides.

structure of APT with the palmitoylated peptides could provide hints to answer these questions, but so far, crystallization (also with the catalytically inactive APT mutant) was not successful, most likely because of the previously described residual "activity", or due to steric problems in the tighly packed APT crystals.

Very interestingly, both peptides show a similar, weak affinity in the low micromolar range to *y*APT (figure 3.27, blue curves), indicating that the palmitoyl moiety is not able to bind properly to the (distorted) binding tunnel of *y*APT (see figure 3.19 and also section 3.2.1). This is in good agreement with the observed weak activity of *y*APT on (lyso-)phospholipids, described in section 3.2.1. The weak, but not totally abolished affinity of both peptides to *y*APT indicate that the palmitoyl moiety might be still able to bind the shortened binding groove of *y*APT like the aliphatic tail of palmostatin (figure 3.19). However, the terminal part of the fatty acid will exceed the length of the groove and would become completely solvent exposed, thus leading to a much more unfavorable binding compared to *h*APT1, where the palmitoyl moiety is entirely embedded in the hydrophobic binding tunnel.

In summary, it was shown that both *h*APT1 and *h*APT2 are able to depalmitoylate the palmitoylated *h*APT1-peptide in solution as well as in the presence of DOPC membranes. No significant difference in turnover of this peptide between both human isoforms was observed for the catalysis in solution ($k_{cat} \sim 27\ s^{-1}$), already showing that also *h*APT2 is in principle able to depalmitoylate *h*APT1 *in vitro*, contrary to published results obtained *in vivo* [74]. Hydrolysis of the palmitoylated *h*APT1-peptide was also observed for both *h*APTs in presence of DOPC model membranes. The turnover decreased in this case more than 40-fold for both proteins. In case of *h*APT2

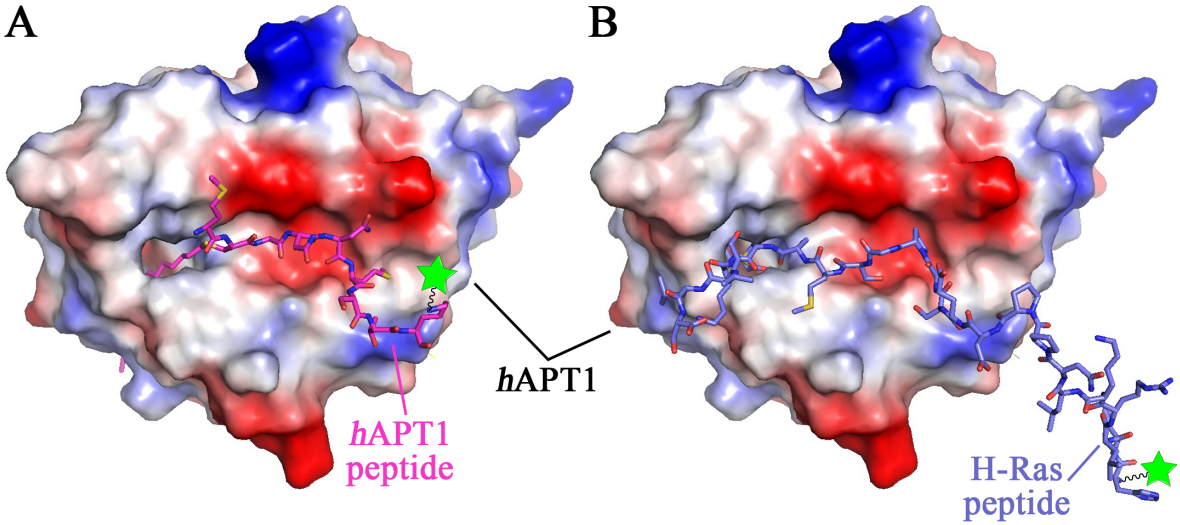

Figure 3.28: Docking of two different palmitoylated peptides to *h*APT1. Both, the palmitoylated *h*APT1 peptide (A) and the palmitoylated H-Ras peptide (B) were docked to the *h*APT1 protein and are shown as sticks. One possible orientation of each peptide is shown that spans the entire shallow groove. The *h*APT1 protein is represented with its electrostatic surface, where blue areas indicate a positive and red areas a negative surface potential. White spots occur at mostly hydrophobic, uncharged amino acid side chains. The green stars connected to each peptide indicate the position of the linked fluorescent FITC label (see also figure 3.24). The docking is based on a *h*APT1–2-bromopalmitate (see section 3.3.1) co-crystal structure and was performed by Dr. Ingrid Vetter using the program GOLD by the Cambridge Crystallographic Data Centre (CCDC) [133]–[135].

(k_{obs} = 0.62 s^{-1}) this process appears almost twice as fast as in the case of *h*APT1 (k_{obs} = 0.38 s^{-1}). Even though the intrinsic dissociation of the peptide from DOPC membranes ($k_{diss} \sim 0.5$ s^{-1}) determined by Kathrin Estel appears to happen almost equally fast, it is most likely not the rate limiting step.

Determination of the binding affinities of two different palmitoylated peptides, the mentioned *h*APT1 peptide and an H-Ras peptide, to catalytically inactive mutants of *h*APT1 and *y*APT indicate that the amino acids sequence of the peptide next to the palmitoylation site might indeed matter since the H-Ras peptide (K_d = 36 nM) showed an almost 30-fold higher affinity than the *h*APT1 peptide (K_d = 985 nM). Furthermore, both palmitoylated peptides show a very weak affinity to the *y*APT protein ($K_d \sim 10$ µM), indicating a substrate specificity of *y*APT for shorter chained substrates.

3.3 Inhibitors of APT activity

One strategy to investigate the role of APTs *in vivo* is to inhibit their intrinsic hydrolase activity and observe resulting phenotypic effects and/or altered palmitoylation states of their postulated substrates. In the past, different attempts were made to find such

APT inhibitors that are specific for APT and, ideally, also specific for the APT isoforms APT1 and APT2. Simple, palmitic acid-like ligands are less specific for APT since they will bind also other enzymes that deal with lipidic moieties, like lipases, but a more detailed knowledge of their binding-site and binding-mode might also reveal differences in fatty acid binding between APT proteins and provide hints on how natural substrates interact with APT. Specific or even isoform-specific inhibitors are perfect tools to study enzyme function within the cellular context.

3.3.1 2-Bromopalmitate (2-BP)

The first described inhibitors of APT, palmostatin B and M (see section 3.1.2.1), bind covalently to the protein, making this class of inhibitors very unspecific since also other hydrolases were identified to be bound, e.g. Palmitoyl-protein thioesterase 1 (PPT1), Ubiquitin thioesterase (OTUB1) or Retinoid-inducible serine carboxy peptidase (RISC) [47], [64] . Besides this, they are unstable and hydrolyze off the protein targets with a halflife of 3.5 min [46] (see also section 3.1.2.1). Thus, the report of 2-bromopalmitate (2-BP) as a non-covalent, uncompetitive inhibitor of both human APTs [97] appeared quite interesting. First, because of the non-covalent binding and second, because only the bromine in alpha-position distinguishes it from palmitic acid, the natural product of APT hydrolysis, which shows a very weak affinity for APT ($K_i \sim$ 130 µM, see figure 3.8). Even more surprising was the description of an uncompetitive binding mode of 2-BP [97] , meaning that it interacts only with the already formed APT-substrate complex. This mechanism would require a second binding site for lipidic substrates besides the substrate-binding tunnel, for instance the shallow groove on the protein surface described in section 1.2.2 and depicted in figure 1.7. Evidence of such a second binding site would also allow speculation about the binding mode of di-palmitoylated substrates of APT like H-Ras or phospholipids. The availability of a generic, non-covalent substrate analog with a relatively good solubility allowed for the first time a proper comparison of APT orthologues from different species regarding the interaction with a palmitoyl moiety. This is interesting from the evolutionary point of view since lower organisms have only one APT protein, while two APT isoforms are present only in higher eukaryotes.

To gather more information about the interaction between 2-BP and APT, the inhibitory constant IC_{50} of 2-BP towards different APT proteins was determined using the OPTS assay at a fixed amount of substrate. To allow measurements at the V_{max} of the different APT proteins, a fixed OPTS concentration of 125 µM was chosen (2.2 - 7.5 times K_m value) that is sufficient to determine a proper initial linear phase. Additionally to measuring of the IC_{50} values, the inhibitory constant K_i was calculated using the Cheng-Prusoff equation (equation 3.3)

$$K_i = \frac{IC_{50}}{1 + \frac{[S]}{K_m}} \tag{3.3}$$

where $[S]$ represents the free substrate concentration and K_m the Michaelis constant of the respective proteintaht was determined from steady-state experiments with OPTS (see section 3.1.1.1). The K_i value takes into account the varying affinities of the different APT proteins to the OPTS substrate and allows a proper comparison of their inhibition by 2-BP, in contrast to the IC_{50}. The Cheng-Prusoff approximation in the form shown above is only true if some assumptions are fulfilled: The inhibition has to be competitive and the concentration of free substrate has to approximately equal the amount of the total substrate. Furthermore, only one class of binding sites and no unspecific binding is allowed and, lastly, the correct determination of K_m is required. Since the determination of K_m might contain errors, as discussed in section 3.1.1.1, the comparison of K_i with the dissociation constant K_d is only partially correct. The K_i is rather displaying an upper limit for the real K_d, which will be reached if all assumptions are perfectly fulfilled. However, in this case calculation of K_i values is the most decent way for the comparison of the strength of APT inhibition by 2-BP.

The K_i of 2-BP binding to *h*APT1 (560 nM) is in the same range as the determined K_d of the palmitoylated *h*APT1-peptide (985 nM, see figures 3.27 and 3.29 and table 3.6), indicating a relatively strong interaction. However, it appears much weaker

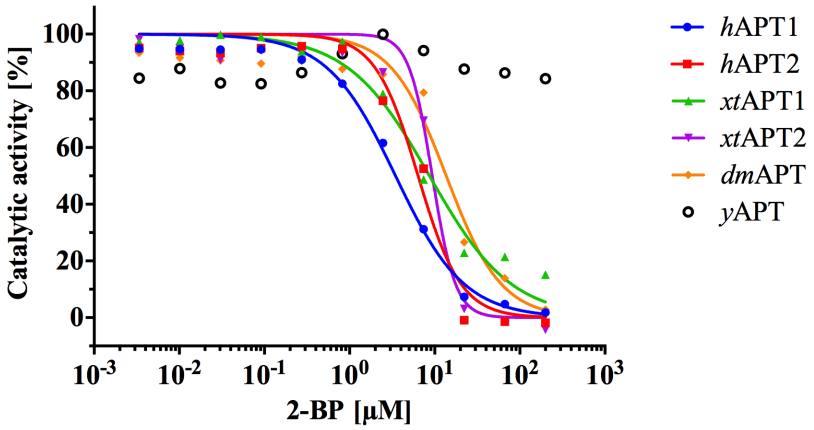

Figure 3.29: Inhibition of APT homologues by 2-BP. The OPTS assay with constant amounts of 125 µM substrate and 5 nM protein was used to determine IC_{50} and K_i values, which are listed in table 3.6

than the binding of the palmitoylated H-Ras peptide to *h*APT1 (36 nM, see figure 3.27). Interestingly, 2-BP shows a 3-fold higher affinity for *h*APT1 (K_i = 560 nM) compared to *h*APT2 (K_i = 1.7 µM) and this also seems to be the case for other APT isoforms 1 compared to the corresponding APT2 variants (table 3.6). In drosophila and yeast only one APT protein can be found. The effect of 2-BP on their activity

Table 3.6: Determined IC_{50} values and calculated K_i values of APT inhibition by 2-BP. The table reports the determined kinetic parameters from the inhibition studies shown in figure 3.29.

Protein	IC_{50} [µM]	K_i [µM]
*h*APT1	3.45 ± 0.59	0.56
*h*APT2	5.74 ± 0.99	1.72
*xt*APT1	8.50 ± 1.94	0.99
*xt*APT2	8.06 ± 2.66	2.55
*dm*APT	18.28 ± 2.52	4.20
*y*APT	> 200	

is significantly different between them: Interestingly, while *dm*APT gets inhibited by 2-BP with a low µM affinity roughly similar to human and xenopus isoform 2 APTs, although a bit weaker, the activity of the yeast APT is not inhibited at all, in spite of the very similar three-dimensional structures. The co-crystal structure of *y*APT with palmostatin M, containing a decyl (C10) moiety (figure 3.19), showed that the binding tunnel of *y*APT is blocked by Phe81 and the aliphatic tail has to exit the tunnel by forming a kink. Thus, 2-BP might not be able to bind to *y*APT with sufficient affinity, most likely because the much longer aliphatic tail of 2-BP (hexadecyl, C16 moiety) is even more unfavorable then the C10-tail of palmostatin M and cannot be forced to this binding site by the formation of a covalent bond as in the case of palmostatins. This observation confirms quite well the detected low affinites of palmitoylated peptides to *y*APT compared to *h*APT1 (figure 3.27).

To validate the report about the uncompetitive binding mode of 2-BP [97] and the linked need of a second binding site, like the shallow groove (figure 1.7), the assay using the intrinsic tryptophan fluorescence of APT (described in section 3.1.2) was used. This system is a convenient tool to distinguish between binding in the binding tunnel or at the shallow groove of *h*APT1, by using the tryptophan mutants described in section 3.1.2. Titration of 2-BP against the three different APT1 mutants resulted in the fluorescence quenching curves depicted in figure 3.30. Both, the wild type protein and the *h*APT1 W37F mutant that displays the fluorescence changes in the binding tunnel, show a very similar and significant dose-dependent quenching behavior, clearly indicating binding of 2-BP in the binding tunnel. To determine the K_d, ligand depletion has to be taken into account when fitting the resulting curves, because the protein concentration had to be kept at 5 µM to maintain a sufficiently high fluorescence signal. The curves were fitted using equation 5.4 (see methods section 5.2.3) assuming a single binding site per monomer, but also taking ligand depletion and non-specific binding into consideration. The determined K_d of 1.5 µM is in good agreement with

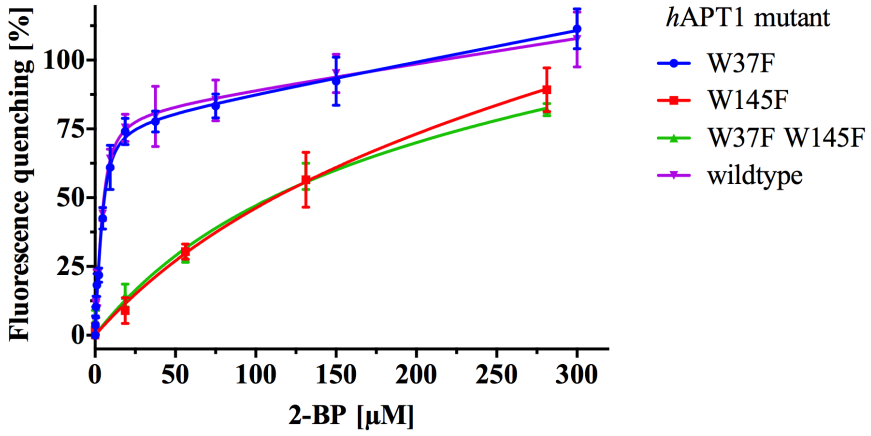

Figure 3.30: 2-BP is quenching Trp-fluorescence of APT upon binding. Quenching of the wild type *h*APT1 and *h*APT1 W37F by 2-BP occurs in a dose-dependent manner. The applied equation for fitting of the curves (see equation 5.4 in section 5.2.3) took ligand depletion and non-specific binding into account. The interaction of 2-BP with *h*APT1 W37F and *h*APT1 W37F W145F was corrected for an initial lag-phase till a concentration of 20 µM, because the binding site at the tunnel was saturated first. Determined K_d values can be found in table 3.7.

the calculated K_i for 2-BP and *h*APT1 using the OPTS-activity assay (0.6 µM; see figure 3.29). The steady increase in fluorescence quenching instead of a stable plateau phase could indicate non-specific binding, which might be detectable because of the presence of Trp72, actually located in the core of the protein (see following text).

Furthermore, it seems that binding of 2-BP to *h*APT1 is preferably taking place in the substrate-binding tunnel: The mutant *h*APT1 W145F, displaying the binding to Trp37 in the shallow groove, shows a significantly different fluorescence quenching upon titration of 2-BP, indicative of a much lower affinity. The data had to be corrected for a lag-phase (see below) of no quenching until a 2-BP concentration of 20 µM. Calculations of the saturation of the binding site (*Bound Fraction*, equation 3.4) in the APT binding tunnel at a substrate concentration $[S]$ of 20 µM 2-BP, assuming a maximal binding B_{max} of 100 % and a K_d of 0.56 µM (see table 3.6) using the equation for fitting of specific binding to one site:

$$Bound\ Fraction = \frac{B_{max} \cdot [S]}{K_d + [S]} \tag{3.4}$$

reveals a saturation of the binding site at the substrate binding tunnel of 97.6 % at 20 µM 2-BP. Thus, the correction for the lag-phase in cases of the *h*APT1 W145F mutant was necessary because the high-affinity binding site in the tunnel is first saturated completely before 2-BP is available to bind to other low-affinity sites. The quenching of Trp37, located in the shallow groove (see figure 3.17), occurs in an almost linear way. The applied fit (methods section 5.2.3) revealed a K_d of 171 µM, but with high uncertainty indicated by an even higher error value (see table 3.7). The

Table 3.7: Determined K_d values of 2-BP binding to different binding sites on the APT surface.

Protein	Represented fluorescence	K_d [µM]
*h*APT1	all	1.63 ± 0.42
*h*APT1 W37F	binding tunnel	1.55 ± 0.37
*h*APT1 W145F	shallow groove	171 ± 240
*h*APT1 W37F W145F	protein core	138 ± 137

low affinity value corresponds to a weak or non-specific binding of 2-BP detected with this mutant. Multiple (non-specific) binding sites might impede a proper fit with the used equation. Titration of higher 2-BP concentrations might lead to a saturation, also of non-specific binding, which could probably allow a better interpretation of the binding curve, which nevertheless allows the qualitative estimation of a weak 2-BP binding. However, as shown below and in section , 2-BP at very high concentrations has additional effects as explained in the following.

The double mutant *h*APT1 W37F W145F that has only one tryptophan (Trp72) left in the core of the protein was tested as a control and shows the same quenching characteristics as the mutant *h*APT1 W145F, indicating that the low affinity binding of 2-BP also affects the protein core. This already indicated that 2-BP might have effects on the folding and stability of the APT protein, as was later also observed in an approach using circular dichroism (see figures 3.31 and 3.32).

These results show that 2-BP binds *h*APT1 with high affinity in the substrate binding tunnel, close to Trp145, with a K_d around 1 µM, indicating a competitive binding mode with OPTS and probably also with natural substrates. However, an additional inhibitory effect via unspecific binding to the APT surface and thus influencing the APT structure cannot be excluded (see circular dichroism studies below). When titrated in concentrations > 20 µM the first binding site becomes almost completely saturated (see aforementioned equation 3.4 and related discussion) and the remaining 2-BP apparently binds to other regions, probably hydrophobic patches, on the APT surface, as indicated by the effects on Trp37 and Trp72. The quenching of the buried Trp72, detected with the double mutant *h*APT1 W37F W145F, indicates that the whole protein may be influenced by 2-BP and the protein structure is somehow altered in such a way that also the microenvironment around Trp72 is undergoing changes. The presence of multiple, low-affinity binding sites and structural changes of APT at higher concentrations of 2-BP could explain the reported uncompetitive binding mode [97].

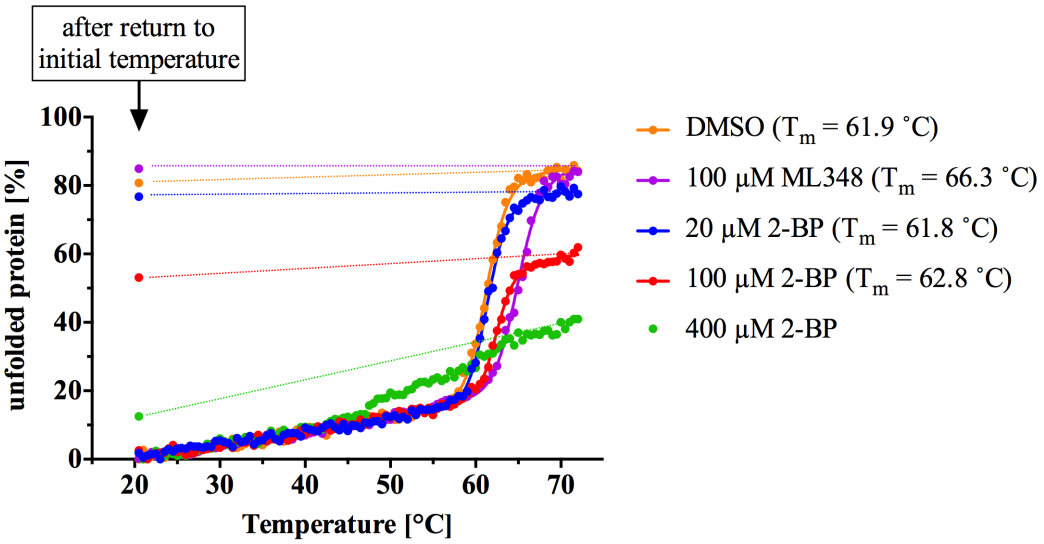

Figure 3.31: *h*APT1 melting curves in presence of 2-BP. Addition of 2-BP does not only lead to a slight increase in melting temperature (+1 °C at 100 µM 2-BP, red curve) but also to a decreased amount of denatured protein at 70 °C and to a more efficient refolding of the protein. Because the final samples with inhibitor present contained intrinsically 1 % DMSO, the same amount of DMSO was added to the control without 2-BP (orange curve). CD values after cooling back to 20 °C are highlighted with the black arrow. Dashed lines link the CD value at 70 °C and the value after refolding. As comparison also the melting curve using the specific APT1 inhibitor ML348 is shown that stabilizes the protein much better (+ 4.4 °C at 100 µM ML348, violet curve).

The hypothesis of 2-BP influence on the global structure of APT is supported by a CD-spectroscopy experiment, which is independent of tryptophan fluorescence. Initially, the experiment was meant to see a shift in the melting point of APT upon ligand binding due to stabilizing effects of the ligand. Different concentrations of 2-BP were added to 20 µM *h*APT1 and a protein unfolding experiment was carried out. As depicted in figure 3.31, the melting point is slightly increased upon 2-BP addition (+1 °C at 100 µM 2-BP, red curve), indicating that 2-BP indeed seems to stabilize the protein, but not as efficient as the specific inhibitor ML348 (see figure 1.8) does (violet curve; + 4.4 °C at 100 µM ML348). But also another, more impressive effect can be seen for 2-BP: The more 2-BP is added, the less the protein seems to loose its structure upon heating: At 400 µM 2-BP the CD signal of structural elements is only reduced by 40 % at 70 °C without showing a sharp transition to an unfolded state. Furthermore, refolding attempts of APT by decreasing the temperature back to the initial value showed that APT is able to refold more efficiently at high concentrations of 2-BP (see dots on the left side of figure 3.31). With the highest 2-BP concentration a CD signal corresponding to 88 % folded protein could be observed after cooling down to the initial temperature of 20 °C again.

These data in combination with the results obtained with the Trp-assay described above suggest that at high concentrations 2-BP can cover the surface of APT forming a

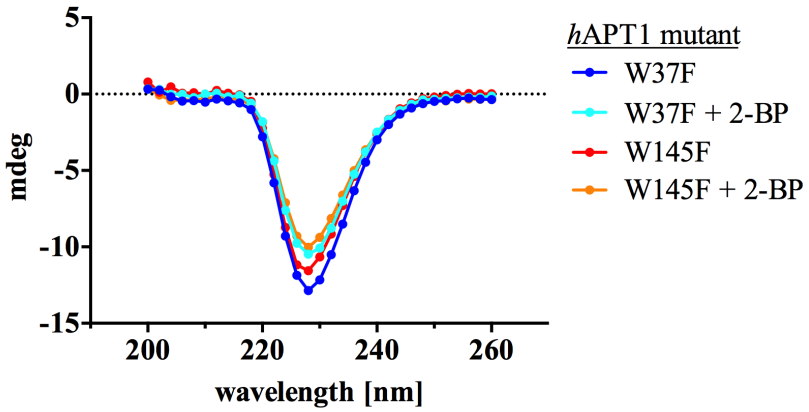

Figure 3.32: Effect of high 2-BP concentrations to the structure of *h*APT1 tryptophan mutants. Upon addition of 300 µM 2-BP the CD signal of the two *h*APT1 mutants W37F and W145F (10 µM each) is reduced by 18 % and 13 %, respectively.

protective shell around the protein which can protect the protein also at high temperatures ($> 70\,^{\circ}$C) and apparently enables a more efficient refolding upon cooling down again. In contrast to PPTS, which irreversibly alters the structure of APT (figure 3.10), addition of high concentrations of 2-BP only leads to a loss of 13 % - 18 % of the CD signal (figure 3.32), suggesting a moderate destabilization of the protein structure. This impact, however modest, could still result in the inhibition of the enzyme. To answer this question it is essential to test the integrity of APT after removal of 2-BP. As already mentioned in section 3.1, the use of detergents in any assay dealing with fatty acid is always tricky: detergents can promote interactions by increasing the solubility of substrates, but they can also impair them by sequestering the substrate or binding to the protein. 2-BP has a quite good solubility compared to palmitic acid or sodium palmitate, so studies using the Trp-assay and *h*APT1 W37F mutant to display binding inside the binding tunnel could be performed without the use of detergent. Strikingly, 2-BP shows another variant of interacting with the detergent CHAPS. Figure 3.33 shows the impressive effect of CHAPS on the preformed *h*APT1/2-BP complex: Addition of 2-BP initially leads to the aforementioned quenching of fluorescence of Trp145 inside the binding tunnel. The subsequent total recovery of initial fluorescence upon addition of the detergent CHAPS indicates firstly that 2-BP is instantaneously extracted from APT and probably sequestered in mixed micelles, and secondly, that 125 µM 2-BP does not unfold *h*APT1 irreversibly. Furthermore, the protein seems to be structurally intact after 2-BP removal since addition of the APT1 specific inhibitor ML348, whose binding is dependent on the three-dimensional shape of the binding tunnel (see section 3.3.2), can still bind and quench the tryptophan signal to a minimum also in presence of CHAPS. CHAPS by itself does not alter the tryptophan fluorescence of *h*APT1 (appendix figure 6.4)

All experiments so far seem to reinforce the idea that the high-affinity binding

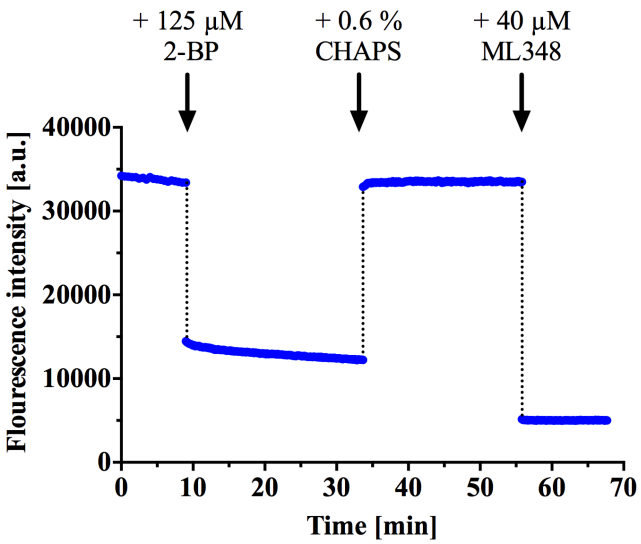

Figure 3.33: Sequestration of 2-BP by CHAPS and extraction from *h*APT1 W37F. Immediately after 2-BP was added to 10 µM *h*APT1 W37F (displaying binding to the substrate tunnel), tryptophan fluorescence was quenched, indicating an occupancy of the binding tunnel. After addition of 0.6 % CHAPS (9.8 mM; CMC = 6- 10 mM, 0.37-0.61 %[99]) the initial fluorescence level was restored by sequestering 2-BP from the APT protein. Addition of 0.6 % CHAPS alone does not influence the intrinsic Trp fluorescence of *h*APT1 W37F (see appendix figure 6.4). Binding of the APT1 specific inhibitor ML348 lets the fluorescence drop to a minimum. The different levels of fluorescence after addition of 2-BP or ML348 can be due the different shapes and thus influence on Trp37 (see figures 3.35 and 3.37).

site of the inhibitor is the substrate-binding tunnel and structural information should confirm this hypothesis. However, several attempts to co-crystallize lipidic compounds like palmitic acid, the product of the natural enzymatic reaction, with APT were not successful except for the serendipitous crystallization of *xt*APT1 with a mixture of palmitic and stearic acid co-purified from *E.coli* by Marco Bürger [87]. Because of the close structural relationship of 2-BP to palmitic acid on one hand and the successful inhibition and binding studies shown above on the other, substitution of palmitic acid by 2-BP in crystallization trials was attempted to examine the binding of fatty acid moieties to APT in greater detail. Although inhibition studies revealed a reasonable affinity of 0.5 - 1 µM of 2-BP to APT (see figure 3.29 and table 3.6 and figure 3.30 and table 3.7), no or very low occupancy of 2-BP was observed in the first APT co-crystal structures. This problem was overcome by taking advantage of the stabilization of the APT structure upon 2-BP addition: the solution of 2-BP and APT was heated slowly up to 40 °C prior to crystallization setup. Strikingly, the opaque solution of 2-BP and APT became almost completely clear after the heating, without any sign of precipitation. This led to a much more efficient binding of the inhibitor to APT and apparently without denaturation of the protein so that co-crystal structures with a high occupancy of 2-BP could be obtained. Crystallization conditions and crystallographic

statistics can be found in tables 6.5 and 6.4 in the appendix.

Figure 3.34 gives an overview of 2-BP binding to both *h*APT isoforms. As expected from the binding experiments (figure 3.30), the substrate-binding tunnel is indeed the binding site for 2-BP in *h*APT1 as well as in *h*APT2. The carboxyl group of 2-BP is

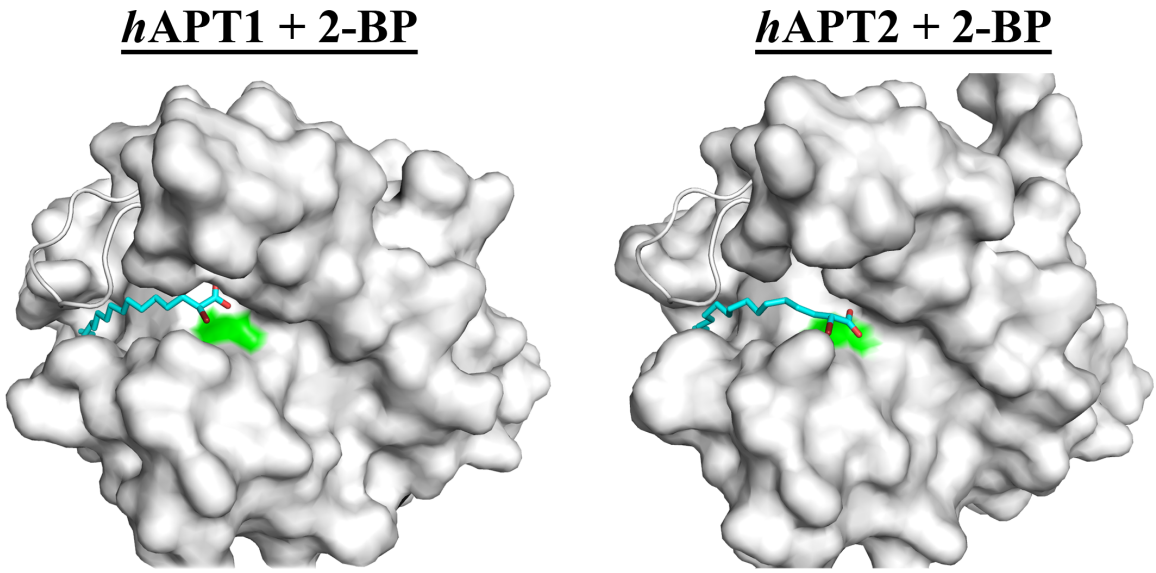

Figure 3.34: Co-crystal structures of 2-BP bound to both human APT isoforms. The inhibitor 2-BP (shown as cyan sticks) binds to the substrate-binding tunnel of *h*APT1 and *h*APT2. It spans the entire tunnel with the carboxyl group of 2-BP located next to the catalytic serine (shown as green spot). For the sake of clarity the lid loop structures of both proteins are shown as ribbons of the backbone without their surface, which would obstruct a proper view onto the ligands. Crystallization conditions and crystallographic statistics can be found in tables 6.5 and 6.4 in the appendix.

placed next to the catalytic site and the palmitoyl moiety is spanning the whole tunnel, also passing in front of the sensor Trp145 in *h*APT1. The fatty acid tail of 2-BP adopts the same orientation in both APT proteins (figure 3.35A) and contacts mostly identical residues (figure 3.35B). The only difference resides in the positioning of the head-group of 2-BP. When bound to *h*APT2 the carbonyl-carbon is shifted 2.7 Å more towards the tunnel entrance and the distance to the oxygen of the active serine is thereby decreased by 25 % compared to 2-BP bound to *h*APT1. In this position the carboxyl group can interact with His210 from the catalytic triad and with the backbone of Leu33 and Gln123. A possible reason for the shift might be the steric hindrance by Leu78, which is present in *h*APT2 but not in *h*APT1. The orientation of the corresponding amino acid Ile75 in *h*APT1 allows the carboxyl group of the inhibitor to form an H-bond to Gln120, which is not possible in the case of *h*APT2 because the terminal methyl group of Leu78 seems to impede this arrangement. Furthermore, the carboxyl head group of 2-BP seems to be differently located in the oxyanion hole, formed by the main chain amides of Leu30/33 and Gln120/123 in *h*APT1/2 respectively, which might stabilize the binding of 2-BP in *h*APT1 compared to *h*APT2.

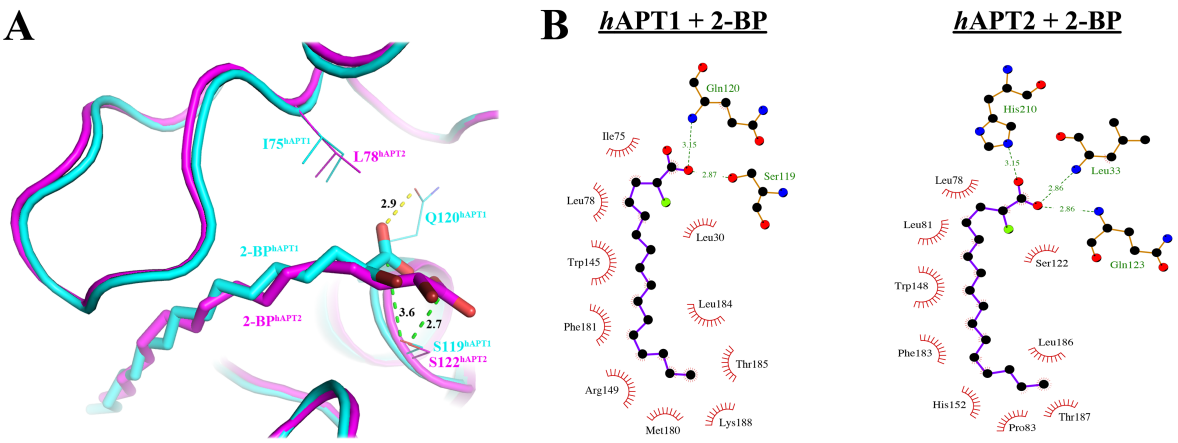

Figure 3.35: Superimposition of 2-BP bound to *h*APT1 and *h*APT2 and interaction plot of involved amino acids. (A) The co-crystal structures of 2-BP bound to *h*APT1 and 2 were superimposed to show differences in the binding position of the inhibitor. The proteins are shown in cartoon style and isoform 1 is colored in cyan, isoform 2 in magenta. The closest distance of the carbonyl-carbon of the inhibitor to the active serine residue is indicated with green dots and labeled in Ångström for both structures. The H-bond of 2-BP to Gln120 in *h*APT1 is highlighted as yellow dots and labeled with its length in Ångström. The side chain of the active serine and of selected residues are also shown as sticks. (B) Shown are 2D diagrams of 2-BP binding to *h*APT1 and *h*APT2. Red arcs with spokes around the involved amino acids represent hydrophobic contacts. Amino acids that form H-bond to the inhibitors are shown in a ball-and-stick representation and contacts are represented in green dashes lines with the corresponding distance in Ångström. The diagrams were created with the software LigPlus+[136]

In summary, 2-BP can bind to almost all tested APT proteins, except for yeast APT. Thereby, the activity of proteins of isoform 1 (K_i = 0.56 - 1 µM) is better inhibited than isoform 2 APTs (K_i = 1.7 - 2.6 µM). *dm*APT (K_i = 4.2 µM) shows a weaker inhibition that equals APT2 more than APT1. Again, the homologue from yeast is an exception because it is not influenced in its activity by 2-BP at all. This suggest once more that long-chained substrates or ligands are not the preferred substrates of *y*APT, thus confirming the same indications obtained with the turbidity-assay (as test for activity on (lyso-)phospholipases (figure 3.21)) and the fluorescence polarization assay, indicating weak binding of palmitoylated peptides (figure 3.27). The substrate-binding tunnel could be identified as the preferred, primary binding site of 2-BP with a K_i of 0.5 - 1 µM in *h*APT1, characterizing 2-BP as a reversible competitive inhibitor, contrary to previous reports [97] . Low affinity binding sites of 2-BP (K_i > 100 µM) at the protein surface, e.g. the shallow groove, are confirmed by intrinsic tryptophan assays. The protection of the protein from thermal denaturation at higher 2-BP concentrations could indicate a surfactant-like behavior of 2-BP by covering the APT surface. Crystal structures of 2-BP bound to *h*APT1 and *h*APT2 revealed that a single substitution in the binding tunnel (Ile75/Leu78) most likely is the reason for different interactions of the 2-BP head group in the two isoforms, while the aliphatic tail is oriented almost

identically. This suggests that different amino acid compositions around the active site might cause differences in substrate specificity. The absent 2-BP inhibition of *y*APT could structurally be traced to the reduction of the tunnel length by Phe81 (see and figure 3.19). 2-BP does not seem to be able to compete against Phe81 for occupation of the tunnel space, resulting in the absence of any impairment in OPTS catalysis upon 2-BP treatment.

3.3.2 The APT isoform specific inhibitors ML348 and ML349

In 2012, Adibekian *et al.* used an activity-based protein profiling (ABPP) approach to identify small molecules that bind to human Acyl Protein Thioesterases. They found a class of piperazine amides and described two small molecules (ML348 and ML349, see figure 1.8) that can act as potent and reversible inhibitors of *h*APT activity, each one selective for one of the two APT isoforms [98], [137]. Since both isoforms share a very similar shaped binding tunnel, detailed information of the binding site and binding mode of both inhibitors were of great interest to identify differences providing isoform selectivity. This knowledge is not only interesting for further improvement and development of inhibitors and probes, but is essential to unravel characteristic features of APT isoforms and maybe also to get some hints about the specificity for the up to now still unknown substrates and thus real function of APTs. Thus, several different crystallization approaches were tried to co-crystallize the two protein-inhibitor pairs, which was especially important in case of *h*APT2 that tends to form crystals of bad quality. APT proteins are usually forming crystal dimers that are interacting via hydrophobic patches, also in the standard *h*APT2 construct lacking the first 5 amino acids. Here, dimers are formed in which the flexible N-termini of two monomers are located in the dimer interface (figure 3.36A). This often resulted in macroscopically nice crystals, but the corresponding diffraction patterns indicated a disorder within the crystal and often multiple lattices. In contrast, truncation of the first N-terminal 14 amino acids (called *h*APT2 Δ14 in the following) led to a different arrangement of the protein molecules in the crystal (figure 3.36B) that does not show the dimer arrangement seen for the standard *h*APT2 construct. This resulted in better ordered crystals and thus in a better reproducible and improved X-ray diffraction data quality.

*h*APT1 did crystallize in a straight forward way with ML348. Thus, high-resolution co-crystal structures of *h*APT1 with ML348 (1.7 Å) as well as *h*APT2 with ML349 (1.1 Å) could be solved (see tables 6.2 and 6.3 in appendix for crystallization conditions and crystallographic statistics). As expected, the interaction of both inhibitors takes place in the substrate-binding tunnel of the proteins. Since no covalent bond is present, the inhibitors can be confirmed as reversible and competitive. The ligands are sandwiched between the lid loop and the inner wall of the substrate binding tunnel

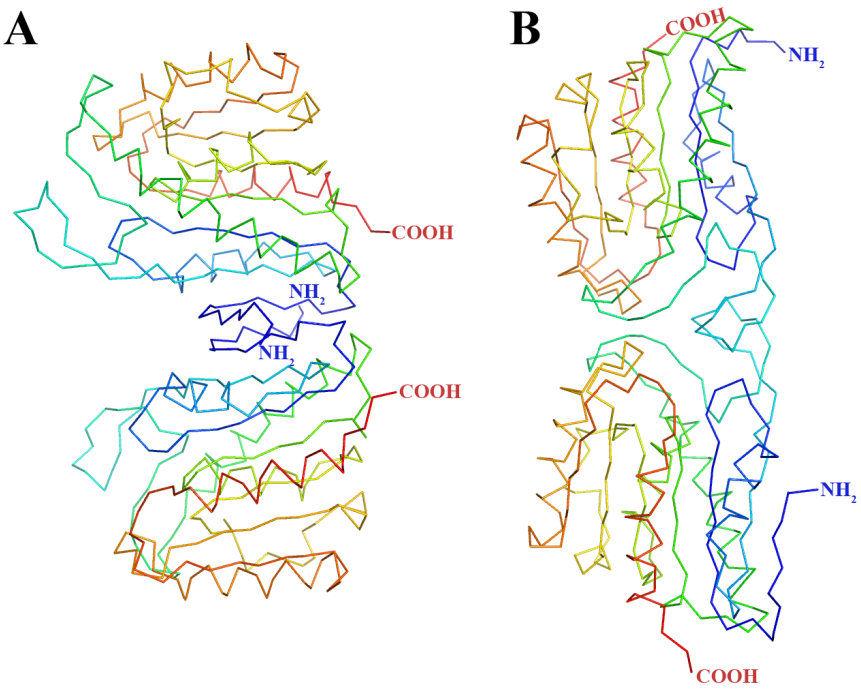

Figure 3.36: Comparison of dimer formation of *h*APT2 and *h*APT2 Δ14 in protein crystals. Shown are the crystal dimers with the largest interaction area of *h*APT2 (A) and the shorter construct *h*APT2 Δ14 (B). The interaction area of the shown dimers was determined using the PISA software [138] and is 1070 Å^2 for *h*APT2 and 804 Å^2 for *h*APT2 Δ14. The protein backbones are shown as ribbons and each monomer is rainbow colored from their N-terminus (blue) to their C-terminal end (red).

and, interestingly, the binding is mainly based on hydrophobic interactions inside of the tunnel.

In the ML348–*h*APT1 structure (figure 3.37) only two hydrogen bonds to the side chain of Arg149 and to a water molecule can be found. The inhibitor is completely embedded within the binding tunnel (figure 3.37B), reminiscent of the *induced fit* model known from enzyme-substrate interactions, where both binding partners arrange in such a way that a shape-complementary complex is formed [139]. The lid loop, which plays an important role for the efficient turnover of substrates by positioning them properly at the active site [88], seems to fulfill a very similar role in ML348 binding.

In the *h*APT2 structure with the second isoform specific inhibitor ML349, the lid loop is equally important: ML349 shows almost the same binding site and mode to *h*APT2 as ML348 to *h*APT1 (figure 3.38). Compared to ML348, ML349 is shifted a bit more to the tunnel entrance towards the active site (Ser122 in *h*APT2) but is still able to span the entire binding tunnel. Again, the hydrophobic interactions are dominating. At both ends of the small molecule one hydrogen bond to *h*APT2 can be formed, one to the catalytic S122 and a second one to T187. The sulfone group of ML349 is additionally interacting with two water molecules that bridge the ligand to the backbone of Leu33 of *h*APT2. Also, the oxygen of the central amide bond of

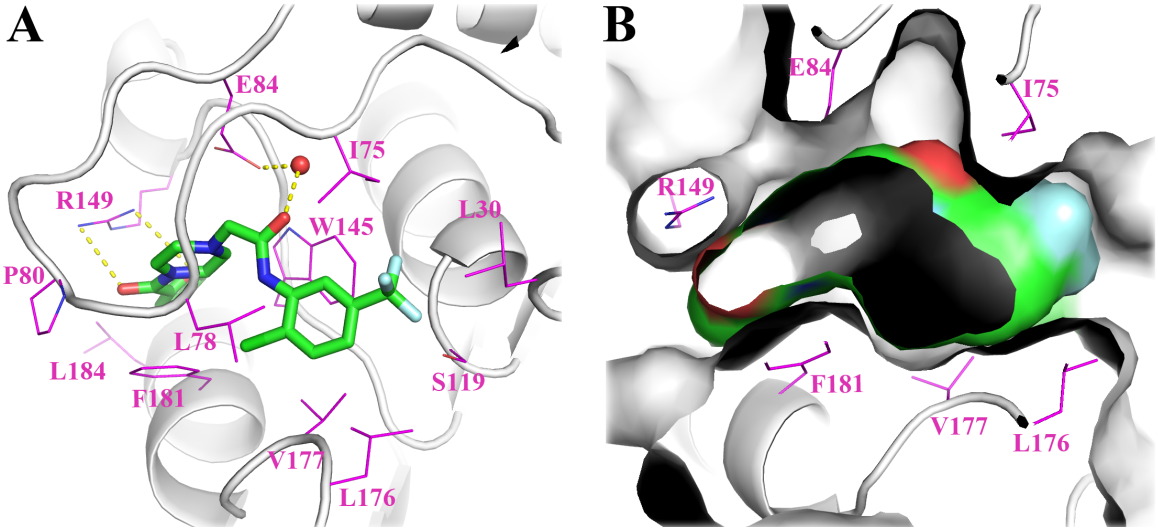

Figure 3.37: Crystal structure of ML348 bound to *h*APT1. (A) The protein's backbone is shown in grey and cartoon style, the ligand ML348 as green sticks. Side chains of amino acids involved in hydrophilic (H-bonds = yellow dots) or hydrophobic contacts are highlighted and labeled in magenta. The catalytically active serine S119 is shown in the same way. The water molecule interacting with ML348 is shown as a red sphere. (B) The surfaces of the protein (grey) and the ligand (green, red, white) are shown. Selected amino acids involved in direct interactions are again depicted as magenta lines. Crystallization condition and crystallographic statistics can be found in tables 6.2 in the appendix.

ML349 has two interactions to conjugated waters that form a bridge to Met79, Gly80 and Pro86 of *h*APT2. When looking at the surfaces of both binding partners (see figure 3.38B) the same scenario can be described as in the case of ML348 and *h*APT1. The ligand is nicely adapted to the shape of the binding tunnel and embedded between the protein core and flexible lid loop.

The structural comparison of the two complexes of *h*APT1 and *h*APT2 revealed that most of the residues involved in the inhibitor binding are identical in both isoforms (figure 3.39). Only at three sites the amino acids differ between the two human APTs: Leu176/Met178, located just outside of the tunnel entrance, Ile75/Leu78 at the entrance and Arg149/His152 at the exit of the tunnel of *h*APT1/*h*APT2 respectively. Due to their position closest to the inhibitors, Ile75/Leu78 and Arg149/His152 were further investigated to determine if they act as selectivity sites for the inhibitors, thus being responsible for the isoform selectivity.

Mutants of *h*APT1 and *h*APT2 were designed where amino acids are swapped to the residue present at this position in the other isoform, to compare their ability to bind the two isoform-specific inhibitors. Thus, the mutants *h*APT1 I75L, *h*APT1 R149H and *h*APT1 I75L R149H were created and, *vice versa*, also the mutants *h*APT2 L78I, *h*APT2 H152R and *h*APT2 L78I H152R. The OPTS activity assay (see section 3.1.1) was used to test the mutants activity in general and also the inhibition of APT activity

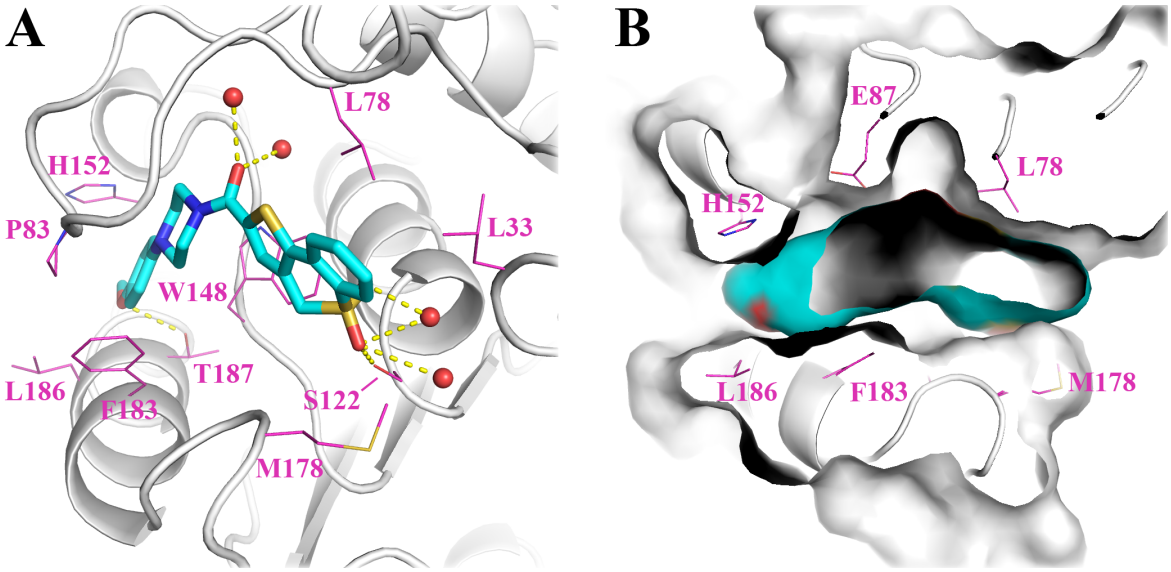

Figure 3.38: Crystal structure of ML349 bound to *h*APT2 Δ14. (A) The protein's backbone is shown in grey and cartoon style, the ligand ML349 in cyan sticks. Side chains of amino acids involved in hydrophilic (H-bonds = yellow dots) or hydrophobic contacts are highlighted and labeled in magenta. The catalytically active serine S122 is shown in the same way. Water molecules that are interacting with the inhibitor are shown as red spheres. (B) The surfaces of the protein (grey) and the ligand (cyan) are shown. Selected amino acids involved in direct interaction are again depicted as magenta lines. Crystallization condition and crystallographic statistics can be found in tables 6.3 in the appendix.

by ML348 and ML349. The determined kinetic parameters can be found in table 3.8.

The K_m of the *h*APT1 mutants to OPTS is increasing from 24 µM for the wild type protein to 30 µM for the single R149H and 39 µM of the single I75L mutant. The K_m of 50 µM of the double mutant *h*APT1 I75L R149H is already similar to the one of the wild type *h*APT2 protein (54 µM). The trend for K_m of the *h*APT2 mutants is more pronounced in the other direction: The single mutant L78I shows already a much lower K_m (32 µM) than the wild type (54 µM). Mutation of H152 to an arginine even leads to a K_m of 14 µM, and the combination of both mutations to 8 µM. Considering the Michaelis-constants as a relative measure of affinity of the proteins to the substrate (see section 3.1.1.1) this implies that the introduced mutations indeed lead to a conversion of binding characteristics from isoform 1 to isoform 2 and *vice versa*. The *h*APT2 double mutant appears to bind OPTS even better than *h*APT1 wild type (8 µM vs. 14 µM). This might be due to other amino acid residues that differ between both APT isoforms and are involved in OPTS binding, like the aforementioned Leu176/Met178 next to the tunnel entrance in *h*APT1 and *h*APT2 respectively. Because of the different shape of the inhibitors compared to OPTS, especially with its huge pyrene head group, they must not necessarily also have an influence on inhibitor binding.

Interestingly, no real trend can be seen in the values of k_{cat}. All mutants of *h*APT1 show a comparable catalytic constant between 2.57 - 2.81 s^{-1}. The same is true for the

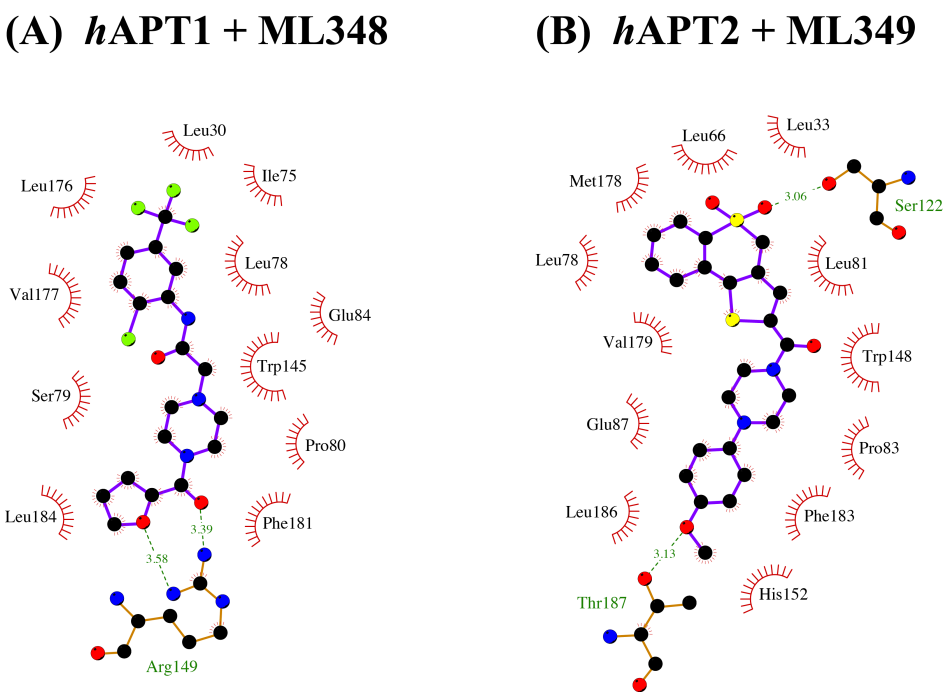

Figure 3.39: 2D diagram of ML348 and ML349 binding to *h*APT1 and *h*APT2. Shown are the interactions of the proteins with the cocrystallized inhibitor. The interaction of ML348 with *h*APT1 is mainly based on hydrophobic contacts indicated by the red arcs with spokes around the involved amino acids. Additionally, Arg149 can interact via H-bonds with the inhibitor, the involved amino acid is shown in a ball-and-stick representation and contacts are represented in green dashes lines with the corresponding distance in Ångström. The interaction of ML349 with *h*APT2 has also largely hydrophobic character. Here two hydrophilic contacts are visible, one to the catalytically active Ser122 the other to Thr187. Interactions to water molecules were omitted for the sake of clarity. The diagrams were created with the software LigPlus+ [136].

wt *h*APT2 and the single mutant L78I. The introduction of the mutation H152R leads to a decrease in the catalytic rate of 30 % to 1.8 s^{-1} that can also be seen for the double mutant *h*APT2 L78I H152R. Thus, the OPTS substrate might be bound tighter, but perhaps in a catalytically less optimal position, so that fewer substrate molecules are converted by the protein in a given period of time.

The determination of the K_m values was also important for the inhibition assay, because obtained IC_{50} values were transformed to K_i using the Cheng-Prusoff equation (see section 5.2.2.2). Although the calculated K_i is not necessarily equal to the real K_d (section 3.3.1), this value is at least comparable throughout the proteins with different affinities towards the substrate, in contrast to the IC_{50} values.

The inhibition of APT activity by ML348 and ML349 was measured using 125 µM OPTS substrate and 5 nM APT (figure 3.40), as used in the 2-BP inhibition assay (see section 3.3.1). The K_i values of ML348 to *h*APT1 of 70 nM and ML349 to *h*APT2 of 50 nM are lower but comparable to the published affinities of 300 nM and 230 nM [98]. The observed differences between K_i values determined here and described in literature [98]

Table 3.8: Kinetic parameters of prepared *h*APT1 and *h*APT2 mutants, using OPTS as substrate.

	K_m [µM]	$k_{cat}[s^{-1}]$	$k_{cat}/K_m[s^{-1}\ \mu M^{-1}]$
*h*APT1	24.46 ± 1.62	2.78 ± 0.05	0.11
*h*APT1 I75L	38.99 ± 3.92	2.57 ± 0.07	0.07
*h*APT1 R149H	30.40 ± 4.52	2.81 ± 0.11	0.09
*h*APT1 I75L R149H	50.06 ± 4.19	2.79 ± 0.07	0.06
*h*APT2	53.63 ± 3.07	2.71 ± 0.05	0.05
*h*APT2 L78I	31.81 ± 1.66	2.50 ± 0.04	0.08
*h*APT2 H152R	14.17 ± 1.14	1.77 ± 0.03	0.13
*h*APT2 L78I H152R	8.05 ± 1.03	1.82 ± 0.05	0.23

could be explained by the different assays and/or procedures: For instance, in contrast to the OPTS assay used here, the assay performed by Adibekian *et al.* is based on the fluorescent substrate resorufin acetate and contained the detergent pluronic F127 (0.2 %, CMC = 0.26 ± 0.03 %[140]). The substrate-sequestering effect of just 0.05 % of this detergent in an activity assay was shown in section 3.1.1 (figure 3.4), which also could have a similar effect on the inhibitor availability. The resorufin acetate substrate does not have a lipidic moiety like OPTS and is thus not able to penetrate the binding tunnel. This might allow (residual) catalytic activity although an inhibitor is bound. At last, Adibekian *et al.* incubated the protein and the inhibitors 15 minutes prior to substrate addition, which was not the case in the OPTS assay. This could have an influence on the detected inhibitory concentration of the compounds if a slow binding of ML348 or ML349 is assumed, perhaps caused by the necessary movement of the lid loop.

As depicted in figure 3.40 and evaluated in table 3.9, the effect of the introduced mutations on the affinity of the isoform selective inhibitors is tremendous: Mutation of a single residue Ile75 (K_i = 1.8 µM) or Arg149 (K_i = 760 nM) in *h*APT1 already leads to a 25- or 10-fold loss of affinity to ML348 compared to the wild type (K_i = 70 nM). The affinity of ML348 to the double mutant *h*APT1 I75L R149H is further decreased to a K_i of 17 µM, indicating a low-affinity binding. While the effect of the Arg149 mutation could be explained by the loss of the hydrogen bond, the dramatic loss of affinity when mutating Ile75 of *h*APT1 to a leucine is not that evident. But figure 3.37B impressively shows that Ile75 is in close proximity to ML348, pushing the molecule to the binding tunnel wall beneath. This tight fixation via hydrophobic

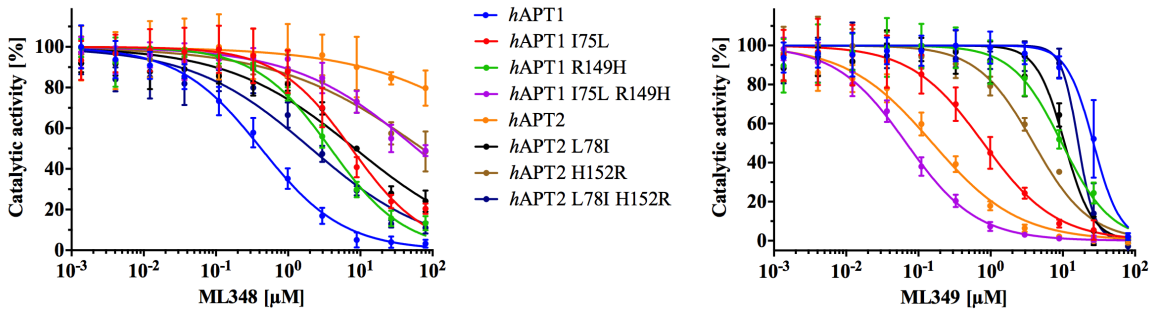

Figure 3.40: Inhibition of *h*APT1 and *h*APT2 and their mutants by ML348 and ML349. The catalysis of 125 µM OPTS by 5 nM APT protein was inhibited by different amounts of ML348 (left chart) or ML349 (right chart). Plotted are the mean values of a triplicate with the corresponding standard error bar. Corresponding IC_{50} values can be found in table 3.9.

Table 3.9: Determined IC_{50} values and calculated K_i values of APT inhibition by ML348 and ML349. The corresponding inhibition studies are shown in figure 3.40.

	ML348		ML349	
	IC_{50} [µM]	**K_i [µM]**	**IC_{50} [µM]**	**K_i [µM]**
*h*APT1	0.42 ± 0.04	0.07	26.56 ± 1.62	4.35
*h*APT1 I75L	7.54 ± 1.11	1.79	0.79 ± 0.11	0.19
*h*APT1 R149H	3.86 ± 0.33	0.76	9.69 ± 1.25	1.90
*h*APT1 I75L R149H	60.20 ± 12.85	17.21	0.07 ± 0.004	0.02
*h*APT2	> 80	> 20	0.16 ± 0.01	0.05
*h*APT2 L78I	8.41 ± 1.40	1.71	10.55 ± 0.99	2.14
*h*APT2 H152R	72.53 ± 14.88	7.38	3.92 ± 0.44	0.40
*h*APT2 L78I H152R	2.08 ± 0.37	0.13	16.39 ± 1.65	0.99

interactions probably contributes to the high affinity, so that minor changes, like the swap of the isoleucine to a leucine, lead to a disturbance of the inhibitor conformation and to less favorable interactions. It seems that the leucine side chain, as present in *h*APT1 I75L or *h*APT2 (figure 3.38B), with its branched terminal dimethyl group would create a clash with the trifluoromethyl moiety of ML348, if not rearranged properly. This necessary reorganization, restricted by the allowed dihedral angles of the amino acid and also by the arrangement of the surrounding side chains, might result in the observed loss of affinity.

ML348 does not inhibit *h*APT2 wild type significantly (K_i > 20 µM) and the single mutant *h*APT2 H152R only slightly (K_i = 7.4 µM). Introduction of an isoleucine at position 78 of *h*APT2 leads to an improved binding of the inhibitor (K_i = 1.7 µM) and the combination of both mutations results in a binding affinity of similar strength (K_i

= 130 nM) as the wild type *h*APT1 (K_i = 70 nM). Thus, the presence of an isoleucine close to the tunnel entrance and an arginine at the exit leads to an affinity to ML348 in the nanomolar range, no matter which isoform-character the rest of the protein shows. If the amino acids leucine and histidine are located at these positions as in *h*APT1 I75L R149H and *h*APT2, almost no inhibition by ML348 can be detected. Although both sites are contributing to the interaction, the amino acid at the entrance seems to be more relevant to the binding of ML348 than the residue at the binding tunnel exit. This suggests that the entrance of the tunnel constitutes the major selectivity site and the exit a minor one.

In contrast to ML348, the isoform 2 specific inhibitor ML349 shows a strong binding to the wild type *h*APT2 (K_i = 50 nM), which is weakened when His152 is mutated to an arginine (K_i = 400 nM), present at this position in *h*APT1. The mutation of Leu78 of *h*APT2 to an isoleucine results in a drastic loss of affinity (K_i = 2.1 µM; table 3.9). Interestingly, the combination of both does not lead to a further decline in binding, possibly because the inhibitor has then more freedom to shift slightly to the back of the binding pocket which might allow the formation of new stabilizing contacts.

The wild type *h*APT1 protein shows a weak micromolar affinity (K_i = 4.4 µM) towards ML349 that is significantly strengthened when a histidine at position 149 is inserted (K_i = 1.9 µM) instead of the canonical arginine. An even more significant increase in affinity can be observed when a leucine instead of an isoleucine is placed at position 75 of *h*APT1 (K_i = 190 nM). Combination of both mutations leads to an even better binding site for ML349 in *h*APT1 (K_i = 20 nM) than the *h*APT2 wild type (K_i = 50 nM).

Thus, the *h*APT2 specific inhibitor ML349 obviously requires the properties of Leu75, which interacts perfectly with the planar aromatic ring system of the head group of ML349, thereby "pushing" the ligand towards the lid loop (figure 3.38). The histidine at the end of the binding tunnel is less important, but is apparently more favored than a longer more flexible side chain as present in arginine. The results determined for ML349 confirm those obtained with ML348: The entrance as well as the exit of the tunnel are the main selectivity sites for discrimination between ML348 and ML349, whereby the entrance seems to be the major contributor to the isoform selectivity.

Co-crystallization of the APT mutants with the isoform selective inhibitors was challenging, but two co-crystal structures of *h*APT1 mutants could be obtained. The first structure, *h*APT1 R149H with ML348 (K_i = 760 nM, K_i(*h*APT1) = 70 nM), still shows 100 % occupancy of ML348 at the binding site. Superimposition of all four monomers present in the asymmetric unit shows that ML348 is in a very similar position around the trifluoromethyl group next to the active site but shows multiple geometries in the back close to the mutated site H149 (figure 3.41A). This suggests

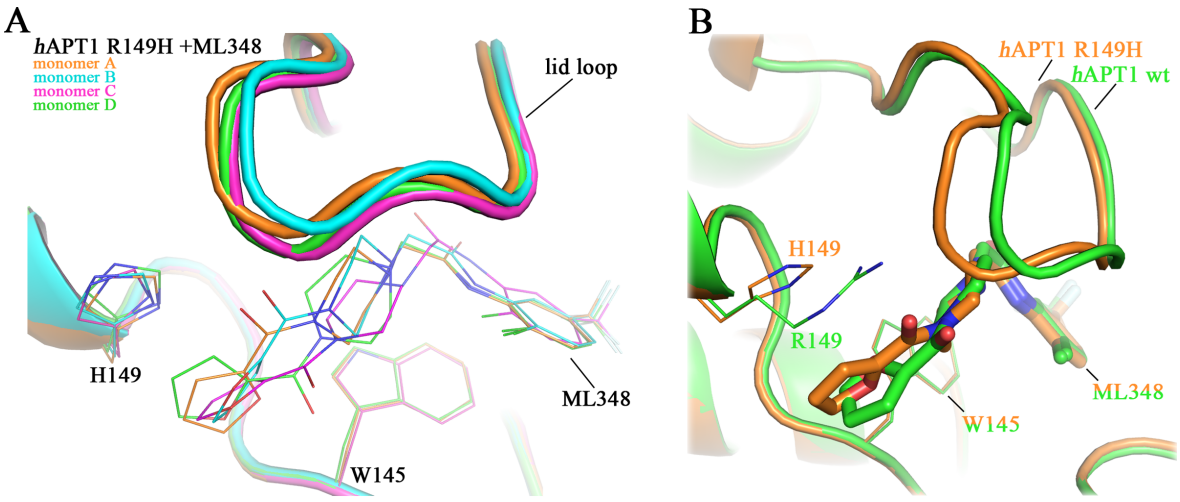

Figure 3.41: Co-crystal structure of *h*APT1 R149H and ML348 and comparison to the wild type situation. (A) Superimposition of all four *h*APT1 R149H monomers present in the asymmetric unit. The backbones of the proteins are differently colored and shown in cartoon style, the side chain of the introduced mutation H149 is shown as sticks. As a reference point also the side chain of W145 is shown as lines, as well as the bound inhibitors. (B) Superimposition of ML348 bound to wt *h*APT1 (green) and *h*APT1 R149H (orange). Both proteins show only minor differences in their structure, as shown for the site of mutation (R149H), the lid loop and the tail-part of the inhibitor next to R149/H149. Crystallization conditions and crystallographic statistics can be found in tables 6.6 in the appendix.

that replacing the arginine by a histidine leads to a less optimal coordination of the ligand at this site, most probably by the loss of the electrostatic interactions between R149 and the oxygens of the terminal furan and amide group of ML348 (see figure 3.37A and figure 3.39). The lid loop is adapting to the altered ML348 conformation in *h*APT1 R149H by moving slightly to the inside and towards the shorter histidine H149 (figure 3.41B). Such a rearrangement of the lid loop suggests that it could also play an important role in adapting to natural substrates of varying size in the binding tunnel, as also discussed in the thesis of Arthur Porfetye [88] .

The replacement of Gln83 in *h*APT1 by a proline, the corresponding residue in *h*APT2 at position 86, was also considered potentially interesting, since this residue is located at one of the hinge-regions of the lid loop. Since a electrostatic interaction of Gln83 with the inhibitor is very unlikely because in all available *h*APT1 structures the glutamine side chain is not pointing into the binding tunnel, the idea was that the lid loop of *h*APT2 might be less flexible due to the more rigid proline at this position and thus might not be able to adapt its conformation to ML348. According to this idea the mutants *h*APT1 Q83P R149H and *h*APT1 I75L Q83P R149H were made, but initial inhibition experiments showed that the mutants *h*APT1 R149H and *h*APT1 Q83P R149H have very similar binding behavior towards ML348 and ML349-OMe (variant of ML349, missing the terminal methoxy group), while the additional

introduction of the I75L mutation had a much more significant impact (see figure 6.5 in the appendix). Thus, the *h*APT1 mutants containing Q83P were not fully kinetically investigated and experiments focussed on the mutants discussed above (figure 3.40 and table 3.9). Nevertheless, a crystal structure could be obtained of a triple mutant *h*APT1 I75L Q83P R149H in complex with ML348, although a very weak binding of ML348 was expected from the initial inhibition studies ($IC_{50} > 100$ µM; see figure 6.5 in the appendix). The presumed weak interaction is also reflected in the occupancy of the binding tunnel by ML348. Only two of the four proteins present in the asymmetric unit show an electron density that corresponds to the structure of ML348 (see figure 3.42). While one of them (monomer A) is very well defined (figure 3.42A), the density

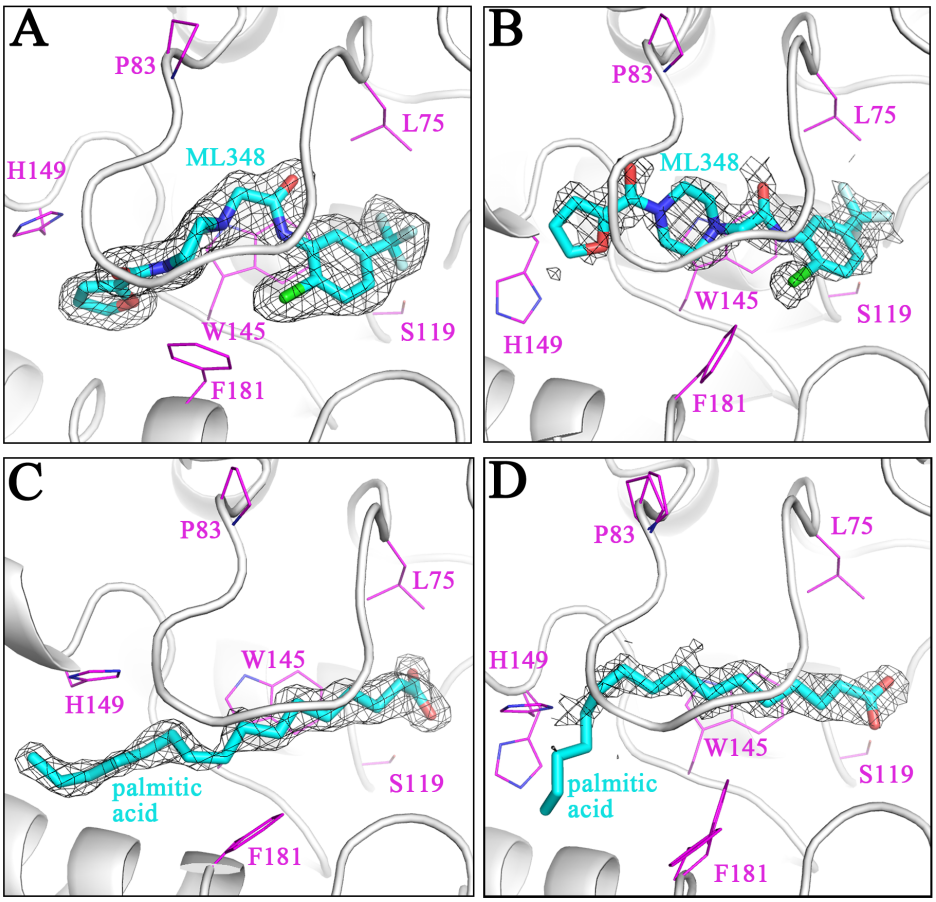

Figure 3.42: The four *h*APT1 I75L Q83P R149H monomers of the asymmetric unit show four different electron densities in their binding tunnel. *h*APT1 I75L Q83P R149H is shown in cartoon style and colored grey, the different ligands are shown as cyan sticks. The side chains of selected amino acids are shown as magenta lines and are labelled accordingly. The $2F_o$-F_c electron density visible in the binding tunnel is shown as black mesh and contoured to 1σ. Crystallization conditions and crystallographic statistics can be found in tables 6.7 in the appendix.

of the other one (monomer B) appears more diffuse (figure 3.42B). Surprisingly, the arrangement of ML348 that fits best to the weaker density in monomer B is different from the binding mode visible in monomer A as well as from the one determined for the

wild type protein (see figure 3.37). Furthermore, side chains of the protein in monomer B, for instance of His149 and Phe181, differ significantly in their orientation compared to structures with a "canonically" bound inhibitor. The two other monomers of the asymmetric unit (figure 3.37 C and D) show an elongated electron density in the binding tunnel, which would fit very well to a saturated fatty acid. The origin of this fatty acid is unknown, probably it is co-purified from *E.coli* as in the case of the mentioned serendipitous co-crystallization of *xt*APT1 with palmitic and stearic acid [87]. Thus, as in the case of *xt*APT1, it might be possible that the density visible in monomers C and D of *h*APT1 I75L Q83P R149H corresponds to a mixture if stearic and palmitic acid. These observations nicely match the determined weak IC_{50} (>100 µM) of ML348 to this *h*APT1 mutant: Upon mutation of critical amino acids the interaction between ligand and protein is weakened, leading to several different binding modes. As a consequence, the flexibility of the ligand and of involved residues is increased and thus less defined electron density is detectable.

Obviously, the introduced mutations can drastically change the nature of the protein with respect to its ability to bind the isoform selective inhibitors ML348 and ML349. Exploiting the isoform selectivity of the small molecules, the inhibitors were used as probes to characterize the binding tunnels of APT orthologues from xenopus, drosophila and yeast and potentially classify them as APT1- or APT2-like.

Inhibition experiments using the OPTS assay showed that the isoform 1 specific inhibitor ML348 indeed inhibits *h*APT1 and *xt*APT1 with a comparable nanomolar affinity, while all other tested proteins (*h*APT2, *xt*APT2, *dm*APT and *y*APT) are not influenced in their activity up to 80 µM ML348 (figure 3.43). In contrast, ML349

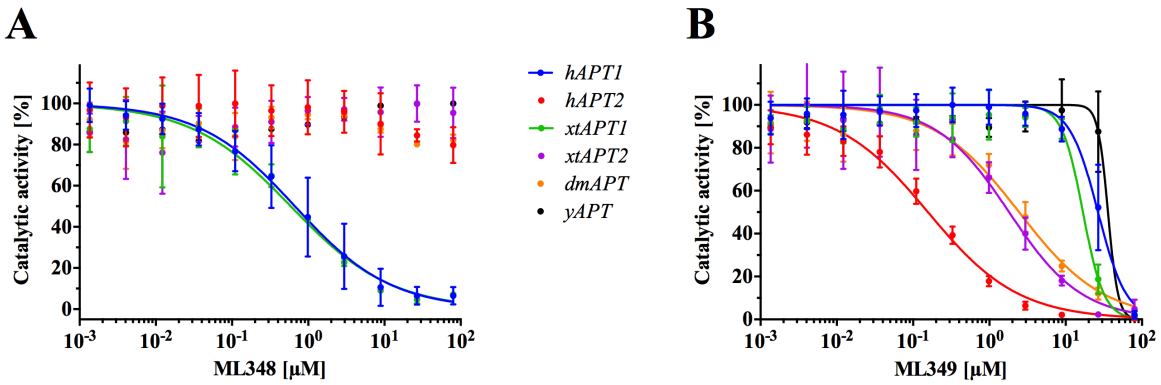

Figure 3.43: Inhibition of APT homologs by ML348 and ML349. The catalysis of 125 µM OPTS by 5 nM APT protein was inhibited by different amounts of ML348 (left) or ML349 (right). Plotted are the mean values of a triplicate with the corresponding standard error bar.. Corresponding IC_{50} values can be found in table 3.10.

seems to be able to bind to all tested proteins, although much weaker to the APT1 isoforms and to *y*APT. *h*APT2 shows the highest affinity of 50 nM, *xt*APT2 and *dm*APT are inhibited with a K_i of approximately 500 nM. The other tested proteins

Table 3.10: Determined IC_{50} values and calculated K_i values of inhibition of APT homologs by ML348 and ML349. Corresponding IC_{50} and K_i values of inhibition studies shown in figure 3.43.

	ML348		**ML349**	
	IC_{50} [µM]	**K_i [µM]**	**IC_{50} [µM]**	**K_i [µM]**
*h*APT1	0.42 ± 0.04	0.07	26.56 ± 1.62	4.35
*h*APT2	> 80	> 20	0.16 ± 0.01	0.05
*xt*APT1	0.59 ± 0.11	0.07	16.85 ± 1.49	1.97
*xt*APT2	> 80	> 20	1.81 ± 0.36	0.57
*dm*APT	> 80	> 20	2.45 ± 0.37	0.56
*y*APT	> 80	> 20	35.88 ± 17.06	6.20

*h*APT1, *xt*APT1 and *y*APT seem to have a very similar low micromolar affinity (table 3.10), but their steep dose-response curves appear conspicuous. The activity of *y*APT for instance is decreasing from ∼85 % at a ML349 concentration of 27 µM to 0.3 % at 80 µM inhibitor. While the curves of *h*APT2, *xt*APT2 and *dm*APT inhibition by ML349 show a well fitting sigmoidal dose-response with a Hill coefficient of ∼1 (indication of one binding site for ML349), the curves of *h*APT1, *xt*APT1 and *y*APT show much higher Hill coefficients of ∼2, ∼3 and ∼6, respectively. These high values of the curve slopes could indicate the existence of several binding sites for ML349, whereby the slope will increase with the number of inhibitor sites [141],[142], but this is very unlikely considering the 3D strcuture of the APTs. Also, phase transitions of the inhibitor like precipitation or colloid formation that show a sharp concentration dependence could lead to such a steep dose-response curve, if coupled to inhibition [142]. Validation of both explanations requires further experiments that examine the inhibitor concentrations between 1 µM - 100 µM in greater detail. For example, CD-experiments as done for PPTS and 2-BP (see figures 3.10 and 3.32) could reveal if the structure of APTs is influenced by higher concentrations of ML349, an effect that could hint towards destructive ML349-aggregate formation similar to PPTS. Thus, a regular, competitive binding of ML349 into the binding tunnel as seen for *h*APT2 and expected for *xt*APT2 and *dm*APT (just with slightly lower affinity)seems unlikely, so the observed loss of activity of *h*APT1, *xt*APT1 and *y*APT might be most likely due to side effects of high concentrations ML349.

A sequence alignment of APTs (see figure 6.8 in the appendix) suggests that the amino acids that were mutated and described above, i.e. Ile75/Leu78 and Arg149/His152 of *h*APT1/*h*APT2 respectively, seem to be conserved within the two isoforms APT1 and APT2. *h*APT1 and *xt*APT1 are the only orthologues being inhibited by ML348 and are also the only ones that show Arg149 and Ile75. Conversely, the proteins with a

higher affinity to ML349 are also the ones where His152 and Leu78 are present. Following this hypothesis, the APT from *D. melanogaster* would be classified as an isoform 2 APT, while *y*APT cannot be assigned to one of the isoforms.

The binding characteristics of *y*APT seems to be unique among all APTs investigated. Neither 2-BP (see 3.3.1), nor the two isoform selective inhibitors can significantly inhibit its enzymatic activity. Arthur Porfetye was able to solve structures of the covalent inhibitors palmostatin B and M (see sections 1.2.2 and 3.1.2.1) bound to *y*APT [88]. Both palmostatins, contrary to the expectations, do not show a straight aliphatic tail in the expected substrate-binding tunnel. Instead, the amino acid Phe81, located in the lid loop region of *y*APT, is located at a position where the other APTs show an open tunnel, thus blocking it. To adjust to the covalently bound palmostatins, other amino acids in the lid loop and at the outer tunnel wall move from their position in the apo form and allow the palmostatins to stick out of the side of the APT, i.e. the aliphatic tail of the palmostatins is curved. Since *y*APT is the only tested protein having a phenylalanine at this position, the structural data could explain the resistance of the protein against the assayed, non-covalent inhibitors 2-BP, ML348 and ML349.

In summary, using X-ray crystallography the binding mode of the isoform selective inhibitors ML348 and ML349 to their intended protein targets *h*APT1 and *h*APT2 could be revealed. Strikingly, both inhibitors are perfectly embedded between the lid loop and the binding tunnel underneath, stabilized by mainly hydrophobic interaction and only few polar contacts. Analysis of amino acids involved in binding of both ligands revealed two sites that are critical for the selectivity of APT in inhibitor binding: Ile75/Leu78 at the entrance of the binding tunnel close to the active site, and Arg149/His152 at the tunnel exit of *h*APT1/*h*APT2, respectively. According to this hypothesis, appropriate mutants of *h*APT1 and *h*APT2 were designed and their sensitivity for ML348 and ML349 was tested using the established OPTS assay. The results did not only confirm the assumption that both sites are critical for the binding of each inhibitor, but they are also characterizing the tunnel shape of *h*APT1 and *h*APT2, since their mutation to the amino acid present in the other isoform swaps the specificity for the isoform selective inhibitors. Determination of the inhibition of APT homologues from other species revealed that *xt*APT1 clearly shows the binding characteristics of *h*APT1, while *xt*APT2 and *dm*APT behaved like *h*APT2. Again, *y*APT is an exception because no significant inhibition could be observed with both inhibitors, indicating that a binding tunnel as present in *h*APT1 or *h*APT2 is not available in this homologue, consistent with the yAPT–Palmostatin M crystal structure (figure 3.19).

3.3.3 Development of an APT2 specific inhibitor using ligand- and structure-based drug design

To develop initial inhibitor-hits to lead compounds further modifications of the isoform selective inhibitors ML348 and ML349 must be attempted to improve their affinity for APT. Since this was already intensively done by Adibekian *et al.*[98] for the moieties at both ends of the molecules and since the core part is not easily modifiable, a new screening campaign was launched to specifically find APT2 selective inhibitors harboring a different core structure.

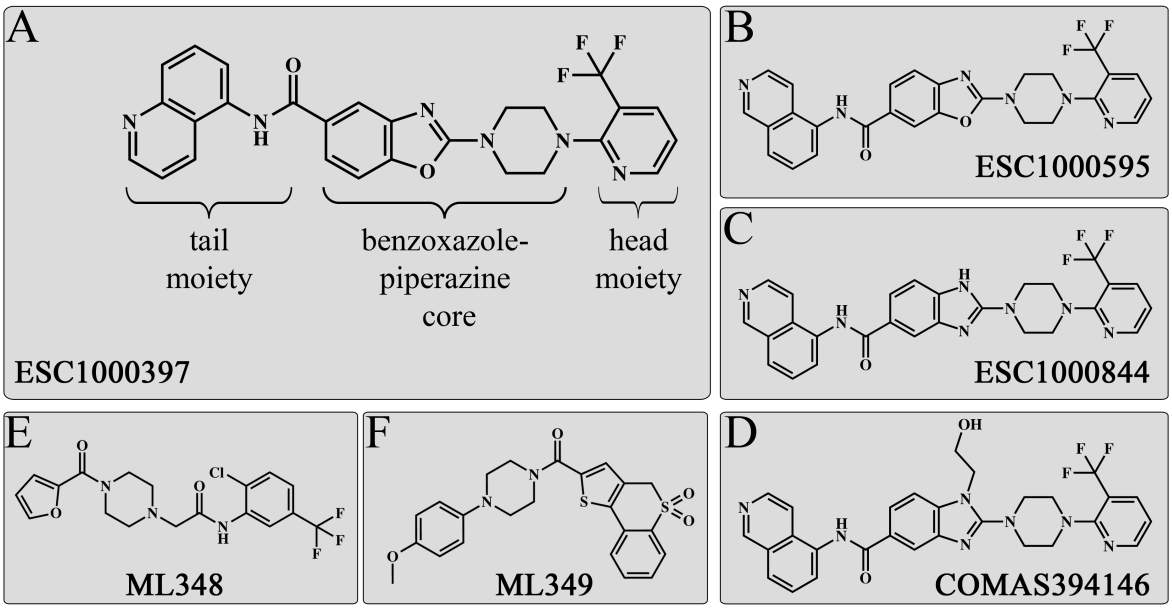

Figure 3.44: Selection of derivatives found to inhibit *h*APT2 activity. The inhibitors ESC1000397 (A) and ESC1000595 (B) are based on a benzoxazole-piperazine core and differ in their tail moiety and in their connection to the core. To be able to modify the core the benzoxazole was replaced by a benzimidazole (ESC1000844, C) and decorated with an ethoxy group in the case of COMAS394146 (D). For comparison the published isoform selective inhibitors ML348 (E) and ML349 (F) by Adibekian *et al.*[98] are shown.

This project was done in collaboration with the European Lead Factory (ELF), a collaborative public-private partnership between the European Screening Centre (ESC), the European Federation of Pharmaceutical Industries and Associations (EFPIA), small and medium-sized enterprises (SMEs) and public institutions that all share their knowledge and skills to deliver innovative drug discovery starting points. Within this initiative an activity based screening of 500,000 compounds using the DiFMUO-approach (see section 3.1.1) was performed to identify selective inhibitors of *h*APT2 activity. The screen revealed a group of small molecules that contain a core of a benzoxazole linked to a piperazine (figure 3.44). In a second step, the "head"- (connected to the piperazine) and the "tail"-groups (linked via an amide bond to the benzoxazole)

were further modified in a ligand-based drug design approach performed at the European Screening Centre. The small molecule found to be the most active, ESC1000397, contains a trifluoromethyl-pyridine as head group, while the tail is modified with a quinoline moiety (figure 3.44A). As a part of this thesis the identified hits were validated using the OPTS assay (see section 3.1.1). Furthermore, attempts were launched to determine co-crystal structures to understand the molecular interactions between the small molecules and the protein. In a structure-based drug design approach, this information would help to improve the compounds.

As listed in table 3.11, in the OPTS assay ESC1000397 inhibited *h*APT2 in a competitive and isoform specific manner with an IC_{50} of 0.95 µM ± 0.08 µM that corresponds to a K_i of 0.29 µM (according to the Cheng-Prusoff equation, see section 3.3.1 and equation 5.3 in section 5.2.2.2). Even before optimization, the K_i of the compound was already comparable with the K_i of ML349 to *h*APT2 (published K_i: 0.23 µM[98] , 0.05 µM in OPTS assay, see table 3.9).

The co-crystal structure of *h*APT2 Δ14 and ESC1000397 was solved at 2.6 Å resolution (figure 3.45). Although resolution and electron density of the inhibitor are

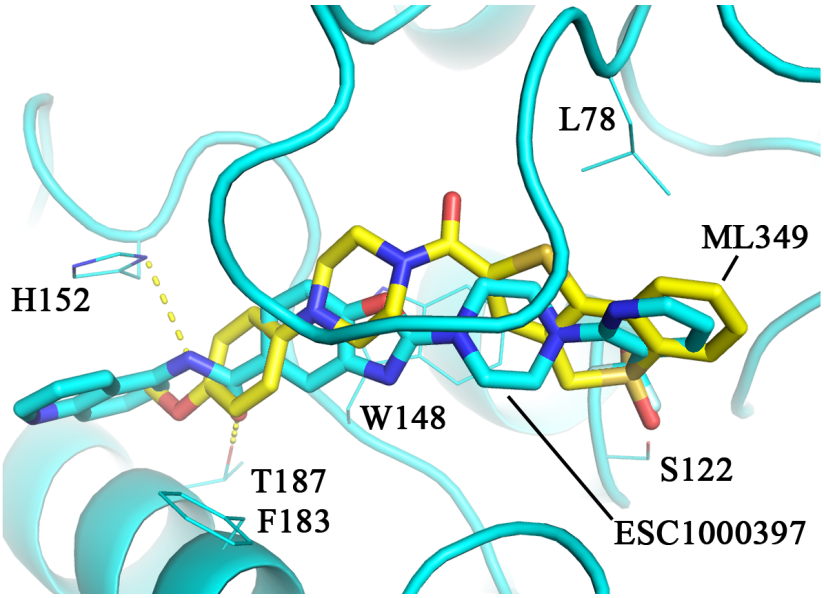

Figure 3.45: Co-crystal structure of ESC1000397 with *h*APT2 and comparison to ML349. The ligand ESC1000397 spans the entire binding tunnel. While the trifluoromethyl-pyridine head group is placed next to the catalytic serine 122, the quinoline at the tail can interact with His152 via $\pi - \pi$ stacking and a hydrogen bond. An additional H-bond might be formed by the interaction to Thr187. The *h*APT2 protein is represented in cartoon style, the ligand is shown as sticks. Side chains of selected amino acids are shown as thin lines and yellow dashed lines represent hydrogen bonds between inhibitor and protein. For comparison of the binding-modes the published isoform 2 selective inhibitor ML349 from the solved co-crystal structure with *h*APT2 Δ14 (see 3.38) was superimposed and is represented as yellow sticks. Crystallization conditions and crystallographic statistics of the shown structure are listed in table 6.8.

not ideal (see appended figure 6.6), the binding site and mode could be revealed with

sufficient accuracy. Similar to the isoform specific inhibitors ML348 and ML349 (figures 3.37 and 3.38) the binding of ESC1000397 to *h*APT2 occurs mainly through hydrophobic interactions and the inhibitor is also embedded in the binding tunnel and sandwiched by the lid loop. Due to the increased length of the molecule, ESC1000397 is able to span a greater part of the binding tunnel compared to ML348 and ML349. Furthermore, because of the amide-linked quinoline moiety, it is able to form an attractive $\pi - \pi$ interaction and a hydrogen (H-) bond to His152, as well as an H-bond to Thr187. During the optimization process at the European Screening Centre, the terminal quinoline was replaced by an isoquinoline among many different other substituents. When this new moiety was additionally shifted from position 5 to position 6 of the benzoxazole, the K_i of the resulting compound ESC1000595 (figure 3.44B) to *h*APT2 improved 5-fold in the DiFMUO- and 2-fold in the OPTS-assay compared to ESC1000397 (see figure 3.46 and table 3.11). The differences between the K_i values

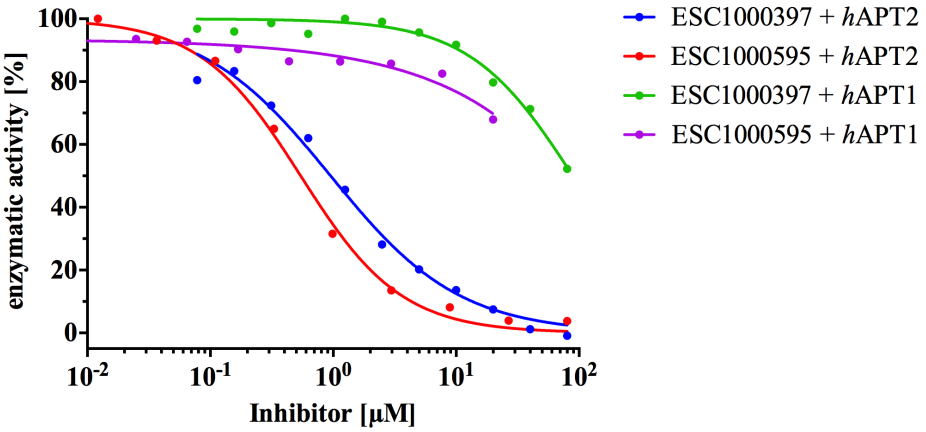

Figure 3.46: The small molecules ESC1000397 and ESC1000595 completely inhibit *h*APT2, but *h*APT1 activity only weakly. Inhibition of *h*APT2 and *h*APT1 was determined using the OPTS assay with 125 µM substrate and 5 nM protein. The DMSO concentration was kept at 1 %.

determined with both assay systems may have several reasons. Besides the mentioned inaccuracies using the Cheng-Prusoff correction for determining K_i values (see sections 3.1.1.1 and 3.3.1) two more aspects have to be considered in this case. First, in contrast to the OPTS assay, in the DiFMUO approach performed at the European Lead factory (ELF) the inhibitor was pre-incubated with the protein for 30 min before the substrate was added. Especially for the binding of sterically demanding inhibitors which require the adaptation of the lid loop of APT, a slow binding inhibition might be plausible and would require a pre-incubation for the determination of more accurate IC_{50} values. However, in experiments performed at the ELF concerning this question, no influence of the pre-incubation on the IC_{50} could be observed, so this effect could be excluded for this type of competitive inhibitors. This finding is in agreement with the tryptophan fluorescence assay performed in this thesis (see figure 3.33), where also no indication

Table 3.11: Measured IC_{50} and calculated K_i values of ESC1000397 and ESC1000595 binding to *h*APT2 using the DiFMUO and OPTS assay. The K_m values, necessary for the calculation of the stated K_i values, were determined by Marco Bürger [87] and are listed in section 5.2.2.2.

			ESC1000397	ESC1000595
DiFMUO assay	**IC_{50} [µM]**	***h*APT1**	> 20	> 20
		***h*APT2**	0.21	0.04
	K_i [µM]	***h*APT1**	> 10	> 10
		***h*APT2**	0.09	0.02
OPTS assay	**IC_{50} [µM]**	***h*APT1**	88.97 ± 8.47	> 100
		***h*APT2**	0.95 ± 0.08	0.56 ± 0.08
	K_i [µM]	***h*APT1**	15	> 30
		***h*APT2**	0.29	0.17

for slow binding could be detected. Second, the use of 0.01 % (w/v) Triton-X100 (= 0.155 mM; the CMC is 0.02 % (w/v) = 0.31 mM) in the case of the DiFMUO assay (see section 5.2.2.2) - in contrast to the OPTS assay - might not only influence binding of the substrates but also of the inhibitors. Examples of the drastic effects of detergents in such assay systems are covered in section 3.1.1 and 3.3.1 (see figures 3.2, 3.4 and 3.33). Furthermore, the K_m value of the DiFMUO substrate to the proteins, necessary for the calculation of the corresponding K_i values, was not determined under the same conditions as the stated IC_{50} values, but taken from previous experiments described in the thesis of Marco Bürger [87] (see section 5.2.2.2), who used detergent-free conditions similar to the assay buffer used in the OPTS approach. Thus, most probably the influence of the detergent on the substrate and the inhibitors is the dominant effect that is responsible for the different K_i values.

A high-resolution X-ray structure (1.5 Å) of ESC1000595 bound to *h*APT2 Δ14 could be solved and shows that the inhibitor adopts a different geometry compared to ESC1000397, although the general binding mode is maintained. As depicted in figure 3.47, the molecule is shifted closer to the tunnel entrance next to the active site, the head group still facing the catalytic serine. The benzoxazole is rotated by 180 °, thus allowing the tail to orientate in a similar way as in the case of ESC1000397. Due to the rearrangement and the resulting shift of the molecule, the position of the isoquinoline group to His152 is slightly changed, possibly optimizing the $\pi - \pi$ interaction and thus leading to the observed slight increase in affinity. On the other hand, the distances between the amide of the inhibitor and the amino acids His152 and Thr187 are increased from 3.4 Å to 3.7 Å and from 3.0 Å to 5.0 Å respectively. Thus, the formation of direct stabilizing hydrogen bonds, i.e. without a bridging water, is most likely impossible for ESC1000595.

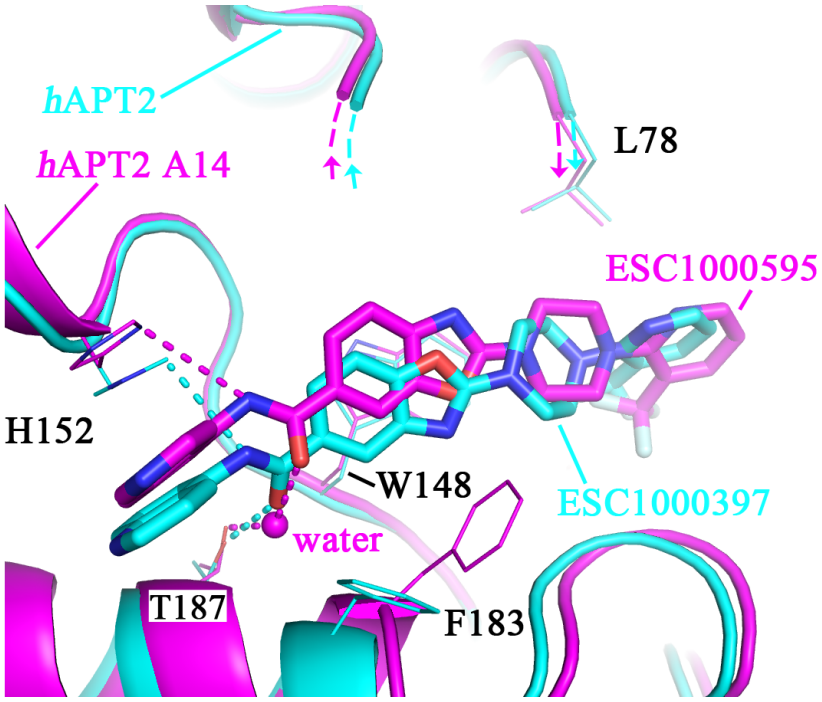

Figure 3.47: Comparison of the binding mode of the small molecules ESC1000397 and ESC1000595 to *h*APT2. The co-crystal structure of ESC1000397 and *h*APT2 is shown in cyan, the structure of ESC1000595 and *h*APT2 Δ14 in magenta. Hydrogen bonds between inhibitors and protein are shown as dashed lines and are colored according to the structure they belong to. A water molecule present in the ESC1000595-*h*APT2 Δ14 structure is shown as a sphere. Side chains of selected amino acids are shown as thin lines and labeled in black. For the sake of clarity the lid loop is omitted in both structures but dashed lines and arrows indicate its position. Crystallization conditions and crystallographic statistics of the shown structure are listed in table 6.9.

Interestingly, the loss of the direct interaction to Thr187 is "rescued" by the coordination of an additional water molecule in the co-crystal structure of ESC1000595. The water is placed exactly at the position were the H-bond forming carbonyl group of ESC1000397 is located, thus bridging Thr187 and ESC1000595 (see figure 3.47). Also, the protein is adapting in an induced-fit like manner to the changed geometry of the new ligand. For instance, the side chain of Phe183 is significantly shifted away from its position in the structure with ESC1000397 and the whole lid loop is adjusting to this situation with a slight shift (not visible in figure 3.47). It could be possible that the rearrangement of these protein features corresponds to a more favorable state of the protein, for instance a more rigid conformation of the lid loop that is enabled by changes in the geometry of the inhibitor. That might also explain the higher quality of the crystal structure.

As shown in figure 3.48 and table 3.12 the *h*APT1 and *h*APT2 mutants introduced in section 3.3.2 were tested for inhibition by ESC1000595. In contrast to the isoform selective inhibitors ML348 and ML349, where the selectivity site at the tunnel entrance seems to be more important, the second selectivity site at the tunnel exit is more crucial

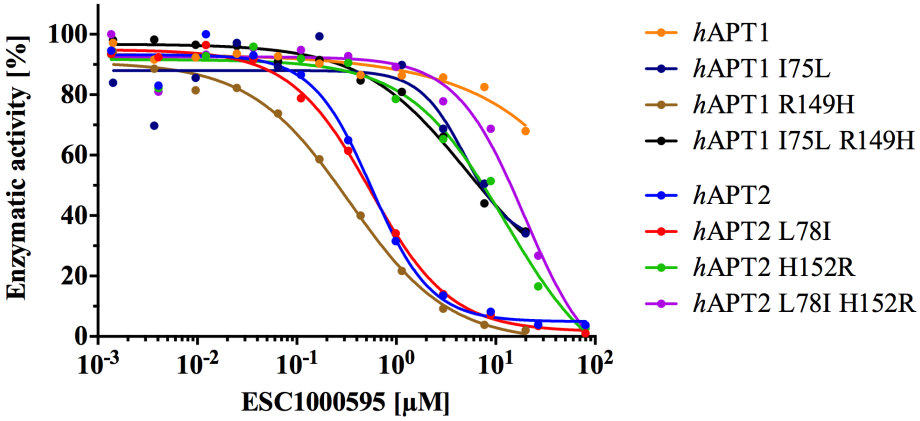

Figure 3.48: Inhibition of both human APT isoforms and their mutants by ESC1000595. Using the OPTS assay (125 µM substrate and 5 nM protein) the inhibition of *h*APT1 and *h*APT2 mutants upon titration with ESC1000595 was tested.

Table 3.12: Determined IC_{50} values and calculated K_i values of inhibition of human APT mutants by ESC1000595. Mutations at equivalent positions in *h*APT1 and *h*APT2 are shown on the same line. K_m values of each mutant to the OPTS substrate are listed in table 3.8.

***h*APT1**	**IC_{50} [µM]**	**K_i [µM]**	**K_i [µM]**	**IC_{50} [µM]**	***h*APT2**
wt	> 80	> 20	0.17	0.56 ± 0.08	wt
I75L	4.92 ± 3.10	1.17	0.11	0.55 ± 0.04	L78I
R149H	0.34 ± 0.04	0.07	1.27	12.51 ± 6.26	H152R
I75L R149H	5.14 ± 2.76	1.47	1.18	19.56 ± 8.73	L78I H152R

in the case of ESC1000595. When the canonical His152 in *h*APT2 is mutated to an arginine that is present in *h*APT1 at this position, the affinity of the inhibitor is reduced 10-fold, most likely because of the loss of the stabilizing $\pi - \pi$ interaction to the histidine side chain. *Vice versa,* this interaction can also be achieved by mutation of Arg149 in *h*APT1 to histidine that leads to a strong interaction between protein and inhibitor, comparable to *h*APT2 (see table 3.12). The influence of the other selectivity site is more complicated to interpret. In the case of a mutation of Leu78 to isoleucine in *h*APT2 no significant change in K_i can be observed compared to the wild type protein. This mutation also does not show a further influence on inhibitor binding when introduced to the *h*APT2 H152R protein. According to these results, it seems that this site only has a minor influence on ESC1000595 interaction. Interestingly, the situation is different when introducing equivalent mutations to *h*APT1. The exchange of Ile75 to leucine allows the inhibitor to bind with a reasonable affinity around 1 µM, while the activity of wild type *h*APT1 is only influenced at inhibitor concentrations $>$ 80 µM. On the other hand, introduction of I75L mutation to *h*APT1 R149H reduces the gained affinity from 70 nM to 1.5 µM, comparable with the *h*APT1 I75L single mutant.

Taken together, these findings imply an alternative binding mode of the inhibitor when the I75L mutation is present in *h*APT1. In this case the inhibitor binding becomes almost independent of the presence of a histidine at position 149, in contrast to the wild type and in contrast to any mutant of *h*APT2. This again argues that additional residues might be involved that generally allow this alternative binding mode in case of *h*APT1 L75I but not in *h*APT2. Leu176 in *h*APT1 that corresponds to Met178 in *h*APT2 (see section 3.3.2) might for instance serve as a critical residue in this case. Since it is located on the opposite site of Ile75/Leu78 at the tunnel entrance and close to the head group of the inhibitor, it could indeed influence the binding mode of the inhibitor in combination with the I75L mutation. It might be even possible that the inhibitor rotates by 180 ° in the binding tunnel, which might explain the loss of sensitivity to the R149H mutation in *h*APT1.

When studying the crystal structure of ESC1000595 in complex with *h*APT2 Δ14, a pocket next to the inhibitor was noticed, as illustrated in figure 3.49. This pocket

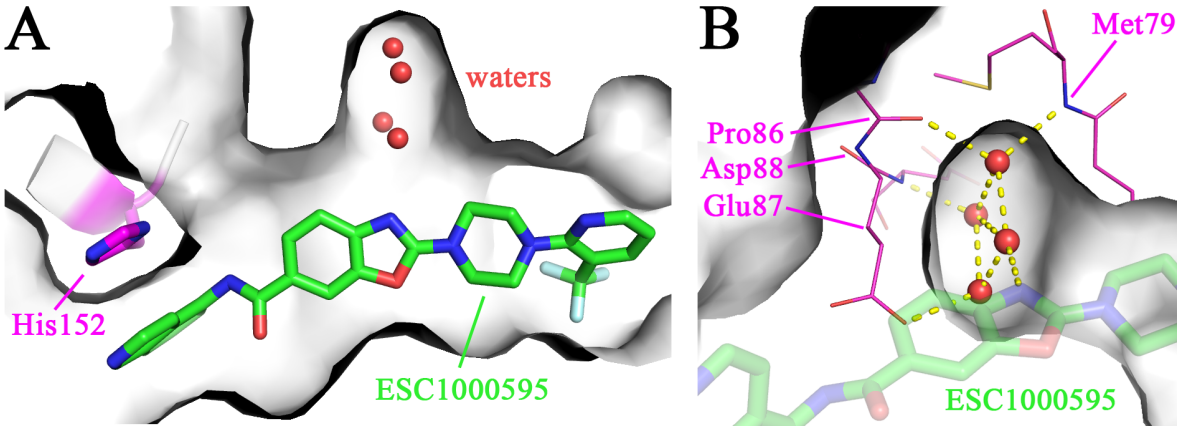

Figure 3.49: A pocket of *h*APT2 Δ14 next to the ESC1000595 inhibitor is occupied by four water molecules. (A) The position of the inhibitor ESC1000595 within the binding tunnel of *h*APT2 is shown. A pocket, occupied by four water molecules, is visible above the benzoxazole moiety of the small molecule.The surface of *h*APT2 is shown in grey, His152 and the inhibitor as sticks. The four water molecules are shown as red spheres. (B) The interaction network of the water molecules within the pocket is shown in greater detail. Hydrogen bonds formed by the water molecules are highlighted in yellow dashed lines and involved amino acids are shown as thin magenta lines. Crystallization conditions and crystallographic statistics of the shown structure are listed in table 6.9.

is also present in the apo form of *h*APT2, but interestingly, the potentially modifiable nitrogen of the benzoxazole is placed directly at the pocket entry. Four water molecules are occupying this pocket, that are coordinated by the hydrophilic side chain of Glu87 and the protein backbone of Pro86, Asp88 and Met79. It appears feasible to address this pocket by modifying the inhibitor with moieties that take over the positions of the water molecules to mimic their attractive interactions to the protein, leading to an increase in inhibitor affinity and potentially also selectivity.

Since direct modification of the nitrogen of the benzoxazole would lead to a chiral

center and thus to an increased synthetical effort, the benzoxazole was therefore replaced by a modifiable benzimidazole. The resulting inhibitor ESC1000844 (see figure 3.44C) shows a slightly reduced affinity of K_i = 0.14 µM compared to ESC1000595 (K_i = 0.02 µM) in the DiFMUO assay, while no inhibition of *h*APT1 could be observed up to a inhibitor concentration of 20 µM. The loss of affinity is most likely due to the minor changes in geometry of the inhibitor and is acceptable since this particular compound did only serve as a modifiable precursor. The synthetical work for creating variants of ESC1000844 was done by Dr. Axel Pahl from the Compound Management and Screening Center (COMAS), who also performed a docking study based on the *h*APT2-ESC1000595 co-crystal structure to identify worthwhile benzimidazole-modifications. As depicted in figure 3.50 several small molecules were identified, show-

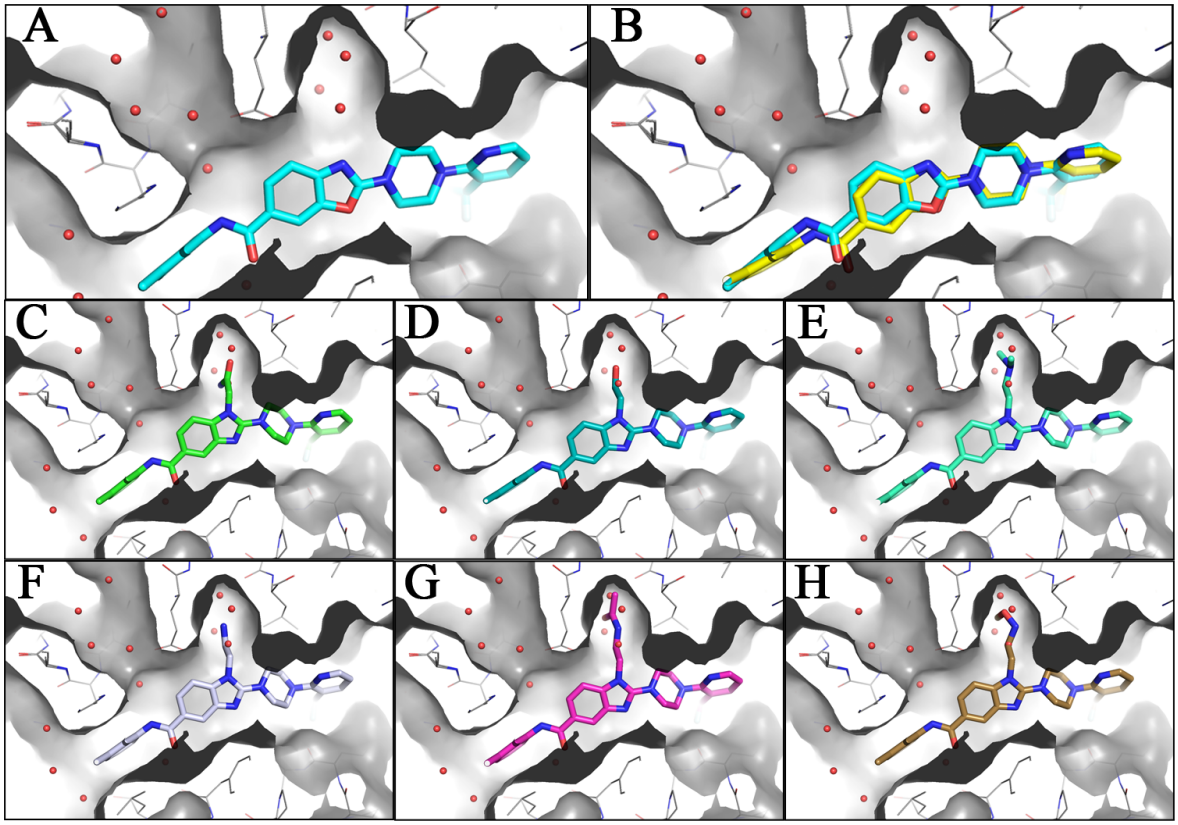

Figure 3.50: Molecular docking study to find suitable modifications of the specific APT2 inhibitor ESC1000844. Shown are selected results of a molecular docking study. (A) shows the X-ray co-crystal structure of ESC1000595 and *h*APT2 Δ14, that served as basis of the docking. After the inhibitor was removed from the structure *in silico,* different modified compounds were docked into the binding pocket. (B) shows a control run, where ESC1000595 was docked back into the structure. Since only minor changes are occurring compared to the real crystal structure the specific settings of the docking procedure were apparently chosen properly. Figures (C) - (H) show different derivatives of ESC1000844 (figure 3.44C), that in contrast to ESC1000595 contains a modifiable benzimidazole core that is decorated with moieties addressing the additional binding pocket. (D) shows the first synthesized compound COMAS394146. Dr. Axel Pahl performed the molecular docking using the program AutoDock Vina.

ing promising docking scores. In the first synthesized molecule of this series, COMAS394146 (figure 3.44D and 3.50D), one of the nitrogens of the benzimidazole was modified with an ethoxy moiety. In the OPTS activity assay (figure 3.51) this com-

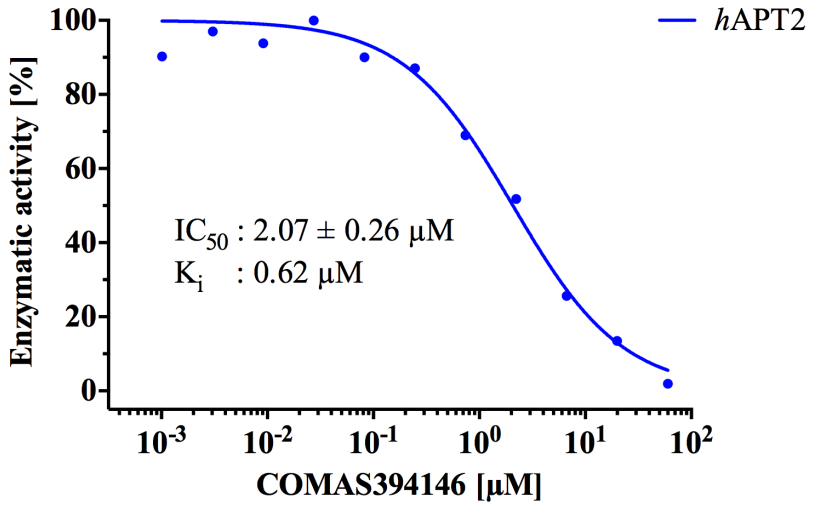

Figure 3.51: *h*APT2 activity is inhibited by COMAS394146. Using the OPTS assay (125 µM substrate and 5 nM protein) the inhibition of *h*APT2 activity upon titration with COMAS394146 was tested.

pound showed a reduced but still reasonable affinity of K_i = 0.62 µM to *h*APT2 compared to ESC1000595 (0.17 µM).Although binding less tight, the sub-micromolar K_i implies that the identified pocket (see figure 3.49) was most likely addressed because a much more dramatic loss of affinity would be expected otherwise. Probably the newly achieved interactions to the protein led to slight changes of the inhibitor geometry and thus to a weakening of existing interactions or the relatively stiff ethoxy moiety led to unfavorable steric clashes in the pocket. A co-crystal structure was pursued to reveal the exact binding mode of COMAS394146 and provide hints how to fine-tune the inhibitor. This crystallization attempt unfortunately was not successful to date, perhaps due to an increased flexibility of the lid region, induced by the more bulky substituents, an effect that is often observed in APT structures, as the lid region is involved in crystal contacts in most of the cases.

4 Discussion

Acyl Protein Thioesterases were mentioned for the first time in 1998 when Duncan and Gilman renamed a protein from rat that was previously described as lysophospholipase1 (LYPLA1). The basis of this name change was the ability to depalmitoylate the Gα subunit and H-Ras more efficiently than lysophospholipids. Later, the same authors identified an APT orthologue in *S.cerevisiae* that was deemed to be responsible for deacylation of the Gα subunit of yeast *in vivo*. Since APT proteins are well conserved in eukaryotes (see section 1.2.2), a certain essential function in biological processes can be assumed. Several protein and non-protein substrates were proposed in the past, but unfortunately the exact function of APT still remains elusive and an explanation for a supposed difference in substrate selectivity of the two APT isoforms (APT1 and 2) that are present in higher eukaryotic organisms is still missing.

This thesis provides new insights into possible physiological roles of APT and its isoforms, thereby focusing on the interaction of different substrates, ligands and inhibitors with APT proteins. For this purpose, different assay systems had to be established: A reliable activity assay was needed that is independent of additives, e.g. detergents, to quantify catalytic activities and also the inhibition of APT. Using this assay, described APT inhibitors were validated and in combination with X-Ray crystallography also their exact binding-mode was revealed. Beside the artificial inhibitors, the binding and/or hydrolysis of natural substrates was explored, from palmitic acid via (lyso-)phospholipids to palmitoylated peptides. Comparison of different APT isoforms and homologues from different species revealed significant, characteristic differences between them. Considering also homologues from lower eukaryotic species provided insights onto APT from an evolutionary point of view.

4.1 Establishing a detergent-free, reliable fluorescence based activity assay

First of all, a sensitive and reliable activity assay was developed (section 3.1.1). To be independent of detergents that are frequently used but are influencing the substrate availability and thus the measured protein activity (figures 3.2 and 3.4), the well sol-

uble octanoyl ester (OPTS) of the fluorescent 1-hydroxypyrene-3,6,8-trisulfonic acid trisodium salt (HPTS, figure 3.1) was introduced successfully as a substrate for APT and proved to meet the defined requirements. It turned out that APTs of isoform 1 (*h*APT1 and *xt*APT1) show lower K_m values (K_m ∼20 µM) and efficiency (k_{cat}/K_m = 0.11-0.14 $s^{-1}µM^{-1}$) on OPTS than APT2 proteins (*h*APT2 and *xt*APT2; K_m ∼ 55 µM, k_{cat}/K_m ∼20 $s^{-1}µM^{-1}$), but a similar k_{cat} (2.3 - 2.7 s^{-1}). *dm*APT, which is so far not assigned to an isoform, showed kinetic values between those of APT1 and APT2 proteins, although having a slightly faster turnover (K_m = 37 µM, k_{cat}/K_m = 0.08 $s^{-1}µM^{-1}$, k_{cat} = 3.1 s^{-1}) . The APT homologue from yeast (*y*APT) has a K_m value (26 µM) similar to APT1, but a significantly higher turnover (k_{cat} = 13 s^{-1}) and efficiency (k_{cat}/K_m = 0.5 $s^{-1}µM^{-1}$), thus appearing unique amongst the tested proteins.

To investigate the substrate specificity of APT on longer chained substrates, the well soluble lauroyl- (LPTS) and palmitoyl- (PPTS) esters of HPTS were successfully synthesized. Surprisingly, a complete loss of APT activity at higher concentrations of LPTS (250 µM) and PPTS (30 µM) was observed (figure 3.6). After product inhibition by palmitic acid could be excluded as cause of this effect (figures 3.8 and 3.9), the intense study of this phenomenon using PPTS revealed that most likely substrate-aggregates are formed, initially by $\pi - \pi$ interactions of the pyrene head group and stabilized by the long aliphatic chains. The PPTS aggregates inhibit APT irreversibly by changing its structure, confirmed by circular dichroism measurements (figure 3.10), but those aggregates could not inhibit the activity of lipases from *Candida rugosa* (figure 3.10), so PPTS is not a general denaturating agent. The addition of 10 µM fatty-acid binding protein 2 (FABP2) or 10 % DMSO can prevent the formation of these destructive aggregates but, unfortunately, also influences the kinetics of the catalysis (figure 3.12) and in case of FABP2 also leads to high background hydrolysis (figure 3.11). Since *h*APT1 appears to be the most resistant protein to the PPTS-aggregates, kinetics could be obtained at only 1 % DMSO for OPTS, LPTS and PPTS (figures 3.15 and 3.16 and table 3.4), showing that the affinity of the substrate is increasing 35-fold from OPTS (K_m = 24 µM) to PPTS (K_m = 0.7 µM) with increasing chain-length. Since the k_{cat}values are similar for all three substrates, also the catalytic efficiency increased 60-fold when using PPTS (k_{cat}/K_m = 6.4 s^{-1} $µM^{-1}$) instead of OPTS (k_{cat}/K_m = 0.11 s^{-1} $µM^{-1}$), indicating that at least *h*APT1 has a preferred substrate selectivity for longer chained, e.g. palmitoylated, substrates.

4.2 APT activity on natural substrates

The conversion of the artificial substrate OPTS was shown to be a convenient tool to detect APT activity, but, especially because of the huge pyrene head group that has to be placed close to the active site, a interference on natural substrates appears

questionable. Therefore, other test systems were established to measure the activity of APT on (lyso-)phospholipids (that was so far only shown for APTs from a few organisms, mostly higher eukaryotic species like human, mouse or rabbit [52],[54],[55],[57]) and on palmitoylated peptides.

4.2.1 The (lyso-)phospholipase activity of APTs

To compare the activities of APTs from different evolutionary stages, an agar-based turbidity assay was setup using egg-yolk as (lyso-)phospholipid-rich substrate and olive oil as triglyceride source (section 3.2.1). Clear zones in the egg-yolk containing agar, as indication of activity, of comparable sizes could be observed for both human and xenopus isoforms, as well as for the APT from drosophila, indicating significant activity on (lyso-)phospholipids (figure 3.21A). *y*APT showed a 50 % reduced clear zone, thus again appearing unique compared to the other APTs. None of these enzymes showed a sign of activity in the agar containing olive oil, in contrast to lipases from *Candida rugosa* (figure 3.21B). To see what makes *y*APT so unique, this enzyme was investigated in more detail.

According to the structural information available in our group *y*APT does not show an open, preformed binding tunnel like *h*APT1, *h*APT2, *xt*APT1, *xt*APT2 or *dm*APT [87] . The primary reason for this is a phenylalanine (Phe81) located in the lid loop of *y*APT and turned into the "canonical" tunnel, thereby shortening it tremendously (figure 3.19). Furthermore, a tryptophan (Trp77), also located in the lid loop, sits right opposite the active site at the entrance of the binding tunnel and might have a gate-keeper function [87] , since it can adapt to different substrates. Thus, Trp77 was mutated to the sterically less demanding amino acids phenylalanine and alanine. Using the egg yolk based turbidity assay, indeed, an increased activity could be observed when sterically less demanding amino acids are present at this position, indicating a possible involvement of Trp77 in substrate binding. The investigation of F81 mutants is still ongoing.

The determination of kinetic parameters for the catalysis of lysophospholipids and phospholipids is not straight forward, mainly because of their poor solubility in aqueous buffer. However, ESI-MS analyses were attempted revealing (apparent) slow turnover values of $\sim 1.5 \cdot 10^{-4}$ for lyso-palmitoylphosphocholine (lyso-PPC) and $\sim 4 \cdot 10^{-5}$ for di-palmitoylphosphocholine for both human isoforms (figure 3.23), that could be associated approximately with the observed clear zones in the egg-yolk agar.

In summary, APTs can hydrolyze (lyso-)phospholipids, but they appear very slow, especially yAPT, so the question was if they are faster on their other postulated substrates.

4.2.2 Depalmitoylation of a palmitoylated *h*APT1-peptide and a palmitoylated H-Ras peptide in presence and absence of membranes

The ESI-MS analyses described for the lipids were also performed using a fluorescein-tagged nonapeptide that represents the N-terminus of *h*APT1 and is palmitoylated on the cysteine at position 2. Both, *h*APT1 and *h*APT2, showed a similar catalytic activity (apparent k_{cat} ~27 s^{-1}, figure 3.23) on this peptide, which appears to be 4-5 orders of magnitude higher than the determined values for (lyso-)phospholipids and clearly shows that also *h*APT2 is able to depalmitoylate the N-terminus of *h*APT1, different to the observations *in vivo* [74]. Although it was reported that soluble APT depalmitoylates substrates on all membranes of the cell [31], it remained unclear if APTs can bind to membrane-inserted substrates and/or if one or both APT isoforms require cofactors for this activity. For instance, an *in vivo* study by Ahearn *et al.* suggested that FKBP12 binds to H-Ras and N-Ras in a palmitoylation-dependent fashion and is substantially involved in Ras depalmitoylation by accelerating the hydrolysis through a *cis-trans* isomerization of a peptidyl-prolyl bond in close proximity to the palmitoylated cysteines of H-Ras [33].

A fluorescence polarization approach was used to show binding of the palmitoylated, FITC-labeled *h*APT1-peptide to DOPC vesicles (figure 3.25A) and also the release of this peptide by (catalytically active) *h*APT1 and *h*APT2. Analysis of the velocity of catalysis revealed apparent k_{cat} values of 0.38 s^{-1} for *h*APT1 and 0.62 s^{-1} for *h*APT2 (figure 3.25B) under non substrate saturating conditions that were chosen to allow measurement of the (fast) release in the plate reader. The difference between *h*APT1 and *h*APT2 is small, but repeated experiments indicated that it is significant. The decreased velocity compared to the peptide catalysis in solution might be either due to the non-saturating conditions or to a rate-limiting extraction of the peptide out of the DOPC membrane that could then be done more efficiently by *h*APT2 than by *h*APT1. Further experiments with different amounts of peptide or protein should confirm this finding and also will be compared to determine the influence of the intrinsic dissociation rate of the peptide (~0.5 s^{-1}, measured by Kathrin Estel) from the vesicles. If the rates of depalmitoylation by APT would be confirmed to be faster than the dissociation rate of the peptide alone, an "active" extraction of the peptide by one or both APT isoforms could be assumed, or the possibility that APTs could cleave the palmitoylated peptide inside of the membrane. Co-factors like FKBP12 have to be considered that could enable or further accelerate depalmitoylation of membrane-bound substrates at a physiological reasonable speed.

To compare binding of the *h*APT1-peptide with one of the proposed natural substrates, the mono-palmitoylated C-terminus of H-Ras was used in the same fluorescence

polarization experiment. Unfortunately, no FP signal was seen upon binding to vesicles, most likely because of the high mobility of the fluorophore in the significant longer (24 amino acids) H-Ras peptide. But, interestingly, binding to catalytically inactive APT mutants from human (*h*APT1 S119A) and yeast (*y*APT S119A) showed a clear increase of the FP for both, the *h*APT1- and the H-Ras peptide, indicating that the mobility of the (fluorophore of the) H-Ras peptide is significantly decreased upon binding to *h*APT1 compared to the interaction with DOPC vesicles. This experiment clearly showed that the affinity of the longer H-Ras peptide to *h*APT1 (K_d= 36 nM) is about 30-fold higher than of the short *h*APT1-peptide (K_d= 985 nM), indicating additional interaction sites between protein and peptide outside the binding tunnel. Since both peptides are sufficiently long to span the supposed second binding site (figure 3.28) at the shallow groove, either the sequence next to the palmitoylation site matters, indicating a preferred sequence for the interaction with APT, or the H-Ras peptide is able to interact with other binding sites beside the shallow groove with APT. Competition experiments with unlabeled peptides should show if the fluorescein fluorophore also contributes to the affinity.

In contrast to *h*APT1 S119A, the counterpart from yeast, *y*APT S119A, only showed a weak micromolar affinity to both palmitoylated peptides, 8.5 µM to the *h*APT1- , 12 µM to the H-Ras peptide (figure 3.27). This finding again indicates that long chained substrates are not the preferred substrates of *y*APT, as already seen for (lyso-)phospholipids. The structural reason for this, as already mentioned above, could be, in contrast to other APTs investigated, the shortening of the binding tunnel by Phe81 of *y*APT, indicating that yAPT might be more closely related to carboxylesterases that also feature a shallow active site (see section 4.4.1.2 below).

4.3 Revealing the molecular interactions of APT inhibitors

4.3.1 The tryptophan fluorescence assay and binding of Palmostatin M and 2-Bromopalmitate

Beside the natural substrates described above also published inhibitors of APT activity were used to study their interaction to different APT proteins. So far, APT-related phenotypic effects could only be observed in cells that were treated either with the covalent inhibitor palmostatin B (a derivative of Palmostatin M, see figure 1.8) or 2-bromopalmitate (2-BP). These inhibitors do not have a high selectivity for APT, thus especially upon 2-BP treatment not only APTs will be inhibited but also closely related (unknown) hydrolases which could act as redundant (thio-)esterases and are

thus usually able to compensate the loss of APT activity upon treatment with specific inhibitors. In addition, the whole palmitoylome of the cell will be disturbed and thus of course also (palmitoylated) APT itself. To extend the possibilities to characterize ligand binding to APT, complementary to the OPTS assay - to test for APT activity and inhibition - and X-ray crystallography - to reveal the binding mode of inhibitors - another assay was established. The additional assay (Trp-assay, section 3.1.2) is based on the intrinsic tryptophan fluorescence of APT that is quenched upon ligand binding close to a tryptophan side chain. The positioning of the three tryptophans in *h*APT1 is very beneficial (figure 3.17), since one of them creates a wall of the binding tunnel (Trp145), the second is located in the middle of the shallow groove (Trp37) and the last one in the core of the protein (Trp72). The use of corresponding *h*APT1 mutants allows detection of ligand binding into the tunnel (*h*APT1 W37F), to the shallow groove (*h*APT1 W145F) or indirect effects on the global structure of *h*APT1 (*h*APT1 W37F W145F). Palmostatin M (see section 1.2.4 with figure 1.8), a rather unspecific inhibitor that was reported to bind covalently to the active serine residue of APT, was used to successfully prove the proper functioning of this assay. Binding was only detected in the binding tunnel and only if the active serine was present. Furthermore, the halftime of Palmostatin M at the active site before its hydrolysis could be determined (8.3 min) that is in the range of the reported one (3.5 min [46]), that was determined in the presence of Triton-X100 and at 37 °C, in contrast to the measurement in this thesis.

This Trp-assay was also used to characterize the interaction of APT with 2-bromo-palmitate (2-BP). 2-BP was reported to show an uncompetitive binding mode to both *h*APT1 and *h*APT2 [97], that would require another binding site besides the binding tunnel. The Trp-assay was used to check if perhaps the shallow groove could act as such an interaction site since a PEG molecule was found at this position in a structurally closely related carboxylesterase (see figure 1.6), indicating a potential interaction site. The Trp-assays clearly showed that the binding tunnel is the by far preferred binding site of 2-BP with a K_d of 1.6 µM to *h*APT1 (figure 3.30 and table 3.7). The existence of a second, low affinity site was confirmed since also the fluorescence of Trp37 in the shallow groove was influenced, but only at significantly higher 2-BP concentrations (K_d ~170 µM), which could maybe also explain the published uncompetitive effect. Because also the fluorescence of Trp72, actually buried in the protein's core, was quenched at higher 2-BP concentrations, an influence of 2-BP on the whole structure of APT was suspected. This could be confirmed via circular dichroism experiments (figure 3.31): Interestingly, the APT is apparently protected from thermal denaturation at higher 2-BP concentrations. Experiments using the Trp-assay confirmed that the APT structure is not changed irreversibly (figures 3.32 and 3.33), indicating a surfactant-like behavior of 2-BP by covering the APT surface.

The inhibition of APT proteins by 2-BP could be determined using the OPTS assay

(figure 3.29 and table 3.6), showing that isoform 1 APTs are inhibited more strongly (K_i = 0.6 µM for *h*APT1, K_i = 1.0 µM for *xt*APT1) than the corresponding APT2 proteins (K_i = 1.7 µM for *h*APT2, K_i = 2.6 µM for *xt*APT2). The APT from drosophila is, like the APT2 proteins, weakly inhibited (K_i = 4.2 µM). Strikingly, the *y*APT is not influenced at all in its activity up to 200 µM 2-BP. As already seen for the activity on OPTS, (lyso-)phospholipids and the palmitoylated peptides, the behavior of *y*APT appears unique compared to the other APTs investigated. The absent 2-BP inhibition of *y*APT could structurally be traced again to the reduction of the tunnel length by Phe81 (figure 3.19). 2-BP does not seem to be able to compete against Phe81 for occupation of the tunnel space, resulting in the absence of any impairment in OPTS catalysis upon 2-BP treatment.

High resolution cocrystal structures of 2-BP bound to *h*APT1 and *h*APT2 could be obtained (figures 3.36 and 3.35) and confirmed the binding tunnel as primary binding site for 2-BP. Furthermore, they showed that the aliphatic tail of 2-BP is oriented almost identically in both human isoforms and that the observed difference in binding strength of 2-BP in the OPTS assay (0.6 µM vs. 1.7 µM) might be due to slightly different orientations of the carboxyl-head group of 2-BP: While Ile75 in *h*APT1 allows interaction of the head group with Gln120, thereby orienting the carboxyl group into the oxyanion hole, in *h*APT2 Leu78 (placed at the equivalent position to Ile75 of *h*APT1) seems to impede binding of the head group in the same position as in *h*APT1, thereby pushing the carboxyl towards the active serine. This suggests that different amino acid compositions, e.g. Ile75/Leu78, around the active site could also cause slight differences in substrate specificity due to steric restrictions.

The very similar binding of the aliphatic chain of 2-BP and the observed similar activity of both *h*APT isoforms on palmitoylated substrates, e.g. an N-terminally palmitoylated *h*APT1-peptide, and (lyso-)phospholipids, are indicating that several observed isoform-selectivities in protein depalmitoylation *in vivo* (e.g. BK potassium channels [70], melanoma adhesion molecule MCAM,[71] GAP-43 [72] and *h*APT1 and *h*APT2 themselves [74]) seem to be based on other features than the inability of one or the other isoform to cleave a palmitoyl moiety. The significantly different binding affinities between *h*APT1- and H-Ras peptides to *h*APT1 implies that the selection of palmitoylated peptides/proteins takes place outside the binding tunnel and is thus determined by the amino acid sequence next to the palmitoylation site of the substrate.

4.3.2 The isoform-specificity of APT inhibitors ML348 and ML349

Small molecules that selectively and potently bind to a single protein, thereby inhibiting its enzymatic activity, are crucial achievements in chemical biology, since they can be used as molecular probes to reveal the specific role of a protein *in vivo*. In con-

trast to 2-BP, a pronounced selectivity was observed for the inhibition of APT1 and APT2 by the compounds ML348 and ML349 (figure 1.8). Adibekian *et al.*[98] identified these piperazine amide-based compounds, but their non-structural investigation could not clarify the exact binding mode that is important for further inhibitor development and for the identification of the origins of inhibitor selectivity in *h*APT1 and *h*APT2. To gain this knowledge, both APT isoforms were crystallized with their specific inhibitor. Both co-crystal structures, *h*APT1-ML348 and *h*APT2-ML349, showed that the binding of both inhibitors inside of the preformed binding tunnel is highly dependent on hydrophobic interactions and requires a mutual structural adaptation of both the protein and the inhibitor, reminiscent of the induced-fit model described for enzyme-substrate interactions (figures 3.37 and 3.38). Structural analysis of both complexes revealed two sites, one at the entrance of the binding tunnel close to the active site and the other at the end of the binding tunnel, where *h*APT1 and *h*APT2 show different amino acids involved in inhibitor binding, i.e. Ile75/Leu78 (tunnel entrance) and Arg149/His152 (tunnel exit) of *h*APT1/*h*APT2, respectively. Interestingly, the residues at the former site (Ile75/Leu78) were already found to be involved in the orientation of the head group of 2-BP.

According to this result, APT mutants were designed in which the amino acids of one or both identified sites were swapped to their counterpart present in the other isoform: *h*APT1 I75L, *h*APT1 R149H, and *h*APT1 I75L R149H and *vice versa* *h*APT2 L78I, *h*APT2 H152R, and *h*APT2 L78I H152R. Their basic kinetic parameters (table 3.8), as already done for the wild type proteins, were determined using the fluorescence based OPTS assay that was established in this thesis. It was shown that the difference between both isoforms in affinity to the OPTS substrate (K_m = 24 µM for *h*APT1 and K_m = 54 µM for *h*APT2) could be reduced and reverted by sequential mutation of the amino acid at both sites. Interestingly, also the single mutation R149H in *h*APT1 and especially H152R in *h*APT2 seems to influence the affinity of OPTS to the protein: for the latter the, K_m of the substrate improved 4-fold from 54 µM to 14 µM compared to the wild type protein, for the former the K_m increased slightly from 24 µM to 30 µM. This is surprising, since the aliphatic tail of the OPTS substrate is actually too short to reach this residue at the end of the binding tunnel when bound properly at the tunnel entrance close to the catalytic serine. Thus, a direct interaction between the introduced arginine and OPTS is unlikely and an indirect effect via the lid loop was considered instead: The analysis of four different *h*APT1 structures (apo and with ligands 2-BP and ML348) with 14 monomers in total showed that the conserved Arg149 in APT1 is forming at least one hydrogen bond to the backbone of the lid loop, independently of the bound ligand (figure 4.1A). The average distances of the two terminal nitrogens of the guanidine moiety of the arginine side chain to the carbonyl group of Pro80 in the lid loop are 2.9 ± 0.2 Å and 3.5 ± 0.5 Å, thus both are in the range of a significant

electrostatic interaction [143]. As mentioned before, His152 is present at this position in *h*APT2 and is far too short to interact with the lid loop but, interestingly, it is followed by Arg153, which probably could form an interaction to the loop. Thus, also four different *h*APT2 structures (apo or with the ligands 2-BP, ML349 and the ML349 variant ML349-OMe) with in total 14 monomers were analyzed, as to whether Arg153 is able to form attractive interactions to the lid loop (see figure 4.1B). Here, the distances of the terminal NH_2 groups to the carbonyl oxygen of Pro83 in the lid loop are 3.5 ± 0.4 Å and 4.7 ± 0.7 Å. This gap is much larger than in *h*APT1, so probably only a weak electrostatic interaction [143] will be possible between these two residues in *h*APT2 (of course, the determined distances could be different in solution and under non-crystal conditions in general, but they are more unlikely to be much smaller). Thus, the interaction between Arg149 and Pro80 in *h*APT1 might contribute to a restricted flexibility of the loop region that could impede the binding of sterically demanding molecules, but, on the other hand could strengthen an interaction of sterically less demanding molecules inside the binding tunnel. Since Arg153 and Pro83 in *h*APT2 seem to be too far apart from each other to form stabilizing hydrogen bonds, the lid loop might be able to open up wider and/or easier, thus adapting better or at least differently to bulkier substrates. A higher flexibility of the APT2 lid loop might also explain the more difficult crystallization of this protein due to formation of less ordered crystals (figure 3.36).

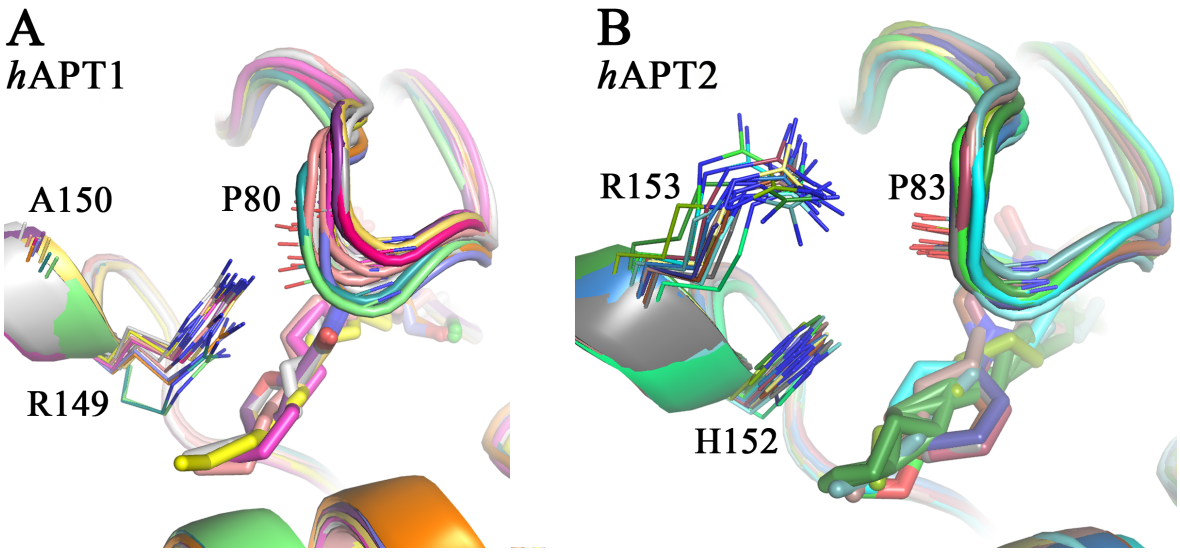

Figure 4.1: Arg149 of *h*APT1 can form a hydrogen bond to the lid loop, but Arg153 in *h*APT2 cannot. For both isoforms, *h*APT1 (A) and *h*APT2 (B) four different crystal structures with 14 APT monomers in total were superimposed. The distances of the terminal nitrogens of Arg149 in *h*APT1 and Arg153 in *h*APT2 to the carbonyl group of a proline in the lid loop were calculated. According to this, Arg149 seems to be able to form a hydrogen bond/electrostatic interaction to the backbone carbonyl of Pro80, while the distance of Arg153 to Pro83 in *h*APT2 is probably too long for an strong electrostatic interaction.

The observation that a swap of the amino acids present at the two identified sites (Ile75/Leu78 and Arg149/His152 of *h*APT1/*h*APT2, respectively) leads also to swap of affinity to OPTS, was shown to be also true for the selective inhibitors ML348 and ML349. Mutation of only these two amino acids to the counterpart present in the other isoform is sufficient to swap the behavior of the proteins regarding the binding of the inhibitors (figure 3.40 and table 3.9). Again, Ile75 in *h*APT1 and the corresponding Leu78 in *h*APT2 create the first selectivity site that is located at the tunnel entrance close to the active site. At the tunnel exit the second selectivity site was identified, formed by Arg149 and His152 in *h*APT1 and *h*APT2, respectively. Thus, the mutant *h*APT1 I75L R149H is almost able to mimic wild type *h*APT2: It is able to bind the *h*APT2-specific inhibitor ML349 with an affinity higher than *h*APT2 wt and binds ML348 with a greatly reduced affinity compared to *h*APT1. *Vice versa*, *h*APT2 L78I H152R gained the ability to bind ML348 strongly but binds ML349 weaker then the wild type *h*APT2 (table 3.9). In comparison, the first selectivity site, Ile75/Leu78 in *h*APT1/*h*APT2, appears more critical for the proper binding of both inhibitors.

Before being able to share these findings, Won *et al.* [144] published their insights about the molecular mechanism of APT inhibition by ML348 and ML349. They also identified Ile75/Leu78 as a selectivity site. In their experiments with the aim to reverse the inhibitor-selectivity of *h*APT1 the single I75L mutation of *h*APT1 led to a 10-fold decrease in ML348 affinity (in this work: 25-fold) and simultaneously to a quite strong binding of ML349 (K_i = 0.37 µM; in this work 0.19 µM). This result is very similar to the findings presented in this study. The differences in K_i values could be due to the different substrate used (fluorogenic resorufin acetate (ResOAc)), see also below. Interestingly, they could observe a complete loss in affinity of ML348 to *h*APT1 upon mutation of S82A and Q83P additionally to I75L. Both mutations are located in the lid loop region of APT and probably influence the proper "sandwiching" of the inhibitor between the lid loop that forms the outer wall of the substrate-binding tunnel. The mutation Q83P was also investigated in this thesis but only within the context of a double (*h*APT1 Q83P R149H) or triple mutant (*h*APT1 I75L Q83P R149H), where it did not show any further influence compared to the R149H mutation on inhibitor binding. Since the additional mutations of S82A and Q83P made by Won *et al.* did not lead to a tight binding of isoform 2 specific inhibitor ML349 (K_i = 1.2 µM, *h*APT2 wt = 0.12 µM), they might just have enlarged the binding tunnel, thus allowing the sterically more demanding ML349 to bind while loosing attractive interactions to ML348. The authors could achieve a complete swap of *h*APT1 selectivity towards the inhibitors when three more mutations were introduced: R149H, A150R and S151A. This 6-fold mutant was detected not to bind ML348 (K_i > 10 µM), but it binds ML349 instead with a reasonable affinity of K_i = 0.18 µM, comparable to wild type *h*APT2 (K_i = 0.12 µM). In this thesis, the double mutant *h*APT1 I75L R149H was already sufficient to

obtain an equivalent result.

Won *et al.* also tried to switch *h*APT2 to *h*APT1 in terms of inhibitor selectivity. As also shown in this thesis, the single mutation of H152R in *h*APT2 leads to a loss of affinity to the isoform 2 specific inhibitor ML349 (K_i = 0.66 µM, this thesis K_i = 0.40 µM) compared to the wild type (K_i = 0.12 µM, this thesis K_i = 0.05 µM). The single L78I mutation, as already seen for the ML348 inhibitor, has a much greater influence on ML349 binding: *h*APT2 L78I does not significantly bind ML349 anymore (K_i > 10 µM, this thesis K_i = 7.4 µM) but shows an increased affinity to ML348 (K_i = 5.8 µM, this thesis K_i = 1.7 µM). Interestingly, in this thesis the mutant *h*APT2 L78I is not loosing as much affinity to ML349 as demonstrated by Won *et al.,* but simultaneously shows a stronger increase in affinity to ML348 compared to the published data. This difference could have various reasons: For instance, the used substrates show a different chain length of their lipidic moiety: OPTS, which was used in this thesis, contains an octanoyl moiety that will reach much deeper into the binding tunnel than the acetate of resorufin acetate (ResOAc) and is probably able to recognize alternative binding modes of the inhibitors inside the binding tunnel that are not discovered using the ResOAc substrate. Won and coworkers again reached a total swap in inhibitor selectivity using a *h*APT2 mutant containing the six mutations L78I, A85S, P86Q, H152R, R153A and A154S (K_i(ML348) = 0.43 µM, K_i(ML349) > 10 µM). Like with *h*APT1, in this work already a double mutant (*h*APT2 L78I H152R) was sufficient to obtain a similar result for ML348 (K_i = 0.13 µM) but not entirely for ML349 (K_i = 1 µM).

To summarize the above, results of Won *et al.* are generally in very good accordance with the findings presented in this thesis. The more precise result of this thesis indicates that only two amino acids, instead of the reported six, are really critical in binding of both isoform specific inhibitors. The fact that mutation of only two amino acids in the binding tunnel of APT does not only almost abolish the binding to an inhibitor, but in fact entirely swap the binding characteristics of the proteins, strongly implies that these residues are key features of each isoform. Furthermore, these selectivity sites are well conserved within both isoforms as shown by a sequence alignment (see figure 6.8).

4.3.2.1 The role of the two selectivity sites in interaction with natural substrates

In contrast to 2-BP, no phenotypic changes of living cells could be detected upon treatment with ML348 or ML349 [95]. However, the inhibitors were not applied together, so that the other APT might have taken over. A siRNA based dual knock down of APT1 and APT2 in N-Ras mutant melanoma cells did not down-regulate N-Ras signaling or decrease cell viability, but only knock down (insufficient) 50 % of each APT1 and APT2 [95].Yeast cells that lack the APT1 gene did not show any abnormalities in

growth and viability [61]. These findings either indicate that protein depalmitoylation in general might not be the main function of APT proteins but rather a side activity or one of many abilities, or that there is a redundant thioesterase function in cells that can compensate for the loss of APTs, like the proposed ABHD17 proteins [76]. Thus, the assignment of specific physiological roles to APT and its isoforms is still ongoing. As the results of the aforementioned inhibitor studies using ML348 and ML349 showed, the amino acids at two positions in the binding tunnel of *h*APT1 and *h*APT2 seem to characterize the binding tunnel of each isoform, thus probably also influencing the binding of natural substrates and leading to a difference in isoform selectivity. As already discussed before, a discrimination of binding of linear palmitoyl moieties inside the binding tunnel seems to be unlikely, thus, a specificity for substrates containing a long linear aliphatic chain has to be achieved via interactions outside the binding tunnel. A substrate selectivity that is achieved inside the binding tunnel seems conceivable only if sterically more demanding substrates are considered, that are sensitive to the characteristic shape of the binding tunnel.

The work of *Manna et al.* proposed *h*APT2 as the major prostaglandin glycerol ester (PG-G) hydrolase in human cancer cells and thus suggested a quite different function for *h*APT2 [73]. In contrast, *h*APT1 was claimed to be unable to hydrolyze PGE_2-G and other PG-G's. This is an interesting observation, but in the study this result could not be substantiated due to the lack of structural information. To get this evidence explaining the described substrate specificity, Dr. Ingrid Vetter performed a molecular docking based on the *h*APT2–2BP structure, since no co-crystal structure of APT2 and a prostaglandin glycerol ester is available so far. Although the docking considers the protein as a static unit and only the ligand as a flexible object, thus neglecting the important adaption and movement of the lid loop, the prostaglandin glycerol ester PGE_2-G could be reasonably placed into the binding tunnel of *h*APT2 as shown in figure 4.2A and B. When superimposing the result of the molecular docking with a *h*APT1 structure, an interesting feature could be identified: In both structures, *h*APT1 and *h*APT2, a pocket next to the binding tunnel is obvious, reaching into the core of the protein (figure 4.2). Interestingly, this pocket is much wider in *h*APT2 (figure 4.2B) than in *h*APT1 (figure 4.2C) and allows an appropriate placement of the cyclopentyl moiety of PGE_2-G only in *h*APT2, while the docking in *h*APT1 leads to severe clashes with the PGE_2-G. Furthermore, it seems that Leu78 of *h*APT2 is significantly contributing to the wider shape of this pocket, while Ile75 present in *h*APT1 seems to narrow the available space in this additional cavity, thereby perhaps impeding a binding of PGE_2-G. This result indicates that Ile75/Leu78 may be not only important for binding of the artificial inhibitors but could also serve as a selectivity site for bulky natural substrates.

As mentioned before (figure 4.1), the amino acids at the second identified selectivity

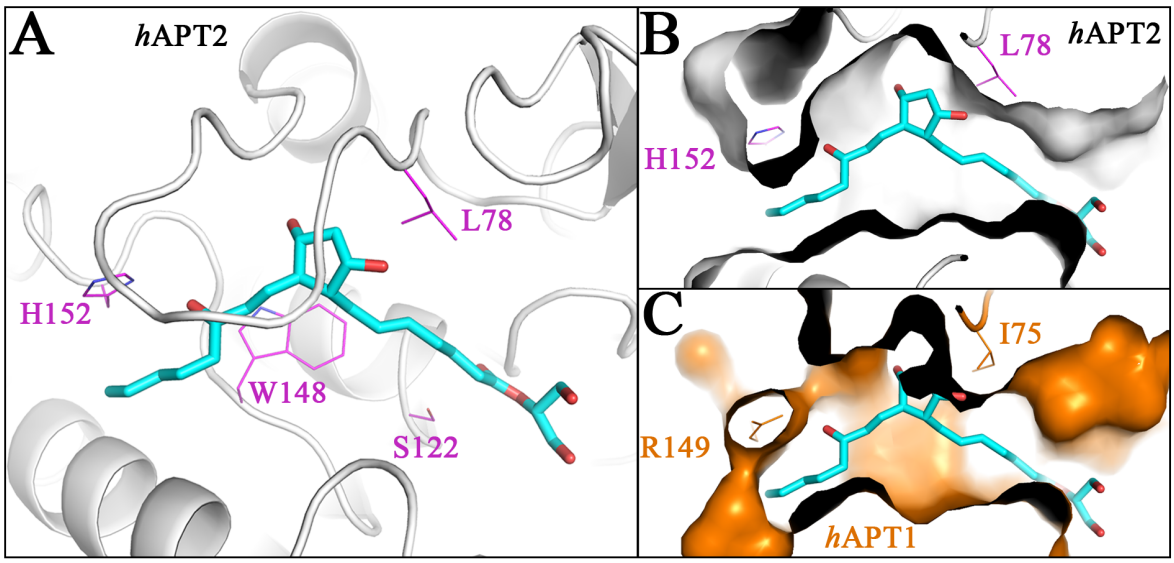

Figure 4.2: Molecular docking of a prostaglandin glycerol ester to *h*APT2 and superimposition with *h*APT1. (A) and (B) show the result of molecular docking of the prostaglandin glycerol ester PGE_2-G to *h*APT2. In (A) the protein is colored in grey and shown in cartoon style, selected side chains are represented as magenta lines and the ligand as cyan sticks. (B) shows the surface of the protein in grey and emphasizes the embedding of the ligand in the binding tunnel. (C) The structure of *h*APT1 was superimposed to the obtained structure from the docking. The orange surface and the shown amino acid side chains belong to *h*APT1. A steric clash of Ile75 with the PGE_2-G molecule is visible. The molecular docking was performed by Dr. Ingrid Vetter using the program GOLD by the Cambridge Crystallographic Data Centre (CCDC) [133]–[135].

site Arg149/His152 in *h*APT1 and *h*APT2, respectively, might have an influence on the flexibility of the lid loop and thus probably also on the binding of the ligand into the tunnel. If an arginine is present at the exit of the binding tunnel, like Arg149 in *h*APT1, an electrostatic interaction to the lid loop could stabilize the structure leading to a more rigid loop. In contrast, if a histidine is present, like His152 in *h*APT2, at most only a weak interaction is possible, potentially allowing the loop to be more flexible. This consideration would also fit to the preference of *h*APT2 for bulky substrates like PGE_2-G, whose binding would be favored by a more open or adjustable lid loop and impeded if attractive interactions, e.g. Arg149–lid loop in *h*APT1, have to be sacrificed.

4.4 Identification and classification of APT proteins

Because of the lack of knowledge about the specific functions of APT1 and APT2, the annotation of proteins as Acyl Protein Thioesterases by functional aspects appears challenging. Currently, proteins are described as APT according to their amino acid identity found in sequence alignments. A closer look into databases quickly reveals the limitation of identifying APTs this way, since there are also many quite similar non-APT proteins. *h*APT1 for instance shares 36 % of the amino acid sequence with the

carboxylesterase PA3859 from *Pseudomonas aeruginosa* (see section 1.2.3) and 33 % with Lysophospholipase-like1 (LYPLAL1), a protein with a very similar (known) 3D structure but described to be unable to hydrolyze palmitoylated proteins because its active site is located next to a shallow groove instead of a long hydrophobic binding tunnel that cannot accommodate the long aliphatic moiety [65] (see also section 1.2.2). On the other hand, a similar level of sequence identity of 37 % can be found between *h*APT1 and the supposed orthologue found in yeast (34 % to *h*APT2). Thus, identification of APT proteins especially in lower organisms does not seem to be reliable if solely based on the overall sequence identity. Furthermore, in practically all higher eukaryotic organisms actually two APT isoforms can be found sharing a very high sequence identity, for instance 64 % in human cells. Thus, also the classification of identified APT proteins as isoform 1 or isoform 2 appears challenging. For instance, a sequence alignment of the single APT orthologue found in *D. melanogaster* reveals 54 % identity to *h*APT1 and 52 % to *h*APT2. Therefore, annotation of APT isoforms based on a simple sequence alignment is only possible in closely related higher eukaryotic organisms where the conservation is sufficiently high. In lower organisms that provide only a single APT protein, it is unclear if these proteins are more similar to APT1 or APT2 or if they are APTs at all. Further steps back in evolution lead to problems of distinguishing APT proteins even from closely related carboxylesterases. Interestingly, the cysteine residue at position 2, that was described to be palmitoylated in *h*APT [74] , appears together with the evolution of the second APT isoform in deuterostomia, while not present in protostomia, although protein palmitoylation is a known post-translational modification in these organisms (see alignment in figure 6.8).

4.4.1 New criteria to identify and classify APT proteins

Therefore, other criteria have to be considered to define an Acyl Protein Thioesterase as such, and to allow their isoform classification. In a first step structural information can be used additionally to primary amino acid sequence analysis. Comparison of the three dimensional structure of APT proteins revealed their unique feature, a solvent accessible, hydrophobic tunnel that spans the entire protein. As mentioned in section 1.2.3, this preformed substrate binding tunnel of APT proteins has not been described for any other member of the α,β-hydrolase family and clearly distinguishes APTs from lipases and carboxylesterases. Lipases are usually interfacially activated and own a huge lid loop structure that covers the hydrophobic active site and is inserted in different topological elements of the regular α,β-hydrolase fold [145] , while in APT proteins the lid loop is always formed by an insertion between canonical sheet β4 and helix αB (figure 1.5). Carboxylesterases lack a binding tunnel and show a shallow binding groove instead, which is completely solvent-exposed (figure 1.6). In all crystal

structures available in our group, APT proteins containing an open binding tunnel also showed a tryptophan inside, that forms one "wall" of the tunnel, while proteins without a proper tunnel (e.g. *y*APT and LYPLAL1) are lacking this amino acid at that position. Given this strong correlation, an APT identification without available structural information could be possible by checking the sequence for the presence of a tryptophan corresponding to the position inside the binding tunnel, i.e. Trp145 in *h*APT1 and Trp148 in *h*APT2. Furthermore, the amino acids at the two selectivity sites (Ile75/Leu78 and Arg149/His152 in *h*APT1 and *h*APT2, respectively) that were identified to characterize the tunnel shape of *h*APT1 and *h*APT2 (section 3.3.2) could also be used for the further classification of identified APT proteins as APT1- or APT2-like, depending on the amino acid present at the particular selectivity site as described in the following.

4.4.1.1 Characterization of predicted APT proteins from different species

The classification APTs of higher eukaryotes that show two APT isoforms like *Mus musculus, Xenopus tropicalis* or *Danio rerio* is straight forward, as expected. As depicted in the sequence alignment (figure 6.8) all indicated APT1 isoforms match the three specifications of an APT1: First, an isoleucine at selectivity site 1, second, an arginine at selectivity site 2 and third, a tryptophan residue at the corresponding site in the supposed binding tunnel (*dr*APT1 shows a 30 amino acid truncation probably due to wrong sequencing). Also the APT2 isoforms of these species match all characteristics of an APT2 protein: First, a leucine at selectivity site 1, second, a histidine at selectivity site 2 and third, a tryptophan residue at the corresponding site in the supposed binding tunnel. This theoretical classification is supported by the results obtained in this thesis (*xt*APT1 and *xt*APT2 are only inhibited by the corresponding isoform selective inhibitor) and by structural data from a previous thesis (*xt*APT1, *xt*APT2 and *dr*APT2 show an open binding tunnel [87]).

Insects like *Drosophila melanogaster* (*dm*APT) and *Bombyx mori* (*bm*APT) show only one APT protein. A sequence alignment using BLAST [146] revealed an identity of 52 % to both human APTs for *bm*APT, while the sequence of *dm*APT is slightly more similar to *h*APT1 (54 %) than to *h*APT2 (52 %). Applying the aforementioned criteria to the APTs from both insects, both APTs would clearly be classified as APT2: Both show the characteristic amino acids of an APT2 at both selectivity sites and a tryptophan residue at the corresponding site in the supposed binding tunnel (figure 6.8). The result for *dm*APT can be confirmed by the experiments shown in this thesis: *dm*APT is able to convert OPTS with an efficiency between APT1 and APT2 proteins (table 3.2), is able to produce a clear zone in the agar-based turbidity assay comparable to human APTs (figure 3.21), shows a low micromolar affinity to 2-BP similar to APT2 proteins (table 3.6) and is, most strikingly, much better inhibited in its activity by the

isoform 2 selective inhibitor ML349 (K_i = 0.56 µM) than by the isoform 1 selective ML348 (K_i > 20 µM). Furthermore, an open binding tunnel can be confirmed for *dm*APT [87]. This observation for the APTs of only two representatives of insects seems to be true for the whole class of these invertebrates: A sequence alignment (performed by Dr. Ingrid Vetter) of all APT-similar proteins in insects available in the UniProt [147] database revealed that all putative APTs show practically only the characteristics of an APT2 isoform.

The APT identified via a BLAST [146] search (50 % identity to *h*APT1, 45 % to *h*APT2) in *Caenorhabditis elegans* seems to be a borderline case. While the leucine at the first selectivity site would argue for a closer relation to the APT2 isoform, the second selectivity site shows the arginine residue of an APT1 isoform, and lastly, the tunnel-tryptophan is replaced by a phenylalanine (see alignment in figure 6.8), which might coincide with differences in the tunnel shape according to the criteria set above. A phenylalanine that could block the binding tunnel, like Phe81 in *y*APT, is not present. Thus, structural information and inhibition studies using ML348/ML349 could reveal the power and also the limits of the proposed hypothesis of identification and classification.

4.4.1.2 Characterization of APTs from protozoa and fungi

Similar to the *C. elegans* case, the APT homologue identified in *Toxoplasma gondii* [148] (*tg*APT) seems to be a borderline case. The sequence alignment (figure 6.8) shows an isoleucine at the first selectivity site close to the active site (APT1 like) but an alanine at the second site at the tunnel exit, so a proper isoform-classification is difficult. At least a tryptophan is present at the canonical site of the substrate-binding tunnel indicating a preformed tunnel and indeed, the crystal structure solved in our group (unpublished result) confirms a preformed, open binding tunnel for this protein and, additionally, an activity assay using pNP-palmitate as substrate revealed a comparable enzymatic activity to *h*APT1 [148]. This indicates that the feature of a preformed, open binding tunnel was already present at a quite early stage of eukaryotes. If *tg*APT and APTs from higher organisms share a similar role within the cells is unclear, especially because in contrast to all other APTs described in this thesis, the toxoplasma homologue shows a highly charged, 38 aa long insert region a few residues after the supposed second selectivity site that is disordered in the X-ray structure and of unknown function. Thus, further investigations concerning the role of the charged regions and inhibition studies using ML348 and ML349 might reveal if this protein is really functionally related to APT proteins from higher organisms.

Following the postulated criteria, the APT-family assignment of *y*APT from *Saccharomyces cerevisiae* has to be re-evaluated. According to the sequence alignment with other APTs (figure 6.8), indeed an isoleucine can be found at the selectivity site

at the tunnel-entrance, but neither an arginine nor histidine can be found at the second selectivity site, nor is a tryptophan present in the supposed binding tunnel region. In addition, the lid loop of *y*APT and *kl*APT (figure 6.8) has an insertion of one residue that changes the conformation of the loop and enables insertion of a phenylalanine into the tunnel. Furthermore, the *y*APT behaved in an unusual way in several assays presented in this thesis: It is neither significantly inhibited by one of the isoform-specific inhibitors, nor does it bind 2-BP. Additionally, it shows a much weaker affinity to palmitoylated peptides and hydrolyzes (lyso-)phospholipids in the egg yolk assay much slower than the other tested APTs. In all *y*APT structures solved in our group, the side chain of Phe81 located in the lid-loop is always rotated into the binding tunnel, thereby shortening it tremendously. This obviously does not allow, for instance, the lipidic tail of palmostatin M to bind into the tunnel as seen in the structure of the covalent complex (figure 3.19). Together with the relatively fast hydrolysis of the short OPTS substrate (table 3.2) and the even faster hydrolysis of acetate esters [87] these data imply that the described APT from yeast seems to be closer related to carboxylesterases than to Acyl Protein Thioesterases from higher organisms, assigning the potential role as an ancestor of the vertebrate APTs to *y*APT. To test this hypothesis *y*APT versions lacking the Phe81 residue will be investigated in upcoming experiments. This mutant presumably features an open binding tunnel that should enable binding of 2-BP, for instance. Furthermore, Trp77, like Phe81 located in the lid loop and not present in all other tested APTs, could serve as a "gatekeeper" residue selecting appropriate substrates. Upon introduction of the W77A mutation into *y*APT the hydrolysis of (lyso-)phospholipids was increased in the agar–based turbidity assay. This result implies that Trp77 could prevent an efficient hydrolysis of branched, poly-lipidated residues like phospholipids. On the other hand, the bulky side chain of Trp77 might also promote the rate of hydrolysis of mono-lipidated substrates like OPTS by supporting a more efficient arrangement of the ligand at the active site, resulting in the observed fast hydrolysis of OPTS by *y*APT compared to the other tested APTs (table 3.2). A significantly more efficient arrangement due to attractive π-π stacking interactions of the pyrene moiety of OPTS and the aromatic side chain of Trp77 seems unlikely because *y*APT was already be identified to be faster than other APTs on short-chained pNP substrates that do not contain a huge aromatic head group [87] .

Thus, also the identification of other fungal "APT" proteins appears challenging, like, for example, the proteins of the fungi *Kluyveromyces lactis* (*kl*APT) and *Schizosaccharomyces pombe* (*sp*APT) that were found by a BLAST [146] search based on the sequence similarity to *h*APT. *kl*APT shows 35 % sequence identity to *h*APT1 and 32 % to *h*APT2, *sp*APT shows 40 % sequence identity to both *h*APT. Both fungal APT show the same features as *y*APT regarding the amino acids at the three crucial positions: At the first selectivity site an isoleucine is present and the tryptophan in

the binding tunnel is replaced by an phenylalanine, like in the case of *y*APT. At the second selectivity site at the tunnel exit an appropriate (Arg or His) residue is lacking (see sequence alignment in figure 6.8). In contrast to *y*APT, both *kl*APT and *sp*APT do not show a phenylalanine, like Phe81 in *y*APT, in their lid loop and only *kl*APT has a tryptophan, like Trp77 in *y*APT, at the proposed position close to the active site. Still, comparison of homology models of several fungi-APTs of the UniProt [147] performed by Dr. Ingrid Vetter, showed no significant conservation of the amino acids at the critical positions. Furthermore, almost all APT-related fungal proteins show an insertion in the lid loop and/or a sterically demanding amino acid at equivalent positions to Phe81 in *y*APT, indicating a closed binding tunnel for both cases, thus, an activity on esters with long aliphatic chains is questionable.

Based on the results of this thesis it seems plausible that APT homologs identified in lower eukaryotic species like fungi and protozoa might indeed be ancestors of human APT proteins, because of the relatively high sequence identity larger than 30 % to *h*APT1 and *h*APT2. But the functional roles of these proteins might have specialized during evolution. The development of an open substrate-binding tunnel has created proteins with a better binding site for longer chained substrates. Along with this, also other modifications occurred, like the loss of the tryptophan in the lid loop, present for instance in *S.cerevisiae* and *K.lactis*. The remarkable similarity of APT homologs from *Bombyx mori* and *Drosophila melanogaster* to *h*APT2 might point to an early formation of isoform 2 APTs from the precursor proteins found in fungi. In higher organisms APT1 emerged probably via a gene-duplication event, a protein still very similar to APT2 in today's vertebrates. Because of the very similar 3D structure, APT1 and APT2 will share many substrates, but single amino acid differences have been shown to alter the affinities to e.g. palmitoylated peptides, and they might significantly change the affinity to special molecules, like prostaglandins, thus leading to a substrate specificity between the two APT isoforms.

5 Materials and Methods

5.1 Materials

5.1.1 Chemicals and Reagents

Unless otherwise stated, buffer ingredients and chemicals were obtained in the highest available purity from Sigma-Aldrich (St. Louis, USA) Carl Roth (Karlsruhe, Germany), VWR Chemicals (Radnor, USA) or AppliChem (Darmstadt, Germany).

Crystallization screens were obtained from Qiagen (Hilden) and aliquoted by Georg Holtermann using a Lissy liquid handling robot (Zinsser Analytics, Frankfurt). Compound ML348 was received from TimTec LLC, Newark, USA and ML349 from Tocris Bioscience, Bristol, UK. The fluorescent substrate 8-octanoyloxypyrene-1,3,6-trisulfonic acid trisodium salt (OPTS) was obtained from Sigma-Aldrich (St. Louis, USA) and the cleavage product 8-hydroxypyrene-1,3,6-trisulfonic acid trisodium salt (HPTS) from Santa Cruz Biotechnology, Dallas, USA.

5.1.2 Kits

The following commercially available kits were used in this thesis.

Table 5.1: Used commercial kits.

Kit	Supplier
QIAprep Spin Miniprep Kit	Qiagen (Hilden, Germany)
Roti-Prep Plasmid MINI	Carl Roth (Karlsruhe, Germany)

5.1.3 Bacterial strains and media

The *Escherichia coli* strain DH5α F- φ80dlacZΔM15 Δ(lacZYA-argF) U169 recA1 endA1 λ- hsdR12(rK-, mK+) supE44, thi-1 gyrA, relA1 was used for transformations, the strains BL21 (DE3) codon+ RIL E. coli B F– dcm ompT hsdS(rB– mB–) gal λ(DE3) and for protein expression.

The used media for bacterial culturing were kindly provided by the media kitchen facility at MPI Dortmund.

Table 5.2: Used media for bacterial culturing.

Medium	Ingredients
Luria Bertani (LB)	10 g/L Bacto tryptone 5 g/L yeast extract 10 g/L NaCl
LB agarose plates	LB-medium 1.5% agarose

5.1.4 Software

Following programs were used for data analysis, figure preparation and creation of this thesis.

Table 5.3: Used software.

Software (Version)	Supplier \ Developers
CCP4i package (6.5.000)	CCP4
ChemBioDraw Ultra (13.0.2.3020)	PerkinElmer
ClustalX (2)	UCD Dublin (D.G. Higgins and P.M Sharp)
Coot (0.8.2)	P. Emsley, B. Lohkamp, W. G. Scott, K. Cowtan
Excel (14.7.3)	Microsoft
Illustrator CS 5.1 (15.1.0)	Adobe Systems
LigPlot+ (1.4.5)	EMBL-EBI (Andrew Wallace and Roman Laskowski)
Lyx (2.2.2)	The LyX Project
Photoshop CS 5.1 (12.1)	Adobe Systems
Prism (6.0h)	Graphpad
PyMOL (1.6.0.0)	Schrödinger LLC

5.1.5 Buffers

Any buffers and solutions that were used are listed and described with the corresponding method.

5.1.6 Machines

The following machines were used during this thesis:

Table 5.4: Machines used in this thesis.

Machine	Manufacturer
Balances	Satorius (Göttingen, Germany)
BioPhotometer	Eppendorf (Hamburg, Germany)
Centrifuges	Beckmann (Münster, Germany) Eppendorf (Hamburg, Germany)
ChemiDoc MP Imaging System	BioRad (Munich, Germany)
CLARIOstar microplate reader	BMG LABTECH (Ortenberg, Germany)
DNA electrophoresis chambers	BioRad (Munich, Germany)
FPLC (Gradifrac systems)	Pharmacia (Stockholm, Sweden)
J-815 CD spectrometer	Jasco (Tokio, Japan)
Liquidator96	Steinbrenner (Wiesenbach)
Magnetic stirrer RCT basic	Eppendorf (Hamburg, Germany)
MAR345 Image Plate Detector	X-Ray Research (Norderstedt, Germany)
MicroMax-007HF rotating anode	Rigaku (Ettlingen, Germany)
Microplate reader Infinite M200 PRO	Tecan (Männedorf, Switzerland)
Microplate reader Safire 2	Tecan (Männedorf, Switzerland)
MicroStar Rotating Anode	Bruker (Billerica, USA)
Mosquito crystal	TTPLabtech (Melbourn, UK)
PAGE chambers	BioRad (Munich, Germany)
pH meter	Knick (Berlin, Germany)
Pipettes	Gilson (Middleton, USA)
Prometheus NT.48	Nanotemper (Munich, Germany)
Rock Imager 1000	Formulatrix (Bedford, USA)
Sonifier 450	Branson (Dietzenbach, Germany)

5.2 Methods

5.2.1 Cloning, Expression and Purification of proteins

The majority of the proteins that are described and used in this thesis were engineered and purified by our technician Patricia Stege.

APT cDNA from used organisms and isoforms were obtained from ImaGenes GmbH (Berlin, Germany). In order to use the Gateway cloning system (Invitrogen, Ther-

moFisher Scientific, Waltham, USA) used primers for amplification also contained Gateway ATT-sites, as well as the sequence for a PreScission protease cleavage site directly upstream of the start codon of the target gene:

Human APT1: 5‘-GGG GAC AAG TTT GTA CAA AAA AGC AGG CTC CCT GGA AGT GCT GTT TCA GGG CCC GAT GTG CGG CAA TAA CAT G-3‘ and 5‘-GGG GAC CAC TTT GTA CAA GAA AGC TGG GTC TCA ATC AAT TGG AGG TAG GAG-3‘

Human APT1 M6: 5‘-GGG GAC AAG TTT GTA CAA AAA AGC AGG CTC CCT GGA AGT GCT GTT TCA GGG CCC GAT GTC AAC CCC GCT GCC C-3‘ and 5‘-GGG GAC CAC TTT GTA CAA GAA AGC TGG GTC TCA ATC AAT TGG AGG TAG GAG-3’

Human APT2: 5‘-GGG GAC AAG TTT GTA CAA AAA AGC AGG CTC CCT GGA AGT GCT GTT TCA GGG CCC GAT GTG TGG TAA CAC CAT G-3‘ and 5‘-GGG GAC CAC TTT GTA CAA GAA AGC TGG GTC TTA GAC AGG AGG CAG CAG CTT-3‘

Human APT2 M6: 5‘-GGG GAC AAG TTT GTA CAA AAA AGC AGG CTC CCT GGA AGT GCT GTT TCA GGG CCC GAT GTC TGT GCC CCT GCT C-3‘ and 5‘-GGG GAC CAC TTT GTA CAA GAA AGC TGG GTC TTA GAC AGG AGG CAG CAG CTT-3‘

Human APT2 ΔA14: 5’-GGG GAC AAG TTT GTA CAA AAA AGC AGG CTC CCT GGA AGT GCT GTT TCA GGG CCC GGC TGC CAC CGT GTC TGG AG-3’ and 5‘-GGG GAC CAC TTT GTA CAA GAA AGC TGG GTC TTA GAC AGG AGG CAG CAG CTT-3‘

Xenopus tropicalis APT1: 5‘-GGG GAC AAG TTT GTA CAA AAA AGC AGG CTC CCT GGA AGT GCT GTT TCA GGG CCC GAT GTG CGG GAA CAC CAT G-3‘ and 5‘-GGG GAC CAC TTT GTA CAA GAA AGC TGG GTC TCA ATT AAC TGG AGG TAG TTG-3‘

Xenopus tropicalis APT2: 5‘-GGG GAC AAG TTT GTA CAA AAA AGC AGG CTC CCT GGA AGT GCT GTT TCA GGG CCC GAT GTG CGG GAA TAA CAT G-3‘ and 5‘-GGG GAC CAC TTT GTA CAA GAA AGC TGG GTC TTA CAC TCG TGG GAG CAC TTT-3‘

Drosophila melanogaster APT: 5‘-GGG GAC AAG TTT GTA CAA AAA AGC AGG CTC CCT GGA AGT GCT GTT TCA GGG CCC GAT GGC TGC GCC GGT CAT T-3‘ and 5‘-GGG GAC CAC TTT GTA CAA GAA AGC TGG GTC TTA GTT TAC CCA TTT ACT GAT-3’

Saccharomyces cerevisiae APT: 5‘-GGG GAC AAG TTT GTA CAA AAA AGC AGG CTC CCT GGA AGT GCT GTT TCA GGG CCC GAT GAA TGG ACT TAG

AGT T-3‘ and 5’-GGG GAC CAC TTT GTA CAA GAA AGC TGG GTC TCA TGA TGA TAA GCT CTT CTT-3’

Wild-type cDNA was first subcloned into pDONR201 (Invitrogen) entry vector before being introduced to a pGEX-4T-3 (GE Healthcare, Buckinghamshire, United Kingdom) expression vector. All further APT mutations were prepared via site directed mutagenesis using designed primers containing the particular mutations in a PCR reaction.

In crystallization approaches the full length APTs from human showed very often a certain disorder within the crystal and thus anisotropic diffraction patterns. This issue was solved by shorten the construct N-terminally by five amino acids. Since then, these constructs *h*APT1 M6 and hAPT2 M6 were also used by default in all *in vitro* assays. In this thesis both constructs are referred to as *wild type* APTs as they contain the wild type amino acid sequence.

5.2.1.1 Polymerase Chain Reaction (PCR)

Using the technique of polymerase chain reaction (PCR) specific DNA sequences were amplified for sequencing (see 5.2.1.3) or for the use of site directed mutagenesis. For the mutagenesis 30-60 ng DNA template, 0.4 mM primer with the particular mutation, 0.2 µg/µL dNTPs, 4 % DMSO, 1x Pfu reaction buffer (Promega) and 1x Pfu-Polymerase (Promega). The PCR program for the Pfu-polymerase was setup as seen in table 5.5. Later Phusion polymerase (Finnzymes) was used instead of Pfu polymerase. In these approaches the PCR program was adapted to the properties of the enzyme (see table 5.5). To remove the methylated wild type DNA the reaction product was digested with 1 unit of the endonuclease DpnI for 1 h at 37 ˚C after PCR.

Table 5.5: Standard PCR programs for site directed mutagenesis using Pfu- and Phusion-polymerase.

Pfu-polymerase			Phusion-polymerase		
	98 ˚C	3 min		98 ˚C	1 min
30x	98 ˚C	20 s	30x	98 ˚C	30 s
	55 ˚C	1 min		60 ˚C	50 s
	65 ˚C	12 min		72 ˚C	3 min
	65 ˚C	10 min		72 ˚C	10 min
	8 ˚C	∞		8 ˚C	∞

5.2.1.2 Transformation and DNA isolation

2 µL of the DpnI digest product was mixed with 100 µL competent DH5α cells on ice and incubated in the cold for 30 min, followed by a heat-shock at 42 °C for 90 s. 800 µL LB medium was added and the mixture was incubated for 1 h at 37 °C under gentle, continuous shaking. The cells were pelleted by centrifugation for 30 s at 13.000 rpm, the supernatant was discarded apart from 50-100 µL in which the pellet was resuspended and subsequently spread onto a LB-agar plate containing 100 µg/mL ampicillin. Plates were incubated over night at 37 °C. The DNA of 3 mL overnight cultures of mono-colonies grown on the agar plates was isolated by using either the QIAprep Spin Miniprep Kit (Qiagen) or the Roti-Prep Plasmid MINI Kit (Carl Roth), following the manufacturer's instructions.

5.2.1.3 DNA sequencing

The success of all cloning or mutagenesis reactions was verified by DNA sequencing, carried out by the in-house sequencing facility. For sample preparation 500-1000 ng of plasmid DNA sample were mixed with 4 µL sequencing buffer, 10 pmol sequencing primer and 2 µL terminator-mix. ddH_2O was added to reach a final volume of 20 µL and 30 PCR cycles were run, each 96 °C for 10 s, 50 °C for 5 s, 60 °C for 2 min. The amplified DNA of this 20 µL approach was precipitated by adding 80 µL ddH_2O, 10 µL 3 M NaAc and 250 µL 100 % EtOH, followed by a centrifugation step for 10 min at 13.000 rpm. The supernatant was discarded and the DNA pellet resuspended in 320 µL 70 % EtOH, again followed by centrifugation for 10 min at 13.000 rpm. The supernatant was removed carefully and entirely.

5.2.1.4 Protein Expression and Purification

All APT proteins were expressed as N-terminally tagged glutathione-S-transferase (GST) fusion proteins. The correct plasmid DNA was transformed into *Escherichia coli* BL21 Codon + RIL cells. The cells were grown at 25 °C in LB media containing 100 µg/mL ampicillin and 25 µg/mL chloramphenicol using a LEX bioreactor (Harbinger Biotech, Toronto, Canada). 0.1 mM IPTG was added at an $OD_{600} \approx 1$ and the protein was expressed over night at 18 °C. The cells were harvested and and lysed in the presence of 0.1 mM PMSF and DNaseI using sonification. After centrifugation at 25.000 g, 4 °C and for 30 min purification of the proteins from the supernatant and subsequent cleavage of the GST-tag was performed using a Glutathione Sepharose 4 fast flow column (GE Healthcare). While bound to the column the GST-tag was removed from the GST-APT fusion proteins with PreScission protease (GE Healthcare). A buffer solution made of 50 mM Tris-HCl pH 8.0, 150 mM NaCl, 5 % Glycerol and 3 mM β-mercaptoethanol was used for GSH affinity chromatography. After elution

the released APT proteins were concentrated (Amicon Ultra Centrifugal Filter, Merck Millipore, Billerica, USA) and a final size exclusion chromatography using a Sephadex G-75 column (GE Healthcare) was performed to separate APT proteins from PreScission protease and possible other impurities. A solution of 20 mM Tris-HCl pH 8.0, 30 mM NaCl, 1 mM TCEP-HCl was used as gel filtration buffer. Proteins were again concentrated and stored as aliquots at -80 °C. All steps of expression and purification were monitored by coomassie staining of SDS-PAGE gels. Purity of final proteins was $\geq$ 95 % and thus suitable for protein crystallization.

5.2.1.5 SDS-PAGE and Coomassie blue staining

Sodium dodecyl sulfate polyacrylamide gel electrophoresis (SDS-PAGE) was used to evaluate the composition and purity of the different steps of protein purification. Due to the treatment with SDS, all proteins show a constant negative charge distribution, so that the migration speed in an electric field through the polyacrylamide gel is only dependent on the size of the protein. Gels used for SDS-PAGE in this thesis consists of two zones. The upper zone contained 5% (w/v) acrylamide/bisacrylamide in 125 mM Tris/HCl pH 6.8 buffer, the second zone 8-18% (w/v) acrylamide/bisacrylamide and 125 mM Tris/HCl pH 8.8. Both solutions were polymerized by adding 0.1 % (w/v) APS and 0.04 % (w/v) TEMED. The samples were mixed with 5x SDS-PAGE loading buffer (0.25 M Tris-HCl pH 6.8, 15 % (w/v) SDS, 50 % (v/v) glycerol, 25 % (v/v) β-mercaptoethanol, 0.01 % (w/v) bromophenol blue) before loaded to the gel. SDS-PAGE was performed using an anode (20 mM Tris pH 8.8, 1.2 % (v/v) HCl) and cathode buffer (1M Tris pH 8.3, 1 M tricine, 30 mM SDS). After finished separation, the proteins in the gel were stained by coomassie staining (0.2 % (w/v) coomassie brilliant blue G250, 7.5 % (v/v) acetic acid, 50 % (v/v) ethanol) followed by destaining of the gel using 10 % (v/v) acetic acid and ddH_2O.

5.2.1.6 Determination of protein concentration

The absorption of protein solutions at 280 nm, mainly caused by the amino acid tryptophan, was measured using a Nanodrop 1000 Photometer (PeqLab). From this absorption protein concentrations were calculated according to the Lambert-Beer law.

5.2.2 Fluorescence based activity assay

A calibration curve of the fluorescence of the reaction product HPTS was recorded (see figure 6.1) to convert initial slopes into product formation per time unit.

5.2.2.1 Steady-state kinetics

Parameters of steady state kinetics were determined by measuring the release of fluorescent HPTS (8-hydroxypyrene-1,3,6-trisulfonic acid) by hydrolysis of OPTS (8-octanoyloxypyrene-1,3,6-trisulfonic acid trisodium salt, Sigma-Aldrich), LPTS (8-lauroyl oxypyrene-1,3,6-trisulfonic acid, self made) or PPTS (8-palmitoyloxypyrene-1,3,6-trisulfonic acid) in a Tecan Infinite M200 microplate reader using 96-well microplates (Greiner Bio-One, Kremsmünster, Austria). The final enzyme concentration was kept at 5 nM for OPTS and 2 nM for LPTS and 1 nM for PPTS. Serial dilutions of the substrate in DMSO were performed in a V-shaped microplate (Sarstedt, Nümbrecht, Germany) before transfer of 2 µL to the corresponding wells in the final plate and proper mixing with 100 µL assay buffer (100 mM KPO_4, 150 mM NaCl, pH 7.4). After adding the enzyme, the formation of fluorescent HPTS was recorded (λ_{ex} = 415 nm, λ_{em} = 520 nm) at 27 °C subsequently. The reaction mixture was shaken prior to every new time point. The background fluorescence with no enzyme present was subtracted and the reaction rates were determined by linear regression analysis ($R^2 \geq 0.98$) of the initial linear phase of hydrolysis. Experiments were performed in triplicates. K_m and k_{cat} values were obtained by non-linear regression fit of Michaelis-Menten equation

$$\upsilon_0 = \frac{\upsilon_{max}\,[S]}{K_m + [S]} \tag{5.1}$$

parameters υ_0 (initial reaction rate), υ_{max} (maximum reaction rate), $[S]$ (substrate concentration) and K_m (Michaelis constant) to these data using GraphPad Prism version 6.0h.

5.2.2.2 Inhibition studies

For inhibition studies, OPTS substrate concentration was kept at 125 µM, the final enzyme concentration at 5 nM. Inhibitors dissolved in DMSO were serial diluted in a V-shaped microplate (Sarstedt) and 2 µL were transferred to the corresponding wells on the final microplate containing 100 µL substrate solution. Subsequently after enzyme addition the formation of fluorescent HPTS was measured in a Tecan Infinite M200 microplate reader (λ_{ex} = 415 nm, λ_{em} = 520 nm) at 27 °C. The reaction mixture was shaken prior to every new time point. The background fluorescence with no enzyme present was subtracted for each inhibitor concentration respectively and the reaction rate was determined by linear regression analysis ($R^2 \geq 0.98$) of the initial 5 min of hydrolysis. Data were normalized to the reaction rate with no inhibitor present (100 % enzymatic activity) and plotted semi-logarithmically. IC_{50} values of the sigmoidal curve could be obtained by non-linear regression analysis using the equation

$$Y = \frac{100}{1 + 10^{(logIC_{50} - X)\, HillSlope}} \tag{5.2}$$

of GraphPad Prism version 6.0h software, where Y is the percentage of catalytic activity of the enzyme, X the inhibitor concentration, IC_{50} the inhibitor concentration necessary to result in 50 % residual enzyme activity and the $HillSlope$ describes the slope of the sigmoidal curve between both plateaus. Stated K_i values were calculated using the Cheng-Prusoff transformation [149]

$$K_i = \frac{IC_{50}}{1 + \frac{[S]}{K_m}} \tag{5.3}$$

where $[S]$ represents the constant substrate concentration and K_m the determined Michaelis constant for the used protein from steady-state experiments with OPTS. Experiments were performed in triplicates.

For the inhibition experiment using palmitic acid as potential inhibitor, the best possible way of dissolving the fatty acid in assay buffer had to be found. Following the procedure that worked best in my hands, 50 % ethanol in water was added to sodium palmitate to reach a theoretical concentration of 100 mM sodium palmitate. The "solution" was intensively vortexed for 5 min to break big solid particles of the palmitate. Sonication of this solution for 5 min at room temperature lead to a white, more viscous emulsion, which was finally heat up three times for 10 s in a 95 °C heating block, resulting in a clear, single-phase solution. The final concentration of EtOH in the assay was kept constant at 1 %.

5.2.2.3 Inhibition studies at the European Lead Factory (ELF)

For the identification of potential *h*APT2 inhibitors at the ELF, DiFMUO (6,8-difluoro-4-methylumbelliferyl octanoate) was used as an APT substrate (see also section 3.1.1 and figure 3.1). In a black 1536-well microplate (Corning Inc., Corning, USA) 50 nM *h*APT2 was incubated for 30 min in assay buffer (20 mM HEPES pH 7.5, 150 mM NaCl, 0.01% Triton X100) before the compounds at different concentrations were added. After an incubation for 30 min the DiFMUO substrate was added (final concentration 7.5 µM) and the fluorescence readout was performed at room temperature using an EnVision plate reader (λ_{ex} = 355 nm, λ_{em} = 460 nm). The final DMSO concentration was kept at 1 %. Determination of IC_{50}values followed the procedure described in section 5.2.2.2. The K_m values of DiFMUO to APT, necessary for the calculation of corresponding K_i values using the Cheng-Prusoff transformation (see equation 5.3), were determined by Marco Bürger [87] (2.1 ± 0.6 µM for *h*APT1 and 6.1 ± 0.8 µM for *h*APT2).

5.2.3 Intrinsic tryptophan fluorescence based binding assay

Intrinsic tryptophan fluorescence of various proteins (final concentration: 5 µM) in assay buffer was measured in a Tecan Infinite M200 microplate reader in a 96-well microplate (Greiner Bio-One). The excitation wavelength λ_{ex} was always set to 280 nm, while the emission was recorded at the mutant-specific wavelength λ_{em}, that is 334 nm for *h*APT1 wt, 336 nm for *h*APT1 W37F, 324 nm for *h*APT1 W145F and 318 nm for *h*APT1 W37F W145F. Emission spectra for each mutant are attached in figure 6.2. The assay was setup by the transfer of 2 µL of the serial diluted ligand in DMSO to 98 µL assay buffer (100 mM KPO_4, 150 mM NaCl, pH 7.4) in corresponding wells on the microplate and a subsequent proper mixing. 2 µL of protein in assay buffer were added and incubated for 10 min before read-out. Data were normalized to the individual minimum fluorescence expected (quenching effect = 100 %) and resulting curves were analyzed using a modified version of the equation described by Li *et al.* [150] :

$$\%Quen = Off + F_{max}\left\{\frac{\sqrt{(f\,[P_t] + [L_t] + K_d)^2 - 4f\,[P_t][L_t]}}{2f\,[P_t]}\right\} + Ns\,[L_t] \qquad (5.4)$$

$\%Quen$ represents the calculated percentage quenching, Off allows the fit through zero and F_{max} is the maximal amplitude of quenching. The factor f is a parameter that helps to optimize the fit if more or less than one binding site is involved. Included are also the total concentrations of the protein P_t and of the ligand L_t and K_d the apparent dissociation constant. This original equation was supplemented by the term $Ns\,[L_t]$ that corrects for non-specific ligand binding. The whole term emerges from the classical quadratic equation for steady-state equilibrium binding that takes ligand depletion into account.

Determination of the halftime of palmostatin hydrolysis was only possible for those inhibitor concentrations that show both, a stable initial and final plateau. Appropriate curves were chosen and the rate constant K was determined using the fit "Plateau followed by one phase association" that determines the individual starting point of visible hydrolysis before fitting a classical one phase association equation. Halftime was then calculated by $ln2/K$.

$$Y = Y_0 \qquad (5.5)$$

$$Y = Y_0 + (Plateau - Y_0)(1 - e^{-K(X - X_0)}) \qquad (5.6)$$

The first equation will be used when $X < X_0$, the second after X_0 is reached. In this particular case X is the time and X_0 the time when hydrolysis gets visible due to

the fluorescent increase. Y is the fluorescence and Y_0 the value of the initial plateau, when fluorescence is minimal due to quenching by palmostatin M. *Plateau* is the final fluorescence value that will be reached when all palmostatin is hydrolyzed. K is the rate constant of hydrolysis reaction.

5.2.4 Determination of melting points using intrinsic protein fluorescence

For the determination of melting points via the intrinsic protein fluorescence a Prometheus NT.48 (Nanotemper, Munich, Germany) machine was used. 20 µL of a 10 µM protein solution were absorbed into a measuring capillary (nanoDSF Grade Standard Capillaries, Nanotemper). The fluorescence was measured at 330 nm (fluorescence maxima of native protein) and 350 nm (fluorescence maxima of denatured protein) in a temperature range between 20 °C and 90 °C and with a temperature slope of 2 °C/min. The inflection point was determined by the software for both wavelength and for the ratio of fluorescence intensities at 350 nm and 330 nm. For a "easy to read" representation the first deviation was calculated, turning the inflection points to global maxima oder minima of the curve.

5.2.5 Agar-based turbidity assay

An egg yolk of a commercial hen egg was isolated from the white, diluted 1:4 with 0.85 % NaCl buffer and homogenized carefully. The suspension was centrifuged at 3500 rpm for 2 min at 20 °C to separate the insoluble and solid components. The supernatant (buffer A) was aliquoted to new tubes and, if necessary, flash frozen and stored at - 20 °C. For agar preparation, 0.6 % (w/v) agarose was dissolved in 0.05 M NaAc (pH 7.5) in a flask and heated till the boiling point. The hot solution was allowed to cool down to a temperature of 50 °C before 3 % (v/v) buffer A and 1 % (v/v) 0.01 M $CaCl_2$ were added. The cloudy agar solution was poured in 150 mm tissue-culture plates until a thickness of about 5 mm was reached. After the agar hardened completely little holes were cut out using a modified pipette tip. The holes were filled completely with the protein of interest and the lidded plates were incubated overnight at 37 °C. Imaging was done using a ChemiDoc MP Imaging System (BioRad).

5.2.6 Electron spray ionization - Mass spectrometry (ESI-MS)

The enzymatic reaction of APT protein and substrate of desired concentrations was performed in glass vials using 5 mM $(NH_4)_2CO_3$ buffer, pH 7.4. At certain time points a sample of 50 µL of the reaction mixture was mixed with 50 µL MeOH to stop catalysis and simultaneously prepare a proper sample for ESI-MS analysis. 10 µL of

each sample was directly injected into the ESI-MS system without using any column for sample separation. The resulted spectra were analysed using the Xcalibur software (ThermoFisher, Waltham, USA). Because no standard could be established, the peak intensities of at least six samples of each time point were averaged and plottet against the time point they were taken from the reaction.

5.2.7 Circular dichroism (CD) spectroscopy

The phenomenon of circular dichroism (CD) describes the characteristic of chiral molecules to absorb left- and right-circularly polarized light differently. CD is measured as the absorption of left- and right-circularly polarized light and is defined as:

$$\Delta\varepsilon(\lambda) = \varepsilon_L(\lambda) - \varepsilon_R(\lambda) \tag{5.7}$$

where ε_L and ε_R are the extinction coefficients for the left- and right- circularly polarized components at wavelength λ . Commonly CD data are reported as ellipticity (θ) in degrees (deg) which is directly related to absorbance as

$$\theta = 32.98\,\Delta\varepsilon \tag{5.8}$$

The secondary structure of proteins is usually analyzed in the far UV range (below 250 nm), where the peptide-bond contributions dominate the CD spectra in which the two main secondary structures show characteristic bands. Alpha helices are characterized by two negative bands at 222 nm and 208 nm and a positive band at 192 nm, while typical beta sheets generate a negative band at 215 nm and a positive band near 198 nm [151] . Since Acyl Protein Thioesterases are belonging to the protein family of α,β-hydrolases a typical CD-spectrum of the native protein shows a broad negative peak around 210-230 nm.

For experiments shown in this thesis, circular dichroism (CD) data were recorded at a Jasco J-815 spectrometer using a cell with 0.05 cm path length. Ligands dissolved in DMSO were added to the protein in assay buffer (see section 5.2.2.1). The DMSO concentration was always kept at 2 %. Due to absorption of DMSO, unfolding of APT was detected at 228 nm with a heating rate of 2 °C per minute, starting from 20 °C. Before and after determination of melting curves a CD-spectrum from 260-200 nm was recorded. Values of the resulting melting curves were normalized (0 mdeg = 100 % unfolded protein) and the melting temperature (T_m) could be obtained applying the following equation as fit:

$$Y = \frac{(y_n + m_n T) + (y_d + m_d T)e^{(\Delta H_m / R(\frac{1}{T_m} - \frac{1}{T}))}}{1 + e^{(\Delta H_m / R(\frac{1}{T_m} - \frac{1}{T}))}} \tag{5.9}$$

Fitted values are the extrapolated signals at 0 Kelvin of the native (y_n) and denatured (y_d) protein, the curve's slope before (m_n) and after (m_d) denaturation, the folding enthalpy ΔH_m , the gas constant R, the temperature T and T_m, the temperature at which 50 % of the protein is unfolded.

5.2.8 Fluorescence polarization (FP)

The principle of fluorescence anisotropy or fluorescence polarization was used to detect and evaluate peptide-protein interactions. During the measurement the sample is excited with vertically polarized light and the intensity of the parallel ($I_{\parallel}$) and perpendicularly ($I_{\perp}$) emitted light is individually detected. The anisotropy r and the directly convertible polarization P are calculated via

$$r = \frac{I_{\parallel} - I_{\perp}}{I_{\parallel} + 2I_{\perp}} \tag{5.10}$$

$$P = \frac{3r}{2 + r} \tag{5.11}$$

The change of fluorescence anisotropy r with time t is dependent on the rotational correlation time θ, that is again dependent on the viscosity η, the molecular volume V of the fluorescent object and the product of the gas constant R and temperature T. Since the change of viscosity and temperature during the measurement can be neglected, the change of anisotropy is only dependent on the molecular volume of the fluorescent molecule.

$$r(t) = r_0 e^{-t/\theta} \tag{5.12}$$

$$\theta = \frac{\eta V}{RT} \tag{5.13}$$

If the molecular volume of the fluorescent species is increased, for instance upon interaction with a protein, the rotational correlation time is increased too, as well as the resulting anisotropy.

For fluorescence polarization assays 5 µL of the binding partner in FP-buffer (5 mM NH_4CO_3, pH 7.4) were added to 95 µL of the fluorescein labeled peptide in 96-well microplates (Greiner Bio-One). In dose-dependent experiments the dilution of the binding partner was carried out in V-shaped microplates (Sarstedt). Depending on the experiment the readout (λ_{ex}= 470 nm, λ_{em}= 525 nm), using a Tecan Safire 2 or BMG Labtech Clariostar microplate reader, was started subsequently after mixing and fluorescence was tracked over time or the covered plate was incubated for 15 min at room temperature prior to an end-point measurement. The signal gain and the focal height were automatically optimized once and kept constant for all following experiments to

allow comparison of different individual measurements and their parameters, especially of the detected absolute fluorescence intensity.

Vesicles for FP experiments were produced as follows: A solution of 1,2-dioleoyl -sn-glycero-3-phosphocholine (DOPC; Avanti Polar Lipids, Inc., USA) in chloroform was evaporated to dryness, redissolved as a 10 mM solution in FP-buffer and sonicated for 15 min at room temperature. Afterwards 5 cycles of flash-freezing in liquid nitrogen and thawing for 10 min at 37 °C were performed to create DOPC vesicles. After 5 min of sonication the vesicle solution was extruded using a mini-extruder (Avanti Polar Lipids) and a membrane with a pore-size of 0.1 µm. The obtained large, unilamellar vesicles were subsequently used or stored at 4 °C for a maximum period of 2 days. Rate constants from the decrease in polarization could be determined by using the "Two-phase decay" equation of GraphPad Prism 6.0h software:

$$Y = Plateau + S_f\, e^{-K_f\, X} + S_s\, e^{-K_s\, X} \tag{5.14}$$

In this case Y is the measured fluorescence polarization and $Plateau$ the initial Y-value, X represents the time, K_f and K_s are the rate constants and S_f and S_s the spans of the fast and slow phase, respectively. In their definition

$$S_f = (Y_0 - Plateau)\, P_f \cdot 0.01 \tag{5.15}$$

$$S_s = (Y_0 - Plateau)\, (100 - P_f) \cdot 0.01 \tag{5.16}$$

Y_0 is the value of Y at time point 0 and P_f is the fraction of the Y-signal of the fast phase in percent.

5.2.9 Organic synthesis of pyrene based substrates

With great guidance of Philipp Ochtrop and according to literature [100]–[103] two more fluorescent substrates were synthesized, based on the commercially available HPTS.

5.2.9.1 8-lauroyloxypyrene-1,3,6-trisulfonic acid (LPTS)

8-hydroxypyrene-1,3,6-trisulfonic acid trisodium salt (200 mg, 0.31 mmol, 1 eq) was dissolved in 5 mL dry DMF and triethylamine (128 µL, 0.92 mmol, 3 eq) was added under argon atmosphere. After cooling down the reaction to 0 °C lauroyl chloride (213 µL, 0.92 mmol, 3 eq) was added and the mixture was allowed to stir for 15 min at 0 °C. Stirring was continued for 2 more hours at room temperature. Solvent was removed by evaporation and the yellowish solid was washed twice with toluene before extracted with water out of a dichloromethane phase using a separation funnel. The aqueous phase was collected and lyophilized over night. Counter ions were exchanged

to sodium using an ion exchange column (V = 10 mL). Product containing fractions were identified using TLC and fluorescent properties of the compounds under UV-light. Product containing fractions were combined after ion exchange column and lyophilized over night. A reversed phase C18 column was used to separate the product that was afterwards characterized using NMR and high resolution ESI-MS.

HRMS (ESI): *m/z* calculated for $C_{28}H_{31}O_{11}S_3$: 639.10340 [M–H]$^-$; found: 639.10443.

^{1}H-NMR (500 MHz, D_2O): δ= 9.31-9.24 (m, 2H), 9.21 (d, J=9.9 Hz, 2H), 8.59 (s, 1H), 8.53 (d, J=9.3 Hz, 1H), 2.94 (t, J=6.7 Hz, 2H), 2.00-1.81 (m, 2H), 1.30-1.11 (m, 16H), 0.56 (t, J=6.2 Hz, 3H).

5.2.9.2 8-palmitoyloxypyrene-1,3,6-trisulfonic acid (PPTS)

Synthesis, purification and identification of PPTS followed the instructions given for synthesis of LPTS under 5.2.9.1. Following amounts of chemicals were used in this approach: 8-hydroxypyrene-1,3,6-trisulfonic acid trisodium salt (95 mg, 0.15 mmol, 1 eq), triethylamine (100 µL, 0.72 mmol, 5 eq) and palmitoyl chloride (300 µL, 0.99 mmol, 6 eq).

HRMS (ESI): *m/z* calculated for $C_{32}H_{39}O_{11}S_3$: 695.16600 [M–H]$^-$; found: 695.16767.

^{1}H-NMR (400 MHz, D_2O): δ= 9.18-9.08 (m, 3H), 8.98 (d, J=9.8 Hz, 1H), 8.45 (s, 1H), 8.20 (d, J= 9.6 Hz, 1H), 2.75 (t, J= 7.3 Hz, 2H), 1.79-1.69 (m, 2H), 1.34-1.20 (m, 24H), 0.96 (t, J= 6.7 Hz, 3H).

5.2.10 X-ray crystallography

5.2.10.1 Protein crystallization and crystal handling

Highly pure proteins (see 5.2.1.4) with a concentration of 1.0 – 1.5 mM (25 – 40 mg/mL) were used for protein crystallization attempts. The human APT constructs hAPT1 M6 and hAPT2 M6 were used by default for crystallization and are referred to as *wild type* proteins although lacking the first five amino acids (see also section 5.2.1). For cocrystallization approaches ligands dissolved in DMSO were added to the protein solution in a 1.5 – 3 fold molar excess and carefully warmed up to 40 – 45 °C prior to usage in crystallization experiments. Total DMSO concentration was kept below 5 %. The screening for successful crystallization conditions was performed at 20 °C in TTP IQintelli 96-well sitting drop plates (TTP Labtech, Melbourn, UK) using different pre-composed crystallization screens from Qiagen. By default 100 nL of the protein solution or protein-ligand solution were mixed on the plates with 100 nL of mother liquor by a TTP labtech Mosquito pipetting robot. 70 µL of mother liquor were used as reservoir. The crystallization plates were tightly sealed to allow vapor diffusion

between drop and reservoir and crystallization progress was tracked in a Formulatrix Rock Imager.

When screening experiments resulted only in tiny or non-diffracting crystals 24-well refinement plates were setup manually. For this purpose tissue culture plates from Linbro or Crychem were used. The original crystallization condition was recreated with systematic variation in salt or precipitant concentration, pH or other ingredients. In these approaches the method of hanging-drop vapor diffusion was used, so 1 µL of each, the protein and reservoir solution were combined on a glass coverslip that was put upside down over 500 µL reservoir solution in the corresponding well in the refinement plate. Grown crystals were separated using pre-mounted CryoLoops (Hampton). If necessary, crystals were rapidly transferred to a drop of reservoir solution containing additional cryogenic ingredients for couple of seconds before flash frozen in liquid nitrogen.

5.2.10.2 X-ray diffraction data collection

Crystal diffraction was first tested in-house at 100 K using either a Bruker Microstar or a Rigaku Micromax HF-007 rotating anode and mar345 CCD detectors. Test images to evaluate the capability of diffraction and to determine first parameters of crystal packing were recorded with 1 ° rotation and 3 to 5 min exposure time per image.

By default, complete data sets of crystal diffraction were recorded on beamline PXII of the Swiss Light Source (SLS) at the Paul Scherrer Institute (Villigen, Switzerland), in some cases at beamline P11 of PETRA III at Deutsches Elektronen-Synchrotron (DESY, Hamburg, Germany). At synchrotrons crystals were usually tested with a flux of about $3{\cdot}10^{11}$ph/s at a wavelength of 1.0 Å (12.7 keV), 0.25 ° rotation and 0.1 s exposure time per image. If necessary parameters were adjusted, like recording a dataset at a different wavelength to detect anomalous signal for a corresponding element present in a ligand.

5.2.10.3 Data processing

Datasets of diffraction were indexed, integrated and scaled using XDS and XSCALE and converted to .mtz file format by XDSCONV, all part of the XDS program package [152]. All phases for structures shown in this thesis could be obtained by maximum likelihood molecular replacement using PhaserMR [153] from the CCP4i program package [154]. The structure was iteratively refined using refmac5 [155] and coot [156], also part of the CCP4 program package [154].

5.2.10.4 Structure validation and illustration

All structure models were validated by using implemented plugins of coot [156] , like revealing Ramachandran [157] outliers. Furthermore models were uploaded to the validation service of the protein data bank (PDB) [158] . All shown images of crystal structures were generated using PyMOL version 1.6.0.0.

6 Appendices

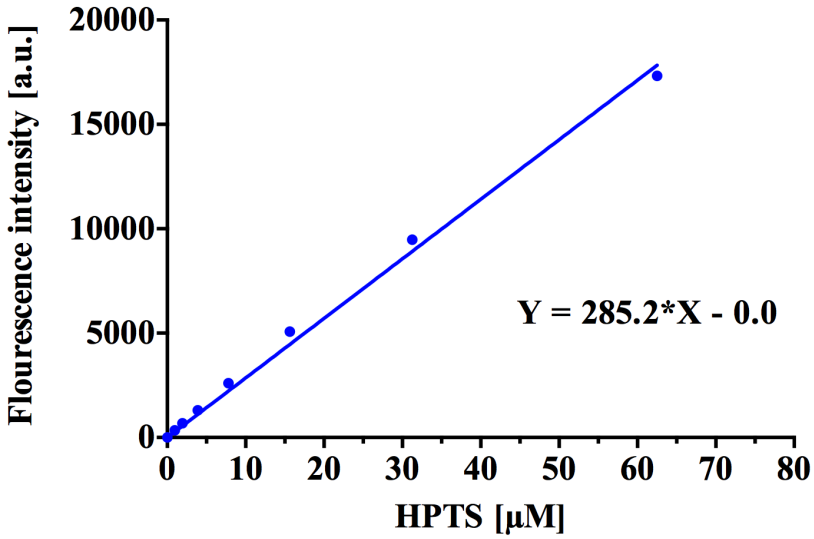

Figure 6.1: Calibration curve of HPTS for conversion of initial slopes to substrate turnover.

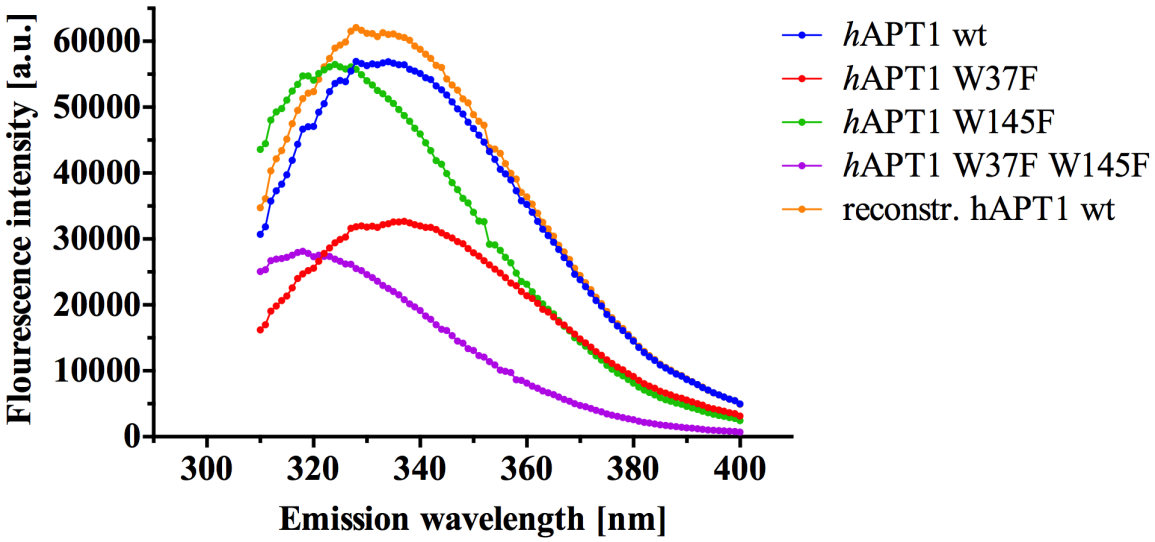

Figure 6.2: Emission spectra of three tryptophan mutants of *h*APT1. Excitation wavelength was 280 nm in all cases. The curve of the reconstructed *h*APT1 wt arised from the addition of the fluorescence from *h*APT1 W37F and *h*APT1 W145F and the subtraction of the fluorescence of the double mutant *h*APT1 W37F W140F, to correct for the double included fluorescence of the third tryptophan W72.

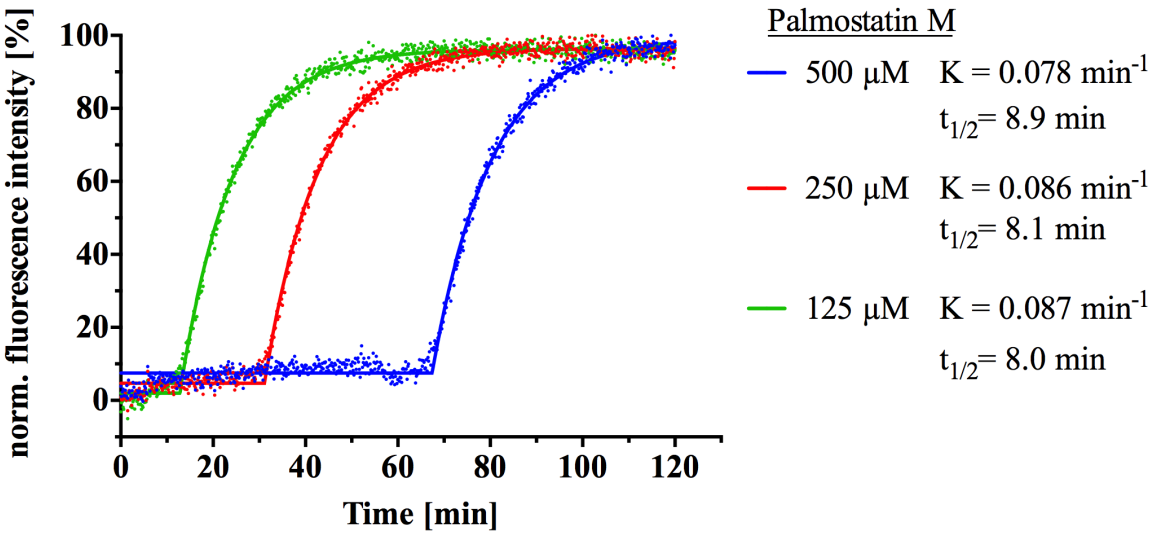

Figure 6.3: Halftime of palmostatin M hydrolysis from *h*APT1. The colored dots represent the normalized measured fluorescence at a certain time. The continuos line shows the result of the corresponding fit (see section 5.2.3). K is the rate of hydrolysis and $t_{1/2}$ the halftime (see methods section 5.2.3).

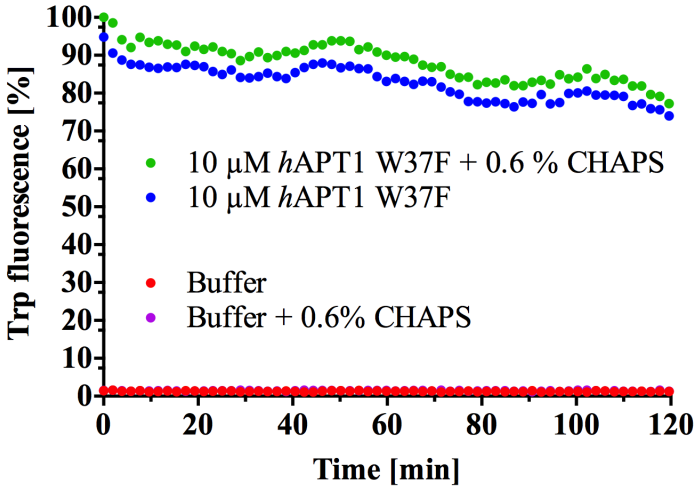

Figure 6.4: *h*APT1 W37F fluorescence is not changed upon addition of 0.6 % CHAPS. Presence of 0.6 % (9.8 mM) of CHAPS detergent is not altering the intrinsic tryptophan fluorescence of *h*APT1 W37F compared to the situation without CHAPS. CHAPS also does not show any auto-fluorescence. The decrease in fluorescence over time (22 % in 120 min) might be a photobleaching effect. Data were normalized to the globally highest fluorescence (= 100 %) and to no fluorescence (= 0 %).

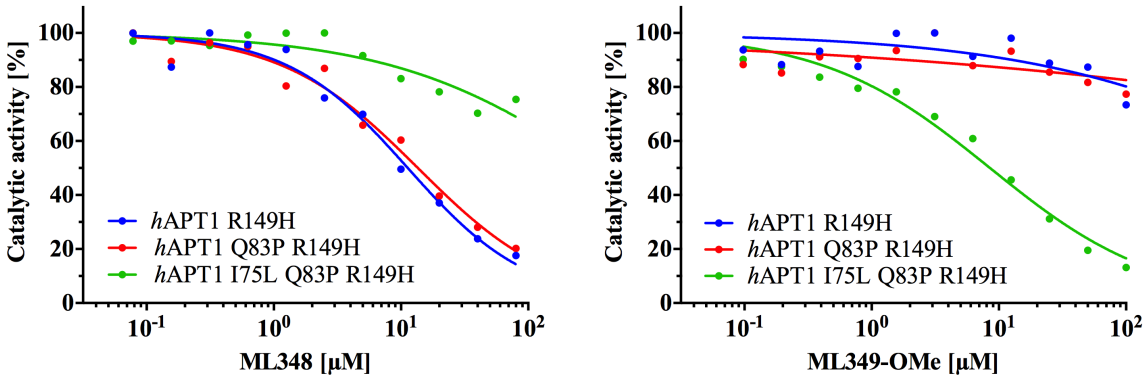

	IC_{50} [µM]	
	ML348	**ML349-OMe**
*h*APT1 R149H	11.3	> 100
*h*APT1 Q83P R149H	13.6	> 100
*h*APT1 I75L Q83P R149H	>100	8.5

Figure 6.5: Comparison of the inhibition of *h*APT1 mutants R149H, Q83P R149H and I75L Q83P R149H by ML348 and ML349-OMe. The inhibition of the three *h*APT1 mutants *h*APT1 R149H, *h*APT1 Q83P R149H and *h*APT1 I75L Q83P R149H by ML348 and ML349-OMe is shown. ML349-OMe is a variant of the published ML349 inhibitor, missing the terminal methoxy moiety (described as compound 4 in [98]). The introduction of the Q83P mutation results in only minor changes of inhibition by ML348 and ML349-OMe, while introduction of the I75L mutation leads to a significant loss in case of ML348 and a significant increase of inhibition in case of ML349-OMe. Because *h*APT1 mutants containing the Q78P mutation were not fully kinetically investigated no K_i values are stated.

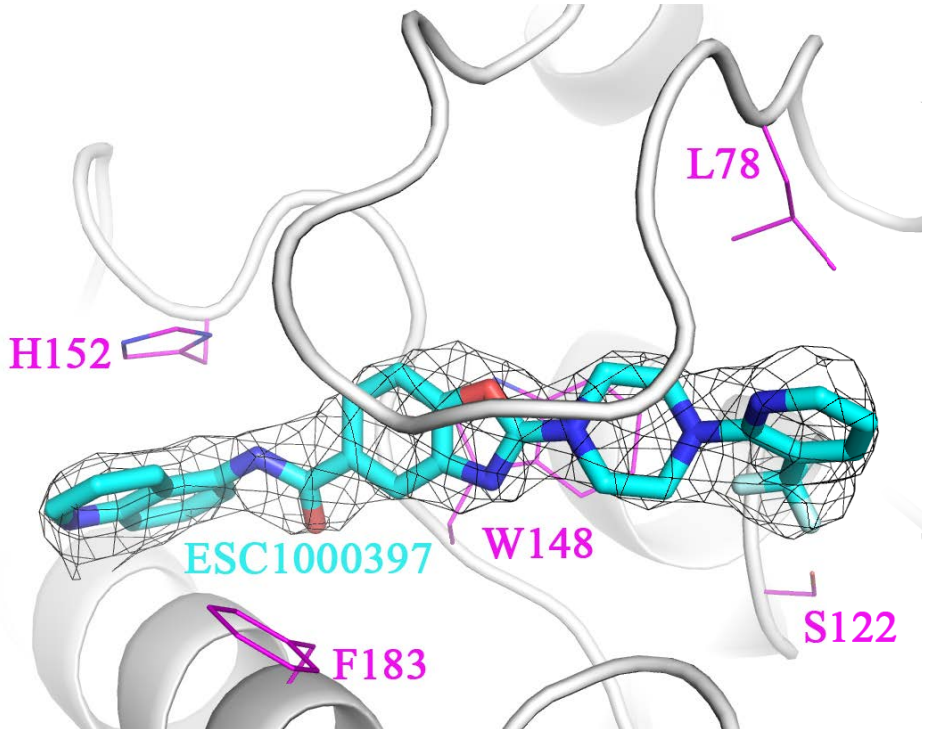

Figure 6.6: ESC1000397 and corresponding electron density in complex with *h*APT2. The protein is shown in cartoon style and colored in grey, selected side chains are shown as lines and highlighted in magenta. The inhibitor ESC1000397 is represented as cyan sticks. The $2F_o$-$F_c$electron density of ESC1000397 contoured to 1 σ is shown as black mesh.

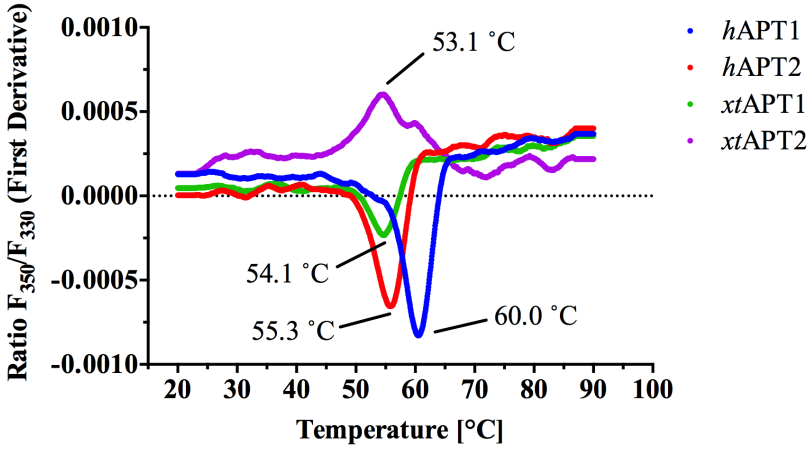

Figure 6.7: Determination of the melting points of *h*APT1, *h*APT2, *xt*APT1 and *xt*APT2. The melting points of the four APT proteins (10 µM, 1 % DMSO) were determined measuring the intrinsic protein fluorescence at 330 nm and 350 nm at different temperature, using a Prometheus NT.48 (Nanotemper, Germany) machine (see methods section 6.7). For the representation the ratio of the first deviations of the fluorescence intensity at 350 nm and 330 nm was calculated and plotted against the temperature. Thus, a maximum or minimum in the curve indicate the inflection point of the actual melting curve (see section 5.2.4 methods for details).

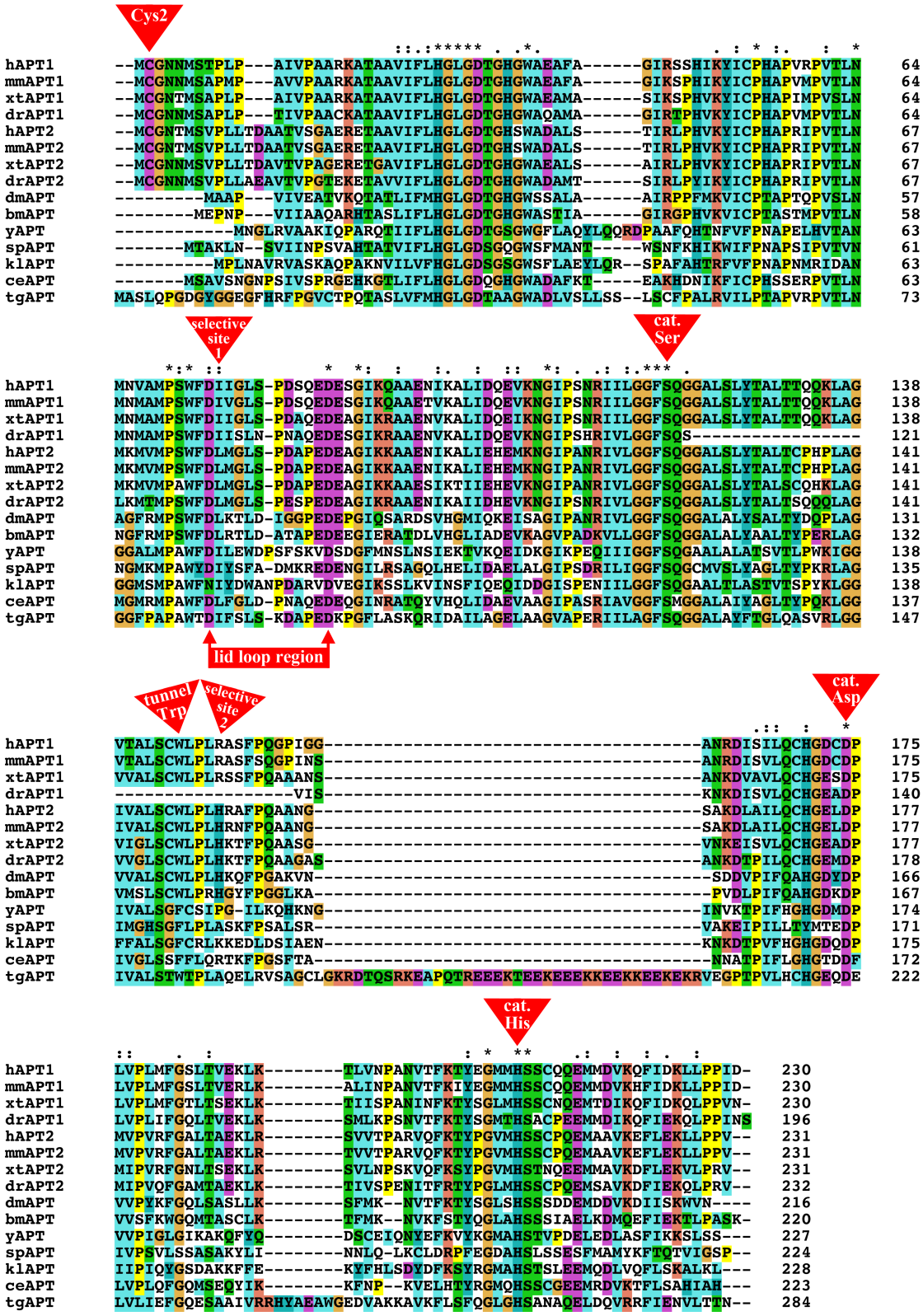

Figure 6.8: Sequence alignment of APT homologues from different species. The conservation of residues is highlighted using the following color scheme: Hydrophobic amino acids are colored blue, positively charged red, negatively charged magenta, polar residues green, glycines orange and prolines yellow. Unconserved parts remain uncolored. The line above the alignment marks either single, fully conserved residues (*), or closely related residues at this position (:) or positions of similar but not closely related residues (.). The numbering corresponds to the last residue of this line. The red arrowheads indicate common, characteristic positions of APT proteins. More information about the aligned proteins and their origins are listed in table 6.1. The sequences were aligned using the software ClustalX [159],[160].

Table 6.1: List of proteins investigated in this thesis and/or used for sequence alignment. Proteins marked with an asterisk (*) were used in functional and/or structural experiments in this thesis. All other listed proteins were used mainly for sequence alignment and in discussions about evolution of APT proteins. The enzymes are listed in the order of their appearance in the sequence alignment (see figure 6.8).

Protein	Organism	Trivial name	NCBI Reference
*h*APT1*	*Homo sapiens*	Human	NP_006321.1
*mm*APT1	*Mus musculus*	Mouse	NP_032892.1
*xt*APT1*	*Xenopus tropicalis*	Clawed frog	NP_001005699.1
*dr*APT1	*Danio rerio*	Zebrafish	NP_001017616.1
*h*APT2*	*Homo sapiens*	Human	NP_009191.1
*mm*APT2	*Mus musculus*	Mouse	NP_036072.1
*xt*APT2*	*Xenopus tropicalis*	Clawed frog	NP_989287.1
*dr*APT2	*Danio rerio*	Zebrafish	NP_957043.1
*dm*APT*	*Drosophila melanogaster*	Fruit fly	NP_652674.1
*bm*APT	*Bombyx mori*	Silk moth	NP_001040255.1
*ce*APT	*Caenorhabditis elegans*	Worm	NP_492213.1
*y*APT*	*Saccharomyces cerevisiae*	(Budding) Yeast	NP_013219.1
*sp*APT	*Schizosaccharomyces pombe*	(Fission) Yeast	NP_594165.1
*kl*APT	*Kluyveromyces lactis*		XP_455883.1
*tg*APT	*Toxoplasma gondii*		AGJ01119

Table 6.2: Crystallographic statistics of the co-crystal structure of *h*APT1 and ML348. Values for the highest shell are given in parentheses.

***h*APT1 + ML348**		
Conditions	Qiagen PEGs Suite, well D4. 0.1 M Sodium HEPES pH 7.5, 25 % (w/v) PEG 8000	
Data collection		
	Space group	$P12_11$
	a, b, c [Å]	74.35, 79.57, 89.46
	α, β, γ [°]	90.000, 90.858, 90.000
	Resolution [Å]	46.66 - 1.39 (1.48 - 1.39)
	I/σI	16.62 (2.92)
	Completeness [%]	99.6 (99.2)
	Redundancy	6.8 (6.5)
	Wavelength [Å]	1.00005
	CC ½	99.9 (84.9)
	Monomers/au	4
Refinement		
	Resolution [Å]	46.66 - 1.7 (1.6 - 1.7)
	No. reflections	114193
	R_{work}	16.4 (23.7)
	R_{free}	20.1 (30.6)
	Number of atoms	
	Protein	6910
	Ligand	116
	Water	1051
	Mean B-factor [Å^2]	25.6
	RMSD	
	Bond lengths [Å]	0.024
	Bond angles [°]	2.29
	Ramachandran plot	
	in favored regions [%]	97.1
	outliers [%]	0.0
	Clashscore	4.93
	Rotamer outlier [%]	1.34
	Molprobity score	1.52

Table 6.3: Crystallographic statistics of the co-crystal structure of *h*APT2 Δ14 and ML349. Values for the highest shell are given in parentheses.

***h*APT2 Δ14 + ML349**		
Conditions	Qiagen PACT Suite, well A4. 0.1 M SPG buffer pH 7, 25% (w/v) PEG 1500	
Data collection		
	Space group	$P12_11$
	a, b, c [Å]	38.49, 74.34, 71.68
	α, β, γ [°]	90.000, 93.854, 90.000
	Resolution [Å]	38.40 - 1.10 (1.17 - 1.10)
	I/σI	12.12 (2.32)
	Completeness [%]	97.3 (93.2)
	Redundancy	6.8 (6.9)
	Wavelength [Å]	0.7749
	CC ½	99.9 (83.7)
	Monomers/au	2
Refinement		
	Resolution [Å]	38.17 - 1.1 (1.2 - 1.1)
	No. reflections	150382
	R_{work}	19.0
	R_{free}	21.7
	Number of atoms	4817
	Protein	4129
	Ligand	177
	Water	511
	Mean B-factor [Å^2]	15.7
	RMSD	
	Bond lengths [Å]	0.03
	Bond angles [°]	2.91
	Ramachandran plot	
	in favored regions [%]	97.8
	outliers [%]	0.2
	Clashscore	21.57
	Rotamer outlier [%]	1.8
	Molprobity score	2.08

Table 6.4: Crystallographic statistics of the co-crystal structure of *h*APT2 and 2-BP. Values for the highest shell are given in parentheses.

***h*APT2 + 2-BP**		
Conditions	Qiagen PEGs Suite, well B4. 0.1 M Sodium HEPES pH 7.5, 25% (v/v) PEG 550 MME	
Data collection		
	Space group	C121
	a, b, c [Å]	77.75, 79.34, 139.02
	α, β, γ [°]	90.00, 93.43, 90.00
	Resolution [Å]	46.27 - 1.58 (1.68 - 1.58)
	I/σI	10.61 (1.58)
	Completeness [%]	99.9 (100.0)
	Redundancy	6.8 (6.8)
	Wavelength [Å]	0.91909
	CC 1/2	99.9 (44.0)
	Monomers/au	4
Refinement		
	Resolution [Å]	46.26 - 1.90 (2.0 - 1.9)
	No. reflections	63134
	R_{work}	20.42
	R_{free}	27.32
	Number of atoms	7159
	Protein	6749
	Ligand	226
	Water	184
	Mean B-factor [Å^2]	40.84
	RMSD	
	Bond lengths [Å]	0.016
	Bond angles [°]	1.919
	Ramachandran plot	
	in favored regions [%]	95
	outliers [%]	0.5
	Clashscore	11.38
	Rotamer outlier [%]	1.66
	Molprobity score	2.09

Table 6.5: Crystallographic statistics of the co-crystal structure of *h*APT1 and 2-BP. Values for the highest shell are given in parentheses.

***h*APT1 + 2-BP**		
Conditions	Qiagen JCSG Core III Suite, well D8. 0.1 M HEPES pH 6.5, 5% (w/v) PEG 6000	
Data collection		
	Space group	$P2_12_12_1$
	a, b, c [Å]	58.81, 109.95, 175.01
	α, β, γ [°]	90.00, 90.00, 90.00
	Resolution [Å]	48.81 - 1.50 (1.59 - 1.50)
	I/σI	18.48 (2.38)
	Completeness [%]	99.9 (100)
	Redundancy	12.9 (11.5)
	Wavelength [Å]	0.9204
	CC ½	99.9 (72.1)
	Monomers/au	4
Refinement		
	Resolution [Å]	48.81 - 2.10 (2.2 - 2.1)
	No. reflections	63734
	R_{work}	19.2
	R_{free}	24.9
	Number of atoms	7256
	Protein	6729
	Ligand	129
	Water	398
	Mean B-factor [Å^2]	31.707
	RMSD	
	Bond lengths [Å]	0.0199
	Bond angles [°]	2.08
	Ramachandran plot	
	in favored regions [%]	96.5
	outliers [%]	0
	Clashscore	7.19
	Rotamer outlier [%]	3.54
	Molprobity score	2.0

Table 6.6: Crystallographic statistics of the co-crystal structure of *h*APT1 R149H and ML348. Values for the highest shell are given in parentheses.

***h*APT1 R149H + ML348**		
Conditions	Qiagen PEGs Suite, well A12. 0.1 M MES pH 6.5, 25% (w/v) PEG 2000 MME	
Data collection		
	Space group	$P12_11$
	a, b, c [Å]	76.930, 55.470, 101.890
	α, β, γ [°]	90.00, 111.77, 90.00
	Resolution [Å]	47.85 - 1.19 (1.27 - 1.19)
	I/σI	10.88 (3.6)
	Completeness [%]	95.9 (92.4)
	Redundancy	3.5 (3.6)
	Wavelength [Å]	1.00004
	CC 1/2	99.4 (93.4)
	Monomers/au	4
Refinement		
	Resolution [Å]	47.31 - 1.50 (1.6 - 1.5)
	No. reflections	116924
	R_{work}	17.6
	R_{free}	21.5
	Number of atoms	7915
	Protein	6938
	Ligand	140
	Water	837
	Mean B-factor [Å^2]	21.897
	RMSD	
	Bond lengths [Å]	0.025
	Bond angles [°]	2.351
	Ramachandran plot	
	in favored regions [%]	96.6
	outliers [%]	0.2
	Clashscore	8.78
	Rotamer outlier [%]	0.79
	Molprobity score	1.69

Table 6.7: Crystallographic statistics of the co-crystal structure of *h*APT1 I75L Q83P R149H and ML348. Values for the highest shell are given in parentheses.

hAPT1 I75L Q83P R149H + ML348

Conditions	Qiagen JCSG Core III Suite, well B1. 0.1 M $MgCl_2$, 0.1 M Tris pH 8.5, 20% (w/v) PEG 8000	
Data collection		
	Space group	P 12_11
	a, b, c [Å]	77.260, 77.840, 90.440
	α, β, γ [°]	90.00, 109.98, 90.00
	Resolution [Å]	47.74 - 1.55 (1.64 - 1.55)
	I/σI	15.58 (2.87)
	Completeness [%]	92.0 (81.1)
	Redundancy	3.4 (3.4)
	Wavelength [Å]	1.5
	CC ½	99.8 (85.3)
	Monomers/au	4
Refinement		
	Resolution [Å]	40.69 - 1.80 (1.70 - 1.80)
	No. reflections	82349
	R_{work}	15.9
	R_{free}	20.4
	Number of atoms	8281
	Protein	7065
	Ligand	113
	Water	1111
	Mean B-factor [Å^2]	20.281
	RMSD	
	Bond lengths [Å]	0.023
	Bond angles [°]	2.125
	Ramachandran plot	
	in favored regions [%]	96.4
	outliers [%]	0
	Clashscore	11.9
	Rotamer outlier [%]	2.81
	Molprobity score	2.17

Table 6.8: Crystallographic statistics of the co-crystal structure of *h*APT2 and ESC1000397. Values for the highest shell are given in parentheses.

hAPT2 + ESC1000397

Conditions	Qiagen JCSG Core III Suite, well E8. 0.2 M Ca-acetate, 0.1 M Na-cacodylate pH 6.5, 18% (w/v) PEG 8000	
Data collection		
	Space group	P $4_2$22
	a, b, c [Å]	56.200, 56.200, 135.330
	α, β, γ [°]	90.00, 90.00, 90.00
	Resolution [Å]	43.53 - 2.15 (2.28 - 2.15)
	I/σI	13.72 (1.90)
	Completeness [%]	99.4 (98.8)
	Redundancy	13.9 (14.0)
	Wavelength [Å]	1.00007
	CC ½	99.8 (82.9)
	Monomers/au	1
Refinement		
	Resolution [Å]	43.23 - 2.30 (2.4 - 2.3)
	No. reflections	10183
	R_{work}	24.7
	R_{free}	30.4
	Number of atoms	1715
	Protein	1663
	Ligand	45
	Water	7
	Mean B-factor [Å^2]	61.369
	RMSD	
	Bond lengths [Å]	0.013
	Bond angles [°]	1.667
	Ramachandran plot	
	in favored regions [%]	95.5
	outliers [%]	0.9
	Clashscore	10.6
	Rotamer outlier [%]	4.55
	Molprobity score	2.36

Table 6.9: Crystallographic statistics of the co-crystal structure of *h*APT2 A14 and ESC1000595. Values for the highest shell are given in parentheses.

hAPT2 A14 + ESC1000595

Conditions	Qiagen PACT Suite, well F1. 0.2 M NaF, 0.1 M Bis Tris propane pH 6.5, 20% (w/v) PEG 3350	
Data collection		
	Space group	P 12_11
	a, b, c [Å]	38.650, 75.830, 71.480
	α, β, γ [°]	90.00, 92.14, 90.00
	Resolution [Å]	10.16 (1.77)
	I/σI	38.61 - 1.40 (1.48 - 1.40)
	Completeness [%]	99.3 (98.2)
	Redundancy	6.5 (6.5)
	Wavelength [Å]	0.99989
	CC ½	99.7 (76.5)
	Monomers/au	2
Refinement		
	Resolution [Å]	38.62 - 1.50 (1.60 -1.50)
	No. reflections	62195
	R_{work}	19.75
	R_{free}	24.75
	Number of atoms	3988
	Protein	3480
	Ligand	432
	Water	76
	Mean B-factor [Å^2]	20.288
	RMSD	
	Bond lengths [Å]	0.023
	Bond angles [°]	2.326
	Ramachandran plot	
	in favored regions [%]	97.4
	outliers [%]	0.2
	Clashscore	9.95
	Rotamer outlier [%]	2.96
	Molprobity score	2.03

References

[1] Milburn, M. V. *et al.* Molecular switch for signal transduction: structural differences between active and inactive forms of protooncogenic ras proteins. *Science* **247**, 939–945 (1990).

[2] Burgering, B. M. & Bos, J. L. Regulation of Ras-mediated signalling: more than one way to skin a cat. *Trends in biochemical sciences* **20**, 18–22 (1995).

[3] Marais, R. & Marshall, C. J. Control of the ERK MAP kinase cascade by Ras and Raf. *Cancer surveys* **27**, 101–125 (1996).

[4] Wennerberg, K., Rossman, K. L. & Der, C. J. The Ras superfamily at a glance. *Journal of cell science* **118**, 843–846 (2005).

[5] Egan, S. E. *et al.* Association of Sos Ras exchange protein with Grb2 is implicated in tyrosine kinase signal transduction and transformation. *Nature* **363**, 45–51 (1993).

[6] Li, N. *et al.* Guanine-nucleotide-releasing factor hSos1 binds to Grb2 and links receptor tyrosine kinases to Ras signalling. *Nature* **363**, 85–88 (1993).

[7] Rozakis-Adcock, M., Fernley, R., Wade, J., Pawson, T. & Bowtell, D. The SH2 and SH3 domains of mammalian Grb2 couple the EGF receptor to the Ras activator mSos1. *Nature* **363**, 83–85 (1993).

[8] Downward, J. Control of ras activation. *Cancer surveys* **27**, 87–100 (1996).

[9] Trahey, M. & McCormick, F. A cytoplasmic protein stimulates normal N-ras p21 GTPase, but does not affect oncogenic mutants. *Science* **238**, 542–545 (1987).

[10] Wittinghofer, A. & Waldmann, H. Ras—A Molecular Switch Involved in Tumor Formation. *Angewandte Chemie* **39**, 4192–4214 (2000).

[11] Fernández-Medarde, A. & Santos, E. Ras in cancer and developmental diseases. *Genes & cancer* **2**, 344–358 (2011).

[12] Barbacid, M. ras GENES. *Annual review of biochemistry* **56**, 779–827 (1987).

[13] Lowy, D. R. & Willumsen, B. M. Function and regulation of ras. *Annual review of biochemistry* **62**, 851–891 (1993).

[14] Harvey, J. J. An Unidentified Virus which causes the Rapid Production of Tumours in Mice. *Nature* **204**, 1104–1105 (1964).

[15] Hall, A., Marshall, C. J., Spurr, N. K. & Weiss, R. A. Identification of transforming gene in two human sarcoma cell lines as a new member of the ras gene family located on chromosome 1. *Nature* **303**, 396–400 (1983).

[16] Kirsten, W. H. & Mayer, L. A. Morphologic Responses to a Murine Erythroblastosis Virus2. *JNCI: Journal of the National Cancer Institute* (1967).

[17] Shimizu, K. *et al.* Structure of the Ki-ras gene of the human lung carcinoma cell line Calu-1. *Nature* **304**, 497–500 (1983).

[18] Eisenberg, S. *et al.* The role of palmitoylation in regulating Ras localization and function. *Biochem. Soc. Trans.* **41**, 79–83 (2013).

[19] Choy, E. *et al.* Endomembrane trafficking of ras: the CAAX motif targets proteins to the ER and Golgi. *Cell* **98**, 69–80 (1999).

[20] Casey, P. J., Solski, P. A., Der, C. J. & Buss, J. E. p21ras is modified by a farnesyl isoprenoid. *Proceedings of the National Academy of Sciences of the United States of America* **86**, 8323–8327 (1989).

[21] Seabra, M. C., Reiss, Y., Casey, P. J., Brown, M. S. & Goldstein, J. L. Protein farnesyltransferase and geranylgeranyltransferase share a common alpha subunit. *Cell* **65**, 429–434 (1991).

[22] Silvius, J. R. & l'Heureux, F. Fluorimetric evaluation of the affinities of isoprenylated peptides for lipid bilayers. *Biochemistry* **33**, 3014–3022 (1994).

[23] Hancock, J. F., Paterson, H. & Marshall, C. J. A polybasic domain or palmitoylation is required in addition to the CAAX motif to localize p21ras to the plasma membrane. *Cell* **63**, 133–139 (1990).

[24] Magee, A. I., Gutierrez, L., McKay, I. A., Marshall, C. J. & Hall, A. Dynamic fatty acylation of p21N-ras. *The EMBO Journal* **6**, 3353 (1987).

[25] Buss, J. E. & Sefton, B. M. Direct identification of palmitic acid as the lipid attached to p21ras. *Molecular and Cellular Biology* **6**, 116–122 (1986).

[26] Hancock, J. F., Magee, A. I., Childs, J. E. & Marshall, C. J. All ras proteins are polyisoprenylated but only some are palmitoylated. *Cell* **57**, 1167–1177 (1989).

[27] Rocks, O. *et al.* An acylation cycle regulates localization and activity of palmitoylated Ras isoforms. *Science* **307**, 1746–1752 (2005).

[28] Rocks, O. *et al.* The palmitoylation machinery is a spatially organizing system for peripheral membrane proteins. *Cell* **141**, 458–471 (2010).

[29] Apolloni, A., Prior, I. A., Lindsay, M., Parton, R. G. & Hancock, J. F. H-ras but not K-ras traffics to the plasma membrane through the exocytic pathway. *Molecular and Cellular Biology* **20**, 2475–2487 (2000).

[30] Zimmermann, G. *et al.* Small molecule inhibition of the KRAS-PDEδ interaction impairs oncogenic KRAS signalling. *Nature* **497**, 638–642 (2013).

[31] Vartak, N. & Bastiaens, P. Spatial cycles in G-protein crowd control. *The EMBO Journal* **29**, 2689–2699 (2010).

[32] Dekker, F. J. *et al.* Small-molecule inhibition of APT1 affects Ras localization and signaling. *Nature chemical biology* **6**, 449–456 (2010).

[33] Ahearn, I. M. *et al.* FKBP12 binds to acylated H-ras and promotes depalmitoylation. *Molecular cell* **41**, 173–185 (2011).

[34] Baines, A. T., Xu, D. & Der, C. J. Inhibition of Ras for cancer treatment: the search continues. *Future medicinal chemistry* **3**, 1787–1808 (2011).

[35] Wang, W., Fang, G. & Rudolph, J. Ras inhibition via direct Ras binding–is there a path forward? *Bioorganic & medicinal chemistry letters* **22**, 5766–5776 (2012).

[36] Spiegel, J., Cromm, P. M., Zimmermann, G., Grossmann, T. N. & Waldmann, H. small-molecule modulation of ras signaling. *Nature chemical biology* **10**, 613–622 (2014).

[37] Lito, P., Rosen, N. & Solit, D. B. Tumor adaptation and resistance to RAF inhibitors. *Nature medicine* **19**, 1401–1409 (2013).

[38] James, G. L. *et al.* Benzodiazepine peptidomimetics: potent inhibitors of Ras farnesylation in animal cells. *Science* **260**, 1937–1942 (1993).

[39] Kohl, N. E. *et al.* Selective inhibition of ras-dependent transformation by a farnesyltransferase inhibitor. *Science* **260**, 1934–1937 (1993).

[40] Kohl, N. E. *et al.* Inhibition of farnesyltransferase induces regression of mammary and salivary carcinomas in ras transgenic mice. *Nature medicine* **1**, 792–797 (1995).

[41] Berndt, N., Hamilton, A. D. & Sebti, S. M. Targeting protein prenylation for cancer therapy. *Nature Publishing Group* **11**, 775–791 (2011).

[42] Rowell, C. A., Kowalczyk, J. J., Lewis, M. D. & Garcia, A. M. Direct Demonstration of Geranylgeranylation and Farnesylation of Ki-Ras in Vivo. *Journal of Biological Chemistry* **272**, 14093–14097 (1997).

[43] Whyte, D. B. *et al.* K- and N-Ras Are Geranylgeranylated in Cells Treated with Farnesyl Protein Transferase Inhibitors. *Journal of Biological Chemistry* **272**, 14459–14464 (1997).

[44] Lerner, E. C. *et al.* Inhibition of the prenylation of K-Ras, but not H- or N-Ras, is highly resistant to CAAX peptidomimetics and requires both a farnesyltransferase and a geranylgeranyltransferase I inhibitor in human tumor cell lines. *Oncogene* **15**, 1283–1288 (1997).

[45] Sun, J., Qian, Y., Hamilton, A. D. & Sebti, S. M. Both farnesyltransferase and geranylgeranyltransferase I inhibitors are required for inhibition of oncogenic K-Ras prenylation but each alone is sufficient to suppress human tumor growth in nude mouse xenografts. *Oncogene* **16**, 1467–1473 (1998).

[46] Hedberg, C. *et al.* Development of highly potent inhibitors of the Ras-targeting human acyl protein thioesterases based on substrate similarity design. *Angewandte Chemie (International ed. in English)* **50**, 9832–9837 (2011).

[47] Rusch, M. *et al.* Identification of Acyl Protein Thioesterases 1 and 2 as the Cellular Targets of the Ras-Signaling Modulators Palmostatin B and M. *Angewandte Chemie (International ed. in English)* **50**, 9838–9842 (2011).

[48] Dekker, F. J. & Hedberg, C. Small molecule inhibition of protein depalmitoylation as a new approach towards downregulation of oncogenic Ras signalling. *Bioorganic & medicinal chemistry* **19**, 1376–1380 (2011).

[49] Long, J. Z. & Cravatt, B. F. The metabolic serine hydrolases and their functions in mammalian physiology and disease. *Chemical reviews* **111**, 6022–6063 (2011).

[50] Bachovchin, D. A. & Cravatt, B. F. The pharmacological landscape and therapeutic potential of serine hydrolases. *Nature Reviews Drug Discovery* **11**, 52–68 (2012).

[51] Simon, G. M. & Cravatt, B. F. Activity-based proteomics of enzyme superfamilies: serine hydrolases as a case study. *Journal of Biological Chemistry* **285**, 11051–11055 (2010).

[52] Zhang, Y. Y. & Dennis, E. A. Purification and characterization of a lysophospholipase from a macrophage-like cell line P388D1. *Journal of Biological Chemistry* (1988).

[53] Stafford, R. E., Zhang, Y. Y., Deems, R. A. & Dennis, E. A. Kinetic analysis and substrate specificity of a lysophospholipase from the macrophage-like cell line P388D1. *Biochimica et biophysica acta* **1167**, 43–48 (1993).

[54] Wang, A., Deems, R. A. & Dennis, E. A. Cloning, expression, and catalytic mechanism of murine lysophospholipase I. *The Journal of biological chemistry* **272**, 12723–12729 (1997).

[55] Portilla, D. & Dai, G. Purification of a novel calcium-independent phospholipase A2 from rabbit kidney. *The Journal of biological chemistry* **271**, 15451–15457 (1996).

[56] Portilla, D. *et al.* cDNA cloning and expression of a novel family of enzymes with calcium-independent phospholipase A2 and lysophospholipase activities. *Journal of the American Society of Nephrology : JASN* **9**, 1178–1186 (1998).

[57] Sugimoto, H., Hayashi, H. & Yamashita, S. Purification, cDNA Cloning, and Regulation of Lysophospholipase from Rat Liver. *Journal of Biological Chemistry* **271**, 7705–7711 (1996).

[58] Wang, A. & Dennis, E. A. Mammalian lysophospholipases. *Biochimica et biophysica acta* **1439**, 1–16 (1999).

[59] Toyoda, T., Sugimoto, H. & Yamashita, S. Sequence, expression in Escherichia coli, and characterization of lysophospholipase II. *Biochimica et biophysica acta* **1437**, 182–193 (1999).

[60] Duncan, J. A. & Gilman, A. G. A cytoplasmic acyl-protein thioesterase that removes palmitate from G protein alpha subunits and p21(RAS). *The Journal of biological chemistry* **273**, 15830–15837 (1998).

[61] Duncan, J. A. & Gilman, A. G. Characterization of Saccharomyces cerevisiae acyl-protein thioesterase 1, the enzyme responsible for G protein alpha subunit deacylation in vivo. *The Journal of biological chemistry* **277**, 31740–31752 (2002).

[62] Devedjiev, Y., Dauter, Z., Kuznetsov, S. R., Jones, T. L. & Derewenda, Z. S. Crystal structure of the human acyl protein thioesterase I from a single X-ray data set to 1.5 A. *Structure* **8**, 1137–1146 (2000).

[63] Hirano, T. *et al.* Thioesterase activity and subcellular localization of acylprotein thioesterase 1/lysophospholipase 1. *Biochimica et biophysica acta* **1791**, 797–805 (2009).

[64] Davda, D. & Martin, B. R. Acyl protein thioesterase inhibitors as probes of dynamic S-palmitoylation. *MedChemComm* **5**, 268–276 (2014).

[65] Bürger, M. *et al.* Crystal structure of the predicted phospholipase LYPLAL1 reveals unexpected functional plasticity despite close relationship to acyl protein thioesterases. *Journal of Lipid Research* **53**, 43–50 (2012).

[66] Verkruyse, L. A. & Hofmann, S. L. Lysosomal targeting of palmitoyl-protein thioesterase. *The Journal of biological chemistry* **271**, 15831–15836 (1996).

[67] Hellsten, E., Vesa, J., Olkkonen, V. M., Jalanko, A. & Peltonen, L. Human palmitoyl protein thioesterase: evidence for lysosomal targeting of the enzyme and disturbed cellular routing in infantile neuronal ceroid lipofuscinosis. *The EMBO Journal* **15**, 5240–5245 (1996).

[68] Yeh, D. C., Duncan, J. A., Yamashita, S. & Michel, T. Depalmitoylation of endothelial nitric-oxide synthase by acyl-protein thioesterase 1 is potentiated by Ca(2+)-calmodulin. *The Journal of biological chemistry* **274**, 33148–33154 (1999).

[69] Flaumenhaft, R., Rozenvayn, N., Feng, D. & Dvorak, A. M. SNAP-23 and syntaxin-2 localize to the extracellular surface of the platelet plasma membrane. *Blood* **110**, 1492–1501 (2007).

[70] Tian, L., McClafferty, H., Knaus, H.-G., Ruth, P. & Shipston, M. J. Distinct acyl protein transferases and thioesterases control surface expression of calcium-activated potassium channels. *Journal of Biological Chemistry* **287**, 14718–14725 (2012).

[71] Wang, W., Runkle, K. B., Terkowski, S. M., Ekaireb, R. I. & Witze, E. S. Protein Depalmitoylation Is Induced by Wnt5a and Promotes Polarized Cell Behavior. *Journal of Biological Chemistry* **290**, 15707–15716 (2015).

[72] Tomatis, V. M., Trenchi, A., Gomez, G. A. & Daniotti, J. L. Acyl-protein thioesterase 2 catalyzes the deacylation of peripheral membrane-associated GAP-43. *PloS one* **5**, e15045 (2010).

[73] Manna, J. D. *et al.* Identification of the Major Prostaglandin Glycerol Ester Hydrolase in Human Cancer Cells. *Journal of Biological Chemistry* (2014).

[74] Kong, E. *et al.* Dynamic Palmitoylation Links Cytosol-Membrane Shuttling of Acyl-protein Thioesterase-1 and Acyl-protein Thioesterase-2 with That of Proto-oncogene H-Ras Product and Growth-associated Protein-43. *Journal of Biological Chemistry* **288**, 9112–9125 (2013).

[75] Vartak, N. *et al.* The autodepalmitoylating activity of APT maintains the spatial organization of palmitoylated membrane proteins. *Biophysical journal* **106**, 93–105 (2014).

[76] Lin, D. T. S. & Conibear, E. ABHD17 proteins are novel protein depalmitoylases that regulate N-Ras palmitate turnover and subcellular localization. *eLife* **4** (2015).

[77] Pleiss, J., Fischer, M., Peiker, M. & Thiele, C. Lipase engineering database: understanding and exploiting sequence–structure–function relationships. *Journal of Molecular Catalysis B: Enzymatic* **10**, 491–508 (2000).

[78] Fischer, M. & Pleiss, J. The Lipase Engineering Database: a navigation and analysis tool for protein families. *Nucleic Acids Research* **31**, 319–321 (2003).

[79] Lenfant, N. *et al.* ESTHER, the database of the α/β-hydrolase fold superfamily of proteins: tools to explore diversity of functions. *Nucleic Acids Research* **41**, D423–9 (2013).

[80] Marchot, P. & Chatonnet, A. Enzymatic activity and protein interactions in alpha/beta hydrolase fold proteins: moonlighting versus promiscuity. *Protein and peptide letters* **19**, 132–143 (2012).

[81] Verger, R. 'Interfacial activation'of lipases: facts and artifacts. *Trends in Biotechnology* (1997).

[82] Schmid, R. D. & Verger, R. Lipases: Interfacial Enzymes with Attractive Applications. *Angewandte Chemie* **37**, 1608–1633 (1998).

[83] Brocca, S. *et al.* Sequence of the lid affects activity and specificity of Candida rugosa lipase isoenzymes. *Protein science : a publication of the Protein Society* **12**, 2312–2319 (2003).

[84] Chahiniana, H. & Sarda, L. Distinction Between Esterases and Lipases: Comparative Biochemical Properties of Sequence-Related Carboxylesterases. *Protein and peptide letters* **16**, 1149–1161 (2009).

[85] Laizure, S. C., Herring, V., Hu, Z., Witbrodt, K. & Parker, R. B. The role of human carboxylesterases in drug metabolism: have we overlooked their importance? *Pharmacotherapy* **33**, 210–222 (2013).

[86] Pesaresi, A. & Lamba, D. Insights into the fatty acid chain length specificity of the carboxylesterase PA3859 from Pseudomonas aeruginosa: A combined structural, biochemical and computational study. *Biochimie* **92**, 1787–1792 (2010).

[87] Bürger, M. *Development of a Gfp-Based Assay for the Structural Elucidation of Nuclear Pore Proteins And Biochemical and Structural Investigations of Acyl Protein Thioesterases* . Ph.D. thesis, Universität Osnabrück (2012).

[88] Porfetye, A. *Structural and Biochemical Characterization of the Lid-Loop of Acyl Protein Thioesterase* . Ph.D. thesis, TU Dortmund (2016).

[89] Zimmermann, T. J. *et al.* Boron-based inhibitors of acyl protein thioesterases 1 and 2. *Chembiochem : a European journal of chemical biology* **14**, 115–122 (2013).

[90] Deck, P. *et al.* Development and biological evaluation of acyl protein thioesterase 1 (APT1) inhibitors. *Angewandte Chemie (International ed. in English)* **44**, 4975–4980 (2005).

[91] Biel, M., Deck, P., Giannis, A. & Waldmann, H. Synthesis and evaluation of acyl protein thioesterase 1 (APT1) inhibitors. *Chemistry (Weinheim an der Bergstrasse, Germany)* **12**, 4121–4143 (2006).

[92] Hadváry, P., Lengsfeld, H. & Wolfer, H. Inhibition of pancreatic lipase in vitroby the covalent inhibitor tetrahydrolipstatin. *Biochemical Journal* **256**, 357–361 (1988).

[93] Borgström, B. Mode of action of tetrahydrolipstatin: a derivative of the naturally occurring lipase inhibitor lipstatin. *Biochimica et biophysica acta* **962**, 308–316 (1988).

[94] Xu, J. *et al.* Inhibiting the palmitoylation/depalmitoylation cycle selectively reduces the growth of hematopoietic cells expressing oncogenic Nras. *Blood* **119**, 1032–1035 (2012).

[95] Vujic, I. *et al.* Acyl protein thioesterase 1 and 2 (APT-1, APT-2) inhibitors palmostatin B, ML348 and ML349 have different effects on NRAS mutant melanoma cells. *Oncotarget* (2016).

[96] Jennings, B. C. *et al.* 2-Bromopalmitate and 2-(2-hydroxy-5-nitro-benzylidene)-benzo[b]thiophen-3-one inhibit DHHC-mediated palmitoylation in vitro. *Journal of Lipid Research* **50**, 233–242 (2009).

[97] Pedro, M. P. *et al.* 2-Bromopalmitate Reduces Protein Deacylation by Inhibition of Acyl-Protein Thioesterase Enzymatic Activities. *PloS one* **8**, e75232 (2013).

[98] Adibekian, A. *et al.* Confirming Target Engagement for Reversible Inhibitors in Vivo by Kinetically Tuned Activity-Based Probes. *Journal of the American Chemical Society* **134**, 10345–10348 (2012).

[99] Bhairi, S. M. A Guide to the Properties and Uses of Detergents in Biological Systems. Calbiochem-Novabiochem (2001).

[100] Wolfbeis, O. S. & Koller, E. Fluorimetric assay of hydrolases at longwave excitation and emission wavelengths with new substrates possessing unique water solubility. *Analytical biochemistry* **129**, 365–370 (1983).

[101] Koller, E. & Wolfbeis, O. S. Photometric and fluorometric continuous kinetic assay of acid phosphatases with new substrates possessing longwave absorption and emission maxima. *Analytical biochemistry* **143**, 146–151 (1984).

[102] Koller, E. & Wolfbeis, O. S. Verfahren zur Herstellung von neuen Pyrensulfonsaeurederivaten. *Patentschrift AT385755B* 1–10 (1986).

[103] Koller, E. & Wolfbeis, O. S. Pyrenexulfonic acids useful in fluorescent lipid probes. *United States Patent 4,844,841* 1–9 (1989).

[104] Maron, S. H., Elder, M. E. & Ulevitch, I. N. Determination of Surface Area and Particle Size of Synthetic Latex by Adsorption .6. Critical Micelle Concentrations of Various Emulsifiers in Latex. *Journal of Colloid Science* **9**, 382–384 (1954).

[105] Thongngam, M. & McClements, D. J. Influence of pH, ionic strength, and temperature on self-association and interactions of sodium dodecyl sulfate in the absence and presence of chitosan. *Langmuir : the ACS journal of surfaces and colloids* **21**, 79–86 (2005).

[106] Lakowicz, J. R. *Principles of fluorescence spectroscopy* (New York, New York, 2006), 3rd edn.

[107] Birks, J. B. Excimers. *Reports on progress in physics* (1975).

[108] Winnik, F. M. Photophysics of preassociated pyrenes in aqueous polymer solutions and in other organized media. *Chemical reviews* (1993).

[109] Haedler, A. T. *et al.* Controlling the π-stacking behavior of pyrene derivatives: influence of H-bonding and steric effects in different states of aggregation. *Chemphyschem : a European journal of chemical physics and physical chemistry* **14**, 1818–1829 (2013).

[110] Hanhoff, T., Lücke, C. & Spener, F. Insights into binding of fatty acids by fatty acid binding proteins. *Molecular and cellular biochemistry* **239**, 45–54 (2002).

[111] Smathers, R. L. & Petersen, D. R. The human fatty acid-binding protein family: evolutionary divergences and functions. *Human genomics* **5**, 170–191 (2011).

[112] Storch, J. & McDermott, L. Structural and functional analysis of fatty acid-binding proteins. *Journal of Lipid Research* **50 Suppl**, S126–31 (2009).

[113] Ionescu, L. G., Tokuhiro, T., Czerniawski, B. J. & Smith, E. S. Formation of Micelles of Cetyltrimethylammonium Bromide in Water-Dimethyl Sulfoxide Solutions. *Solution Chemistry of ...* 487–496 (1979).

[114] Harutyunyan, L. R. & Markarian, S. A. Effect of dimethylsulfoxide and diethylsulfoxide on micellization and viscometric properties of cetylpyridinium bromide aqueous solutions - ScienceDirect. *Journal of Molecular Liquids* (2011).

[115] Vuppugalla, R., Chang, S.-Y., Zhang, H., Marathe, P. H. & Rodrigues, D. A. Effect of commonly used organic solvents on the kinetics of cytochrome P450 2B6- and 2C8-dependent activity in human liver microsomes. *Drug metabolism and disposition: the biological fate of chemicals* **35**, 1990–1995 (2007).

[116] Bjorkling, F. *et al.* The Effect of Dimethylsulfoxide on the Enantioselectivity in the Pig-Liver Esterase Catalyzed-Hydrolysis of Dialkylated Propanedioic Acid Dimethyl Esters. *Bioorganic Chemistry* **14**, 176–181 (1986).

[117] Tanizawa, K. & Bender, M. L. The application of insolubilized alpha-chymotrypsin to kinetic studies on the effect of aprotic dipolar organic solvents. *The Journal of biological chemistry* **249**, 2130–2134 (1974).

[118] van der Vusse, G. J. Albumin as Fatty Acid Transporter. *Drug Metabolism and Pharmacokinetics* **24**, 300–307 (2009).

[119] Bar-Even, A. *et al.* The moderately efficient enzyme: evolutionary and physicochemical trends shaping enzyme parameters. *Biochemistry* **50**, 4402–4410 (2011).

[120] Schomburg, I., Hofmann, O., Baensch, C., Chang, A. & Schomburg, D. Enzyme data and metabolic information: BRENDA, a resource for research in biology, biochemistry, and medicine. *Gene Funct. Dis.* **3-4**, 109–118 (2000).

[121] Placzek, S. *et al.* BRENDA in 2017: new perspectives and new tools in BRENDA. *Nucleic Acids Research* **45**, D380–D388 (2017).

[122] Matveeva, E. G., Morisseau, C., Goodrow, M. H., Mullin, C. & Hammock, B. D. Tryptophan fluorescence quenching by enzyme inhibitors as a tool for enzyme active site structure investigation: epoxide hydrolase. *Current pharmaceutical biotechnology* **10**, 589–599 (2009).

[123] Hauptman, J. Orlistat: selective inhibition of caloric absorption can affect long-term body weight. *Endocrine* **13**, 201–206 (2000).

[124] Liu, N.-N. *et al.* Full-Length cDNA Cloning, Molecular Characterization and Differential Expression Analysis of Lysophospholipase I from Ovis aries. *International journal of molecular sciences* **17** (2016).

[125] Huopalahti, R., López-Fandiño, R., Anton, M. & Schade, R. Chapter 1 - Composition and Structure of Hen Egg Yolk . In *Bioactive Egg Compounds*, 1–6 (Springer Science & Business Media, 2007).

[126] Palacios, L. E. & Wang, T. Egg-yolk lipid fractionation and lecithin characterization. *Journal of the American Oil Chemists' Society* **82**, 571–578 (2005).

[127] Aparicio, R. & Harwood, J. (eds.) *Handbook of Olive Oil* (Springer US, Boston, MA, 2013).

[128] Wymann, M. P. & Schneiter, R. Lipid signalling in disease. *Nature Publishing Group* **9**, 162–176 (2008).

[129] Moerke, N. J. *Fluorescence Polarization (FP) Assays for Monitoring Peptide-Protein or Nucleic Acid-Protein Binding*, vol. 9 (John Wiley & Sons, Inc., Hoboken, NJ, USA, 2009).

[130] Hilvert, D. Critical analysis of antibody catalysis. *Annual review of biochemistry* **69**, 751–793 (2000).

[131] Tanaka, F. Catalytic Antibodies as Designer Proteases and Esterases. *Chemical reviews* **102**, 4885–4906 (2002).

[132] Yin, J., Andryski, S. E., Beuscher, A. E., Stevens, R. C. & Schultz, P. G. Structural evidence for substrate strain in antibody catalysis. *Proceedings of the National Academy of Sciences of the United States of America* **100**, 856–861 (2003).

[133] Jones, G., Willett, P. & Glen, R. C. Molecular recognition of receptor sites using a genetic algorithm with a description of desolvation. *Journal of molecular biology* **245**, 43–53 (1995).

[134] Jones, G., Willett, P., Glen, R. C., Leach, A. R. & Taylor, R. Development and validation of a genetic algorithm for flexible docking. *Journal of molecular biology* **267**, 727–748 (1997).

[135] Verdonk, M. L., Cole, J. C., Hartshorn, M. J., Murray, C. W. & Taylor, R. D. Improved protein-ligand docking using GOLD. *Proteins* **52**, 609–623 (2003).

[136] Wallace, A. C., Laskowski, R. A. & Thornton, J. M. LIGPLOT: a program to generate schematic diagrams of protein-ligand interactions. *"Protein Engineering, Design and Selection"* **8**, 127–134 (1995).

[137] Adibekian, A. *et al.* Optimization and characterization of a triazole urea dual inhibitor for lysophospholipase 1 (LYPLA1) and lysophospholipase 2 (LYPLA2). *Probe Report - Molecular Libraries* 1–42 (2011).

[138] Krissinel, E. & Henrick, K. Inference of macromolecular assemblies from crystalline state. *Journal of molecular biology* **372**, 774–797 (2007).

[139] Koshland, D. E. Application of a Theory of Enzyme Specificity to Protein Synthesis. *Proceedings of the National Academy of Sciences of the United States of America* **44**, 98–104 (1958).

[140] Sharma, P. K. & Bhatia, S. R. Effect of anti-inflammatories on Pluronic F127: micellar assembly, gelation and partitioning. *International journal of pharmaceutics* **278**, 361–377 (2004).

[141] Segel, I. H. *Enzyme Kinetics.* Behavior and Analysis of Rapid Equilibrium and Steady-State Enzyme Systems (Wiley-Interscience, 1993).

[142] Shoichet, B. K. Interpreting steep dose-response curves in early inhibitor discovery. *Journal of Medicinal Chemistry* **49**, 7274–7277 (2006).

[143] Jeffrey, G. A. *An Introduction to Hydrogen Bonding* (Oxford University Press on Demand, 1997).

[144] Won, S. J. *et al.* Molecular Mechanism for Isoform-Selective Inhibition of Acyl Protein Thioesterases 1 and 2 (APT1 and APT2). *ACS chemical biology* **11**, 3374–3382 (2016).

[145] Khan, F. I. *et al.* The Lid Domain in Lipases: Structural and Functional Determinant of Enzymatic Properties. *Frontiers in bioengineering and biotechnology* **5**, 16 (2017).

[146] Johnson, M. *et al.* NCBI BLAST: a better web interface. *Nucleic Acids Research* **36**, W5–9 (2008).

[147] The UniProt Consortium. UniProt: the universal protein knowledgebase. *Nucleic Acids Research* **45**, D158–D169 (2017).

[148] Kemp, L. E. *et al.* Characterisation of a serine hydrolase targeted by acyl protein thioesterase inhibitors in Toxoplasma gondii. *The Journal of biological chemistry* **288**, 27002–27018 (2013).

[149] Cheng, Y. & Prusoff, W. H. Relationship between the inhibition constant (K1) and the concentration of inhibitor which causes 50 per cent inhibition (I50) of an enzymatic reaction. *Biochemical pharmacology* **22**, 3099–3108 (1973).

[150] Li, F., Xia, Y., Meiler, J. & Ferguson-Miller, S. Characterization and Modeling of the Oligomeric State and Ligand Binding Behavior of Purified Translocator Protein 18 kDa from Rhodobacter sphaeroides. *Biochemistry* **52**, 5884–5899 (2013).

[151] Sreerama, N. & Woody, R. W. Computation and analysis of protein circular dichroism spectra. *Methods in enzymology* **383**, 318–351 (2004).

[152] Kabsch, W. XDS. *Acta crystallographica. Section D, Biological crystallography* **66**, 125–132 (2010).

[153] McCoy, A. J. *et al.* Phaser crystallographic software. *Journal of applied crystallography* **40**, 658–674 (2007).

[154] Evans, P. R. An introduction to data reduction: space-group determination, scaling and intensity statistics. *Acta crystallographica. Section D, Biological crystallography* **67**, 282–292 (2011).

[155] Murshudov, G. N. *et al.* REFMAC5 for the refinement of macromolecular crystal structures. *Acta crystallographica. Section D, Biological crystallography* **67**, 355–367 (2011).

[156] Emsley, P., Lohkamp, B., Scott, W. G. & Cowtan, K. Features and development of Coot. *Acta crystallographica. Section D, Biological crystallography* **66**, 486–501 (2010).

[157] Ramachandran, G. N., Ramakrishnan, C. & Sasisekharan, V. Stereochemistry of polypeptide chain configurations. *Journal of molecular biology* **7**, 95–99 (1963).

[158] Berman, H., Henrick, K. & Nakamura, H. Announcing the worldwide Protein Data Bank. *Nature structural biology* **10**, 980 (2003).

[159] Higgins, D. G. & Sharp, P. M. CLUSTAL: a package for performing multiple sequence alignment on a microcomputer. *Gene* **73**, 237–244 (1988).

[160] Larkin, M. A. *et al.* Clustal W and Clustal X version 2.0. *Bioinformatics (Oxford, England)* **23**, 2947–2948 (2007).

7 Acknowledgements

First of all, I gratefully thank my thesis advisor Dr. Ingrid Vetter for her continuous support and patient guidance throughout the years. I really appreciated her impartial view on new ideas, the critical discussions about them and also the freedom to follow new approaches. I would like to thank Prof. Dr. Roland Winter for assuming the responsibility and taking the time of being the first reviewer of my thesis. As well I thank Prof. Dr. Andrea Musacchio for his ideas and critical comments on my research project and for the time to serve as second evaluator of my PhD thesis.

Very special thanks go out to our technician Patricia Stege. Her contribution to this thesis is tremendous, not only because of the production of almost all investigated proteins in this thesis, but also for her engagement to keep the lab running smoothly and on a high standard. I thank my colleagues Arthur Porfetye for his guidance and support especially at the beginning of my thesis and Kathrin Estel for her ideas and collaboration in the lab and in the office. I very much appreciated the help of Philipp Ochtrop with the organic synthesis of new substrate compounds and the support of Janine Schulte-Zweckel in performing ESI-MS analysis.

I would like to thank all past and present members of Department 1 at the MPI Dortmund for the great working atmosphere, the discussion of scientific ideas and the support and guidance in case of problems. Special thanks to Arsen Petrovic, Giuseppe Ciossani, Satya Pentakota, Marion Pesenti, Charlotte Smith and Siva Jaganathan. They always had an a sympathetic ear for any kind of problem and were ready at any time for fruitful scientific and non-scientific discussions. Additionally to that, I would like to acknowledge Jenny Keller also for proofreading my thesis and spending her free time on thinking of critical and helpful comments, suggestions and ideas to improve my research and written thesis. I thank the members of the LabDinner Organizing Team, Claudia Breit and Franziska Müller, for keeping this social event running all the time.

Lastly, I thank the people outside the scientific world, my wife, my family and my friends for their continuous support and assistance throughout these years. This work would not have been possible in this way without you!

Affidavit

Eidesstattliche Versicherung (Affidavit)

Baumeister, Stefan — Name, Vorname (Surname, first name)

116936 — Matrikel-Nr. (Enrolment number)

Belehrung:

Wer vorsätzlich gegen eine die Täuschung über Prüfungsleistungen betreffende Regelung einer Hochschulprüfungsordnung verstößt, handelt ordnungswidrig. Die Ordnungswidrigkeit kann mit einer Geldbuße von bis zu 50.000,00 € geahndet werden. Zuständige Verwaltungsbehörde für die Verfolgung und Ahndung von Ordnungswidrigkeiten ist der Kanzler/die Kanzlerin der Technischen Universität Dortmund. Im Falle eines mehrfachen oder sonstigen schwerwiegenden Täuschungsversuches kann der Prüfling zudem exmatrikuliert werden, § 63 Abs. 5 Hochschulgesetz NRW.

Die Abgabe einer falschen Versicherung an Eides statt ist strafbar.

Wer vorsätzlich eine falsche Versicherung an Eides statt abgibt, kann mit einer Freiheitsstrafe bis zu drei Jahren oder mit Geldstrafe bestraft werden, § 156 StGB. Die fahrlässige Abgabe einer falschen Versicherung an Eides statt kann mit einer Freiheitsstrafe bis zu einem Jahr oder Geldstrafe bestraft werden, § 161 StGB.

Die oben stehende Belehrung habe ich zur Kenntnis genommen:

Official notification:

Any person who intentionally breaches any regulation of university examination regulations relating to deception in examination performance is acting improperly. This offence can be punished with a fine of up to EUR 50,000.00. The competent administrative authority for the pursuit and prosecution of offences of this type is the chancellor of the TU Dortmund University. In the case of multiple or other serious attempts at deception, the candidate can also be unenrolled, Section 63, paragraph 5 of the Universities Act of North Rhine-Westphalia.

The submission of a false affidavit is punishable.

Any person who intentionally submits a false affidavit can be punished with a prison sentence of up to three years or a fine, Section 156 of the Criminal Code. The negligent submission of a false affidavit can be punished with a prison sentence of up to one year or a fine, Section 161 of the Criminal Code.

I have taken note of the above official notification.

Dortmund,

Ort, Datum (Place, date)

Unterschrift (Signature)

Titel der Dissertation:
(Title of the thesis):

Investigation of the properties of Acyl Protein Thioesterases and their role in Ras depalmitoylation

Ich versichere hiermit an Eides statt, dass ich die vorliegende Dissertation mit dem Titel selbstständig und ohne unzulässige fremde Hilfe angefertigt habe. Ich habe keine anderen als die angegebenen Quellen und Hilfsmittel benutzt sowie wörtliche und sinngemäße Zitate kenntlich gemacht.
Die Arbeit hat in gegenwärtiger oder in einer anderen Fassung weder der TU Dortmund noch einer anderen Hochschule im Zusammenhang mit einer staatlichen oder akademischen Prüfung vorgelegen.

I hereby swear that I have completed the present dissertation independently and without inadmissible external support. I have not used any sources or tools other than those indicated and have identified literal and analogous quotations.

The thesis in its current version or another version has not been presented to the TU Dortmund University or another university in connection with a state or academic examination.*

*Please be aware that solely the German version of the affidavit ("Eidesstattliche Versicherung") for the PhD thesis is the official and legally binding version.

Dortmund,

Ort, Datum (Place, date)

Unterschrift (Signature)